**United States Geological Survey**
**Award No. 02HQGR0022**

# INCORPORATION OF EARTHQUAKE SOURCE, PROPAGATION PATH, AND SITE UNCERTAINTIES INTO ASSESSMENT OF LIQUEFACTION POTENTIAL; PHASE 1, VALIDATION

Dr. Walter Silva
Dr. Bob Darragh
Dr. Nick Gregor
Pacific Engineering and Analysis
311 Pomona Avenue
El Cerrito, CA 94530
510-528-2821(ph); 510-528-2135 (fax)
**pacificengineering@juno.com**

## TABLE OF CONTENTS

**1.0 INTRODUCTION AND BACKGROUND**

1.1 Current Methods of Evaluating Liquefaction Potential
1.2 Uncertainties in Estimating Liquefaction Resistance
1.3 Accommodating Uncertainties In Estimating Cyclic Demands
1.4 Project Objectives

**2.0 APPROACH**

2.1 Equivalent-Linear Site Response Analyses
2.2 RVT Based Computational Scheme
2.3 Accommodating Parametric Uncertainty In Site Response Analyses
2.4 Accommodating Uncertainty In Control Motions For Future Earthquakes
2.5 Computing Estimates of Cyclic Capacities (CRR)
2.5.1 Computing Estimates of Cyclic Capacities (CRR)
2.5.2 Standard Penetration Resistance Approach For Estimating CRR
2.5.3 Empirical Correlations of CPT With Shear-Wave Velocity
2.5.4 Standard Penetration Resistance Approach For Estimating The Intensity Boundary ($I_{hb}$)

**3.0 RESULTS**

3.1 Evaluation of Appropriate $N_{1,60}$ and Shear-Wave Velocity Correlation Model
3.2 Site Specific Analyses
3.2.1 1989 M 6.9 Loma Prieta Earthquake, Alameda Naval Air Station
3.2.2 1989 M 6.9 Loma Prieta Earthquake, Emeryville Pacific Park Plaza
3.2.3 1989 M 6.9 Loma Prieta Earthquake, Oakland Outter Harbor Wharf
3.2.4 1989 M 6.9 Loma Prieta Earthquake, Oakland Title and Trust
3.2.5 1989 Loma Prieta Earthquake, Treasure Island
3.2.6 1979 M 6.5 Imperial Valley Earthquake, Wildlife Liquefaction Array.
3.2.7 1987 M 6.2 Elmore Ranch, Wildlife Liquefaction Array
3.2.8 1987 M 6.5 Superstition Hills(B) Earthquake, Wildlife Liquefaction Array
3.2.9 1987 M 6.5 Superstition Hills(B) Earthquake, Kornbloom Road
3.2.10 1994 M 6.7 Northridge Earthquake; Newhall West Pico Canyon, P-1
3.2.11 1994 M 6.7 Northridge Earthquake; Newhall West Pico Canyon, P-3
3.2.12 1999 M 7.6 Kocaeli, Turkey Earthquake, Adaparazi
3.2.13 Site Specific Analyses Conclusions

**TABLE OF CONTENTS (cont.)**

3.3 Regional Analyses, 1995 **M** 6.9 Kobe Earthquake
3.3.1 Strong Motion Information
3.3.2 Damage Summary
3.3.3 General Geotechnical Conditions
3.3.3.1 Available Borehole Data and Soil Profiles
3.3.3.2 Estimates of Soil Column and Crustal Shear Wave Velocities
3.3.3.3 Kappa and Q(f)
3.3.3.4 Simulated Motions for the Kobe, Nishinomiya, and Osaka Areas
3.3.4 Simulated Motions for the Kobe, Nishinomiya, and Osaka Areas

**4.0 CONCLUSIONS**

Acknowledgments
References
Tables
Figures

**ABSTRACT**

While the basic engineering approaches to evaluating liquefaction susceptibility are well established and validated, methods of estimating onset of liquefaction that properly incorporate variabilities in earthquake source, path, and site processes are needed to better assess risk levels and mitigate loss of life and property. An approach that rigorously captures uncertainties in assessing a soil's resistance to liquefaction in terms of cyclic demands is an essential step in better quantifying earthquake hazard and resulting risk to life and property, particularly for application to regional analyses (hazard maps). In this project, an approach which naturally accommodates variabilities that affect estimates of liquefaction triggering was validated at sites which did and did not liquefy during past earthquakes, based upon visual evidence. Both site-specific analyses as well as a regional analysis, for the Kobe and Osaka areas in Japan (1995 M 6.9 Kobe earthquake) were performed.

In the site-specific analyses, twelve case history sites (six earthquakes) were studied using available site specific information from detailed site investigations. At all the sites, comparisons were made between observations of whether or not the site liquefied and triggering estimates based on the Andrus and Stokoe (2000) shear-wave velocity based approach. Additional comparisons were made using updated SPT approaches of Seed et al. (2001) and Kayen and Mitchell (1997). For these SPT based methods, correlations between shear-wave velocity and $(N_1)_{60}$ values was used instead of measured SPT values. This approach was implemented to assess both the appropriateness of the three SPT shear-wave velocity models (Section 2.5.3) as well as the performance of the SPT methods for cases where only shear-wave velocity may be estimated. This would apply to regional mapmaking, for instance where surfical geology or NEHRP category based shear-wave velocity profiles (Silva et al., 2000) may be used to generate design motions and consistent liquefaction triggering maps. To validate this regional approach more directly, liquefaction triggering predictions were made for regions which suffered varying degrees of liquefaction during the 1995 **M** 6.9 Kobe, Japan earthquake. In this analysis, finite rupture simulations were used to directly accommodate aspects of rupture directivity, such as duration, on cyclic demands, on CSR and cumulative Arias Intensity. In this regional analysis, 654 sites were analyze and comparisons made between estimates of liquefaction triggering and areal surveys of sand boils as evidence of liquefaction.

In both the site specific and regional analyses, the Andrus and Stokoe (2000) shear-wave velocity approach worked well, accurately predicting cases (regions) where liquefaction occurred and cases (regions) where liquefaction was not observed. Comparisons with SPT based procedures, which included the recently updated CSR approach (Seed et al., 2001) and the Arias Intensity approach (Kayen and Mitchell, 1997), were also made. Both of these approaches are fundamentally based on SPT data and correlations with shear-wave velocity were used to estimate appropriate $(N_1)_{60}$ values. Both of these approaches produced acceptable results but worked less well than the shear-wave velocity method, probably due to the increased variability introduced through estimating $(N_1)_{60}$ values through shear-wave velocity. The $(N_1)_{60}$ and velocity correlations were used to assess these SPT approaches for regional applications, where generic shear-wave velocity models based on surficial geology or NEHRP category are more readily available than associations with $(N_1)_{60}$ values. Additionally, the methodology employed directly addresses the effects of parametric variability of site dynamic material properties on

cyclic demands in a statistically rigorous manner by randomly varying properties using correlation models based on analysis of various on a large number of measured shear-wave velocities. As a result, a fundamentally shear-wave velocity approach was used and variabilities propagated, via correlations, to variabilities in $(N_1)_{60}$ estimates. While the fundamentally shear-wave velocity based approach (Andrus and Stokoe, 2000) clearly was more accurate, the SPT approaches worked rather well, generally being conservative, considering SPT data were not used directly.

## 1.0 INTRODUCTION AND BACKGROUND

One of the most damaging aspects of earthquakes is liquefaction-induced ground failure. Under strong ground shaking, pore water pressure builds up in saturated unconsolidated soils. If the induced shear-strains are large enough over a long enough duration, the pore water pressure can equal or exceed the overburden pressure resulting in a loss of shear strength or soil failure (Seed and Idriss, 1971; Silver and Seed, 1971). On level ground, lifelines may fail and buildings sink or topple due to differential settlements and massive land slides can be induced on sloping ground. Recent earthquakes such as the M 7.6 Chi-Chi, Taiwan; M 7.5 Koaceli, Turkey; M 6.9 Kobe, Japan; M 6.7 Northridge; and M 6.9 Loma Prieta have resulted in hundreds of billions of dollars in damage and years of reconstruction with much of the loss attributed to liquefaction related effects. Relic liquefaction of past earthquakes have reveled massive zones of soil failure suggesting a reoccurrence of the 1812 New Madrid and 1886 Charleston earthquakes could result in catastrophic damage to the infrastructure and potential loss of life (Obermeier et al., 1984, 1985, 1986).

While the basic engineering approaches to evaluating liquefaction susceptibility are well established and validated, methods of estimating onset of liquefaction that properly incorporate uncertainties in earthquake source, path, and site processes are needed to better assess risk levels and mitigate loss of life and property. An approach that rigorously captures uncertainties in assessing a soil's resistance to liquefaction in terms of cyclic demands is an essential step in better quantifying earthquake hazard and resulting risk to life and property.

Ground shaking and fault displacement from large earthquakes also cause heavy damage when they occur in or near metropolitan areas, but the uncertainties associated with their predictions are reasonably well characterized, particularly in tectonically active regions. There are many hundreds of recordings of ground shaking covering rupture distances of 1 to 200 km, varying site conditions from rock to soft soil and, for crustal sources, magnitudes ranging from about 4.5 to 7.5. Additionally, there has been no shortage of theoretical models developed and validated with varying degrees of sophistication in source, path, and site processes. These studies have produced predictive relations for both tectonically active and cratonic regions as well as subduction zones, quantifying strong ground shaking <u>and</u> its uncertainty and how they relate to magnitude, distance, and site condition. Because these ground motion relations characterize not only expected values of response spectral ordinates but their uncertainties as well, decisions regarding levels of risk to structures and lifelines are possible. Additionally fully probabilistic ground shaking hazard assessments, now the standard of practice, can reliably estimate any fractile of expected ground shaking, fully accommodating uncertainties in earthquake sources (locations, magnitudes, and likelihoods of occurrence) as well as ground motions or shaking levels, conditional on **M**, *D*, and site condition (Abrahamson and Shedlock, 1997).

While noteable efforts have been made to characterize the probability of liquefaction (Haldar and Tang, 1979; McGuire et al., 1979; Elton and Hamou, 1990; Power et al., 1991), conditional on soil column susceptibility (Liao et al., 1988) and magnitude (Loertscher and Youd, 1994; Youd and Idriss, 1997; Seed et al., 2001), the effects of uncertainties in source, path, and site processes

on the onset of liquefaction have largely been ignored (Yegian and Whitman, 1978; Atkinson et al., 1984; Kavazanjian et al., 1985; Rockaway et al., 1997; Kayen and Mitchell, 1997; Andrus et al., 2004)). The current state of practice in assessing the onset of liquefaction is fundamentally deterministic (National Research Council, 1985; Glaser and Chung, 1995; Youd and Idriss, 1997) and relies on estimates of expected peak accelerations (generally median values), soil properties (SPT, CPT, shear-wave velocity, Andrus et al., 1999), and empirical comparisons to case history data (CRR). Generally no formal accommodation for variabilities in the ground shaking, soil material properties, or empirical observations of case histories are accommodated in estimates of the onset of liquefaction. As a result, the methodology, by design, is conservative (Silva and Costantino, 1999) with the degree of conservatism largely unquantified. A first step in formally accounting for uncertainty in the prediction of liquefaction resistance is to incorporate source, path, and site process parametric variabilities into estimates of the seismic demands as well as capacities. This will allow more informed and rational decisions regarding risk levels to be made, an essential element in reducing losses due to earthquakes.

## 1.1 Current Methods of Evaluating Liquefaction Potential

The current state of practice in predicting liquefaction resistance of soils in the United States and much of the world is the method pioneered by H. Seed (Seed and Idriss, 1971; Martin et al., 1975; Youd and Idriss, 1997). In this approach, termed the simplified procedure, blow count from the Standard Penetration Test (SPT) is correlated with a parameter representing the seismic demands on the soil. The demands are expressed as the ratio of the average seismic induced shear-stress to the total vertical effective stress within a liquefiable zone, generally within about 50 ft of the surface,

$$CSR = \frac{\tau_{xy}}{\sigma_v^1} \qquad \text{(Seed and Idriss, 1971)} \qquad (1).$$

In practice, demands are usually computed using approximate relations between surface peak acceleration and at-depth cyclic shear stress (Seed and Idriss, 1971; Seed et al., 1983; Youd and Idriss, 1997; Seed et al., 2001).

Analyses of case histories for sites that had liquefied and those that did not, but could have, results in a reasonably good separation between the liquefied and non-liquefied sites, with a deterministic boundary defined as the soils capacity to resist liquefaction or cyclic resistance ratio (CRR) (Youd and Idriss, 1997). Demands (CSR) that exceed the capacity (CRR) result in a factor of safety (CRR/CSR) less than 1 and liquefaction may be expected to occur. The capacity for a given soil deposit is either empirical (case histories, Figure 1) or determined from stress controlled laboratory testing procedures. Both capacities and demands depend upon soil properties such as relative density, fines content (particle size), clay content, geologic age and water content (depth of water table), degree of over consolidation, cementation, previous liquefaction history as well as amplitude and duration of earthquake excitation.

Subsequent to the introduction of the simplified procedure in 1971, the approach has been updated and revised a number of times (Seed, 1979; Seed and Idriss, 1982; Seed et al., 1983;

Youd and Idriss, 1997), with the most recent cast in a probabilistic framework (Seed et al., 2001). Correlations based on the Cone Penetration Test (CPT; Robertson and Canpanella, 1985), the Becker Penetration Test (BPT), as well as shear-wave velocity have been developed over the interveaning years (Youd and Idriss, 1997; Andrus et al., 1999; Andrus and Stokoe, 2000). All of these field measurements provide an indication of the soil's relative density. Relative density along with saturation conditions, effective stress, and grain size determine the soil's resistance to liquefaction, in terms of the cyclic resistance ratio (CRR).

As an alternative to shear stress, shear strain has been shown to be the fundamental controlling factor controlling the buildup of pore water pressure during cyclic loading (Dobry et al., 1981; 1982). An alternative strain based procedure for assessing the liquefaction potential of a soil was developed by Dobry et al. (1982) where

$$Es = \int \tau_{xy} \, d\gamma_{xy} \tag{2}$$

is the strain energy (generally expressed in PSI) and $\tau_{xy}$ and $\gamma_{xy}$ are the induced cyclic shear-stresses and strains respectively. As in the stress based approach, the strain energy density is evaluated over the depth of the liquefiable zone. This approach, although fundamentally sound, has not been widely applied among the geotechnical community.

More recently, an approach based on the energy content of ground shaking through Arias Intensity has been proposed as a measure of seismic demand (Davis and Berrill, 1978; Kayen and Mitchell, 1997). Rather than using either the stress or strain based approaches (Equation 1 or 2), Kayen and Mitchell (1997) correlated liquefaction resistance with the total horizontal component Arias Intensity

$$I_h = I_{xx} + I_{yy} = \frac{\pi}{2g}\left[\int a_x^2(t)\, dt + \int a_y^2(t)\, dt\right] \tag{3}$$

averaged over the liquefiable zone (depth range) in the soil column. The usual units used are m/sec (or cm/sec) and the integral expressions are a direct measure of the cumulative energy absorbed by a set of single degree of freedom lightly damped oscillators. As with the stress and strain based approaches, analyses of empirical case histories showed that liquefied and non-liquefied sites separate out, similar to Figure 1 with $I_h$ replacing CSR defining an equivalent Intensity resistance ratio and a means of assessing the onset of liquefaction based on capacity (resistance to liquefaction) and demand (energy input to the soil column).

The ground motion intensity approach is intuitively appealing as one expects that intensity or energy is a fundamental measure of demands or loads placed on a soil column. However, intensity is also fundamentally a nonlinear parameter and how soil columns with varying dynamic material properties convert the energy into actual work in increasing pore pressure and rearranging particles is poorly understood and may lead to large uncertainties in predicting demands. As with the strain energy density, the use of ground motion energy parameterized through total Arias Intensity shows promise but has not enjoyed widespread use in the geotechnical engineering practice.

## 1.2 Uncertainties in Estimating Liquefaction Resistance

The liquefaction resistance of soils is related to numerous geological, compositional, and state factors (Kramer, 1996). Geological factors include the age of the soil deposit, depositional environment, and hydrological conditions. In general, Holocene-age deposits are more prone to liquefaction than Pleistocene-age soils. Liquefaction occurs in saturated, cohesionless soils and thus depth to the groundwater table is an important consideration in identifying soils that are susceptible to liquefaction. Compositional factors that influence liquefaction resistance include grain size parameters such as the fines content and fabric-related parameters such as cementation. Finally, state factors such as the density, current state of stress, and stress history also have an important influence on liquefaction resistance. To the extent that these soil properties vary spatially, the liquefaction resistance will also vary.

## 1.3 Accommodating Uncertainties In Estimating Cyclic Demands

The stress, strain, and energy approaches to predicting the onset of liquefaction all share common features in estimating seismic demands: both dynamic material properties as well as the character of the seismic loads (stress time histories) are controlling factors. As a result, uncertainty and randomness (epistemic and aleatory variability, Roblee et al., 1996) in dynamic material properties as well as control motions should be accommodated in estimating cyclic demands. An approach that properly accommodates variability will not only result in fractiles for deterministic estimates of demands, from which more informed risk decisions can be made, but provide a more rational basis for fully probabilistic assessments of liquefaction potential. The incorporation of parametric variability allows statistically rigorous assessments to be made of which parameters or suites of parameters control the cyclic demands. With this information, one can rationally design site sampling and testing programs to achieve desired degrees of accuracy as well as ascertain obtainable levels of accuracy, given the variability in control motions. Additionally one can easily evaluate the robustness or sensitivity to input parameters of the three currently available approaches to computing demands. This aspect alone may be significant as a lack of robustness in demand estimates must be compensated by increased accuracy in estimating capacity, since the factor of safety, or estimator of liquefaction likelihood, is the ratio of capacity to demand.

## 1.4 Project Objectives

The objective of this project is to evaluate qualitatively how well the Andrus and Stokoe (2000) shear-wave velocity based technique, coupled with parametric variations in dynamic material properties, works in predicting the onset of liquefaction. The validation compares predictions of liquefaction triggering at specific sites which did and did not liquefy during past earthquakes. As part of the validation, predictions of liquefaction triggering using factor of safety estimates computed from the shear-wave velocity technique are also compared to estimates from the recently updated CSR (Seed et al., 2001) as well as the Arias Intensity (Kayen and Mitchell, 1997) approaches.

In addition to the site-specific liquefaction analyses, comparisons are also made with areas which suffered varying degrees of liquefaction during the 1995 **M** 6.9 Kobe, Japan earthquake.

## 2.0 APPROACH

### 2.1 Equivalent-Linear Site Response Analyses

Each of the approaches to estimating the onset of liquefaction require site response analyses, either on a case by case basis or in developing simplified procedures, which assume generic material properties (Seed and Idriss, 1971; Kayen and Mitchell, 1997; Youd and Idriss, 1997; Seed et al., 2001). Given the seismic loads (control motions or motions input at the base of the soil column), the site response analyses accommodate vertically varying dynamic material properties as well as material nonlinearities. Generally vertically propagating shear-waves are assumed and nonlinear site response is approximated through the equivalent-linear approach.

The equivalent-linear approach, in its present form, was introduced by Seed and Idriss (1970). This scheme is a particular application of the general equivalent-linear theory developed by Iwan (1967). Basically, the approach is to approximate a second order nonlinear equation, over a limited range of its variables, by a linear equation. Formally this is done in such a way that the average of the difference between the two systems is minimized. This was done in an ad-hoc manner for ground response modeling by defining an effective strain which is assumed to exist for the duration of the excitation. This value is usually taken as 65% (although other values have been used) of the peak time-domain strain calculated at the midpoint of each layer, using a linear analysis. Modulus reduction and hysteretic damping curves are then used to define new parameters for each layer based on the effective strain computations. The linear response calculation is repeated, new effective strains evaluated, and iterations performed until the changes in parameters are below some tolerance level. Generally a few iterations are sufficient to achieve a strain-compatible linear solution. This stepwise analysis procedure was formalized into a one-dimensional, vertically propagating shear-wave code called SHAKE (Schnabel et al., 1972). Subsequently, this code has easily become the most widely used analysis package for one-dimensional site response calculations.

The advantages of the equivalent-linear approach are that parameterization of complex nonlinear soil models is avoided and the mathematical simplicity of a linear analysis is preserved. A truly nonlinear approach requires the specification of the shapes of hysteresis curves and their cyclic dependencies through an increased number of material parameters. In the equivalent-linear methodology the soil data are utilized directly and, because at each iteration the problem is linear and the material properties are frequency independent, the damping is rate independent and hysteresis loops close.

Careful validation exercises between equivalent-linear and fully nonlinear formulations using recorded motions from 0.05 to 0.50g showed little difference in results (EPRI, 1993; NUREG/CR-6728). Both formulations compared very favorably to recorded motions suggesting both the adequacy of the vertically propagating shear-wave model and the approximate equivalent-linear formulation. While the assumptions of vertically propagating shear-waves and equivalent-linear soil response certainly represent approximations to actual conditions, their combination has achieved demonstrated success in modeling observations of site effects and represent a stable, mature, and reliable means of estimating the effects of site conditions on strong ground motions (Schnabel et al., 1972; Silva et al., 1988; Schneider et al., 1993; EPRI,

1993; Silva et al., 1997).

To accommodate both uncertainty and randomness in dynamic material properties, SHAKE analyses are typically done for the best estimate shear-wave velocity profile as well as upper- and lower-range profiles. The upper- and lower-ranges are usually specified as twice and one-half the best estimate shear-wave moduli. Depending upon the nature of the structure, the final design spectrum or cyclic demands are then based upon an envelope or average of the analyses.

## 2.2 RVT Based Computational Scheme

The computational scheme employed to compute the site response for this proposed work uses an alternative approach employing random vibration theory (RVT; Boore, 1983). In this approach the control motion power spectrum is propagated through the one-dimensional soil profile using the plane-wave propagators of Silva (1976). In this formulation only SH waves are considered. Arbitrary angles of incidence may be specified but normal incidence is generally used.

In order to treat possible material nonlinearities, an RVT based equivalent-linear formulation is employed. Random process theory is used to predict peak time domain values of shear-strain based upon the shear-strain power spectrum. In this sense the procedure is analogous to the program SHAKE except that peak shear-strains in SHAKE are measured in the time domain. The purely frequency domain approach obviates a time domain control motion and, perhaps just as significant, eliminates the need for a suite of analyses based on different input motions. This arises because each time domain analysis may be viewed as one realization of a random process. Different control motion time histories reflecting different time domain characteristics but with nearly identical response spectra can result in different nonlinear and equivalent-linear response. In this case, several realizations of the random process must be sampled to have a statistically stable estimate of site response. The realizations are usually performed by employing different control motions with approximately the same level of peak accelerations and response spectra.

In the case of the frequency domain approach, the estimates of peak shear-strain as well as oscillator response are, as a result of the random process theory, fundamentally probabilistic in nature. For fixed material properties, stable estimates of site response can then be obtained with a single run and no time history is required. In this approach, RVT is used to estimate peak shear stresses to provide estimates for CSR values (Equation 1) and strain energy (Equation 2) as well as Arias Intensity (Equation 3). Because the RVT approach is configured to compute values for an average horizontal component (Boore, 1983), a factor of two is currently used to approximately accommodate the total (sum of both horizontal components, Equation 3) Arias Intensity. Future validation studies comparing predicted with observed total Arias Intensity are planed to develop an empirical scale factor.

## 2.3 Accommodating Parametric Uncertainty In Site Response Analyses

In the context of the RVT equivalent-linear approach, a more robust method of incorporating variability of dynamic material properties into the computed response has been developed.

Because analyses with multiple time histories are not required, parametric variability can be accurately assessed through a Monte Carlo approach by randomly varying dynamic material properties. This results in median as well as other fractile levels (e.g. $16^{th}$, mean, $84^{th}$) of smooth response spectra at the surface of the site as well as liquefaction parameters with depth. The availability of fractile levels reflecting variability in dynamic material properties then permits a more rational basis for selecting levels of risk.

In order to randomly vary the shear-wave velocity profile, a profile randomization scheme has been developed which varies both layer velocity and thickness. The randomization is based on a correlation model developed from an analysis of variance on about 500 measured shear-wave velocity profiles (EPRI, 1993; Silva et al., 1997). Profile depth (depth to competent material) is also varied on a site specific basis using a uniform distribution. The depth range is generally selected to reflect expected variability over the area considered as well as uncertainty in the estimation of depth to competent material.

To accommodate variability in modulus reduction and hysteretic damping curves on a generic basis, the curves are independently randomized about base case values. A log normal distribution is assumed with a $\sigma_{ln}$ of 0.30 at a cyclic shear strain of $3 \times 10^{-2}$%. These values are based on an analysis of variance of a suite of laboratory test results. An upper and lower bound truncation of $2\sigma$ is used to prevent modulus reduction or damping models that are not physically possible. The random curves are generated by sampling the transformed normal distribution with a $\sigma_{ln}$ of 0.30, computing the change in normalized modulus reduction or percent damping at $3 \times 10^{-2}$% shear strain, and applying this factor at all strains. The random perturbation factor is reduced or tapered near the ends of the strain range to preserve the general shape of the base case curves (Silva, 1992; EPRI, 1993).

## 2.4 Accommodating Uncertainty In Control Motions For Future Earthquakes

For model derived control motions in future applications of the liquefaction triggering methodology for either site specific analyses or in producing maps for areal applications (e.g. HAZUS), uncertainties in source and path parameters are accommodated by randomly varying their values following empirical distributions (EPRI, 1993; Toro et al., 1997). In this validation project involving past earthquakes, the source and path processes are fixed and recorded motions were used at sites where they were available. For these cases shallow deconvolution analyses (Silva et al., 1986) of the average horizontal component response spectra were used to estimate median values of the ground motions and liquefaction parameters. In this process, RVT spectral matching of the response spectra (5% damped) was used to develop power spectra which was then propagated through the soil column using equivalent-linear analyses.

For cases where near by recorded motions were not available, kinematics finite fault simulations were used to generate the site-specific motions as well as liquefaction parameters. For these cases, published slip models as well as regional crustal and Q(f) models were used to generate motions at the base of the soil columns.

To accommodate liquefaction triggering assessments for future earthquakes, both the point source (Boore 1983; 1986; Schneider et al., 1993) and finite-source stochastic models (Silva et

al., 1990; Schneider et al., 1993; Atkinson and Silva, 1997, 2000; Schneider et al., 2000) have been combined with RVT equivalent-linear site response to enable randomly varying source, path, and site parameters in a convenient manner. Both combined models have recently been validated by modeling recorded motions at over 500 sites from 18 earthquakes (**M** 5 to 7.5) at rupture distances ranging from 1 to 480 km and for very stiff to very soft site conditions (Silva et al., 1997).

The point-source model forms the basis for the currently available attenuation relations for the central and eastern United States (Abrahamson and Shedlock, 1997; Toro and Silva, 2001; Toro et al., 1997; EPRI, 1993) and the finite-source model has been used to develop attenuation relations for subduction zone earthquakes (Youngs et al., 1997; Wong et al., 2000; Gregor et al., 2002) as well as scenario earthquake shaking maps for Portland (Wong et al., 2000), Salt Lake City (Wong et al., 2001a), Albuquerque (Wong et al., 2001b), and the San Francisco Bay Area (Schneider et al., 2000).

For the point-source model, source and path parameters that are generally varied include stress drop, Q(f), kappa (considered a path parameter when coupled to equivalent-linear site response), and source depth (EPRI, 1993; Toro et al., 1997). For the finite-source for large earthquakes, point-source stress drop and source depth are replaced by varying slip models as well as nucleation points (Silva, 1992; Roblee et al., 1996; Schneider et al., 2000; Atkinson and Silva, 1997, 2000). Source ruptures for a given scenario (**M**) are randomly initiated at hypocenters along the length of the fault, representing scenarios ranging from unilateral ruptures in opposite directions and various bilateral ruptures in between. The hypocenters are randomized within a nucleation zone (rectangle) which comprises the bottom half and to within 10% of the ends of the rupture surface. The sample distribution of hypocenters is used to model potential variations in source directivity. To represent other random effects of the rupture process, each scenario is generated from a suite of randomly selected slip distributions. The random slip models are generated using a simulation scheme that preserves asperity statistics such as size and number, given a rupture area. The statistics are based on slip models derived from modeling strong ground motions (Abrahamson et al., 1994). Generally 30 realizations are sampled to develop mean estimates as well as standard deviations of the parameters of interest.

## 2.5 Computing Estimates of Cyclic Capacities (CRR)

For this study, the CRR for the soils was determined using the shear-wave velocity profiles as fundamental parameters along with the measured or estimated fines content (i.e., content of soil particles smaller than the 0.075 mm). Standard penetration resistance is estimated using published correlations with shear-wave velocity (Section 2.5.3). Use of the more widespread approach in estimating cyclic demands such as cone penetration tests would have involved developing median values of tip resistance as well as statistical models for the soil profiles analyzed as well as correlations with shear-wave velocity (the fundamental site parameter randomized to capture site variability). The availability and maturity of statistical models for the variability of shear-wave velocities and layer thickness and nonlinear dynamic material properties were compelling arguments for implementing a fundamentally shear-wave velocity approach to estimate cyclic capacities. It is recognized that other engineering approaches for determining the liquefaction resistance of soils may be considered more applicable on a site-

specific basis. In future studies, it may be desirable to evaluate the liquefaction resistance using correlations with either the SPT or CPT in areas where substantial data are available to develop local or regional correlation models.

A particularly attractive advantage in using the shear-wave velocity approach in liquefaction assessment is that it is straightforward and it directly accommodates profile parametric uncertainty in estimates of CRR as well as CSR and Arias Intensity in a statistically rigorous manner. Shear-wave velocity, as well as nonlinear dynamic material properties, can be incorporated in a manner consistent with developing the ground motions, arriving at median and fractile estimates of liquefaction potential that are consistent with median and fractile estimates of ground motions. This is particularly important for loss estimation analyses (e.g., HAZUS) that are fundamentally based on both ground motions and liquefaction (deformation), requiring the same fractile level for both hazards. The approach validated in this study accomplishes this objective in a statistically rigorous manner.

### *2.5.1 Shear-Wave Velocity Approach For Estimating CRR*

The equation for determining the CRR from shear-wave velocity is empirical, and based on case history studies at sites that did and did not liquefy during earthquakes (Andrus and Stokoe, 2000). The equation is:

$$CRR = 0.022\,(K_{a1}\,V_{S1}/100)^2 + 2.8\,[1/V^*_{S1} - K_{a1}\,V_{S1})-1/V^*_{S1}]\,MSF \cdot K_{a2} \qquad (4)$$

$$\begin{aligned} V_{S1}^* &= 215 \text{ m/sec} && FC \le 5\% \\ &= 215 - 0.5\,(FC - 5) \text{ m/sec} && 5\% < FC \le 35^o \\ &= 200 \text{ m/sec} && FC \ge 35\% \end{aligned} \qquad (5)$$

$$MSF = (M/7.5)^{-2.56} \qquad (6)$$

where $V_{S1}$ is the stress-corrected shear-wave velocity, $V^*_{S1}$ is the limiting upper value of $V_{S1}$ for cyclic liquefaction occurrence that depends on fines content $K_{a1,\,2}$ are correction factors for cementation and aging (Andrus and Stokoe, 2004). Because there is currently no widely accepted method for estimating $K_{a1,\,2}$ these values they were taken as 1 for this study.

Cyclic demands are expressed as the ratio of the average seismically-induced shear-stress to the vertical effective overburden stress within a liquefiable zone, generally within about 50 ft (15.2 m) of the ground surface:

$$CSR = \frac{\tau_{xy}}{\sigma'_v} \qquad \text{(Seed and Idriss, 1971)} \qquad (7)$$

In practice, demands are usually computed using approximate and generic relations between

surface peak acceleration and at-depth cyclic shear stress (Seed and Idriss, 1971; Seed *et al.*, 1983; Youd and Idriss, 1997; Seed et al., 2001).

The ratio of capacity (CRR) to demand (CSR) is termed the factor of safety (FS) against liquefaction. Liquefaction is predicted to occur when FS is at or below 1, and not to occur when it exceeds 1. To provide a more rational basis for assessing risk levels, Juang *et al.* (2000, 2001) cast the deterministic factor of safety into an expression for the probability of liquefaction ($P_L$). This mapping function is given by:

$$P_L = 1/(1 + (FS/0.78)^{3.5}) \quad (8)$$

It is based on the field performance data compiled by Andrus and Stokoe (2000) and accommodated the occurrence of sites that should have liquefied but did not, as well as those that did and provides the mechanism for translating liquefaction hazard into liquefaction risk. The Building Seismic Safety Council recommends a margin for the factor of safety against liquefaction of 1.2 to 1.5 for the simplified approach (Seed and Idriss, 1971). The corresponding probabilities are about 20% to 10% (Juang *et al.*, 2001). A factor of safety of 1 corresponds to a probability of about 30%.

For this study, the average CSR for the soil susceptible to liquefaction is determined during the site response analyses. Conditions which determine the CSR are: (1) cyclic shear stresses induced by the earthquake throughout the liquefiable zone, (2) $\sigma_{vo}$ – the total vertical overburden stress, and (3) $\sigma'_{vo}$ – the effective vertical overburden stress. Calculation of the total and effective stress conditions requires estimation of the density of the overlying material.

### *2.5.2 Standard Penetration Resistance Approach For Estimating CRR*

Probably the most widely accepted STP-based correlations is the classic deterministic relationship developed by Seed et al., (1984, 1985). The most recent update of the STP-based correlation, using a greatly expanded and carefully screened case history site and earthquake database, has been developed within a probabilistic framework (Seed et al., 2001). This new relation, cast in terms of $N_{1,60}$ or fully standardized corrected SPR blow counts, produces values for CRR as well as probability of liquefaction, conditional on $N_{1,60}$, CSR, moment magnitude, fines content, and effective overburden pressure. For the validation earthquakes and sites, this model was implemented using measured or inferred values of fines contents and suites of CSR values resulting from randomized dynamic material properties and equivalent-linear RVT site response analyses. $N_{1,60}$ values were estimated based on empirical correlations with shear-wave velocity (Section 2.5.3). For each earthquake and site considered in the validation exercise, median and $\pm$ 1 $\sigma$ estimates of the factor of safety (CRR/CSR) and probability of liquefaction were computed and compared to the consensus visual assessment of whether or not the site liquefied.

### *2.5.3 Empirical Correlations of CPT With Shear-Wave Velocity*

In the validation exercises three empirical blow-count/shear-wave velocity relations were used.

The first was developed by Iwasaki et al., (1987) for the Kobe and Osaka regions of Japan. The relation (Figure 2) is given by

$$V_S = 34.824 \cdot F \cdot (N + 1)^{0.244} \cdot P^{0.175} \tag{9}$$

F = 1.000 Clay

= 0.922 Sand

= 0.851 Clay

P = Mean Overburden Stress.

For this study F was taken as 0.922, the value for sands and N was assumed to reflect $N_{60}$.

The second relation (Imai and Tonouchi, 1982) is given by

$$V_S = 350\ N_{60}^{0.314}\ (\mathrm{ft/sec}) \tag{10}$$

and the third empirical relation is from Sykora and Stokoe (1983)

$$V_S = 350\ N_{60}^{0.27}\ (\mathrm{ft/sec}) \tag{11}$$

All three relations were inverted to estimate $N_{60}$ which was then corrected to $N_{1,\ 60}$ using site specific effective overburden stresses.

### *2.5.4 Standard Penetration Resistance Approach For Estimating The Intensity Boundary ($I_{hb}$)*

The Kayen and Mitchell (1997) Arias Intensity based approach has an intensity boundary ($I_{hb}$) given approximately by (Kayen; personal communication, 2004):

$$\begin{aligned} \mathrm{Log}\,(I_{hb}) = {} & -1.000002\,(N_{160CS})^4 + \\ & 0.0002\,(N_{160CS})^3 - \\ & 0.0031\,(N_{160CS})^2 - \\ & 0.6875\,(N_{160CS})^4 \end{aligned} \tag{12}$$

where $N_{160CS}$ is the $N_{160}$ value adjusted for clean sands. The recommended (Kayen and Mitchell, 1997) clean sand adjustment is

$$N_{1,\,fc} = N1\ (\text{silty sand}) + \Delta N_1 \qquad (13)$$

Where

$$\Delta N_1 = 0 \qquad FC \leq 5\%$$

$$= (FC - 5)\ (7/30) \quad 5\% < FC \leq 35\%$$

$$= 7 \qquad FC > 35\%.$$

Using Equation (12) median and $\pm$ 1 $\sigma$ estimates of the factor of safety (Ihb/Ih) are computed for each validation earthquake and site, using randomized shear-wave velocities to estimate $N_{160CS}$ values, coupled with equivalent-linear site response analyses to provide RVT estimates of Arias Intensity verses depth.

## 3.0 RESULTS

For the validation exercise, two types of comparisons were performed. The first represents site-specific applications wherein a suite of ten well studied sites (6 earthquakes) were analyzed for liquefaction triggering. The sites and earthquakes are listed in Tables 1 and 2. At these sites, comparisons were made between estimated factors of safety and probability of liquefaction and visual manifestations of liquefaction evidence taken from the literature.

In the second approach and comparison which is appropriate to liquefaction hazard mapping, factors of safety and probability of liquefaction are estimated within the Kobe and Osaka areas of Japan for the 1994 **M** 6.9 Kobe earthquake. These liquefaction triggering estimates are then compared to maps of airborne surveillance of liquefaction. This visual comparison reflects qualitative validation or assessment of how well the approach accommodates the areal patterns of observed liquefaction, both in extent as well as degree.

### 3.1 Evaluation of Appropriate $(N_1)_{60}$ and Shear-Wave Velocity Correlation Model

As presented in Section 2.5.3, three approaches or models are used to estimate SPT $(N_1)_{60}$ values conditional on shear-wave velocity (Section 2.5.3). To assess which correlation model is most appropriate for the study sites, comparisons are made between predicted and measured $(N_1)_{60}$ values using two case history data sets (Seed et al., 2001; Kayen and Mitchell, 1997). The results of the comparisons are presented in Figure 3 (listed in Table 2) and show that model 1, based on the Kobe and Osaka soils of Japan, result in the most accurate estimates of the actual SPT averaged over the critical zone at each site. While model 1 does appear to be biased somewhat low, with three predictions with a value near 6 compared to the case history site values near 12, it appears to produce estimates which are significantly more accurate than models 2 and 3, for this sparse data set. As a result of these comparisons, CRR (and probability

of liquefaction) and Ihb values are computed using model 1 for the Seed et al. (2001) and Kayen and Mitchell (1997) approaches, respectively.

## 3.2 Site Specific Analyses

For the sites analyzed the following suites of modulus reduction and damping curves were used. At the San Francisco Bay mud sites: Alameda Naval Air Station, Treasure Island, Emeryville, Oakland Title and Trust, and Oakland Outer Harbor, as well as Adaparazi, the EPRI (1993) curves were used for cohesionless soils, except for the hydraulic fill at Treasure Island where curves based on laboratory testing of those materials (EPRI, 1993) was used. For the cohesive soils at those sites, the mud and clay curves based on testing samples at Treasure Island (EPRI, 1993) were used. In the Imperial Valley, sites Kornbloon and the Wildlife Liquefaction Array used a suite of $G/G_{max}$ and hysteretic damping curves based on modeling strong motions recorded at the El Centro Array from the 1979 **M** 6.5 Imperial Valley Earthquake (Silva et al., 1997). At the West Pico Canyon sites (P-1 and P-3) the EPRI (1993) curves for cohesionless soils were used.

### *3.2.1 1989 M 6.9 Loma Prieta Earthquake, Alameda Naval Air Station*

At this site recorded motions are available and Figure 4a shows the 5% damped response spectra for the average horizontal component. Figures 4b and 4c show the shear-wave velocity profile to depths of 500 ft and 50 ft respectively (Gibbs et al. (1992)). Figure 4d and 4e show the variation with depth of peak acceleration and peak particle velocity respectively, median values and $\pm$ 1 $\sigma$ for a variation in site dynamic material properties. Because the motion is fixed at the surface and deconvolutional analyses are used to generate motions and stresses at depth, little variation is seen in the shallow motions. The peak cyclic shear strains (median and $\pm$ 1 $\sigma$) are shown in Figure 4f and the CSR estimates are shown in Figure 4g,with the horizontal lines indicating the critical layer or liquefiable zone. For the CSR estimates as well as all following parameters, values are computed and plotted only below the depth of the local water table (Table 2) and lognormal distributions are assumed. The following Figure, 4h, shows the estimated (model 1, Section 2.5.3) $(N_1)_{60}$ values and the Arias Intensity, for an average horizontal component, is shown in Figure 4i. Figure 4j shows the strain energy (in PSI) variation with depth and Figure 4k shows the factor of safety (FS) estimates computed using the Andrus and Stokoe (2000) shear-wave velocity approach, with median values varying from about 1 to nearly 0.5 in the critical zone. For the Kayen and Mitchell (1997) Arias Intensity approach, Figure 4l shows the corresponding median FS significantly less than 1 through the liquefiable zone and Figure 4m shows the FS computed for the Seed et al. (2001) SPT approach. For the three approaches, Table 2 shows FS values averaged over depth of 0.90, 0.41, and 0.98 for the AS (Andrus and Stokoe, 2000), KM (Kayen and Mitchell, 1997), and SEA (Seed et al., 2001) respectively. Since the site liquefied (Table 2) all three approaches successfully predict triggering with KM suggesting widespread liquefaction. Figure 4n and 4o show the corresponding estimates of the probabilities of liquefaction (median and $\pm$ 1 $\sigma$ values) for AS and SEA (logistic formulation not yet available for KM).

### *3.2.2 1989 M 6.9 Loma Prieta Earthquake, Emeryville Pacific Park Plaza*

Figure 5a show the average horizontal component response spectra computed for response spectra computed from recorded motions and Figures 5b and 5c show the shear-wave velocity profile (Gibbs et al. (1994)) to 500 ft and 50 ft respectively. The site was improved from a medium dense to an extremely dense condition by vibrocompaction probing (Michell and Wentz (1998). Motions, peak acceleration and peak particle velocity are shown in Figures 5d and 5e respectively with peak shear strain show in Figure 5f. Figure 5g show the variation of CSR estimates with depth as well as the critical zone while Figure 5h shows the $(N_1)_{60}$ estimates and Figures 5i and 5j show the Arias Intensity and strain energy respectively. The AS, KM, and SEA factors of safety are shown in Figures 5k, 5l 5m respectively. All three FS range with depth from 2 (the upper limit median value) to less than 1 near the bottom of the critical zone. Table 2 lists depth averaged values of 1.12, 0.91, and 1.20 for AS, KM, and SEA respectively. Since the site did not show evidence of liquefaction, the AS and SEA FS values, being greater than 1 reflect a successful prediction KM, with a FS of 0.91 expect liquefaction to occur based on the computed Arias Intensity demand. Since the RVT process is currently scaled for an average horizontal component and an ad-hoc factor of two was applied to estimate the total Arias Intensity (Equation 3, sum of both horizontal components), the factor of two may be biased high, resulting in too large a demand. As previously mentioned, empirical studies are planned to provide more accurate estimates of the scale factor. As with the previous site, Figure 5n and 5o show probabilities of liquefaction for AS and SEA respectively. These estimates vary with depth from 5% (the lower bound median) to over 20% at the base of the critical layer.

### *3.2.3 1989 M 6.9 Loma Prieta Earthquake, Oakland Outer Harbor Wharf*

As with the previous site, recorded motions are available and the average horizontal component response spectrum is shown in Figure 6a with the profile (Gibbs et al. (1992)) shown in Figures 6b and 6c over 500 ft and 50 ft respectively. Motions, peak acceleration and peak particle velocity are shown in Figures 6d and 6e respectively with peak shear strain shown in Figure 6f. Estimates of the CSR and critical layer are shown in Figure 6g and $(N_1)_{60}$ in Figure 6h. Figures 6i and 6j show Arias Intensity and strain energy, respectively with the AS, KM, and SEA factors of safety shown in Figures 6k, 6l, and 6m respectively. All three FS average over depth are less than 1 values of 0.68, 0.18, and 0.29 shown in Table 2, which indicates the site liquefied. All three relations then accurately portray an expectation of liquefaction. Probabilities of liquefaction (median estimates) average at or above 40 to 50% in the critical layer for both AS and SEA, Figures 6n and 6o respectively.

### *3.2.4 1989 M 6.9 Loma Prieta Earthquake, Oakland Title and Trust*

Figure 7a shows the average horizontal component response spectrum based on recorded motions and Figures 7b and 7c show the profile (Gibbs et al. (1993)), 500 ft and 50 ft respectively. Figures 7d and 7e show computed motions, peak acceleration and peak particle velocity respectively with Figure 7f showing peak cyclic strains. CSR and $(N_1)_{60}$ estimates are shown in Figures 7g and 7h respectively. The upper limit of $(N_1)_{60}$ was set at a value of 40 to avoid unrealistically high values from the correlations (Section 2.5.3). Arias Intensity and strain energy density estimates are shown in Figures 7i and 7j respectively with AS, KM, and SEA FS shown in Figures 7k, 7l, and 7m respectively. All three approaches give estimates of 2 (upper limit) consistent with the Table 2 indication of no liquefaction. Probabilities of liquefaction are

at 5% the analysis lower limit, Figures 7n and 7o for AS and SEA respectively.

### *3.2.5 1989 Loma Prieta Earthquake, Treasure Island*

The average horizontal component spectrum computed from recorded motions is shown in Figure 8a with the profile (Gibbs et al. (1992); U.S. Navy, personal communication (1995)) shown in Figures 8b and 8c over 500 ft and 50 ft respectively. Figures 8d and 8e show computed motions verses depth, peak acceleration and peak particle velocity respectively. Shear strain and CSR estimates are shown in Figures 8f and 8g respectively with $(N_1)_{60}$ values in Figure 8h. Arias Intensity and strain energy density are shown in Figures 8i and 8j respectively. FS for AS, KM, and SEA are shown in Figure 8k, 8l, and 8m respectively. Table 2 lists depth averaged (over the critical zone) respective values of 1.04, 0.65, and 1.25. Visual evidence show no liquefaction at the site with closest sand boils about 100m distance from the site (Power et al. (1998); Andrus and Stokoe (1993)). Clearly liquefaction of engineering significance did not occur at the site, supporting the AS and SEA FS values of 1.04 and 1.25 respectively. Various investigators (Idriss, 1990; de Alba et al. 1994) have suggested a liquefaction signature in the recorded motions by a loss in high frequency energy content beyond a certain time in the record. If this observation is valid, it suggests the site was close to liquefaction of engineering significance and a depth averaged FS close to 1 by AS is impressive. The low FS value of 0.65 for KM may be another artifact of our ad-hoc scale factor of 2, converting computed average horizontal component Arias Intensity to total (sum of both components) Arias Intensity. As with previous sites, liquefaction probabilities for AS and SEA are shown in Figures 8n and 8o.

### *3.2.6 1979 M 6.5 Imperial Valley Earthquake, Wildlife Liquefaction Array.*

At this site, recorded motions are not available and stochastic finite fault simulations are used to generate control motions at the base of the profile. The slip model used is from Hartzell and Heaton (1983) with a rupture velocity of 0.8 times the shear-wave velocity. A constant slip velocity model is assumed with a slip velocity of 61 cm/sec, based on validation exercises. The crustal model is from Hartzell and Heaton (1983) with the shallow velocities included from a generic shallow model (Silva et al., 1997). Figure 9a show the median and $\pm$ 1 $\sigma$ estimates of the average horizontal component response spectrum and Figures 9b and 9c show the profile (generic Imperial Valley) to 500 ft and 50 ft respectively. Computed motion estimates for peak acceleration and peak particle velocity are shown in Figure 9d and 9e respectively with shear strains and CSR estimates in Figures 9f and 9g respectively. Figures 9h, 9i, and 9j show estimates of $(N_1)_{60}$, Arias Intensity, and strain energy density respectively. FS for AS, KM, and SEA are shown in Figures 9k, 9l, and 9m respectively with all median values above 1, consistent with no liquefaction indicated in Table 2. The FS values above 1 are reflected in the low probabilities shown in Figures 9n and 9o, for approaches AS and SEA respectively.

### *3.2.7 1987 M 6.2 Elmore Ranch, Wildlife Liquefaction Array*

For this earthquake recorded motions are available and Figure 10a shows the average horizontal component response spectrum with the profile (generic Imperial Valley) shown in Figures 10b and 10c, to depths of 500 and 50 ft respectively. Figures 10d and 10e show motions, peak acceleration and peak particle velocity respectively with peak shear strain, CSR, and $(N_1)_{60}$

values shown in Figures 10f, 10g, and 10h respectively. Arias Intensity and strain energy density are shown Figures 10i and 10j respectively with FS for AS, KM, and SEA in Figures 10k, 10l, and 10m respectively. All three FS values are above 1, with respective depth averaged values very close at 1.48, 1.62, and 1.54, all consistent with the no liquefaction indication in Table 2. As with the previous earthquake, low probabilities (near 10%) are shown in Figures 10n and 10o, AS and SEA respectively.

### *3.2.8 1987 M 6.5 Superstition Hills(B) Earthquake, Wildlife Liquefaction Array*

As with the previous earthquake, recorded motions are available and Figure 11a shows the computed average horizontal component response spectrum. Figures 11b and 11c show the profile (generic Imperial Valley), 500 ft and 50 ft respectively. Figures 11d and 11e show motions, peak acceleration and peak particle velocity respectively with peak cyclic strains shown in Figure 11f. Figures 11g and 11h show CSR and $(N_1)_{60}$ estimates respectively with Figures 11i and 11j showing Arias Intensity and strain energy density respectively. FS for AS, KM, and SEA are shown in Figures 11k, 11l and 11m respectively. Respective depth averaged FS values listed in Table 2 are 1.0, 0.77, and 1.02 suggesting borderline liquefaction for AS and SEA, The lower 0.77 value for KM may again be a result of a high bias in the conversion from average component Arias Intensity to total Arias Intensity. However the site did liquefy (Table 2), but with modest pore pressure build-up (Holzer et al. (1989)), so a FS value of 0.77 is not inconsistent with observations. Probabilities of liquefaction are shown in Figures 11n and 11o, AS and SEA respectively, and average around 20%.

### *3.2.9 1987 M 6.5 Superstition Hills(B) Earthquake, Kornbloom Road*

Figure 12a shows the horizontal component response spectrum computed from recorded motions with the profile (generic Imperial Valley) shown in Figures 12b and 12c, to depths of 500 ft and 50 ft respectively. Figures 12d, 12e, and 12f show peak accelerations, peak particle velocities, and peak cyclic shear strains respectively Figures 12g and 12h show CSR and $(N_1)_{60}$ values respectively and Figures 12i and 12j show estimates of Arias Intensity and strain energy density respectively. FS estimates for AS, KM, SEA are shown in Figures 12k, 12l, and 12m respectively with all values at or above 1 and with respective critical depth averaged values (Table 2) of 1.49, 1.27, and 1.56, all consistent with the indicator of no liquefaction (Table 2), corresponding probabilities for AS and SEA are shown in Figures 12n and 12o respectively and range from about 10 to 20%.

### *3.2.10 1994 M 6.7 Northridge Earthquake; Newhall West Pico Canyon, P-1*

For this earthquake recorded motions are available and Figure 13a shows the average horizontal component spectrum with the profile (ROSRINE, 2004) to 500 ft and 50 ft shown in Figures 13b and 13c respectively. Motions, peak acceleration and peak particle velocities and strains are shown in Figures 13d, 13e, and 13f respectively. Figures 13g and 13h show CSR and $(N_1)_{60}$ values respectively with Figures 13i and 13j showing Arias Intensity and strain energy density respectively. FS estimates for AS, KM, and SEA are shown in Figures 13k, 13l, and 13m respectively with respective depth averaged median estimates (Table 2) of 1.10, 0.48, and 0.58. Since liquefaction was observed at this site (Table 2), the AS, FS of 1.10 appropriately reflects

the observations. Probabilities of liquefaction computed for AS and SEA are shown in Figures 13n and 13o respectively and are around 10% to 15% for AS and 20% to 30% for SEA.

### *3.2.11 1994 M 6.7 Northridge Earthquake; Newhall West Pico Canyon, P-3*

At this site recorded motions are not available. The average horizontal component spectrum computed from finite fault simulations is shown in Figure 14a with the profile to 500 ft and 50 ft (ROSRINE, 2004) shown in Figures 14b and 14c respectively. The finite fault simulations use the slip and crustal models of Wald et al. (1996). The rupture velocity is taken as 0.8 times the shear-wave velocity and a constant slip velocity model is assumed with a slip velocity of 63 cm/sec, based on validation exercises. Motions, peak acceleration and peak particle velocities and strains are shown in Figures 14d, 14e, and 14f respectively. Figures 14g and 14h show CSR and $(N_1)_{60}$ values respectively with Figures 14i and 14j showing Arias Intensity and strain energy density respectively. FS estimates for AS, KM, and SEA are shown in Figures 14k, 14l, and 14m respectively with respective depth averaged median estimates (Table 2) of 0.70, 0.42, and 0.37. Since liquefaction was observed at this site (Table 2), the FS estimates of less than 1 are consistent with observations. AS and SEA probabilities of liquefaction, Figures 14n and 14o respectively show values of about 30% and 50%, respectively.

### *3.2.12 1999 M 7.6 Kocaeli, Turkey Earthquake, Adaparazi*

Average horizontal component simulated motions for this site are shown in Figure 15a. The slip and crustal models are from (PEER, 2003 personal communication) with the rupture velocity taken as 0.8 times the shear-wave velocity and a constant slip velocity of 110 cm/sec, based on validation exercises. The soil profile is taken as a generic San Francisco Bay mud profile (Silva et al., 2001), based on observations of the site (Rathje, personal communication, 2002) and is shown in Figures 15b and 15c to depths of 500 ft and 50 ft respectively. Peak accelerations, peak particle velocities, and peak cyclic shear strains are shown in Figures 15d, 15e, and 15f respectively. CSR and $(N_1)_{60}$ estimates are shown in Figures 15g and 15h respectively with Arias Intensity and strain energy density shown in Figures 15i and 15j respectively. FS estimates for AS, KM, and SEA are shown in Figures 15km 15l, and 15m respectively. Respective depth averaged median estimates (Table 2) are 0.85, 0.34, and 0.64, all consistent with the observation of liquefaction (Table 2). Respective probabilities for AS and SEA are shown in Figures 15n and 15o and range, over depth, from about 10% to over 40%.

### *3.2.13 Site Specific Analyses Conclusions*

In this site-specific analyses, twelve case history sites (six earthquakes) were studied using available site specific information from detailed site investigations. At all the sites, comparisons were made between observations of whether or not the site liquefied and triggering estimates based on the Andrus and Stokoe (2000) shear-wave velocity based approach. Additional comparisons were made using updated SPT approaches of Seed et al. (2001) and Kayen and Mitchell (1997). For these SPT based methods, correlations between shear-wave velocity and $(N_1)_{60}$ values was used instead of measured SPT values. This approach was implemented to assess both the appropriateness of the three SPT shear-wave velocity models (Section 2.5.3) as well as the performance of the SPT methods for cases where only shear-wave velocity may be

estimated. This would apply to regional mapmaking, for instance where surfical geology or NEHRP category based shear-wave velocity profiles (Silva et al., 2000) may be used to generate design motions and consistent liquefaction triggering maps.

To summarize the results of the site-specific analyses, Figure 16a shows comparisons of predicted (FS) and observed occurrences of liquefaction at the twelve sites for the AS approach. In general, at all sites, the method shows FS greater than 1 where liquefaction was not observed. At sites where liquefaction occurred, the AS approach has only a single site with FS =1, borderline liquefaction, and all other sites are less than 1. For comparison, Figures 16b and 16c show the KM and SEA results respectively, both using estimates of $(N_1)_{60}$ from shear-wave velocity correlation model 1 (Equation 9). For KM, Figure 16b, two sites which did not liquefy show FS less than 1. As previously mentioned, this may be due to an inappropriate assumed ratio of 2 between average horizontal component and total (sum of both components) Arias Intensity. For the SEA approach Figure 16c shows a single site which did liquefy but with a FS slightly greater than 1. Both the AS and SEA approaches are considered to perform satisfactorily and results such as these can and should be employed generally to develop approach specific modeling uncertainties which <u>must</u> be included in future predictions of liquefaction triggering.

### 3.3 Regional Analyses, 1995 M 6.9 Kobe Earthquake

Recent recordings in the near-source regions of large earthquakes have shown differences in strong ground motion characteristics compared to more distant motions which are of significance to engineering design. Near-source motions (# 10 - 15 km) for large (**M** $ 6 ¼) earthquakes are typified in the time domain by short durations and, at intermediate-to-long periods, by rupture directivity. The effects of rupture directivity are to reduce durations and increase low-frequency spectral content for sites situated with significantly more rupture toward them than away. These effects are significant at close distances, particularly for vertical strike slip ruptures, and their influence on structures, slope stability, and liquefaction potential needs to be assessed. The recent occurrence of the Kobe earthquake, a large (**M** 6.9) predominately vertical strike slip earthquake, with both close-in and more distant firm and soft soil conditions and with mapped liquefaction zones, presents a unique opportunity to evaluate the combination of current approaches to assess liquefaction susceptibility with a finite-fault simulation procedure. The finite-fault simulation naturally accommodates the effects of rupture directivity and short durations for close-in sites, resulting in estimates of liquefaction parameters (cyclic stress ratios, Arias Intensity, and strain energies) appropriate for specific source-site geometries. The approach used in this evaluation is to compare regions of mapped liquefaction (or no liquefaction) to regions where liquefaction is predicted to be extensive, moderate, or not to occur. As part of a previous project (WES, 1999), a large number of SPT and boring log data were gathered and analyzed to develop areal distributions of shallow shear-wave velocity profiles and material descriptions over the wide study area comprising the cities of Kobe, Nishinomiya, and west Osaka. This approach has the advantage of statistical stability by evaluating several hundred sites subjected to varying levels of control motions but is limited by not considering detailed site specific information at each site location. The level of site information available for this study is not unlike the data generally available in the generation of liquefaction hazard maps.

The site response component of the simulations use a random vibration (RVT) equivalent-linear formulation (as in the site-specific analyses, Section 3.2). Since the methodology does not use time histories as control motions for the soil columns, control motion durations are naturally incorporated in the estimates of peak strains (stresses for the cyclic stress ratios) from the strain (stress) power spectra. Shorter control motion durations result in larger estimates of peak time domain motions, strains, and stresses for a given control motion power spectrum. Additionally, random process theory is used to estimate the Arias Intensity and the number of stress cycles over the duration (taken as the time interval between the 5% and 75% Arias Intensity).

### *3.3.1 Strong Motion Information*

Intensity estimates in the region affected by the event refer to the JMA intensity scale. A comparison of this intensity scale, consisting of eight levels of damage, with the Modified Mercalli system used in the United States is shown in Table 3 (Reiter, 1990). In the immediate vicinity of the epicenter at Awaji Island and downtown Kobe City, the intensity was indicated to reach levels 6 and 7, the most severe on the JMA scale. Strong motions caused by the earthquake were recorded at many locations, some of which are shown in Figure 17. Some of the recorded horizontal PGA's are shown on Figure 18. As may be noted, the largest recorded horizontal acceleration for which we have information is 833 gals (0.85g) and occurred at the Fukai station, a shallow soil site in Kobe City (Hamada et al., 1995).

### *3.3.2 Damage Summary*

The vast majority of structural damage occurred in the immediate vicinity of the fault zone from Awaji Island to downtown Kobe, Ashiya, Nishinomiya and Takarazuka cities. Away from the immediate fault region, the intensity levels decreased rapidly as did the damage. The outline of the JMA Intensity 7 zone is shown in Figure 19 (Kimura, 1996) which corresponds approximately to MMI IX. It is indicated that more than 30% of the residential damage occurred in this vicinity. Interestingly this high intensity zone roughly corresponds to the zone of soft soils which lies between rock and hard soils to the north and reclaimed land to the south (Figure 22) forming the edge of the Osaka basin. Depth to basement increases sharply from north to south and is rather uniform along the soft soil high damage zone (Kagawa et al., 1993). The confined high intensity zone may be attributed to shallow soil conditions (Suetomi and Yoshida, 1998) and/or deep basin edge effects (Kawase, 1996).

Soil liquefaction occurred in a large area along the coastline from Kobe to Osaka as well as at several inland locations. Aerial surveys (Hamada, et al., 1995) as well as ground inspection were used to map the zones in which surface expressions of liquefaction (sand boils, fissures, movement of seawalls, damage to embankments, etc.) could be determined. An approximate plot of the areas in which widespread liquefaction occurred as determined from the aerial photos is shown in Figure 20. These zones were generally restricted to the reclaimed lands and man_made islands of the Osaka Bay. Other more restricted areas in which sand boils were noted by field inspections occurred in the coastal zone further east of this area to sites well south of Osaka. Some liquefaction also was noted in inland sites at Nishinomiya and Takarazuka cities northeast of Kobe as well as along the Yodo River in Osaka.

At the artificial island called Port Island, major damage occurred in the northern half of the island which is generally associated with the widespread zones of liquefaction and dynamic settlements induced by the seismic motions. Port Island is a typical off_shore man_made island which was created by placing relatively uncompacted clean sands (weathered granite, Section 2) atop the existing soft silts and clays of the alluvial soils in the harbor. It was constructed in two stages, with the northern half being first constructed. The southern half of Port Island incorporated more effort to preconsolidate the dumped soils by a variety of soil improvement methods. Damage to the island corresponded to these zones, except for wharf areas where damage occurred along the entire island.

Failures also were reported at the site of small earth embankments in the Nishinomiya vicinity and descriptions of these failures are reported by Krinitzsky, et al. (1995). These small dams, known as the Koyoen dams, are part of a reservoir system a few kilometers from the edge of the epicentral region. They are reported to be 8m to 10m high and are approximately 75m long. They suffered extensive damage from the earthquake and the reservoir was empty at the time of inspection. No indications were provided of any additional damage from breaches in the retaining system. This inspection team also reported some damage to the portal structure and the lining of the Rokko Mountain tunnel of the Japan Rail's Shinkansen line. In the Nigawa area of Nishinomiya, a major slide failure occurred in a residential community causing the death of a number of people. Some additional slide areas were encountered near the fault zone on Awaji Island.

### *3.3.3 General Geotechnical Conditions*

The Osaka/Kobe region consists of a complex grouping of soils which varies significantly across the valley and has been significantly altered by the fault dislocations which have occurred over the centuries (Osaka Soil Foundation Map, 1987). The region consists of Holocene alluvial soils with fill around the margins of the bay, all underlain by diluvial (Pleistocene) soils forming a typical basin structure (Figure 21). Since the 1930's, it has been recognized that long term settlement and subsidence is a problem for the softer silt and clay soils in the region. This subsidence has been related to consolidation effects induced by extraction of ground water, which has been exacerbated by the industrialization which has occurred since WWII. Depending upon location, the soil profile consists of alternating layers of softer silt/clay and sands/gravels forming the typical delta formation. The bottom of the softer alluvial soils in the center of Osaka Bay is approximately 100m below average sea level at Osaka Port (O.P.) and occurs at the location of the old Osaka River basin.

The site of Kobe City is located at the southern foot of the Rokko Mountains and is approximately 3 km wide in the NS direction and about 20 km long in the EW direction. It consists of a coastal plain and lands reclaimed from the sea. The Rokko Mountains, with elevations of about 3,000 ft in the east and about 1,500 ft in the west, is composed of a relatively soft granite rock with many faults running generally in the EW direction. The various fault movement occurring over the centuries results in the sharp changes in elevation from the mountains to the bay. The Kobe city area is located in a region of steeply dipping granite basement, from the outcrops of the mountains in the north to the fill along the margins of Osaka Bay (Figure 21). This basin edge geometry is expected to result in large low-frequency

amplification of ground motions (Vidale, 1987; Vidale and Helmberger, 1988; Kawase, 1996).

The Rakko Mountain granite easily weathers and decomposes into the silty soil known as "Masado". It is characterized (Hamada, et al., 1995) by properties of low plasticity, low cohesion, high permeability and ease of erosion. These characteristics are different from those of Masado found in other regions around Osaka. Many alluvial fans have developed along the southern foot of the Rokko Mountains composed of coarse granite materials including sand, gravel and boulders which were transported by rivers heading to the bay.

Significant filling and creation of reclaimed lands of Osaka Bay began in the 1880's with construction of wharves and factories. As described by Hamada et al. (1995), a new reclamation project of cut and fill was conducted from 1953 to 1970, in which the fill material was excavated from the Rokko Mountains and dumped into the sea along the shoreline. The follow on stage of the project, including reclamation of both Port Island and Rokko Island, was initiated in 1966 to expand the port facilities. Similar filling operations have been carried out in the adjacent cities of Ashiya and Nishinomiya. In the filled operation, various methods of soil improvements were applied where major structures were built to accelerate consolidation of the marine clays as well as compaction of the newly dumped fills.

Based on the descriptions provided by Shibata et al. (1996), the effects of the earthquake revealed that the loosely placed weathered Masado granite soil containing gravel sizes can liquefy. This soil was used heavily in the first phase of construction of Port Island as well as at parts of Rokko Island to the east. The results of cyclic triaxial tests indicate that the Masado gravelly soils can liquefy even at relatively high relative densities since the soil possesses contractive behavior during shear straining. Along the coastline to the east towards Osaka, at the mouth of rivers to the bay, the fine grained alluvial surface soils are relatively uniform grained and show tendency to easily liquefy in laboratory cyclic experiments.

#### ***3.3.3.1 Available Borehole Data and Soil Profiles***

A substantial number of borings and standard penetration tests (SPT) have been performed for various projects in the region to clarify foundation conditions beneath structures in the survey area (Figure 22). A number of these are reprinted in Hamada et al. (1995) which were in turn compiled from other sources. As part of an earlier study on assessing liquefaction during the Kobe earthquake (WES, 1999), a large number of soil boring data (SPT and boring logs) were assembled and analyzed to develop shallow generic category shear-wave velocity profiles and material descriptions.

On the basis of these data, the soil sites were divided in three relatively broad categories as shown in Figure 22. The harder sites (termed diluvium) occur at the higher elevations along the mountain side with the softer sites (alluvium) occurring at the base of the mountain along the original coastal plain. The relatively recently reclaimed lands occur adjacent to the coastline and comprise sites with the softest condition of the upper soils. The SPT profiles used in the WES (1999) study are shown schematically in Figures 23 and 24, together with the locations (soil zones) of the specific borings comprising the profiles.

The available boring data were orgainzed by location in the EW direction from the Kobe City area (Zone A), the Nishinomiya area (Zone B) and the Osaka area (Zone C). The distribution of the sample blow count data in each area, for each generic soil type and for specific depth ranges is shown in Tables 4 through 6 and were taken from the WES (1999) study. The distribution of the SPT data indicates the usual stiffening of the soil with depth, but no major difference between the zones.

The generic description of the soil profiles in the reclaimed areas is essentially fill overlying soft Holocene marine clay. These, in turn, rest on a series of Pleistocene deposits which consist of alternate layers of dense sand and gravels, and stiff silty clays and clays. The fill is primarily composed of decomposed granite and Pliocene deposits of mudstone, sandstone and conglomerate, some Pleistocene marine clay, gravels and dredged sands. The fill also contains rubble and refuse from construction sites (Hamada et al., 1995). The thickness of the fill in the survey area varies from 5 m to 25 m generally increasing in thickness toward the bay. On the whole, the SPT N_value ranges between 5 to 20 bpf through the fill with some counts exceeding 50 bpf.

Based on the borehole log information, a generic soil column was developed which consists of the following soil layers from the ground surface down:

surface fill layer (alluvium)
upper sand layer (alluvium)
upper clay layer 1 (alluvium)
upper gravel layer 1 (alluvium)
lower clay layer 2 (diluvium)
lower gravel layer 2 (diluvium)

Not all borings contained all these layers, in which case the specific thicknesses were set to zero in the computations (WES, 1999).

#### ***3.3.3.2 Estimates of Soil Column and Crustal Shear Wave Velocities***

After each soil boring profile was developed for the specific soil layering description mentioned above, the next step in the process was to convert the sample SPT blow count data to estimates of low strain shear wave velocity for use in the site response calculations (WES, 1999). This was done using correlation model 1 (Section 2.5.4) from Iwasaki et al. (1987) and is shown in Figure 2. The borings used in the correlation development extended to depths of about 40m (about 120 ft). To extend the profiles below the blow count data, the 2-D basin model of Kagawa et al., (1993) was placed below the shallow geotechnical profile at each site location. To develop generic profiles for each soil category, all hard, soft, and fill profiles were averaged and the deeper Wald (1996) crustal model added. The shallow profiles are shown in Figure 25 down to 500 ft with the deeper sections shown in Figure 26. Below a depth of about 2 km (shear-wave velocity 3.2 km/sec), all the profiles reflect the deep Wald (1996) crust which was used as the regional deep model at depth (Table 7). For rock sites, two profiles are used: a site-specific Kobe University (KBU) profile from Motosaka and Nagano (1997) and a generic California soft rock profile (Silva et al., 1997). The KBU profile is used only in the validation

exercise for site KBU while the generic soft rock profiles is used for all other rock sites. Figure 27 shows the areal distribution of the rock, hard, soft, and fill shear-wave velocity profiles (Figures 25 and 26) in the Kobe**,** Nishinomiya**,** and Osaka areas. For the simulations, a total of 664 sites were used to cover the three areas (Figure 28).

#### ***3.3.3.3 Kappa and Q(f)***

Shallow crustal damping (kappa) is constrained to have a small strain value of 0.04 sec for the rock, hard, soft, and fill profiles. This value is based on inversions of the rock and soil empirical attenuation relations of Abrahamson and Silva (1997) as well as Sadigh et al. (1997). In these inversions little difference was seen between rock and soil shallow damping values at low levels of loading (expected rock peak accelerations less than about 5%g). To determine appropriate kappa values beneath the nonlinear zones, the small strain damping from the damping curves throughout the nonlinear zones is subtracted from the total kappa value of 0.04 sec. The remaining kappa, generally about 0.03 sec, is applied beneath the nonlinear zones.

The Q(f) model used is 184 $f^{0.6}$ and is appropriate for northern California. It is based on inversions of the 1989 **M** 6.9 Loma Prieta, 1984 **M** 6.2 Morgan Hill, and 1979 **M** 5.7 Coyote Lake earthquakes (Silva et al., 1997). The overall similarity in crustal structures and tectonic environments between the Kobe region and northern California (Wald et al., 1991) suggests that the Q(f) models may be similar. Since most of the sites are at close fault distances, the effects of deep crustal damping are likely to be quite small resulting in little sensitivity of the motions and stress to the particular Q(f) model

#### ***3.3.3.4 Modulus Reduction and Damping Curves***

To approximately account for nonlinear site response at both rock and soil sites, equivalent-linear analyses are used to estimate ground motions, strain energy (PSI), Arias Intensity, and cyclic stress ratios (CSR). For the rock sites, the $G/G_{max}$ and hysteretic damping curves shown in Figure 29 are used. These curves were developed by modeling the strong ground motions predicted at rock sites by the empirical attenuation relation of Abrahamson and Silva (1997) as well as motions recorded at about 200 rock sites from about 15 earthquakes (Silva et al., 1997). For the soil sites, the EPRI (1993) curves are used for the cohesionless soils (Figure 30) while for the clay zones (Section 2), the curves shown in Figure 31 are used. These cohesive soil $G/G_{max}$ and hysteretic curves reflect depth dependency which was found to be required in modeling the motions at the Kobe Port Island (KPI) vertical array. The shallow curves are used in the Pleistocene clays and are consistent with those of Kazama et al. (1998) based on laboratory test data for the same materials. For the fill material (consisting of weathered granite (Masado)), a set of $G/G_{max}$ and hysteretic damping curves (Figure 31) based on gravely soils (Seed et al., 1984) is used. The fill material $G/G_{max}$ and damping values for strains exceeding about 1% were decreased and increased respectively to reflect the shear-wave velocity and damping values at KPI during the mainshock by Kokusho et al. (1996) and Elgamal et al. (1996). Sites are treated as nonlinear to depths of 500 ft or shear-wave velocities exceed depth 3,000 ft/sec, whichever occurs first with depth.

The appropriateness of the suite of $G/G_{max}$ and hysteretic damping curves was assessed by

modeling the motions (5% damped response spectra) at the KPI vertical array using the generic fill profile (Figure 25). The finite-fault model is used to simulate the motions at the deepest accelerograph (83m) as well as at levels 32m, 16m, and the surface. The recorded and computed motions one compared in Figure Set 4.10 (sites KPI, KP2, KP3, and KP4). In general the finite-source model using equivalent-linear soil response captures the motions and changes in motions with depth reasonably well.

#### ***3.3.3.4 Validation of Kobe Earthquake Simulations***

The accuracy of the finite-fault simulations along with the equivalent-linear site responses are evaluated by comparisons to recorded motions (5% damped average horizontal component response spectra) at 25 sites. Figure 17 shows the recording sites in the Kobe/Osaka region and Figure 32 shows the slip model (Wald, 1996), derived from modeling the recorded motions. In general, slip is concentrated in two large zones or asperities. One asperity is located under Awaji Island, toward the southeast portions of the rupture surface and extends to the surface. The second asperity is deep, below about 5 km, and is located beneath the city of Kobe.

The comparison of simulations to recorded motions is shown in Figure Set 33 in terms of average horizontal component response spectra (5% damping). In general, the motions are predicted reasonably well.

Figure 34 shows the modeling bias. The bias plot show little bias over the entire frequency range. In general, the simulations provide a good fit to the data and indicate that the model is capturing the overall character of the motions acceptably well.

### 3.3.4 Simulated Motions for the Kobe, Nishinomiya, and Osaka Areas

To simulate motions, cyclic stress ratios, Arias Intensity, and strain energies at each site location reflecting aleatory variability (randomness) in material properties, fifteen random profiles are generated at each site along with equivalent-linear site response analyses. Shear-wave velocity and layer thicknesses are varied using a statistical model based on an analysis of variance of over 500 shear-wave velocity profiles (EPRI, 1993; Silva et al., 1997). Additionally, for the hard, soft, and fill profiles the depth to 1 km/sec materials (Figure 26) is varied ± 100m, ± 200m, and ± 300m respectively. Median and ± 1F response spectra (112 periods from 0.1 to 100.0 Hz) as well as cyclic stress ratios, Arias Intensities, $(N_1)_{60}$ values, and strain energies verses depth are computed at each site location. CSR, CRR, Arias Intensity, Ihb, strain energy densities, and $(N_1)_{60}$ estimates are averaged over the critical zones of 2m-7m, 4m-7m, 7-9m for the fill, soft, and hard areas (Figure 27) respectively. The water table averages 2.1m, 2.4m, and 7.1m at the fill, soft, and hard sites respectively (WES, 1999).

For the rock, hard, soft, and fill areas (Figure 27), Figure 35 shows the median predicted peak acceleration values. The rock and hard soil sites (hot) have the highest acceleration values which are near 1g. These are the stiffest sites and closest to the rupture surface. The green band, with median peak accelerations in the 0.4 to 0.6g range, generally corresponds to the soft sites (Figure 27). The fill and more distant soft sites (Nishinomiya and Osaka areas) show significantly lower

peak acceleration values being in the 0.3 to 0.4g range. Interestingly, the soft soils with the band of intermediate levels of peak accelerations (green) contains the high intensity (damage) zone (Figure 19) suggesting that the effects of surficial soils may have been a contributing factor. Since few structures are located in the rock and hard soil hill areas, the effects of nonlinear response of the fill soils may have lowered the high frequency (> 1 Hz) motions sufficiently enough to reduce damage levels. This aspect of surficial geology was also demonstrated by Suetomi and Yoshida (1998) and attributed the reduction in motions from the soft to the fill zones to the nonlinear response of the shallow (alluvial) marine clay layer which is thin or absent in the soft soil zone. An alternative explanation is the basin edge effect (Kawase, 1996; Pitarka et al., 1996; Inoue and Miyatake, 1997; Kamae et al., 1998) where edge generated surface waves superpose with direct shear-waves from the source to form a band of enhanced motions which parallels the edge of the basin. It is likely that both effects are present to some degree, however over 70% of the structures damaged in the high intensity zone were of four stories or less (NIST, 1996), suggesting high (> 1 Hz) frequencies and local site response played a major role in the heavily damaged zone in Kobe. To further examine the distribution and frequency range in motions, Figures 36, 37, and 38 show median estimates of 5% damped response spectra at 3 Hz, 1.0 Hz, and 0.5 Hz respectively. At 3 Hz (Figure 36) the green zone still corresponds generally to the heavily damaged or high intensity areas (Figure19), even into Nishinomiya, where structural damage occurred. This trend continues at 1 Hz (Figure 37) but with much more variability along the Kobe high intensity zone. At 0.5 Hz, the largest motions are generally along margins of the Kobe fill areas, away from the heavily damaged zone and is likely due to the strong nonlinearity in the fill and unlying clay materials, shifting the resonances to low frequency, as evidenced in the Port Island recordings (Figure 33). These trends are consistent with the effects of the surficial soils on observed damage patterns in the Kobe and Nishinomiya areas.

To examine liquefaction triggering estimates, Figures 39, 40, and 41 show median estimates of FS for AS, KM, and SEA respectively. In general the patterns are similar showing low FS (< 0.75) along the margins of Osaka Bay in the Kobe and Nishinomiya areas. The approaches of KM and SEA predict more extensive liquefaction than observed (Figure 20) having a large area with FS between 0.75 and 1.00, but capture the overall patterns reasonably well, considering the use of shear-wave velocity to estimate $(N_1)_{60}$ (Section 3.5.1) and the use of the ad-hoc factor of 2.0 to scale the average horizontal component to total cumulative Arias Intensity. The AS approach, Figure 39 predicts extensive liquefaction along the fill areas in Kobe and Nishinomiya (Figure 27) where it occurred (Figure 20) and moderate to little or no liquefaction in the soft zone (Figure 27), where liquefaction occurrence was quite variable. To examine probabilities, Figure 41 and 42 show median estimates for AS and SEA respectively. For the AS approach, zones which showed extensive sand boils (Figure 20) generally show median probabilities above 30%, roughly corresponding to FS values less than 0.75 (Figure 39). The SEA approach shows much wider zones corresponding to probabilities above 30%, particularly in southern Nishinomiya and near the Osaka shoreline.

To complete the plots, Figures 44, 45, 46, and 47 show the median estimates of CSR, Arias Intensity (average horizontal component), $(N_1)_{60}$, and strain energy density. The cyclic demands, in terns of CSR (Figure 44) range from about 0.3 to 0.4 along the coast of Osaka and increase in the soft soils, roughly along the heavily damaged zone (Figure 19). Similar patterns are shown

with Arias Intensity (Figure 45). For the SPT $(N_1)_{60}$ median estimates, Figure 46, low values (< 15) are seen along the bay margins, generally increasing with the soft and hard soils, as expected. The strain energy density shows the highest values along the regions of intense sand boils (Figure 20), suggesting its potential usefulness to assess liquefaction triggering.

In general all three approached are considered to represent very useful tools to quantify liquefaction hazard at regional scales, given generic or regionally calibrated correlations of shear-wave velocity to SPT data or surficial geology and a mechanism to map these attributes over the target area.

## 4.0 CONCLUSIONS

In the site-specific analyses, twelve case history sites (six earthquakes) were studied using available site specific information from detailed site investigations. At all the sites, comparisons were made between observations of whether or not the site liquefied and triggering estimates based on the Andrus and Stokoe (2000) shear-wave velocity based approach. Additional comparisons were made using updated SPT approaches of Seed et al. (2001) and Kayen and Mitchell (1997). For these SPT based methods, correlations between shear-wave velocity and $(N_1)_{60}$ values was used instead of measured SPT values. This approach was implemented to assess both the appropriateness of the three SPT shear-wave velocity models (Section 2.5.3) as well as the performance of the SPT methods for cases where only shear-wave velocity may be estimated. This would apply to regional mapmaking, for instance where surfical geology or NEHRP category based shear-wave velocity profiles (Silva et al., 2000) may be used to generate design motions and consistent liquefaction triggering maps. To validate this regional approach more directly, liquefaction triggering predictions were made for regions which suffered varying degrees of liquefaction during the 1995 **M** 6.9 Kobe, Japan earthquake. In this analysis, finite rupture simulations were used to directly accommodate aspects of rupture directivity, such as duration, on cyclic demands, on CSR and cumulative Arias Intensity. In this regional analysis, 654 sites were analyze and comparisons made between estimates of liquefaction triggering and areal surveys of sand boils as evidence of liquefaction.

In both the site specific and regional analyses, the Andrus and Stokoe (2000) shear-wave velocity approach worked well, accurately predicting cases (regions) where liquefaction occurred and cases (regions) where liquefaction was not observed. Comparisons with SPT based procedures, which included the recently updated CSR approach (Seed et al., 2001) and the Arias Intensity approach (Kayen and Mitchell, 1997), were also made. Both of these approaches are fundamentally based on SPT data and correlations with shear-wave velocity were used to estimate appropriate $(N_1)_{60}$ values. Both of these approaches produced acceptable results but worked less well than the shear-wave velocity method, probably due to the increased variability introduced through estimating $(N_1)_{60}$ values through shear-wave velocity. The $(N_1)_{60}$ and velocity correlations were used to assess these SPT approaches for regional applications, where generic shear-wave velocity models based on surficial geology or NEHRP category are more readily available than associations with $(N_1)_{60}$ values. Additionally, the methodology employed directly addresses the effects of parametric variability of site dynamic material properties on cyclic demands in a statistically rigorous manner by randomly varying properties using correlation models based on analysis of various on a large number of measured shear-wave

velocities. As a result, a fundamentally shear-wave velocity approach was used and variabilities propagated, via correlations, to variabilities in $(N_1)_{60}$ estimates. While the fundamentally shear-wave velocity based approach (Andrus and Stokoe, 2000) clearly was more accurate, the SPT approaches worked rather well, generally being conservative, considering SPT data were not used directly.

**ACKNOWLEDGEMENT**

Discussions with Professors Jon Bray and Ray Seed were very helpful at critical junctures in this work and are greatly appreciated.

*Research supported by the U.S. Geological Survey (USGS), Department of the Interior, under USGS award number (02HQGR0022). The views and conclusions contained in this document are those of the authors and should not be interpreted as necessarily representing the official policies, either express or implied, of the U.S. Government.*"

## REFERENCES


Abrahamson, N.A and K.M. Shedlock (1997). "Overview." *Seis. Research Lett*., 68(1), 9-23.

Abrahamson, N.A. and Silva, W.J. (1997). "Empirical response spectral attenuation relations for shallow crustal earthquakes." *Seism. Soc. Am.,* 68(1), 94-127.

Abrahamson, N.A., Silva, W., and Schneider, J. (1994). "Variability of strong ground motion due to the variability of the seismic slip distribution." *Seis. Research Lett*., 65(1), 1484-1504

Andrus, R.D., Stokoe II, K.H., and Juang, C.H. (2004). "Guide for shear-wave based liquefaction potential evaluation." *Earthq. Spectra,* (20)2, 285-308.

Andrus, R.D., and Stokoe, K.H., II. (2000) Liquefaction resistance of soils from shear-wave velocity, *Journal of Geotechnical and GeoenvironmentalEngineering,* 126(11), 1015-1025.

Andrus, R.D., K.H. Stokoe, and R.M Chung (1999). "*Draft guidelines for evaluating liquefaction resistance using shear wave velocity measurements and simplified procedures*." Building and Fire Research Lab., National Institute of Standards and Tech., NISTIR 6277.

Atkinson, G.M and W.J. Silva (2000). "Stochastic modeling of California ground motions." *Bull. Seism. Soc. Am.* 90(2), 255-274.

Atkinson, G.M and W.J. Silva (1997). "An empirical study of earthquake source spectra for California earthquakes." *Bull. Seism. Soc. Am.* 87(1), 97-113.

Atkinson, G.M., Finn, W.D.L., and Charlwood, R.G. (1984). "Simple computation of liquefaction probability for seismic hazard applications." *Earthquake Spectra*, 1(1), 107-123.

Boore, D.M. (1986). "Short-period P- and S-wave radiation from large earthquakes: implications for spectral scaling relations." Bull. Seism. Soc. Am., 76(1) 43-64.

Boore, D.M. (1983). "Stochastic simulation of high-frequency ground motions based on seismological models of the radiated spectra." *Bull. Seism. Soc. Am.*, 73(6), 1865-1894.

Cetin, K.O., Seed, R.B, Moss, R.E.S., Kiureghian, A. Der, Tokimatsu, K., Harder, Jr.L.F., Kayen, R.E., and Idriss, I.M. (2000). "Field case histories for SPT-based in situ liquefaction portential evaluation." A report on research sponsored by Pacific Gas and Electric Company (PG&E), Contract No. Z-19-2-133, *Geotechnical Engineering Research Report No. UCB/GT-2000/09*

Davis, R.O. and J.B. Berrill (1978). "Energy dissipation and seismic liquefaction in sands.)

*Earthquake Engineering and Structural Dynamics,* 10, 69-68.

de Alba, P., Benoit, J., Pass, D.G., Carter, J.J., Youd, T.L., and Shakal, A.F. (1994). "Deep instrumentation arry at the Treasure Island Naval Station." *The Loma Prieta, California, Earthquake of October 17, 1989 – Strong Ground Motion,* U.S. Geological Survey Professional Paper 1551-A, R.D. Borcherdt, Ed., U.S. Gov. Printing Office, Washington, D.C., pp. A155-A168.

Dobry, R., R. S. Ladd, F. Y. Yokel, R. M. Chung and D. Powell (1982). "Prediction of pore water pressure buildup and liquefaction of sands during earthquakes by the cyclic strain method." *NBS Building Science Series 138*, National Bureau of Standards.

Dobry, R., K.H. Stokoe II, R.S. Ladd, and T. L. Youd (1981). "Liquefaction susceptibility from S-wave velocity." In situ testing to evaluate liquefaction susceptibility. New York: ASCE, Geotechnical Engineering Division, St. Louis, MO (pre-print 81-544), 1-15.

Electric Power Research Institute (1993). "Guidelines for determining design basis ground motions." Palo Alto, Calif: Electric Power Research Institute, vol. 1-5, EPRI TR-102293.

vol. 1: Methodology and guidelines for estimating earthquake ground motion in eastern North America.
vol. 2: Appendices for ground motion estimation.
vol. 3: Appendices for field investigations.
vol. 4: Appendices for laboratory investigations.
vol. 5: Quantification of seismic source effects.

Elgamal, A. W., M . Zeghal and E. Parra (1996). "Liquefaction of Reclaimed Island in Kobe, Japan." Japan Journal, Geotechnical Engineering, *ASCE*, 39_49.

Elton, D.J., and T. Hadj-Hamou (1990). "Liquefaction potential map for Charleston, South Carolina." *Journal of Geotechnical Engineering,* ASCE, ISSN 0733-9410/90/0002-0244/ 116(2), 244-264.

Gibbs, J.F., Fumal,T.E. and Powers, T.J. (1994). "Seismic velocities and geologic logs from borehole measurements at seven strong-motion stations that recorded the 1989 Loma Prieta, Califorinia, earthquake." *USGS Open-File Rept. 94-222.*

Gibbs, J.F., Fumal,T.E. and Powers, T.J. (1993). "Seismic velocities and geologic logs from borehole measurements at eight strong-motion stations that recorded the 1989 Loma Prieta, Califorinia, earthquake." *USGS Open-File Rept. 93-376.*

Gibbs, J.F., T.E. Fumal, D.M. Boore, and W.B. Joyner (1992). "Seismic velocities and geologic logs from borehole measurements at seven strong-motion stations that recorded the Loma Prieta earthquake." USGS Open-File Rept. 92-287.

Glaser, S.D. and R.M. Chung (1995). "Estimation of liquefaction potential by in situ methods."

*Earthquake Spectra,* 11(3), 431-531.

Gregor, N. J., W.J. Silva, R. I.G. Wong and R. Youngs (2002). "Ground motion attenuation relationship for Cascadia subduction zone megathrust earthquakes based on a stochastic finite fault model." *Bull. Seism. Soc. Am.*, 92(5), 1923-1932.

Haldar, A., and W.H. Tang (1979). "Probabilistic evaluation of liquefaction potential." *Journal of the Geotechnical Engineering Division,* ASCE, 105(2), 145-163.

Hamada, M., R. Isoyama and K. Wakamatsu (1995). "Liquefaction, Ground Displacement and Soil Condition in Hanshin Area, The 1995 Hyogoken_Nanbu (Kobe) Earthquake." Assoc. for Development of Earthquake Prediction, School of Engineering, Waseda University.

Hartzell, S.H. and T.H. Heaton (1983). "Inversion of strong ground motion and teleseismic waveform data for the fault rupture history of the 1979 Imperial Valley, California, earthquake." *Bull. Seism. Soc. Am.*, 73(6), 1553-1583.

Holzer, T.L., Youd, T.L., and Hanks, T.C. (1989). "Dynamics of liquefaction during the 1987 Superstition Hills, California, earthquake." *Science,* 244, 56-59.

Idriss, I.M. (1990). "Response of Soft Soil Sites During Earthquakes." *H. Bolton Seed Memorial Symposium,* BiTech Publishers, Vancouver, B.C., vol. 2, 273-289.

Imai, T. and Tonouchi, K. (1982). "*Correlation of N-value with S-wave velocity and shear modulus.*" Proceedings of the Second European Symposium on Penetration Testing, Amsterdam, The Netherlands. Pp. 67-72.

Inoue, T. and T. Miyatake (1997). "3-D simulation of near-field strong ground motion: Basin edge effect derived from rupture directivity." *Geophysical Research Letters,* 24(8), 905-908.

Iwan, W.D. (1967). "On a class of models for the yielding behavior of continuous and composite systems." J. Appl. Mech., 34, 612-617.

Iwasaki, Y. (1997). "Getechnical Data from Geo-Research Institute, Osaka." Personal Communications.

Iwasaki, Y., S. Sawada and T. Kagawa (1987) "Microzonation for Predicting Earthquake in the South of Osaka Prefecture."

Juang, C.H., Andrus, R.D., Jiang, T., and Chen, C.J., 2001, Probability-based liquefaction evaluation using shear wave velocity measurements, Proceedings, 4th International Conference on Recent Advances in Geotechnical Earthquake Engineering and Soil Dynamics, S. Prakash, (ed.), held 26-31 March 2001, San Diego, Calif. University of Missouri at Rolla, Paper 4.25.

Juang, C.H., Chen, C.J., Jiang, T., and Andrus, R.D., 2000, Risk-based liquefaction potential evaluation using SPT, *Canadian Geotechnical Journal*, 37, 1195-1208.

Kagawa, T., S. Sawada, Y. Iwasaki, and A. Nanjo (1993). "On the modelization of deep sedimentary basin structure beneath the Osaka plain." *Abstr. Seismol. Soc. Jpn.,* 2, 112-117 (in Japanese).

Kamae, K., K. Irikura and A. Pitarka (1998). "A Technique for Simulating Strong Ground Motion Using Hybrid Green's Function." *Bull. Seism. Soc. Am.,* 88(2), 357_367.

Kavazanjian, E., R. A. Roth and H. Echezuria (1985). "Liquefaction potential mapping for San Francisco." *J. Geotech. Engrg.,* ASCE, 111(1), 54-76.

Kawase, H. (1996). "The cause of the damage belt in Kobe: "The basin-edge effect," constructive interference of the direct S-wave with the basin-induced diffracted/rayleigh waves." *Seism. Research Lett.* 67(5), 25-34.

Kayen, R.E., and Mitchell, J.K. (1997). "Assessment of liquefaction potential during earthquakes by Arias Intensity." *J. of Geo. And Geoenvironmental,* (123)12, 1162-1174

Kazama, M., A. Yamaguchi and E. Yanagisawa (1998). "Seismic behavior of an underlying alluvial clay on man-made islands during the 1995 Hyogoken-Nambu earthquake." *Special Issue of Soils and Foundations,* 23-32, Japanese Geotechnical Society.

Kimura, M. (1996). "Damage Statistics", Special Issue, Soils and Foundations.

Kokusho, T., K. Sato and M. Matsumoto. (1996) "Nonlinear Dynamic Soil Properties Back_Calculated from Strong Seismic Motions During Hyogoken_Nanbu Earthquake", *11th WCEE*, Mexico.

Krinitzsky, E. L., J.P. Koester and R.L. Hall (1995). "Reconnaissance Report." Waterways Experiment Station.

Iwasaki, Y. S. Sawada and T. Kagawa (1987) "*Microzonation for Predicting Earthgquake in the South of Osaka Prefecture*."

Liao, S.C., D. Veneziano and R.V. Whitman (1988). "Regression models for evaluating liquefaction Probability." *Journal. Geotechnical Engineering*, ASCE, 114(4), 389-411..

Loertscher, T.Y. and T.L. Youd (1994). "Magnitude scaling factors for analysis of liquefaction." T.D. O'Rourke, & M. Hamada, Proc. Fifth U.S.-Japan workshop on earthquake resistant design of lifeline facilities and countermeasures for soil liquefaction. Technical Report NCEER-94-0026, sNOWBIRD, UT. 703-715.

Martin, G.R., Finn, W.D.K., and Seed, H. Bolton (1975). "Fundamentals of Liquefaction under

Cyclic Loading." *J. of the Geotechnical Engineering Division,* ASCE, 101(GT5), 423-438.

McGuire, R.K.,W.J. Silva and C.J. Costantino (2001). "Technical basis for revision of regulatory guidance on design ground motions: hazard- and risk-consistent ground motions spectra guidelines." Prepared for Division of Engineering Technology, Washington, DC, *NUREG/CR-6728.*

McGuire, R.K., and Tatsuoka, F., Iwasaki, T., and Tokida, K. (1979). "Assessment of the probability of liquefaction of water-saturated reclaimed land." Proc. Third Intern. Conf. On Applic. of Stat. and Prob. in Soil and Struct. Engin., Sydney: 786-801.

Mitchell, J. K. and Wentz, Jr. F. J. (1988). "Improved ground performance during the earthquake." *The Loma Prieta, California Earthquake of October 17, 1989 – Liquefaction,* U.S. Geological Survey Professional Paper 1551-B, T.L. Holzer Ed., U.S. Gov. Printing Office, Washington, D.C., pp. B241-B272.

Motosaka, M. and M. Nagano (1997). "Analysis of Amplification Characteristics of Ground Motions in the Heavily Damaged Belt Zone During the 1995 Hyogo_ken Nanbu Earthquake." *Earthquake Eng and Structural Dynamics*, vol. 26, 3377_393.

National Research Council (NRC) (1985). "*Liquefaction of Soils During Earthquakes."* National Academy Press, Washington, DC.

NITST "*The January 17, 1995 Hyogoken-Nanbu (Kobe) earthquake."* NIST Special Publication 901.

Obermeier, S.F. et al. (1986). "Holocene and late Pleistocener(?) earthquake-induced sand blows in coastal South Carolina." *Proc.. Third U.S. Nat. Conf. On Earthquake Engineering,* Charleston, S.C., 1, 197-208.

Obermeier, S.F., et al. (1985). "Geologic evidence for recurrent moderate to large earthquakes near Charleston, South Carolina." *Science,* 277(4685), 408-411.

Obermeier, S.F. et al., (1984). "Liquefaction potential in the Central Mississippi Valley." *Proc., Symp. On the New Madrid Seismic Zone. USGS Open-File Report 84-770.* P. Gori and W.W. Hays, eds.. U.S. Geological Survey, Washington, D.C.. 391-446.

Pitarka, A, K. Irikura, T. Iwata and T. Kagawa (1996). "Basin structure effects in the Kobe area inferred from the modeling of ground motions from two aftershocks of the January 17, 1995, Hyogo-ken Nanbu earthquake." *J. Phys. Earth,* 44, 563-576.

Power, M.S., Egan, J.A., Shewbridge, S.E., deBecker, J., and Faris, J.R. (1998). "Analysis of liquefaction-induced damage on Treasure Island." *The Loma Prieta, California Earthquake of October 17, 1989 – Liquefaction,* U.S. Geological Survey Professional Paper 1551-B, T.L. Holzer Ed., U.S. Gov. Printing Office, Washington, D.C., pp. B87-B119.

Power, M.S., J.R. Wesling, R.C. Perman, R.R. Youngs, and L.A. DiSilvestro (1991). "Evaluation of liquefaction potential in San Jose, California." Geomatrix Consultants, San Francisco, California, Final Technical Report, US Geological Survey Contract No. 14-08-0001-G1359.

Reiter, L. (1990). "*Earthquake Hazard Analysis, Issues and Insights.*" Columbia University Press, New York.

Robertson, P.K., and R.G. Campanella (1985) "Liquefaction potential of sands using the CPT", *Journal of Geotechnical Engineering*, ASCE, 111(3), 384-403.

Roblee, C.J., W.J. Silva, G.R. Toro, and N. Abrahamson (1996). "Variability in Site-Specific Seismic Ground-Motion Predictions." Uncertainty in the Geologic Environment: From Theory to Practice, Proceedings of "Uncertainty '96" *ASCE* Specialty Conference, Edited by C.D. Shackelford, P.P. Nelson, and M.J.S. Roth, Madison, WI, Aug. 1-3, pp. 1113-1133

Rockaway, T.D., J.D. Frost, D.L. Eggert, R. Luna (1997). "Spatial Earthquake Hazard Assessment of Evansville, Indiana." *Seismological Research Lett.*, 68(4), 675-875.

ROSRINE (2004). http://geoinfo.usc.edu/rosrine/

Sadigh, C.-Y. Chang, J.A. Egan, F. Makdisi, and R.R. Youngs (1997). "Attenuation relationships for shallow crustal earthquakes based on California strong motion data." *Seism. Soc. Am.,* 68(1), 180-189.

Schnabel, P.B., Seed, H.B. and Lysmer, J. (1972). "Modification of seismograph records for effects of local soil conditions." *Bull. Seism. Soc. Am.,* 62, 1649-1664.

Schneider, J. and W. J. Silva, and D. Wright (2000). "Earthquake scenario ground motion hazard maps for the San Francisco Bay region." *USGS Grant award* #98-HQ-GR-1004, Final Report.

Schneider, J.F., W.J. Silva, and C.L. Stark (1993). Ground motion model for the 1989 **M** 6.9 Loma Prieta earthquake including effects of source, path and site. *Earthquake Spectra,* 9(2), 251-287.

Seed, R.B, Cetin, K.O., Moss, R.E.S., Kammerer, A.M., Wu, J., Pestana, J.M., and Riemer, M.F. (2001). "Recent advances in soil liquefaction engineering and seismic site response evaluation." *Proceedings: 4th International Conference on Recent Advances in Geotechnical Earthquake Engineering and Soil Dyanamics and Symposium in Honor of Professor W.D. Kiam Finn*, San Diego, California, March 26-31, 2001.

Seed, H.B., Tokimatsu, K., Harder, L.F. and Chung, R.M. (1985). Influence of SPT procedures in soil liquefaction resistance evaluations, *Journal of Geotechnical Engineering,* 111(12), 1425-1445.

Seed, H. B., K. Tokimatsu, L. F. Harder and R. M. Chung (1984). "The Influence of SPT Procedures in Soil Liquefaction Resistance Evaluation." University of California at Berkeley, Report No. UCB/EERC-84115.

Seed, H.B., Idriss, I.M. and Arango, I. (1983). "Evaluation of liquefaction potential using field performance data*." J. Geotech. Engrg. Div*., ASCE. 109(3),458-484.

Seed, H.B., and Idriss, I.M. (1982). "*Ground Motions and Soil Liquefaction During Earthquakes*." Earthq. Eng. Res. Inst. Monograph, Berkeley, California.

Seed, H. B. (1979). "Soil liquefaction and cyclic mobility evaluation for level ground during earthquakes." *Journal of the Geotechnical Engineering Division*, ASCE, 105(GT5), 201-255.

Seed, H.B., C. Ugas and J. Lysmer. (1976). "Site-dependent spectra for earthquake resistant design." *Bull. Seism. Soc. Am.,* 66(1), 221-243.

Seed, H. B. and I. M. Idriss (1971). "Simplified Procedure for Evaluating Soil Liquefaction Potential." *Journal Soil Mechanics and Foundation Division*, ASCE, 97(SM9), 1249-1273.

Seed, H.B. and I.M. Idriss (1970). "Soil moduli and damping factors for dynamic response analyses." Earthq. Eng. Res. Center, Univ. of Calif. at Berkeley, Report No. UCB/EERC-70/10.

Shibata, T., F. Oka and Y. Ozawa (1996). "Characteristics of Ground Deformation due to Liquefaction." Special Issue, Soils and Foundations.

Silver, M.L., and Seed, H.B. (1971) "Volume changes in sand during cyclic loading*", Journal of Soil Mechanics and Foundations Division*, ASCE, Vol. 97, No. SM9, 1171-1182.

Silva, W. J., R.R. Youngs, and I.M. Idriss (2001). "Development of design response spectral shapes for Central and Eastern U.S. (CEUS) and Western U.S. (WUS) rock site conditions."*Proc. of the OECE-NEA (Organization For Economic Coordination and Development of the Nuclear Energy Agency) Workshop on Engineering Characterization of Seismic Input, Nov., 15-17, 1999 NEA/CSNI/R(2000)2,* vol. 1: 185-268.

Silva, W.J. and C. Costantino, and Y. Iwasaki. (1999). "Assessment of liquefaction potential for the 1995 Kobe, Japan earthquake including finite-source effects." Prepared for U.S Army Engineer Waterways Experiment Station, Corps of Engineers Contract #DACW39-97-K-0015.

Silva, W.J. (1997). "Ground motion for new and existing highway facilities." *Proc. Of theFHWA/NCEER Workshop on the Nat'l Representation of Seismic,* I.M. Friedland, M.S Power and R. L. Mayes eds., Technical Report NCEER-97-0010.

Silva, W.J. (1992). "Factors controlling strong ground motions and their associated

uncertainties." *Seismic and Dynamic Analysis and Design Considerations for High Level Nuclear Waste Repositories, ASCE* 132-161.

Silva, W.J., R. Darragh, C. Stark, I. Wong,, J. Stepp, J. Schneider, and S. Chiou (1990). "A methodology to estimate design response spectra in the near-source region of large earthquakes using the Band-Limited-White-Noise ground motion model." Proceedings of the Fourth U.S. National Conference on earthquake Engineering, Palm Springs, Calif. vol. 1, 487-494.

Silva, W.J., N. Abrahamson, G. Toro and C. Costantino. (1997). "Description and validation of the stochastic ground motion model." Report Submitted to Brookhaven National Laboratory, Associated Universities, Inc. Upton, New York 11973, Contract No. 770573.

Silva, W.J., T. Turcotte and Y. Moriwaki (1988). "Soil response to earthquake ground motions." Palo Alto, Calif.: Electric Power Research Institute, Report NP-5747.

Silva, W.J. (1976). "Body waves in a layered anelastic solid." *Bull. Seism. Soc. Am.,* 66(5):1539-1554.

Suetomi, I. and N. Yoshida (1998). "Nonlinear behavior of surface deposit during the 1995 Hyogoken-Nambu earthquake." *Abstr. Special Issue of Soils and Foundations*, Japanese Geotechnical Society

Sykora, D. W. and Stokoe, D. H., II (1983). "*Correlations of in situ measurements in sands with shear-wave velocity.*" Geotechnical Engineering Report GR83-33, The University of Texas at Austin, Austin, TX.

Toro, G.R. and W.J. Silva (2001). "Scenario earthquakes for Saint Louis, MO, and Memphis, TN, and seismic hazard maps for the Central United States Region including the effect of site conditions." *U.S. Geological Survey* Award Number 1434-HQ-97-GR-02981, Final report.

Toro, G.R., N.A. Abrahamson, and J.F. Schneider (1997). "Model of strong ground motions from earthquakes in Central and Eastern North America: Best estimates and uncertainties." Seismological Research Let., 68(1), 41-57.

Vidale, J.E., and Helmberger, D.V. (1988). "Elastic finite-difference modeling of the 1971 San Fernando, California earthquake." *Bull. Seism. Soc. Am.,* 78(1), 122-141.

Vidale, J.E. (1987). "*Application of two-dimensional finite-difference wave simulation to earthquakes, earth structure and seismic hazard*." Ph.D. thesis, California Institute of Technology, Pasadena, CA, 150 pages.

Wald, D.J. (1996). "Slip history of the 1995 Kobe, Japan, earthquake determined from strong motion, teleseismic, and geodetic data." *J. of Physics of the Earth,* 44, 489-504.

WES (1999). "Assessment of liquefaction potential for the 1995 Kobe, Japan earthquake including finite-source effects." Prepared for U.S Army Engineer Waterways Experiment Station, Corps of Engineers Contract #DACW39-97-K-0015.

Wong, I., W. J. Silva, J. Bott, D. Wright, P. Thomas, N. Gregor, S. Li, M. Mabey, A. Sojourner and Y. Wang (2000). "Earthquake scenario and probabilistic ground shaking maps for the Portland, Oregon, Metropolitan Area." Interpretive Map Series IMS-16, State of Oregon Dept. of Geology and Mineral Industries

Wong, I., W.J. Silva, S. Olig, P. Thomas, D. Wright, F. Ashland, , N. Gregor, J. Pechmann, M. Dober, G. Christenson, and R. Gerth (2001). "Microzonation maps for earthquake ground shaking in the Salt Lake City metropolitan area, Utah." *Utah Geological Survey,* in press.

Yegian, M.K. and R.V. Whitman (1978). "Risk analysis for ground failure by liquefaction." *J. of the Geotech. Eng. Div.,* ASCE, 104(GT7), 921-938.

Youd, T.L., and Idriss, I.M., 2001, "Liquefaction resistance of soils: Summary report from the 1996 NCEER and 1998 NCEER/NSF workshop on evaluation of liquefaction resistance of soils," *Journal of Geotechnical and Geo-environmental Engineering*, ASCE, Vol. 127, No. 4, 297-313.

Youd, T.L., and Idriss, I.M., eds., 1997, *Proceedings of the NCEER Workshop on Evaluation of Liquefaction Resistance of Soils*, Technical Report NCEER-97-0022, National Center for Earthquake Engineering Research, 276 p.

Youngs, R.R., S.J. Chiou, W.J. Silva and J. R. Humphrey (1997). "Strong ground motion attenuation relationships for subduction zone earthquakes." *Seism. Research Lett.*, 68(1), 58-73.

| Table 1<br>EARTHQUAKES AND SITES<br>SITE SPECIFIC ANALYSES | | | |
|---|---|---|---|
| Earthquake | Magnitude (**M**) | Site | Rupture Distance (km) |
| 1989 Loma Prieta | 6.9 | Alameda Naval Air Station | 72 |
| | | Emeryville, Pacific Park Plaza | 76 |
| | | Oakland Outer Harbor Wharf | 74 |
| | | Oakland Title and Trust | 72 |
| | | Treasure Island | 77 |
| 1979 Imperial Valley | 6.5 | Wildlife Liquefaction Array | 21 |
| 1987 Elmore Ranch | 6.2 | Wildlife Liquefaction Array | 18 |
| 1987 Superstition Hills (B) | 6.5 | Wildlife Liquefaction Array | 24 |
| 1987 Superstition Hills (B) | 6.5 | Kornbloom Road | 18 |
| 1994 Northridge | 6.7 | Newhall, West Pico Canyon<br>Potrero Canyon (P-1) | 5 |
| | | Potrero Canyon (P-3) | 5 |
| 1999 Kocaeli, Turkey | 7.5 | Adaparazi | 4 |

Table 2
VALIDATION SITE PARAMETER SUMMARY

| Site, Earthquake | FS Andrus-Stokoe | FS Kayen | FS Seed | Critical Layers (m-m) | Fines[7] (%) | Site Liquefied (Yes/No) | PGA (g)[1] | Water Depth (m) | $(N_1)_{60}$ | | | CSR | | Arias Intensity(m/sec) | |
|---|---|---|---|---|---|---|---|---|---|---|---|---|---|---|---|
| | | | | | | | | | PEA[3] | Cetin[4] | Kayen[5] | PEA | Cetin[4] | PEA[6] | Kayen |
| Alameda Naval Air Station, 1989 Loma Prieta | 0.90 | 0.41<br>0.16<br>0.18 | 0.98<br>0.41<br>0.47 | 2.5-5.0 | 10 | Yes | 0.214 | 1.4 | 10.40<br>3.90<br>4.50 | | 11 | 0.203 | | 1.78 | 0.80 |
| Emeryville Pacific Park Plaza, 1989 Loma Prieta | 1.12 | 0.91<br>0.31<br>0.42 | 1.20<br>0.43<br>0.53 | 1.5-5.2 | 5 | No | 0.224 | 2.95 | 20.20<br>9.30<br>11.00 | | | 0.220 | | 2.12 | |
| Oakland Outer Harbor Wharf, 1989 Loma Prieta | 0.68 | 0.18<br>0.10<br>0.11 | 0.29<br>0.13<br>0.20 | 6.27-7.62 | 5 | Yes | 0.271 | 3.0 | 6.10<br>3.70<br>4.40 | 13.1 | 13 | 0.225 | 0.165 | 2.40 | 1.71 |
| Oakland Title and Trust, 1989 Loma Prieta | 2.00 | 1.81<br>0.93<br>1.60 | 1.97<br>1.81<br>1.91 | 6.9-7.9 | 5 | No | 0.202 | 6.4 | 37.30<br>23.40<br>32.10 | | | 0.133 | | 1.50 | |
| Treasure Island, 1989 Loma Prieta | 1.04 | 0.65<br>0.39<br>0.41 | 1.25<br>1.01<br>1.04 | 4.3-6.9 | 20 | No | 0.137 | 1.4 | 6.70<br>3.40<br>4.00 | 7.8 | 5 | 0.140 | 0.160 | 0.73 | 0.54 |
| Wildlife Array, 1979 Imperial Valley | 1.38 | 1.97<br>1.95<br>1.95 | 1.51<br>1.17<br>1.23 | 2.65-7.4 | 16 | No | 0.137[2] | 1.2 | 12.30<br>4.80<br>5.70 | 12.8 | 10<br>16.5 | 0.136 | 0.134 | 1.16 | |
| Wildlife Array, 1987 Elmore Ranch | 1.48 | 1.62<br>1.17<br>1.27 | 1.54<br>1.17<br>1.25 | 2.65-7.4 | 16 | No | 0.149 | 1.2 | 12.30<br>4.80<br>5.80 | 12.8 | 10<br>16.5 | 0.136 | 0.100 | 0.26 | 0.44 |
| Wildlife Array, 1987 Superstition Hills(B) | 1.00 | 0.77<br>0.30<br>0.36 | 1.02<br>0.48<br>0.56 | 2.65-7.4 | 16 | Yes | 0.223 | 1.2 | 12.30<br>4.80<br>5.80 | 12.8 | 10<br>16.5 | 0.231 | 0.202 | 1.13 | 1.97<br>(1.37) |
| Kornbloom Road, 1987 Superstition Hills(B) | 1.49 | 1.27<br>0.76<br>0.87 | 1.56<br>1.27<br>1.33 | 2.65-5.6 | 33 | No | 0.130 | 2.65 | 10.10<br>4.30<br>6.00 | 7.2 | | 0.107<br><br>0.379 | 0.130 | 0.51<br><br>7.80 | |

| Table 2 (cont.)<br>VALIDATION SITE PARAMETER SUMMARY | | | | | | | | | | | | | | | |
|---|---|---|---|---|---|---|---|---|---|---|---|---|---|---|---|
| Site, Earthquake | FS Andrus-Stokoe | FS Kayen | FS Seed | Critical Layers (m-m) | Fines[7] (%) | Site Liquefied (Yes/No) | PGA (g)[1] | Water Depth (m) | $(N_1)_{60}$ | | | CSR | | Arias Intensity(m/sec) | |
| | | | | | | | | | PEA[3] | Cetin[4] | Kayen[5] | PEA[3] | Cetin[4] | PEA[6] | Cetin |
| Site P-1; Newhall,<br>West Pico Canyon,<br>1994 Northridge | 1.76 | 1.18<br>0.46<br>0.87 | 1.43<br>0.80<br>0.97 | 6.0-7.0 | 37 | No | 0.346 | 3.29 | 24.20<br>14.81<br>19.54 | | | 0.269 | | 4.25 | |
| Site P-3; ; Newhall,<br>West Pico Canyon<br>1994 Northridge | 0.70 | 0.42<br>0.27<br>0.35 | 0.37<br>0.21<br>0.27 | 6.0-7.0 | 33 | Yes | 0.416[2] | 3.29 | 5.80<br>3.60<br>4.50 | 10.5 | | 0.262 | 0.254 | 1.40 | |
| Adaparazi, 1999<br>Kocaeli, Turkey | 0.85 | 0.26<br>0.06<br>0.08 | 0.34<br>0.13<br>0.15 | 1.25-5.0 | >60 | Yes | 0.411[2] | 1.25 | 3.50<br>5.40<br>6.50 | | | 0.379 | | 7.80 | |

NOTES:

[1]PGA from average horizontal component

[2] PGA from finite fault simulations

[3]Predicted $(N_1)_{60}$ from shear-wave velocity correlations using three relations:

1) Iwasaki et al. (1987), Equation (9) (top value)
2) Imai and Tonouchi (1982), Equation (10) (middle value)
3) Sykora and Stokoe (1983), Equation (11) (bottom value)

[4]$(N_1)_{60}$ value from Cetin et al. (2000)

[5]Values of $(N_1)_{60}$ from Kayen and Mitchell (1997). The top value is $(N_1)_{60}$. and it may be an average of values. The bottom value is $(N_{1,\,fc})_{60}$ corrected for fines content.

[6]Arias Intensity from finite fault simulations multiplied by 2.0 (ad-hoc value) to be similar to Arias Intensity from Kayen and Mitchell (1997). They use sum of the Arias Intensity from both horizontal components. The finite fault simulations use the average horizontal component to compute the Arias Intensity.

[7]For the Seed et al. (2001) methodology the regressed relationship for fines content is given for 5% to 35%. For sites with fines content > 35%, a value of 35% was implemented.

| Table 3<br>**COMPARISON OF INTENSITY SCALES (from Reiter, 1990)** | |
|---|---|
| Modified Mercalli (MM) 1931 | Japanese Scale 1960 |
| I | 0 |
| II | 1 |
| III | 2 |
| IV | 2.3 |
| V | 3 |
| VI | 4 |
| VII | 4.5 |
| VIII | 5 |
| IX | 6 |
| X | 6 |
| XI | 7 |
| XII | 7 |

Table 4
PERCENTILE DISTRIBUTION OF SPT'S FOR SANDY SOILS*

| Zone | Site Category | Depth Range (m) | SPT Blow Count Range N60 | | | | | | Sum |
|---|---|---|---|---|---|---|---|---|---|
| | | | 0-5 | 5-10 | 10-20 | 20-30 | 30-50 | >50 | |
| A | Hard Ground | 0-5 | 14 | 14 | 54 | 14 | 4 | 0 | 100 |
| | | 5-10 | 0 | 0 | 19 | 38 | 43 | 0 | 100 |
| | | 10-15 | 0 | 0 | 10 | 25 | 65 | 0 | 100 |
| | | 15-20 | 0 | 0 | 5 | 15 | 80 | 0 | 100 |
| | Soft Ground | 0-5 | 0 | 10 | 44 | 23 | 23 | 0 | 100 |
| | | 5-10 | 0 | 0 | 11 | 41 | 48 | 0 | 100 |
| | | 10-15 | 0 | 2 | 4 | 12 | 82 | 0 | 100 |
| | | 15-20 | 0 | 0 | 2 | 6 | 73 | 19 | 100 |
| | Reclaimed Land | 0-5 | 0 | 45 | 55 | 0 | 0 | 0 | 100 |
| | | 5-10 | 0 | 0 | 50 | 50 | 0 | 0 | 100 |
| | | 10-15 | 0 | 0 | 0 | 60 | 40 | 0 | 100 |
| | | 15-20 | 0 | 0 | 28 | 28 | 44 | 0 | 100 |
| B | Hard Ground | 0-5 | 0 | 4 | 41 | 19 | 24 | 3 | 100 |
| | | 5-10 | 0 | 4 | 27 | 22 | 40 | 7 | 100 |
| | | 10-15 | 0 | 0 | 0 | 10 | 75 | 15 | 100 |
| | | 15-20 | 0 | 0 | 0 | 3 | 75 | 22 | 100 |
| | Soft Ground | 0-5 | 0 | 21 | 67 | 8 | 4 | 0 | 100 |
| | | 5-10 | 0 | 3 | 55 | 30 | 12 | 0 | 100 |
| | | 10-15 | 0 | 4 | 24 | 33 | 33 | 6 | 100 |
| | | 15-20 | 0 | 4 | 26 | 31 | 31 | 8 | 100 |
| | Reclaimed Land | 0-5 | 0 | 10 | 90 | 0 | 0 | 0 | 100 |
| | | 5-10 | 0 | 0 | 78 | 22 | 0 | 0 | 100 |
| | | 10-15 | 0 | 0 | 50 | 30 | 20 | 0 | 100 |
| | | 15-20 | 0 | 0 | 37 | 19 | 44 | 0 | 100 |

*from WES (1999)

| Table 5<br>PERCENTILE DISTRIBUTION OF SPT'S FOR CLAY SOILS* | | | | | | | | | | |
|---|---|---|---|---|---|---|---|---|---|---|
| Zone | Site Category | Depth Range (m) | SPT Blow Count Range N60 | | | | | | | Sum |
| | | | 0-2 | 2-4 | 4-8 | 8-12 | 12-20 | 20-30 | >30 | |
| A | Hard Ground | 0-5 | 0 | 10 | 70 | 10 | 10 | 0 | 0 | 100 |
| | | 5-10 | 0 | 2 | 30 | 40 | 22 | 0 | 6 | 100 |
| | | 10-15 | 0 | 0 | 22 | 35 | 33 | 5 | 5 | 100 |
| | | 15-20 | 0 | 0 | 0 | 10 | 60 | 25 | 5 | 100 |
| | Soft Ground | 0-5 | 0 | 37 | 24 | 23 | 9 | 3 | 4 | 100 |
| | | 5-10 | 0 | 5 | 46 | 14 | 22 | 3 | 10 | 100 |
| | | 10-15 | 0 | 2 | 25 | 23 | 24 | 11 | 15 | 100 |
| | | 15-20 | 0 | 0 | 7 | 25 | 25 | 23 | 20 | 100 |
| | Reclaimed Land | 0-5 | 0 | 0 | 0 | 0 | 0 | 0 | 0 | 100 |
| | | 5-10 | 0 | 0 | 40 | 60 | 0 | 0 | 0 | 100 |
| | | 10-15 | 0 | 0 | 40 | 60 | 0 | 0 | 0 | 100 |
| | | 15-20 | 0 | 0 | 100 | 0 | 0 | 0 | 0 | 100 |
| B | Hard Ground | 0-5 | 0 | 10 | 27 | 22 | 31 | 5 | 5 | 100 |
| | | 5-10 | 0 | 4 | 0 | 16 | 45 | 10 | 25 | 100 |
| | | 10-15 | 0 | 0 | 0 | 8 | 42 | 50 | 0 | 100 |
| | | 15-20 | 0 | 0 | 0 | 15 | 45 | 0 | 40 | 100 |
| | Soft Ground | | (0-2) | (2-5) | (5-10) | (10-20) | (20-30) | >30 | | |
| | | 0-5 | 2 | 49 | 43 | 4 | 2 | 0 | | 100 |
| | | 5-10 | 0 | 49 | 41 | 10 | 0 | 0 | | 100 |
| | | 10-15 | 0 | 45 | 45 | 10 | 0 | 0 | | 100 |
| | | 15-20 | 0 | 17 | 44 | 23 | 8 | 8 | | 100 |
| | Reclaimed Land | 0-5 | 23 | 67 | 10 | 0 | 0 | 0 | | 100 |
| | | 5-10 | 5 | 45 | 50 | 0 | 0 | 0 | | 100 |
| | | 10-15 | 0 | 39 | 44 | 13 | 4 | 0 | | 100 |
| | | 15-20 | 0 | 5 | 50 | 45 | 0 | 0 | | 100 |

*from WES (1999)

| Table 6<br>PERCENTILE DISTRIBUTION OF SPT'S FOR GRAVELLY SOILS* | | | | | | | | | |
|---|---|---|---|---|---|---|---|---|---|
| Zone | Site Category | Depth Range (m) | SPT Blow Count Range N60 | | | | | | Sum |
| | | | 0-5 | 5-10 | 10-20 | 20-30 | 30-50 | >50 | |
| A | Hard Ground | 0-5 | 0 | 6 | 27 | 31 | 29 | 7 | 100 |
| | | 5-10 | 0 | 0 | 2 | 9 | 80 | 9 | 100 |
| | | 10-15 | 0 | 0 | 0 | 2 | 97 | 1 | 100 |
| | | 15-20 | 0 | 0 | 0 | 4 | 73 | 23 | 100 |
| | Soft Ground | 0-5 | 0 | 5 | 27 | 34 | 34 | 0 | 100 |
| | | 5-10 | 0 | 0 | 0 | 4 | 75 | 21 | 100 |
| | | 10-15 | 0 | 0 | 0 | 0 | 55 | 45 | 100 |
| | | 15-20 | 0 | 0 | 0 | 0 | 55 | 45 | 100 |
| | Reclaimed Land | 0-5 | 0 | 31 | 50 | 12 | 0 | 7 | 100 |
| | | 5-10 | 0 | 20 | 0 | 0 | 80 | 0 | 100 |
| | | 10-15 | 20 | 6 | 0 | 0 | 75 | 5 | 100 |
| | | 15-20 | 0 | 0 | 0 | 0 | 100 | 0 | 100 |
| B | Hard Ground | 0-5 | 12 | 10 | 21 | 38 | 19 | 0 | 100 |
| | | 5-10 | 0 | 0 | 0 | 25 | 50 | 25 | 100 |
| | | 10-15 | 0 | 0 | 0 | 30 | 70 | 0 | 100 |
| | | 15-20 | 0 | 0 | 0 | 0 | 48 | 52 | 100 |
| | Soft Ground | 0-5 | 9 | 21 | 33 | 31 | 4 | 2 | 100 |
| | | 5-10 | 2 | 2 | 4 | 26 | 50 | 16 | 100 |
| | | 10-15 | 0 | 0 | 0 | 15 | 50 | 35 | 100 |
| | | 15-20 | 0 | 0 | 0 | 0 | 49 | 51 | 100 |
| | Reclaimed Land | 0-5 | 20 | 30 | 50 | 0 | 0 | 0 | 100 |
| | | 5-10 | 3 | 0 | 0 | 76 | 21 | 0 | 100 |
| | | 10-15 | 0 | 3 | 0 | 2 | 95 | 0 | 100 |
| | | 15-20 | 0 | 0 | 0 | 7 | 54 | 39 | 100 |

*from WES (1999)

| Table 7<br>Kobe Regional Velocity Model<br>Rock Sites (Wald, 1996) | | | | |
|---|---|---|---|---|
| $V_p$ (km/s) | $V_S$ (km/s) | Density (gm/cc) | Thickness (km) | Depth (km) |
| 2.50 | 1.00 | 2.10 | 0.10 | 0.00 |
| 3.20 | 1.80 | 2.10 | 0.40 | 0.10 |
| 5.50 | 3.20 | 2.60 | 4.50 | 0.50 |
| 6.00 | 3.46 | 2.70 | 22.00 | 5.00 |
| 6.80 | 3.83 | 2.87 | 5.00 | 27.00 |
| 7.80 | 4.50 | 3.50 | | 32.00 |
| Soil Sites | | | | |
| 0.60 | 0.30 | 1.70 | 0.10 | 0.00 |
| 1.20 | 0.50 | 1.82 | 0.10 | 0.10 |
| 2.50 | 1.00 | 2.10 | 1.00 | 0.20 |
| 3.20 | 1.80 | 2.10 | 0.40 | 1.20 |
| 5.50 | 3.20 | 2.60 | 4.50 | 1.60 |
| 6.00 | 3.46 | 2.70 | 20.90 | 6.10 |
| 6.80 | 3.38 | 2.87 | 5.00 | 27.00 |
| 7.80 | 4.50 | 3.50 | | 32.00 |

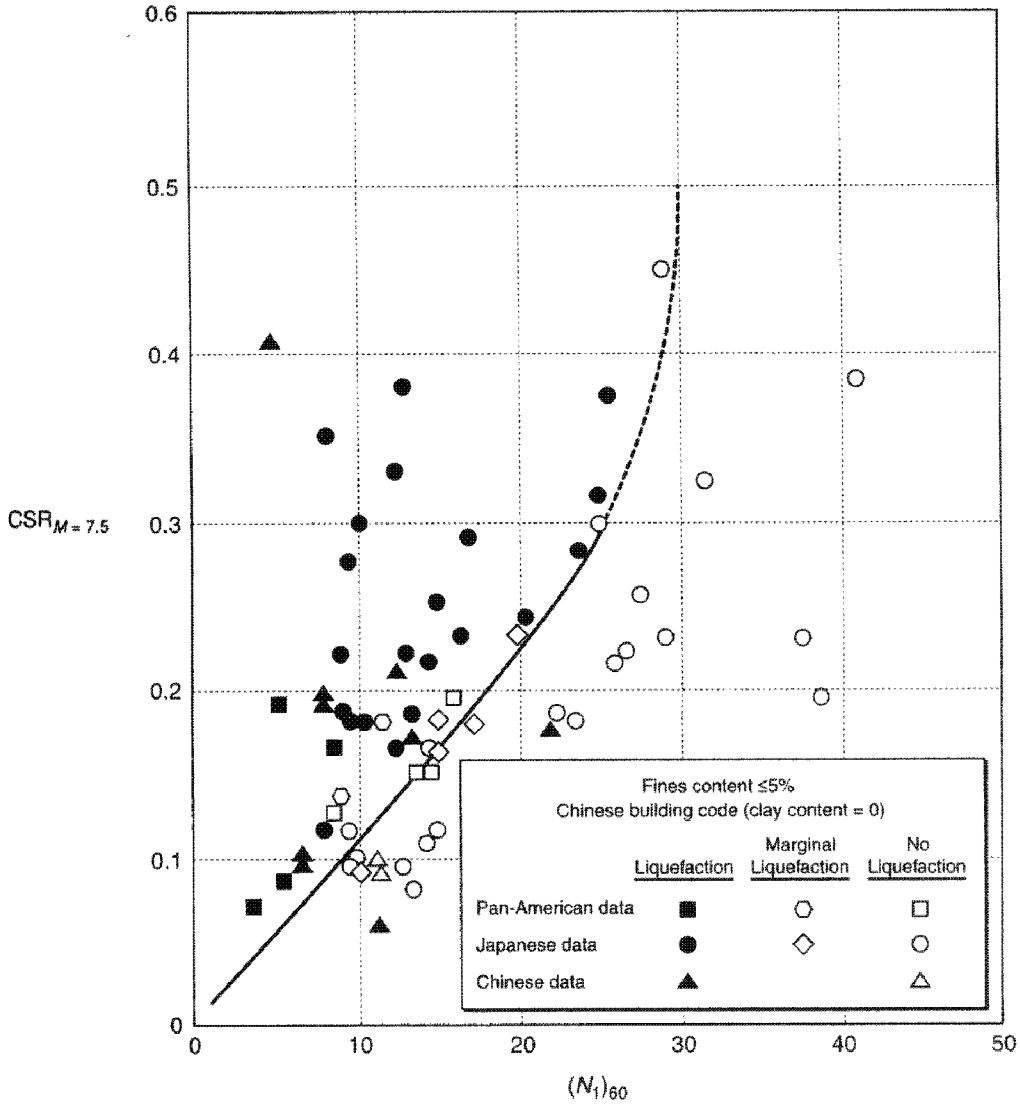


Figure 1. Relationship between cyclic stress ratios causing liquefaction and $(N_1)_{60}$ values for clean sands in **M** 7.5 earthquakes (Seed et al., 1975).

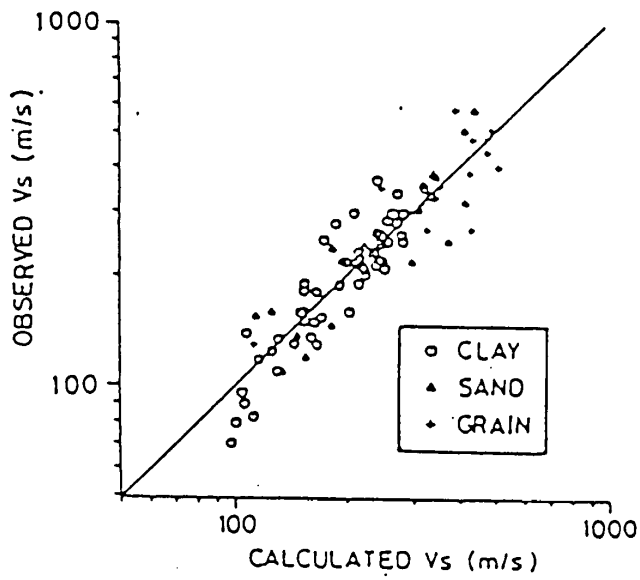


$$V_S = 34.824 \cdot F \cdot (N + 1)^{0.244} P^{0.175}$$

F = 1.000 Clay

= 0.922 Sand

= 0.851 Gravel

N = SPT Blow Count

P = Mean Interguanular Pressure

$$= \frac{2}{3}(\gamma D - u)$$

Figure 2. Regional (Kobe, Osaka; Japan) shear-wave velocity and SPT correlation (Iwasaki et al., 1987). Figure compares predicted and measured shear-wave velocities.

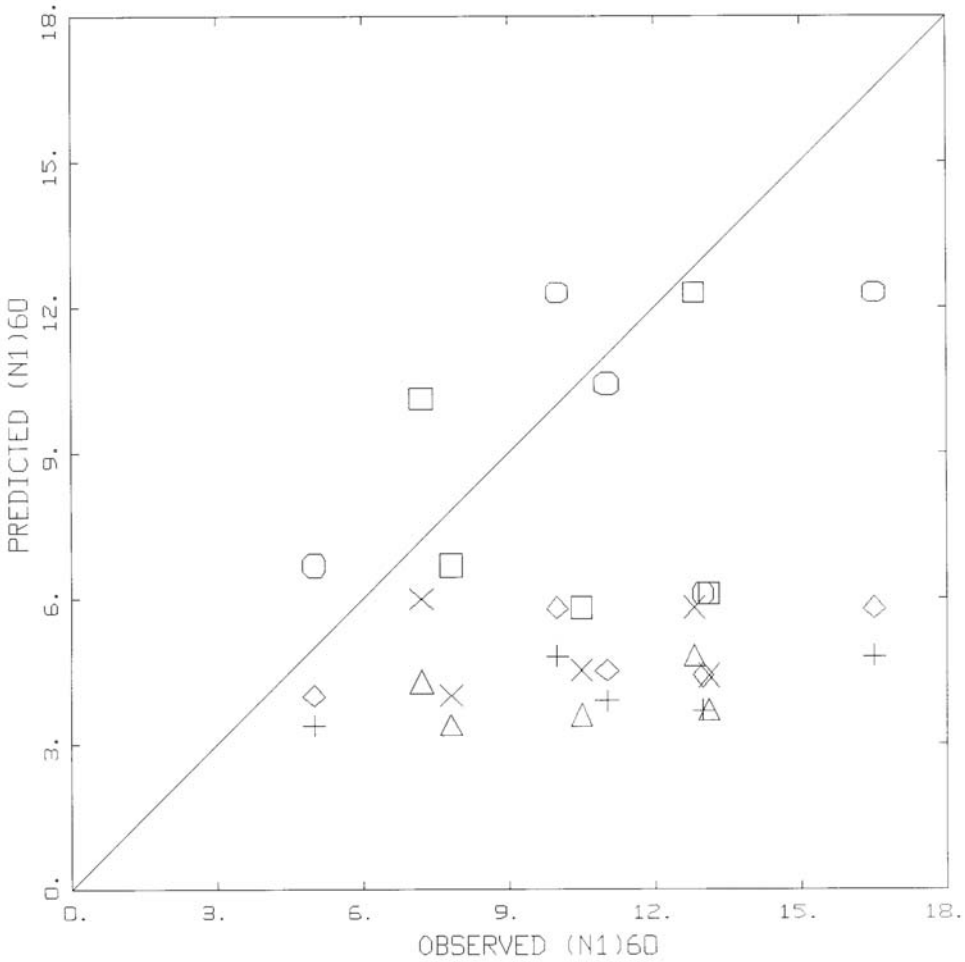


BLOW COUNT
(N1)60

LEGEND

- MODEL 1 VS. SEED OBSERVED
- MODEL 1 VS. KAYEN OBSERVED
- MODEL 2 VS. SEED OBSERVED
- MODEL 2 VS. KAYEN OBSERVED
- MODEL 3 VS. SEED OBSERVED
- MODEL 3 VS. KAYEN OBSERVED
- OBSERVED = PREDICTED LINE

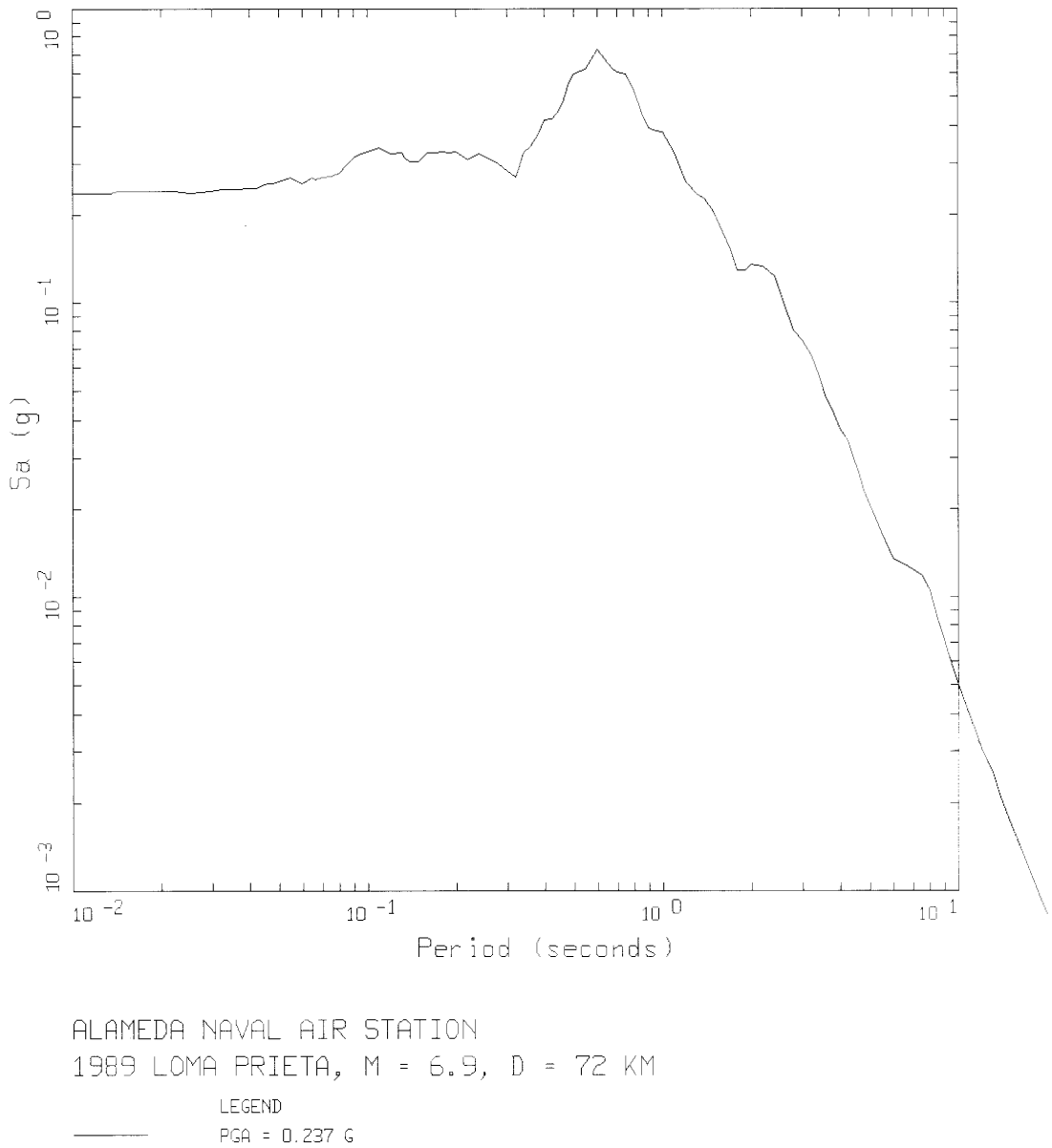


Figure 4a. Average horizontal component response spectra computed from recorded motions: Alameda Naval Air Station, Loma Prieta earthquake.

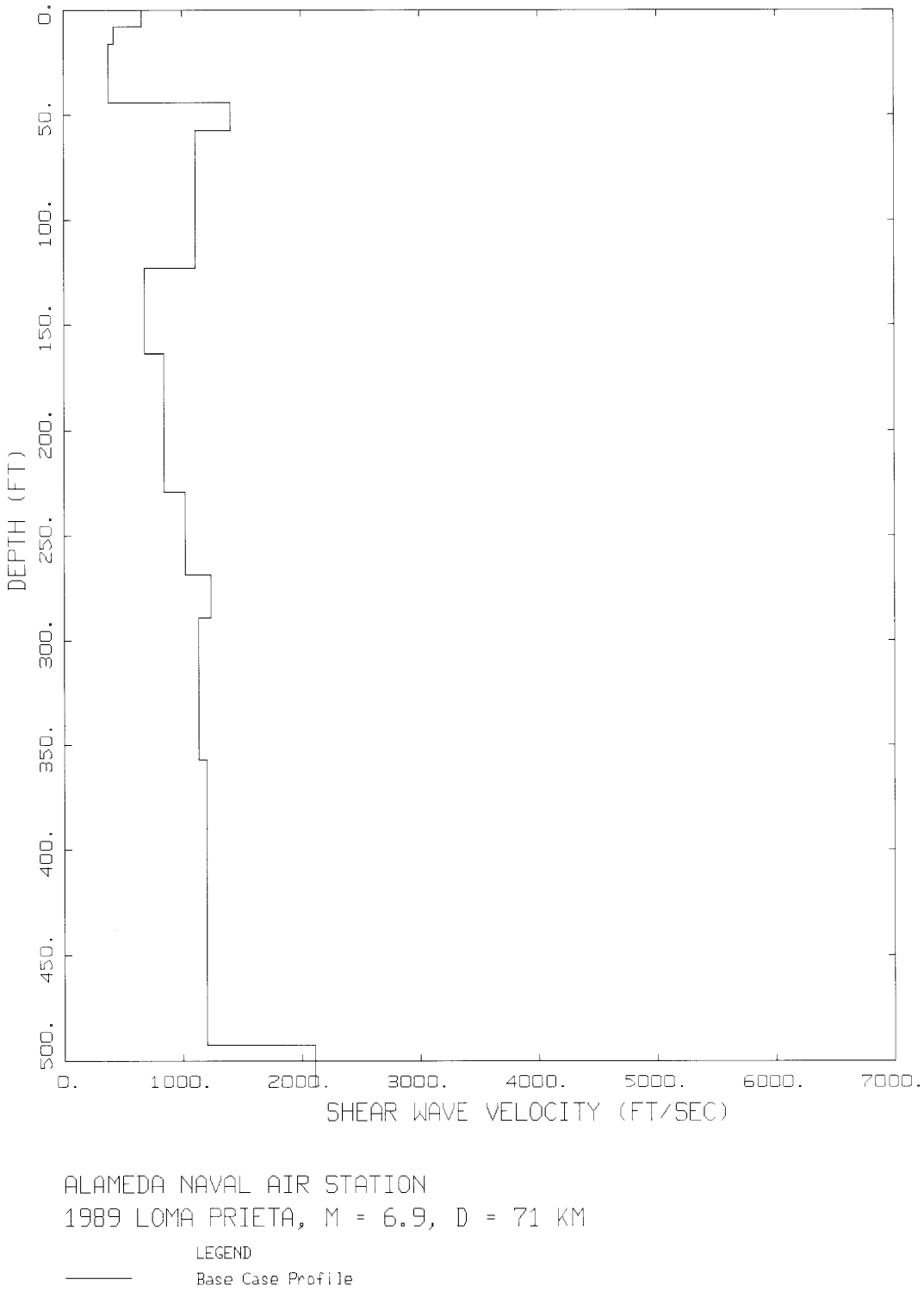


Figure 4b. Shear-wave velocity profile (measured) at the Alameda Naval Air Station to a depth of 500 ft.

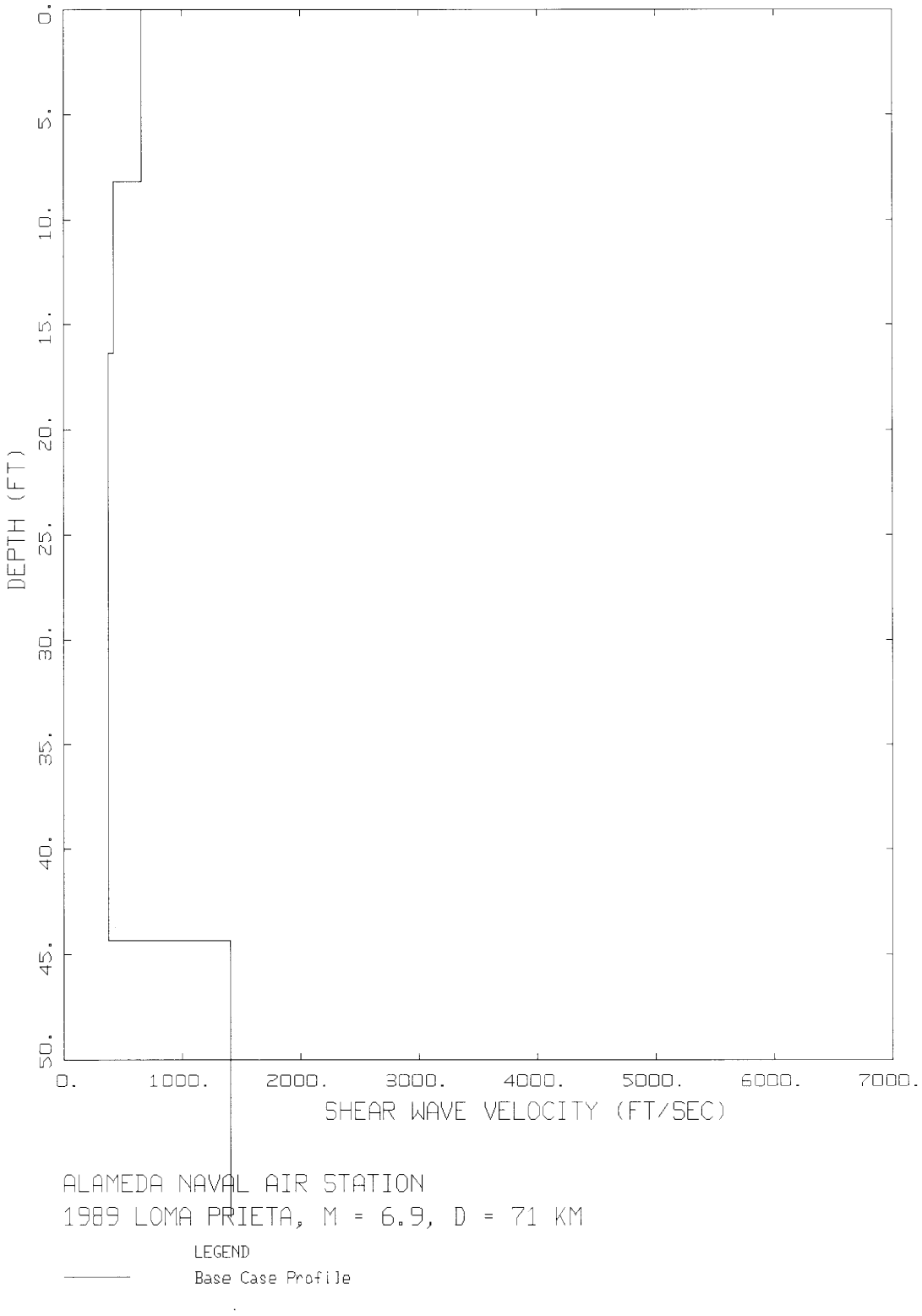


Figure 4c. Shear-wave velocity profile (measured) at the Alameda Naval Air Station to a depth of 50 ft.

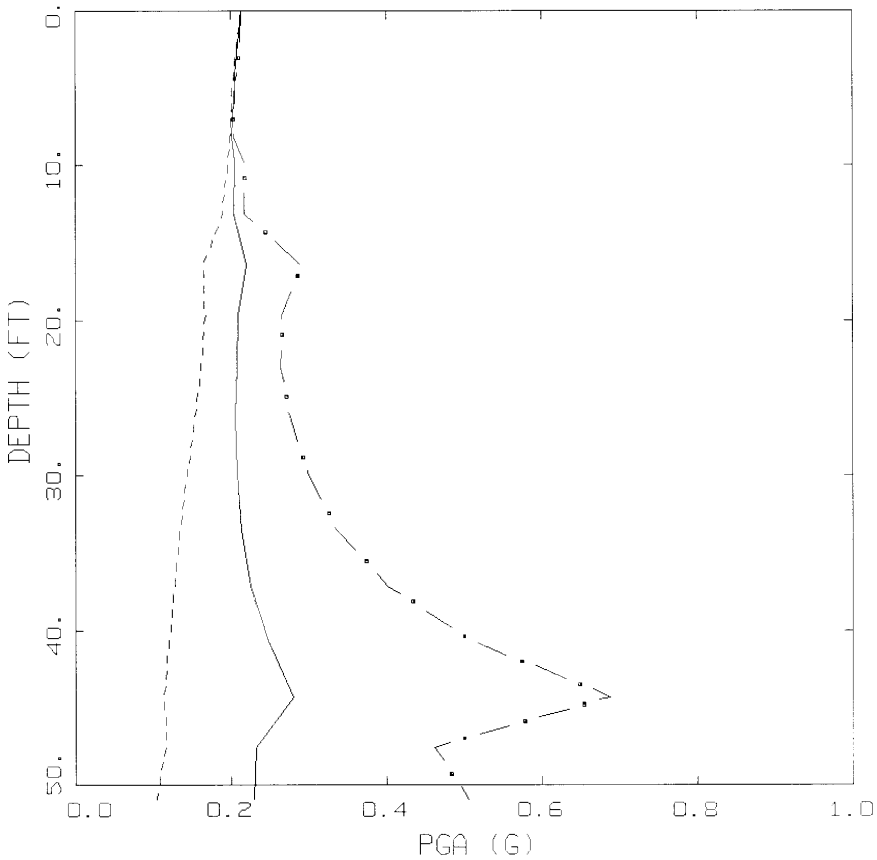


ALAMEDA NAVAL AIR STATION
1989 LOMA PRIETA, M = 6.9, D = 71 KM

LEGEND

— · — PGA: 84TH PERCENTILE

——— PGA: 50TH PERCENTILE

- - - - - PGA: 16TH PERCENTILE

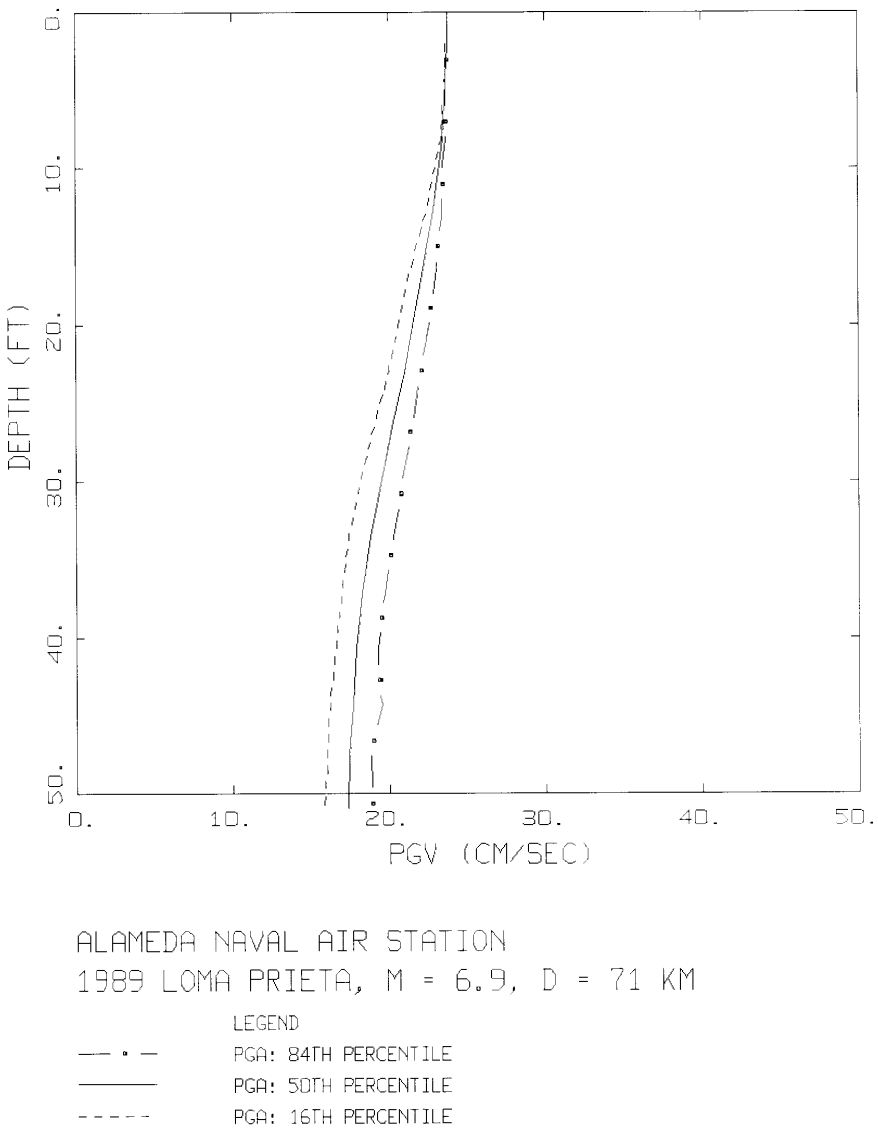


Figure 4e. Variation of peak particle velocity (cm/sec) verses depth computed with a suite of random profiles at the Alameda Naval Air Station. Average horizontal spectrum (Figure 4a) based on recorded motions used as control motions.

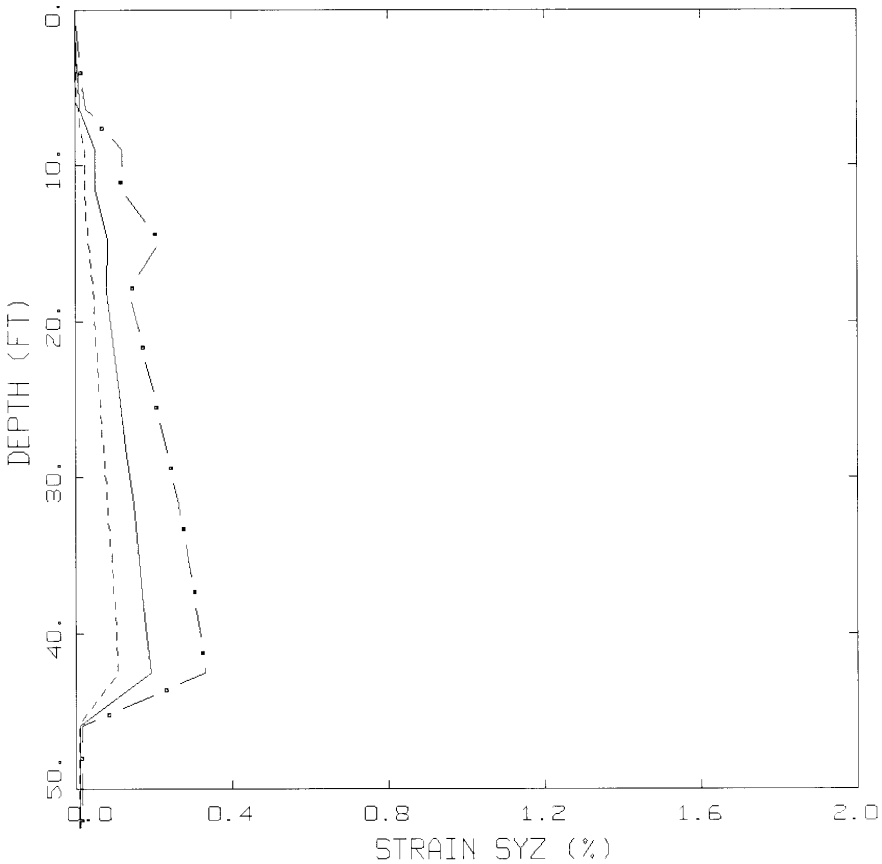


ALAMEDA NAVAL AIR STATION
1989 LOMA PRIETA, M = 6.9, D = 71 KM

LEGEND

—— • —— PGA: 84TH PERCENTILE

———— PGA: 50TH PERCENTILE

- - - - - PGA: 16TH PERCENTILE

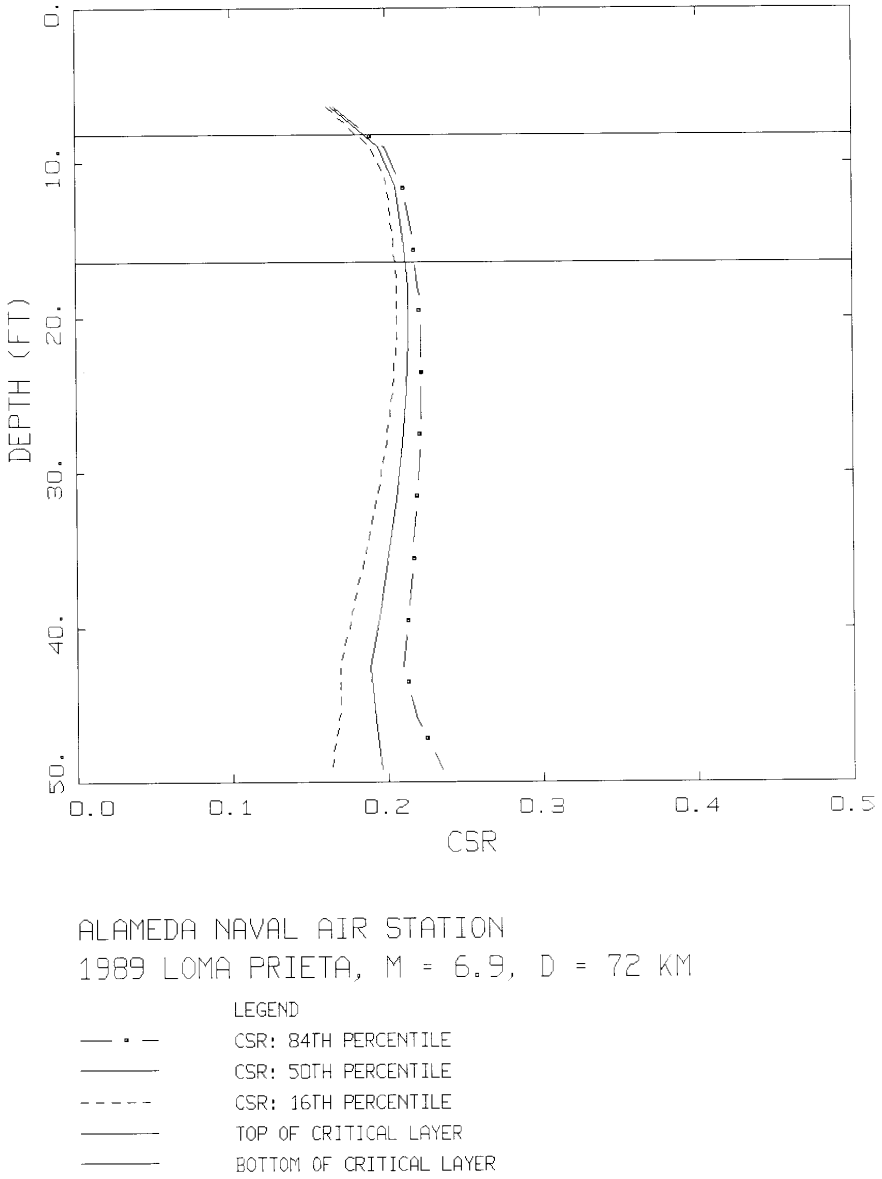


Figure 4g. Variation of CSR verses depth computed with a suite of random profiles at the Alameda Naval Air Station. Average horizontal spectrum (Figure 4a) based on recorded motions used as control motions. Critical layer indicated with horizontal lines.

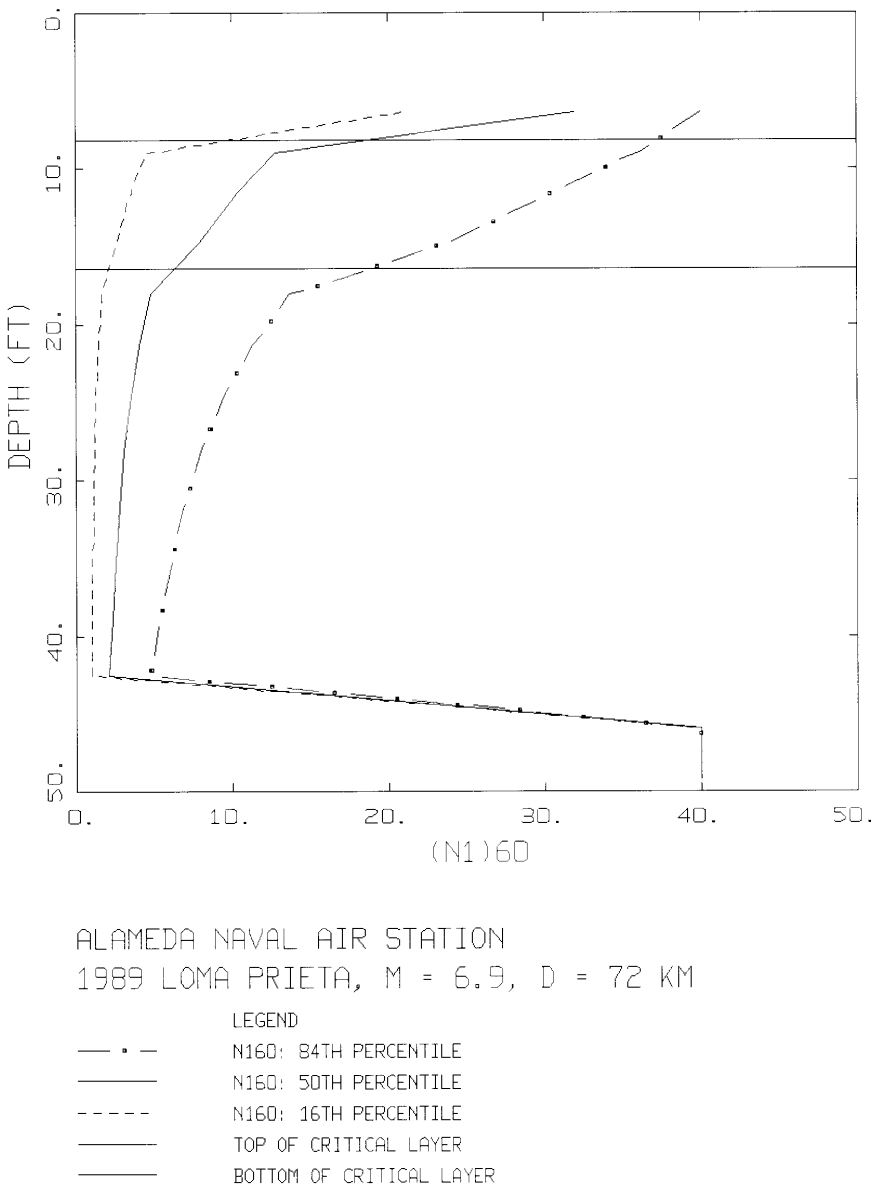


Figure 4h. Variation of peak $(N_1)_{60}$ verses depth computed with a suite of random profiles at the Alameda Naval Air Station using the shear-wave velocity correlation model of Iwasaki et al. (1987). Average horizontal spectrum (Figure 4a) based on recorded motions used as control motions. Critical layer indicated with horizontal lines.

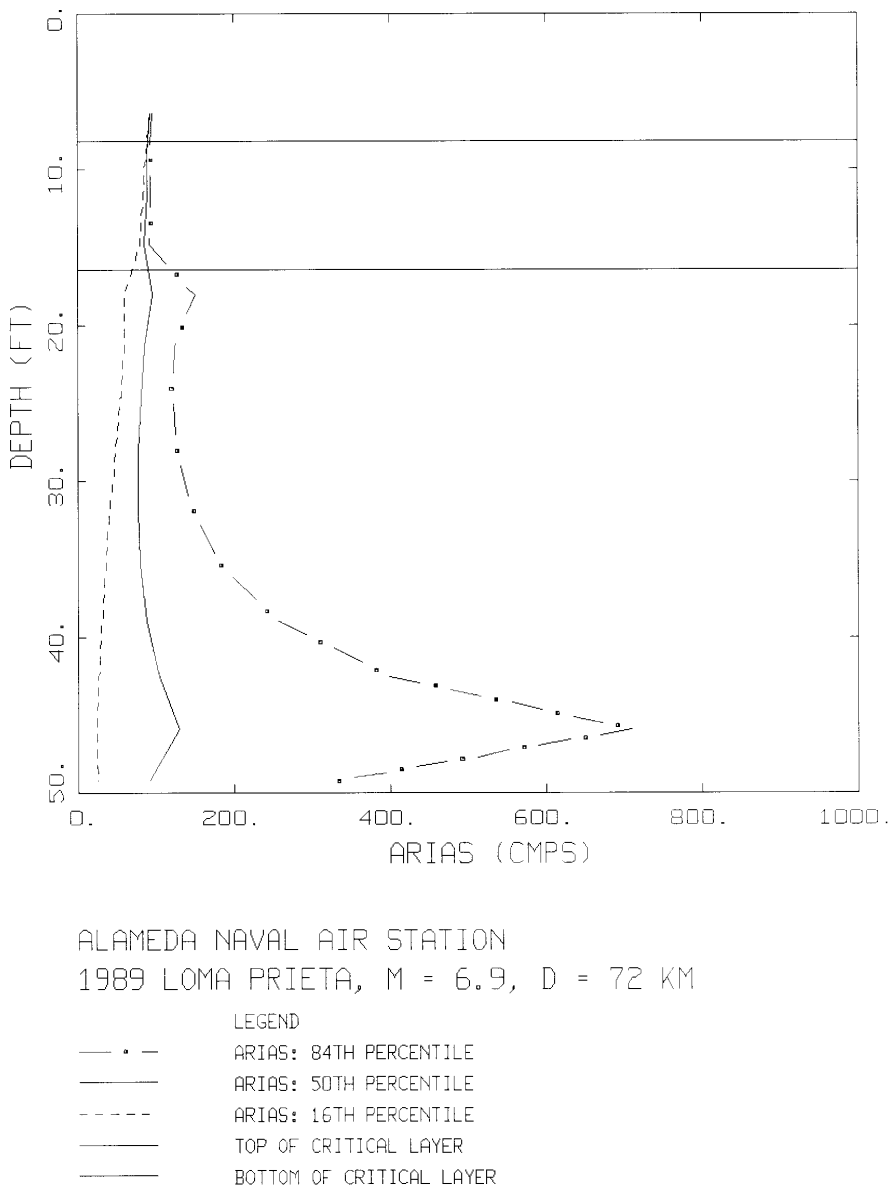


Figure 4i. Variation of Arias Intensity (cm/sec) verses depth computed with a suite of random profiles at the Alameda Naval Air Station. Average horizontal spectrum (Figure 4a) based on recorded motions used as control motions. Critical layer indicated with horizontal lines.

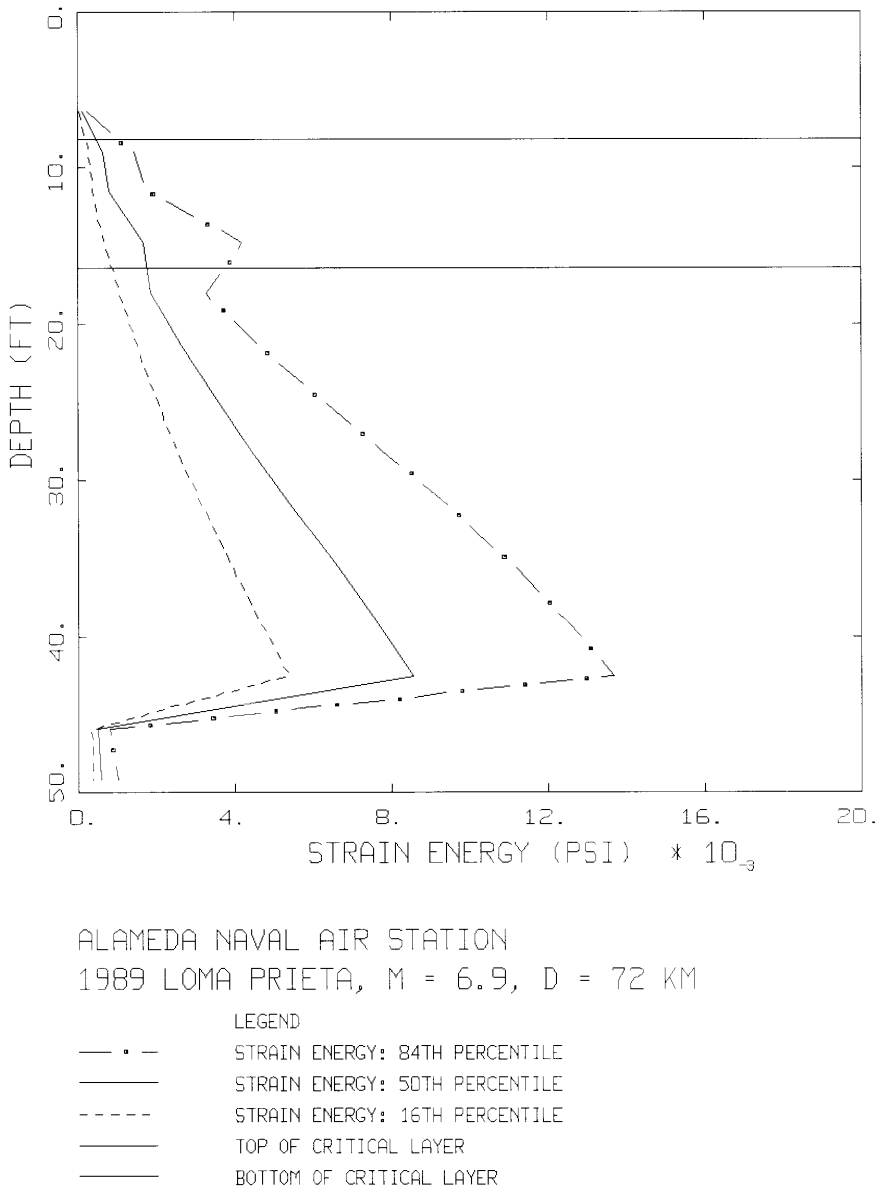


Figure 4j Variation of strain energy (PSI) verses depth computed with a suite of random profiles at the Alameda Naval Air Station. Average horizontal spectrum (Figure 4a) based on recorded motions used as control motions. Critical layer indicated with horizontal lines.

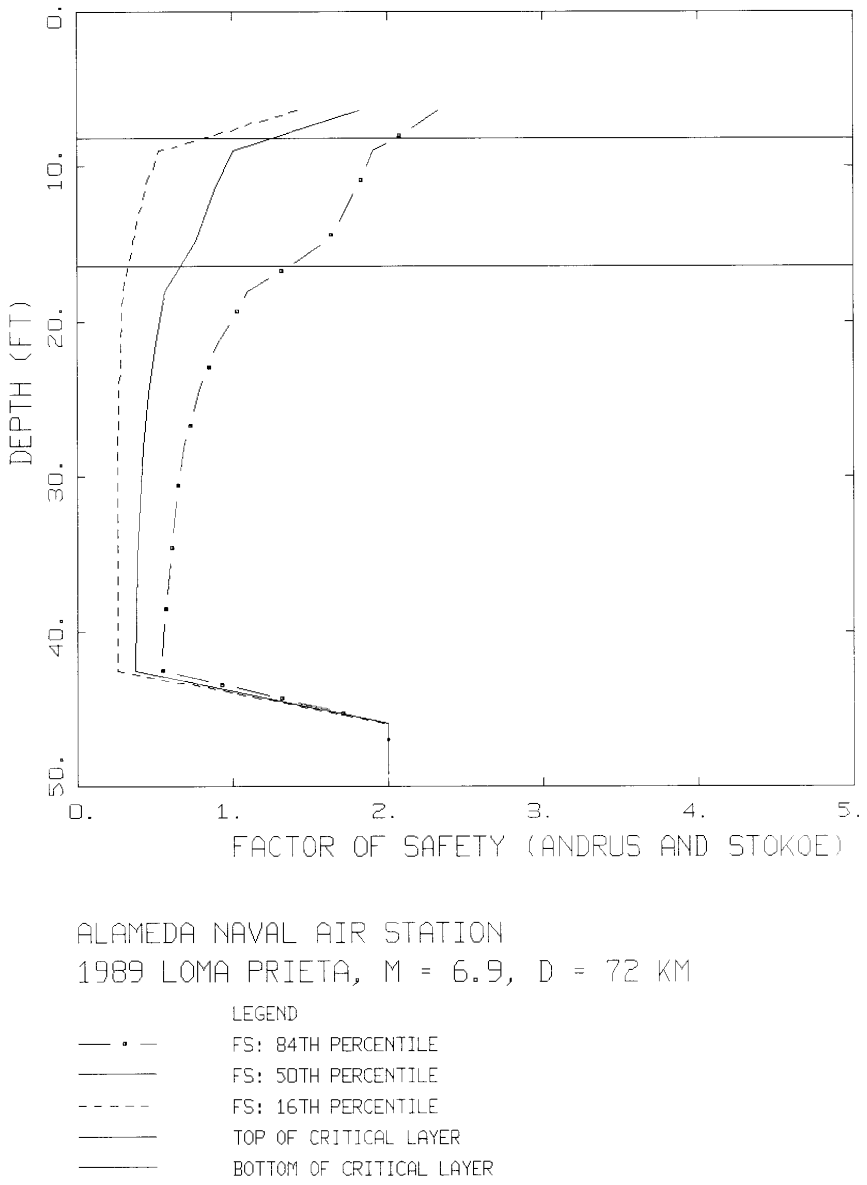


Figure 4k. Variation of the factor of safety using the Andrus and Stokoe (2004) shear-wave velocity based approach verses depth computed with a suite of random profiles at the Alameda Naval Air Station. Average horizontal spectrum (Figure 4a) based on recorded motions used as control motions. Critical layer indicated with horizontal lines.

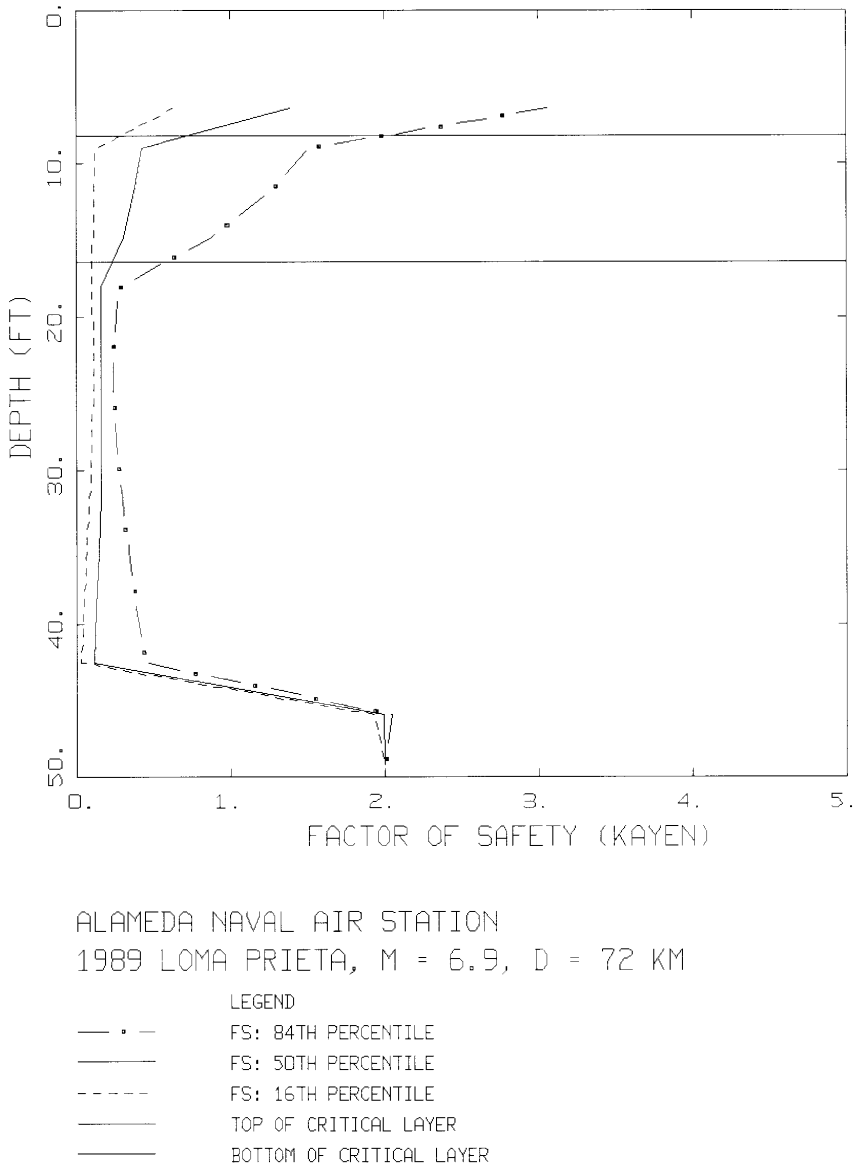


Figure 4l. Variation of the factor of safety using the Kayen and Mitchell (1997) Arias Intensity based approach verses depth computed with a suite of random profiles at the Alameda Naval Air Station. Average horizontal spectrum (Figure 4a) based on recorded motions used as control motions. Critical layer indicated with horizontal lines.

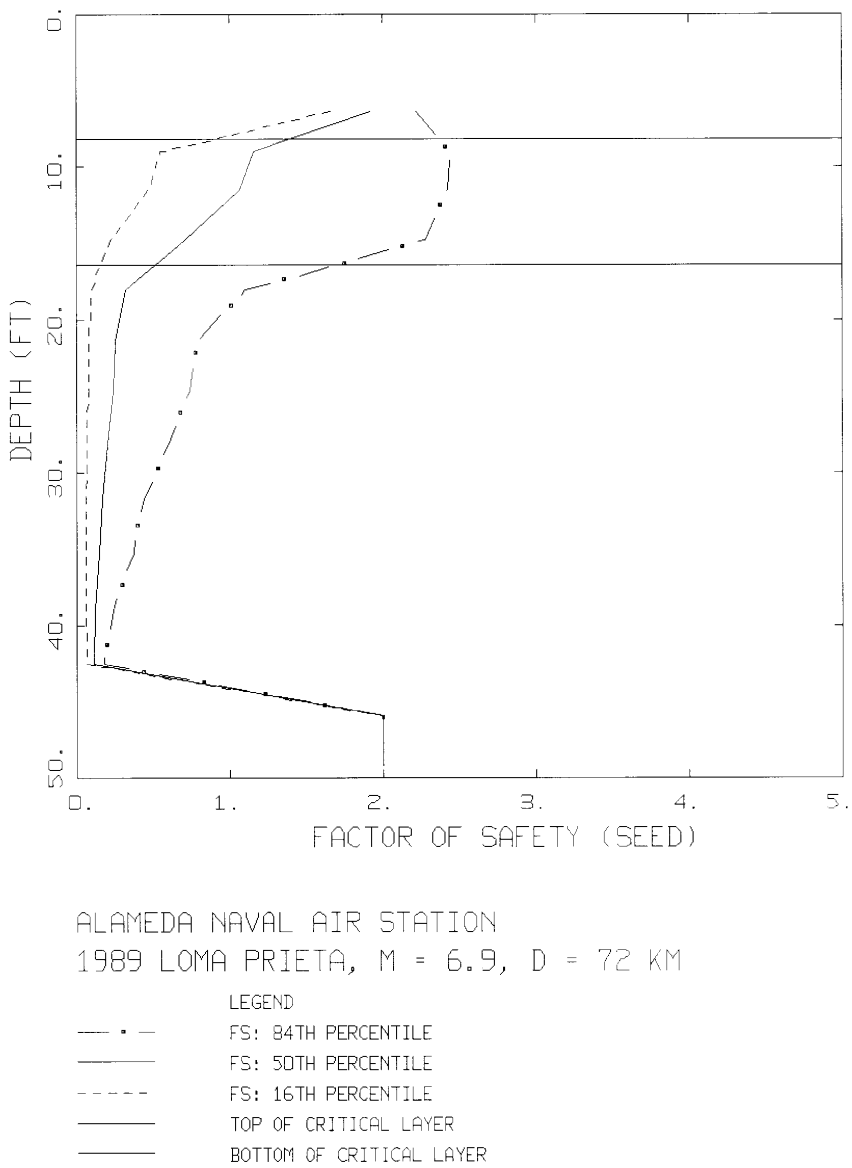


Figure 4m. Variation of the factor of the factor of safety using the Seed et al., (2002) SPT based approach verses depth computed with a suite of random profiles at the Alameda Naval Air Station. Average horizontal spectrum (Figure 4a) based on recorded motions used as control motions. Critical layer indicated with horizontal lines.

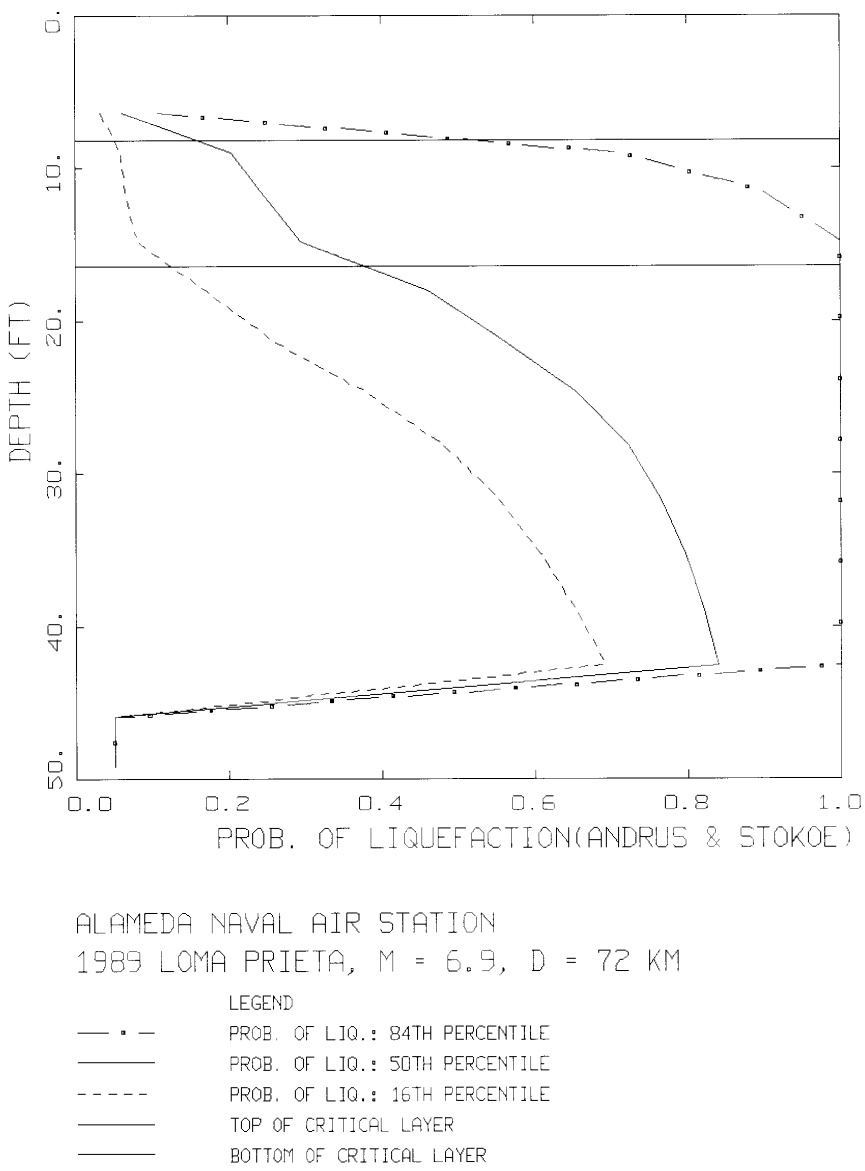


Figure 4n. Variation of the probability of liquefaction using the Andrus and Stokoe (2004) shear-wave velocity based approach verses depth computed with a suite of random profiles the Alameda Naval Air Station. Average horizontal spectrum (Figure 4a) based on recorded motions used as control motions. Critical layer indicated with horizontal lines.

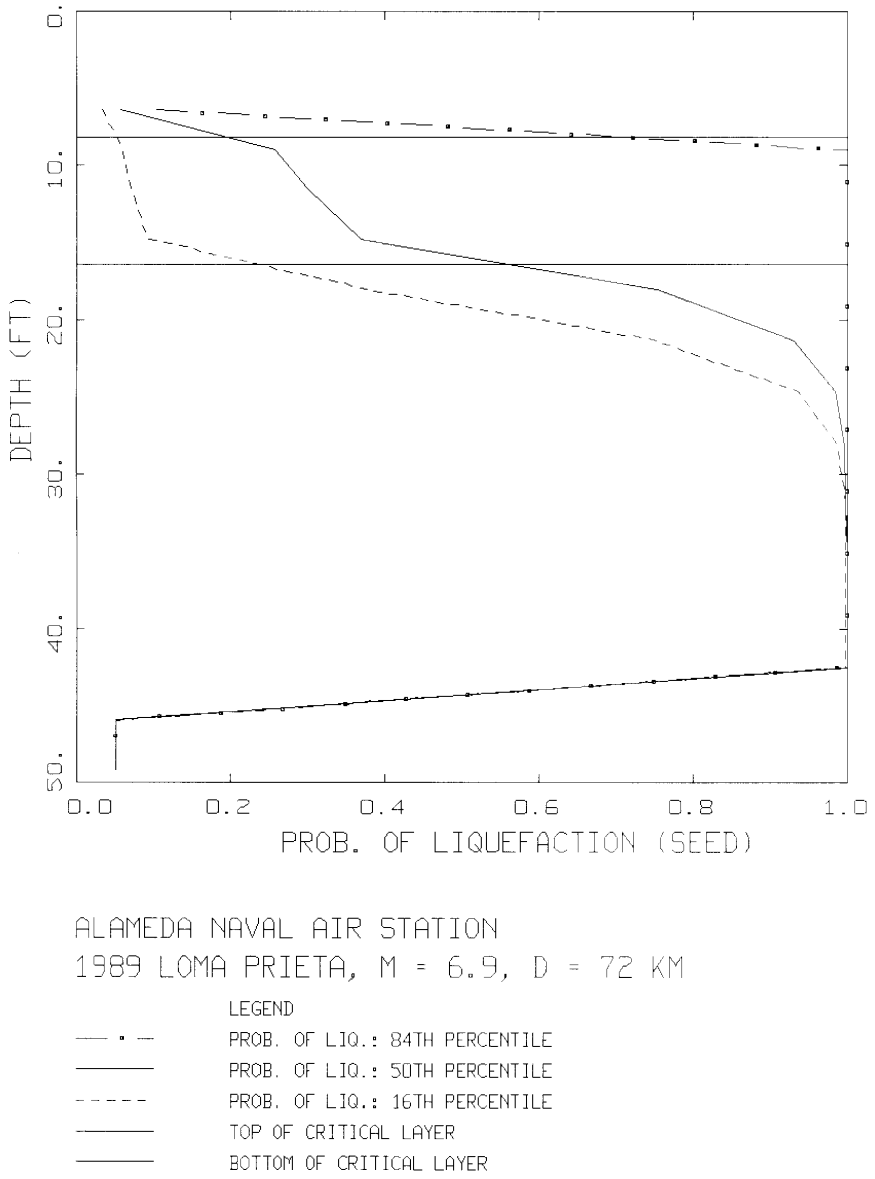


Figure 4o. Variation probability of liquefaction using the Seed et al. (2002) SPT based approach verses depth computed with a suite of random profiles at the Alameda Naval Air Station. Average horizontal spectrum (Figure 4a) based on recorded motions used as control motions. Critical layer indicated with horizontal lines.

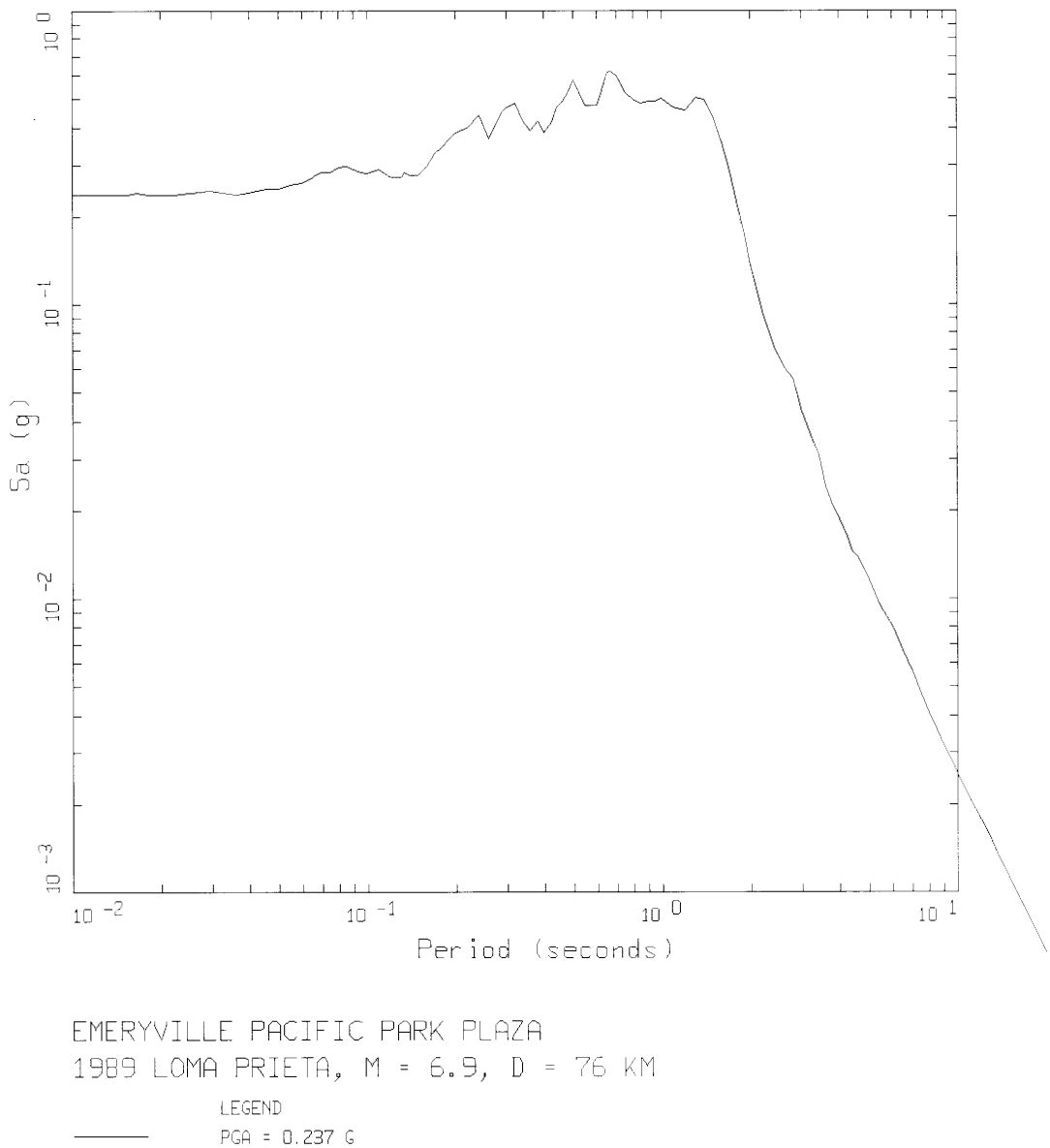


Figure 5a. Average horizontal component response spectra computed from recorded motions: Emeryville Pacific Park Plaza site, Loma Prieta earthquake.

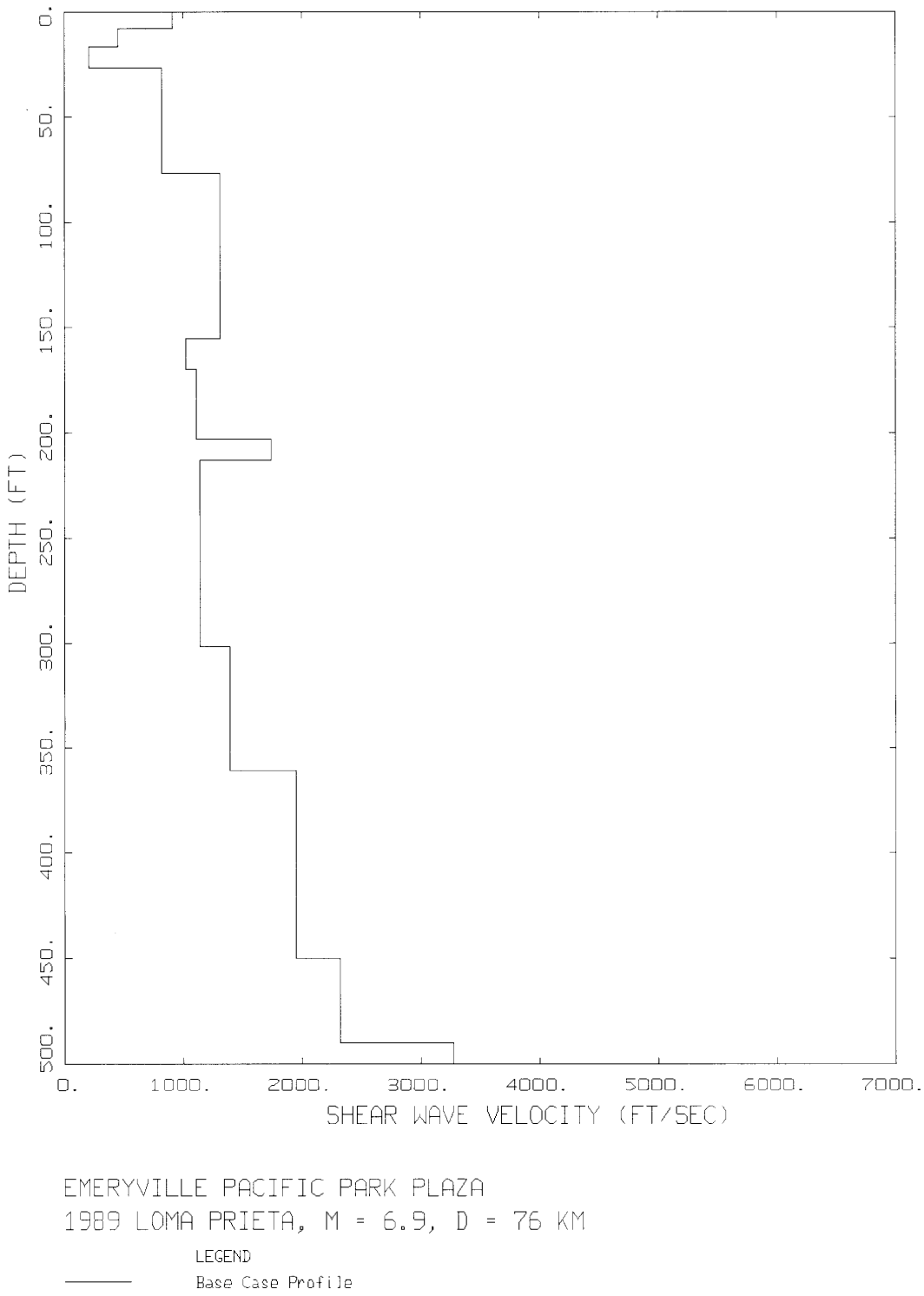


Figure 5b. Shear-wave velocity profile (measured) at the Emeryville Pacific Park Plaza site to a depth of 500 ft.

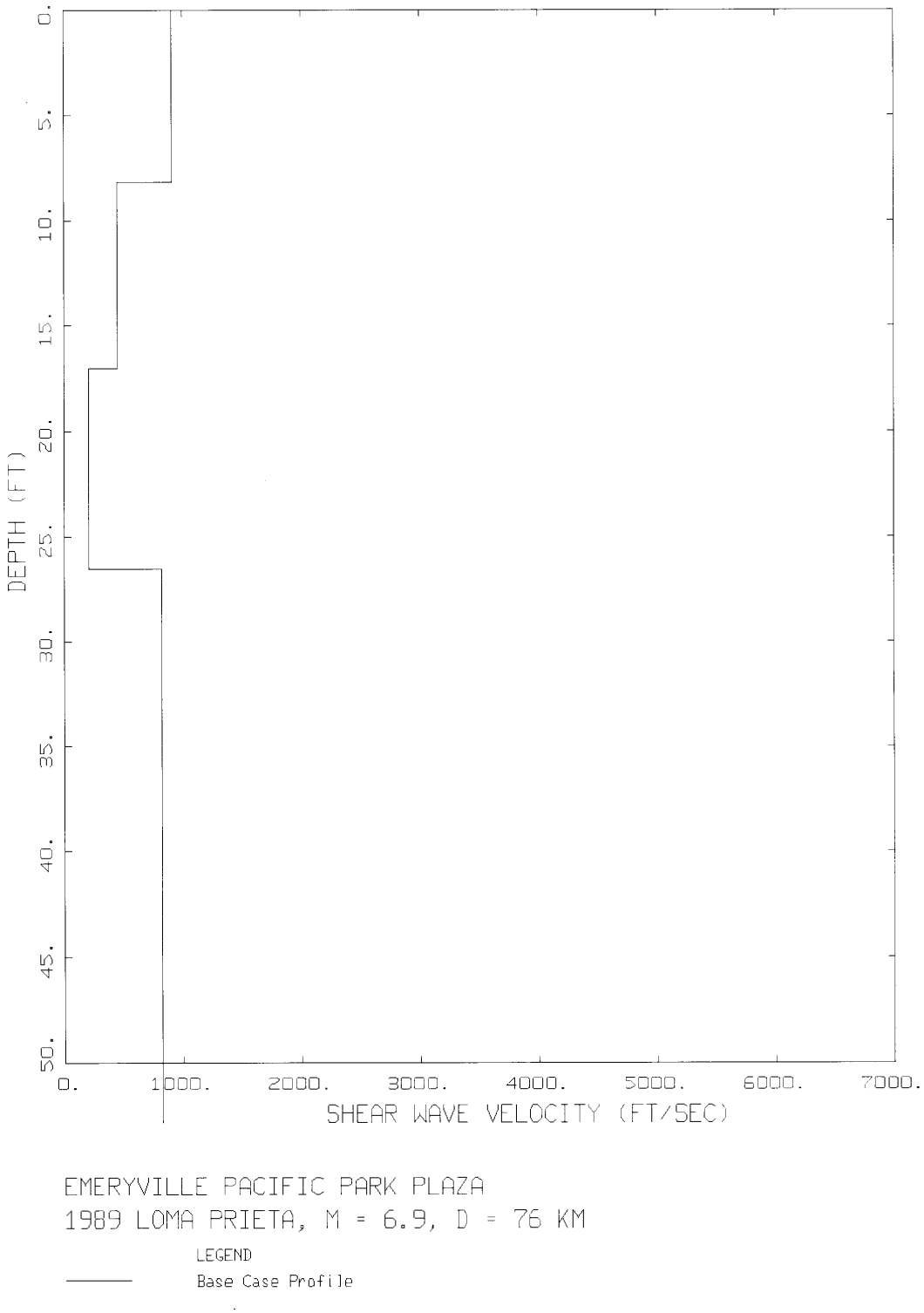


Figure 5c. Shear-wave velocity profile (measured) at the Emeryville Pacific Park Plaza site to a depth of 50 ft.

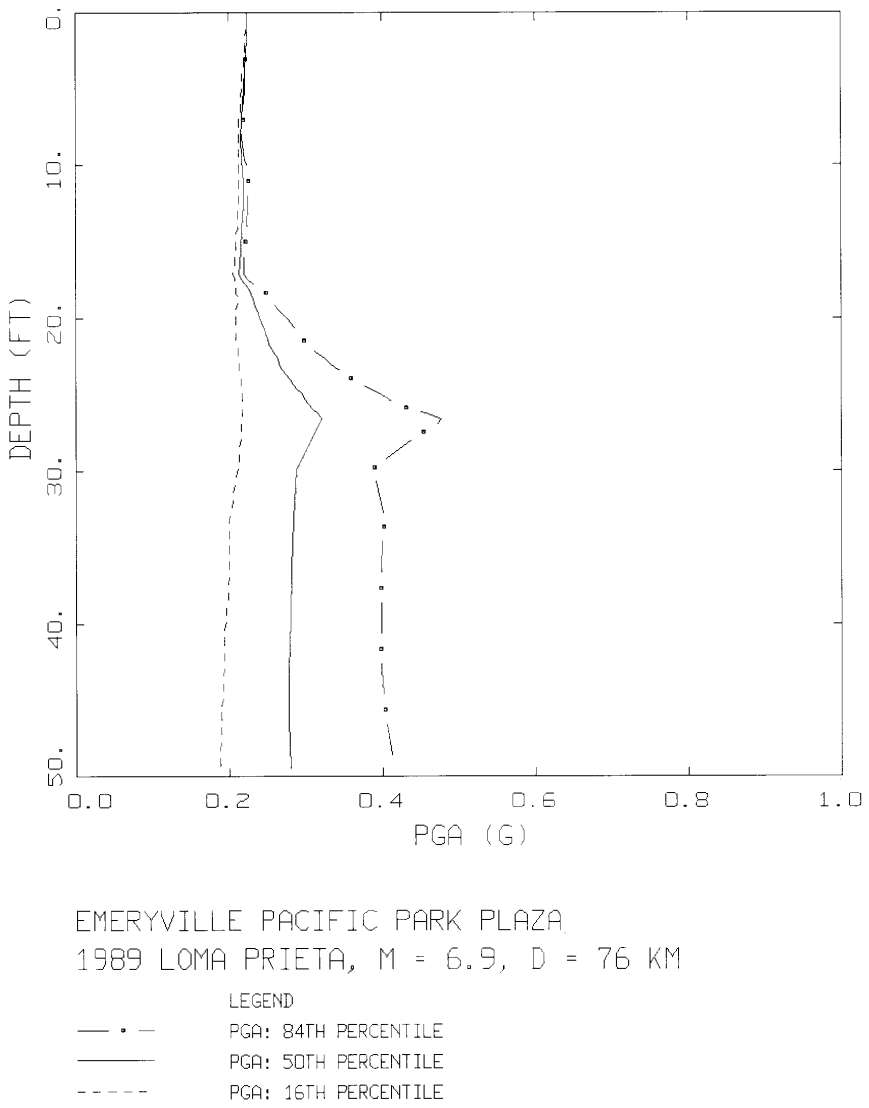


Figure 5d. Variation of peak acceleration(g) (Average horizontal component) verses depth computed for a suite of random profiles at the Emeryville Pacific Park Plaza site. Average horizontal spectrum (Figure 5a) based on recorded motions used as control motions.

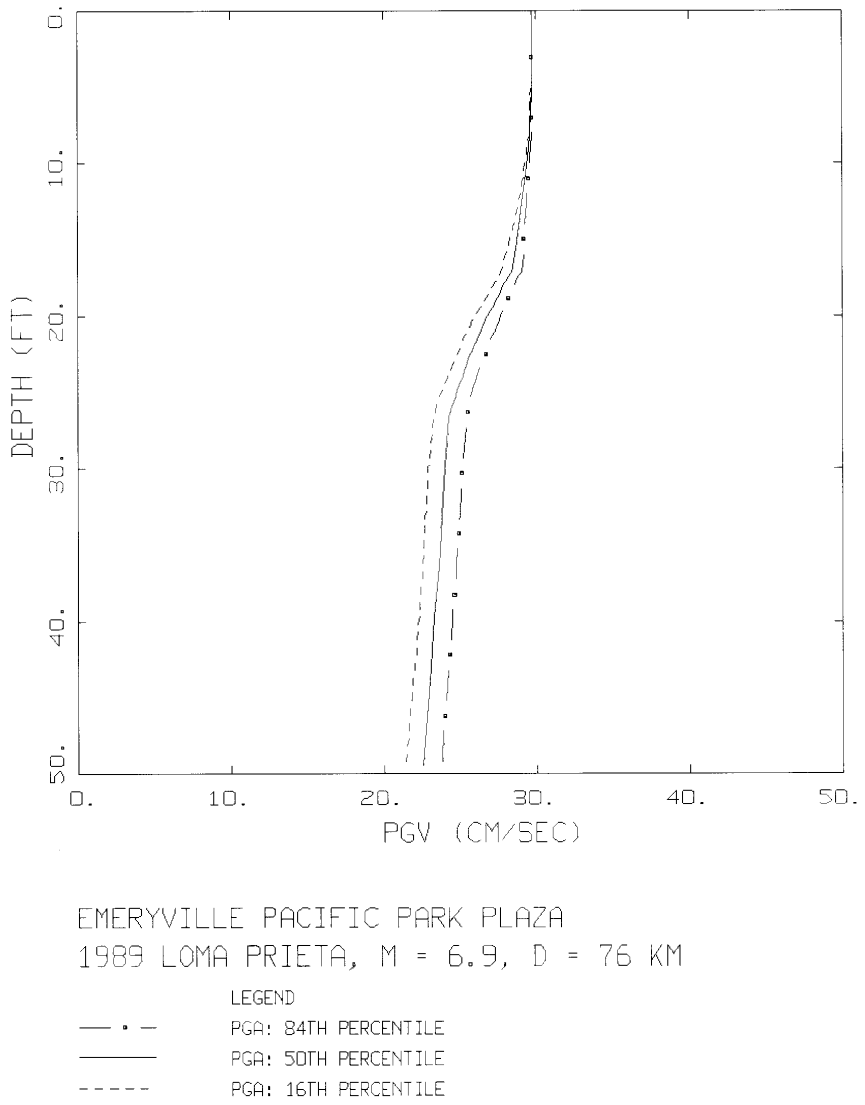


Figure 5e. Variation of peak particle velocity (cm/sec) verses depth computed for a suite of random profiles at the Emeryville Pacific Park Plaza site. Average horizontal spectrum (Figure 5a) based on recorded motions used as control motions.

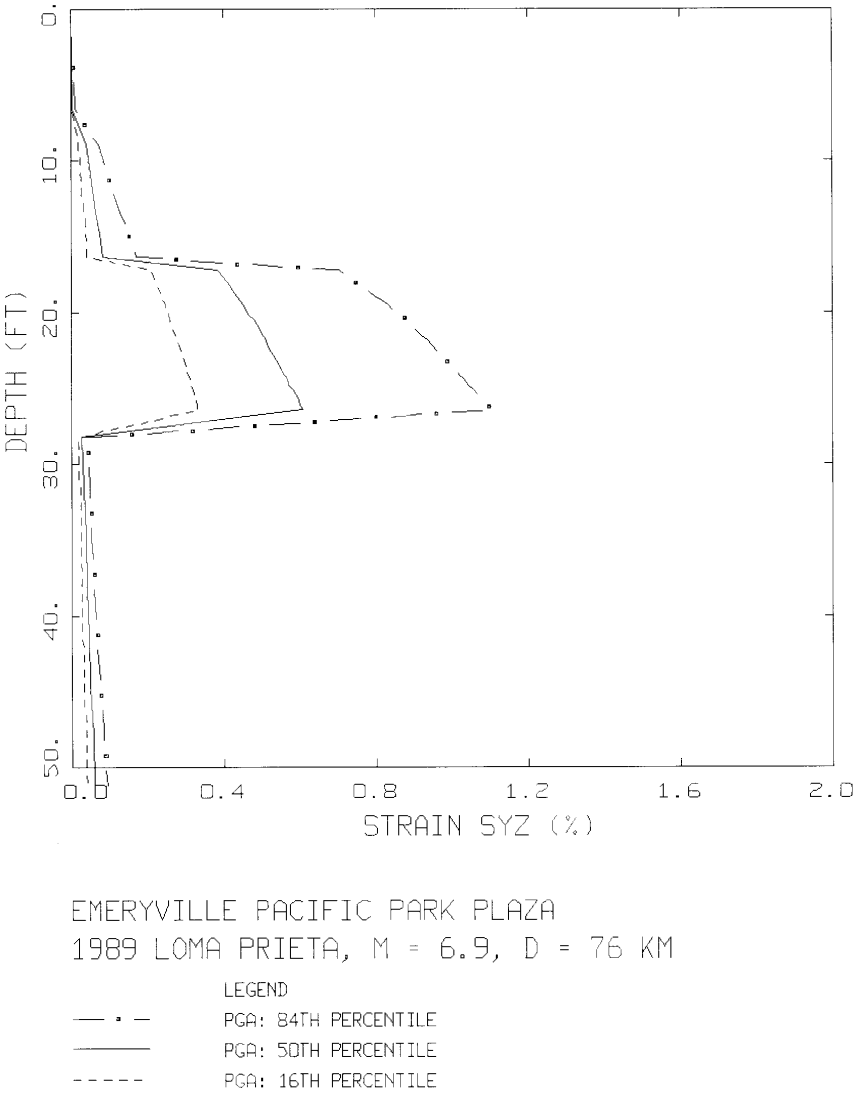


Figure 5f. Variation of peak shear strain(%) verses depth computed for a suite of random profiles at the Emeryville Pacific Park Plaza site. Average horizontal spectrum (Figure 5a) based on recorded motions used as control motions.

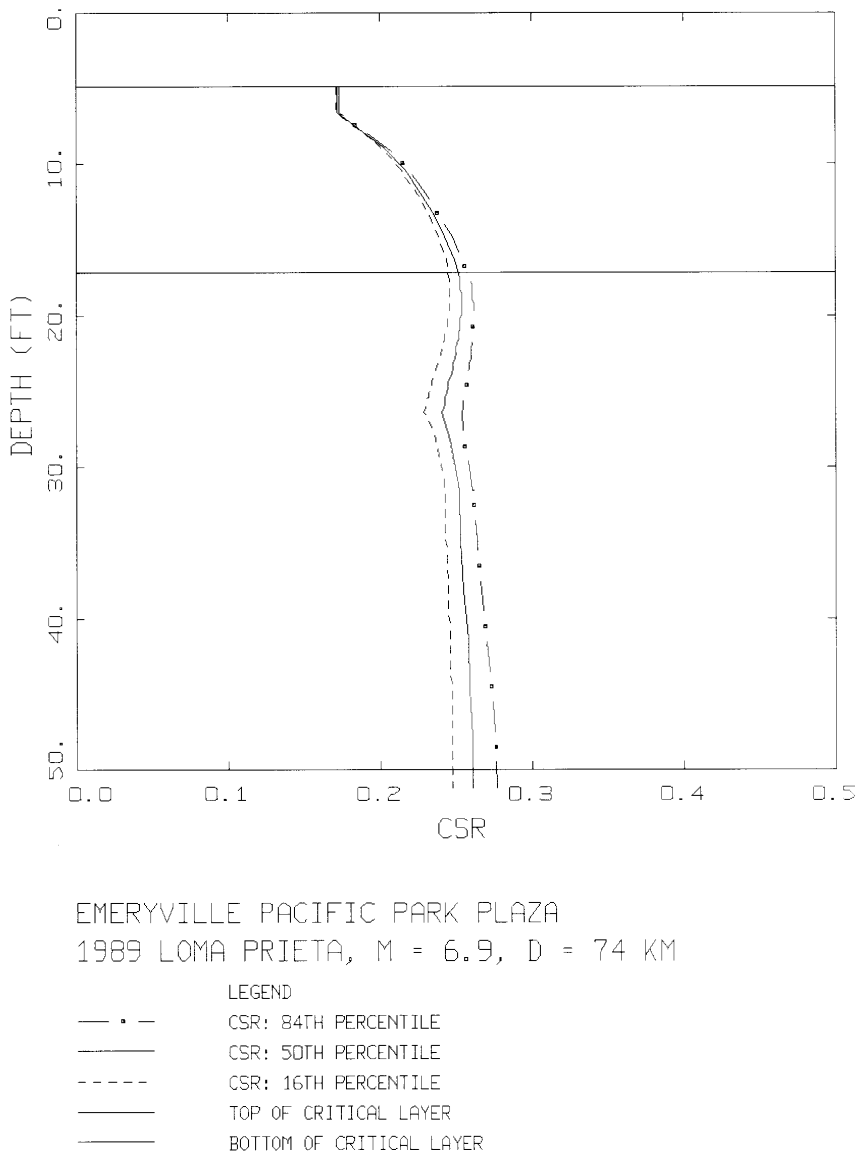


Figure 5g. Variation of CSR verses depth computed for a suite of random profiles at Emeryville Pacific Park Plaza site. Average horizontal spectrum (Figure 5a) based on recorded motions used as control motions. Critical layer indicated with horizontal lines.

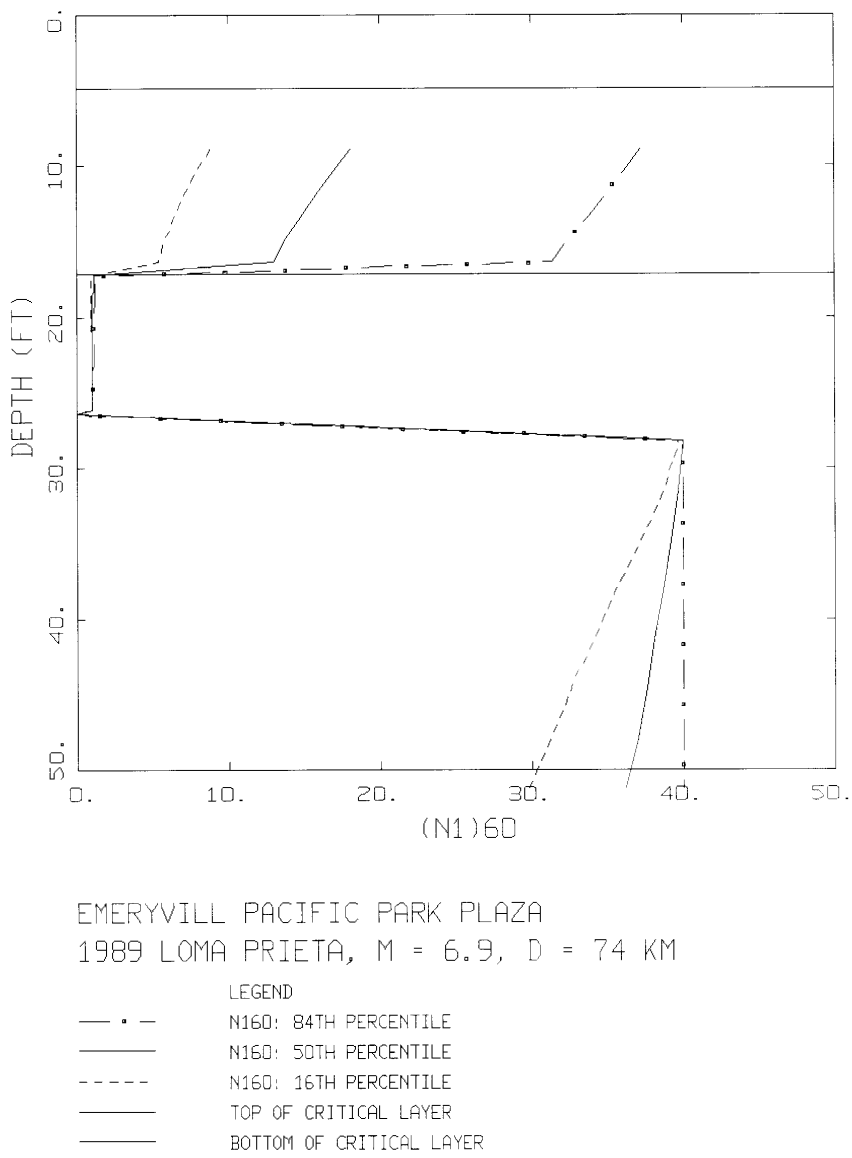


Figure 5h. Variation of peak $(N_1)_{60}$ verses depth computed for a suite of random profiles at the Emeryville Pacific Park Plaza site using the shear-wave velocity correlation model of Iwasaki et al., (1987). Average horizontal spectrum (Figure 5a) based on recorded motions used as control motions. Critical layer indicated with horizontal lines.

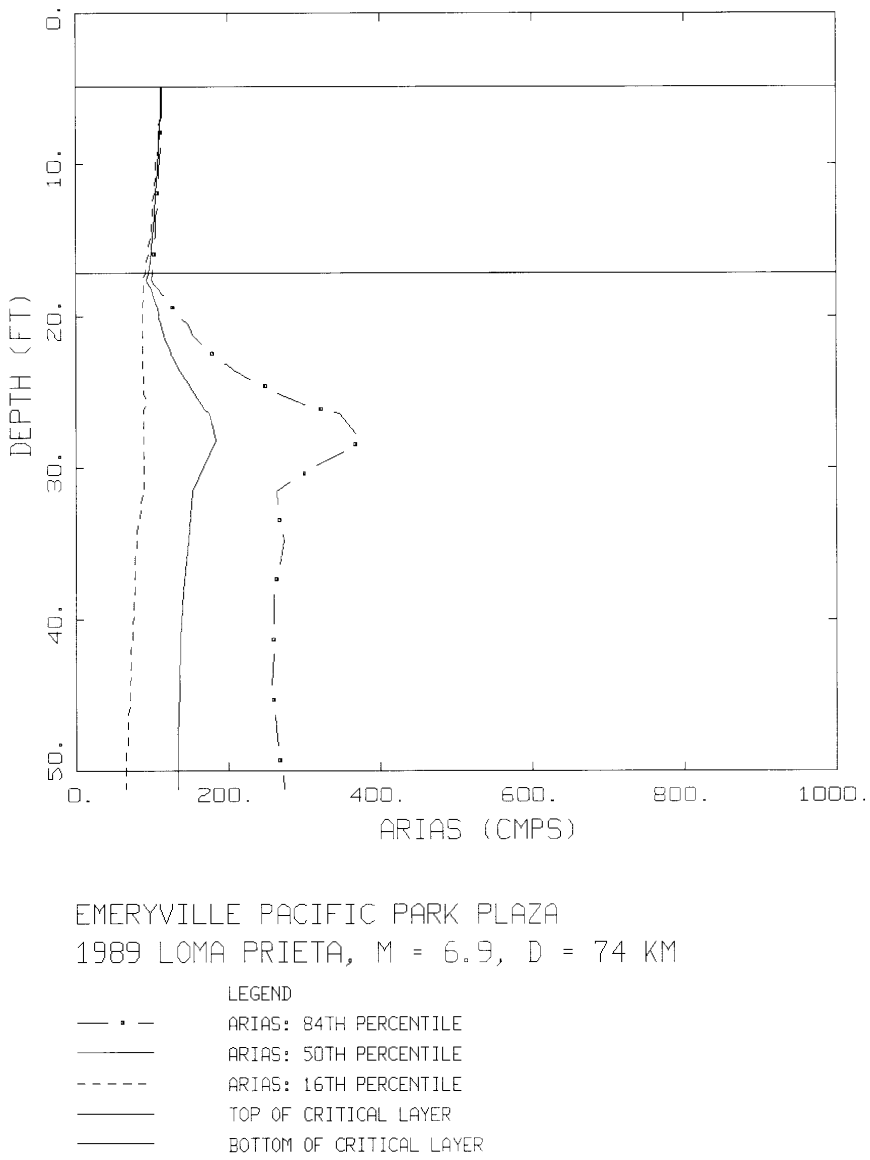


Figure 5i. Variation of Arias Intensity (cm/sec) verses depth computed for a suite of random profiles at the Emeryville Pacific Park Plaza site. Average horizontal spectrum (Figure 5a) based on recorded motions used as control motions. Critical layer indicated with horizontal lines.

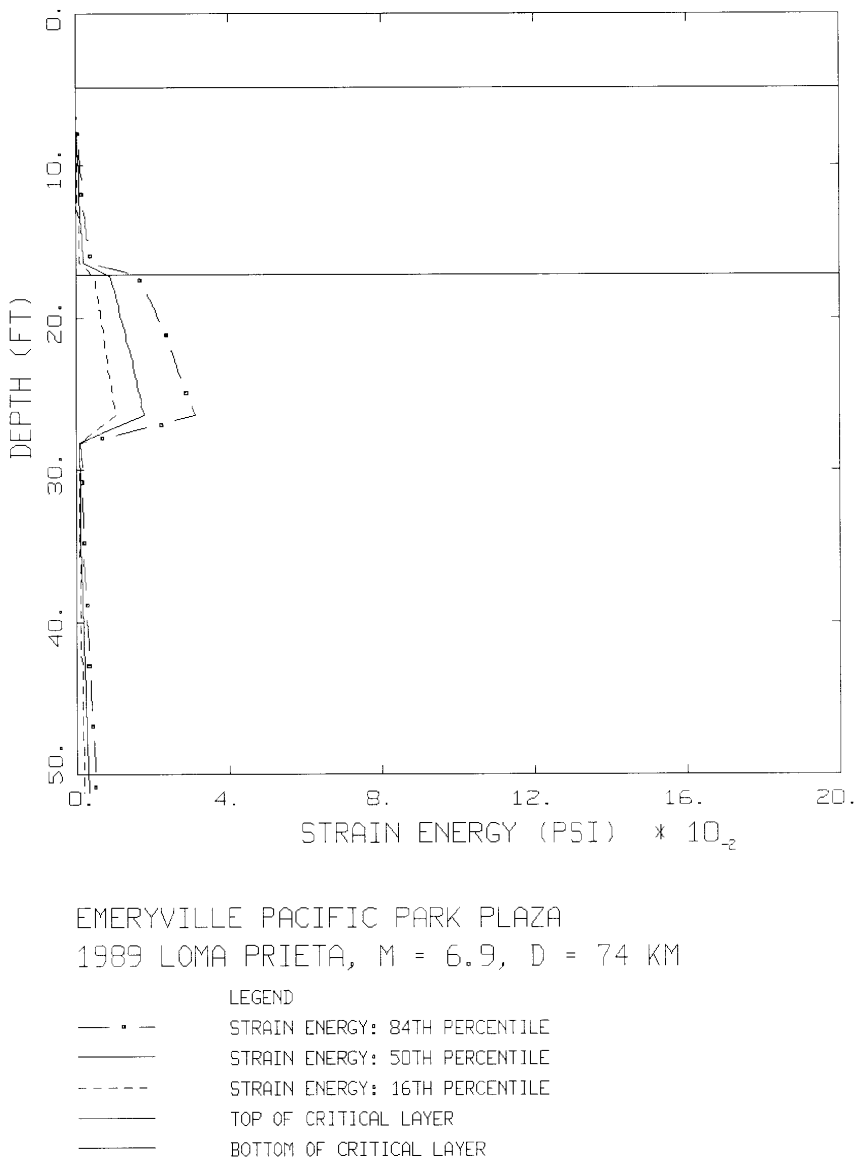


Figure 5j Variation of strain energy (PSI) verses depth computed for a suite of random profiles at the Emeryville Pacific Park Plaza site. Average horizontal spectrum (Figure 5a) based on recorded motions used as control motions. Critical layer indicated with horizontal lines.

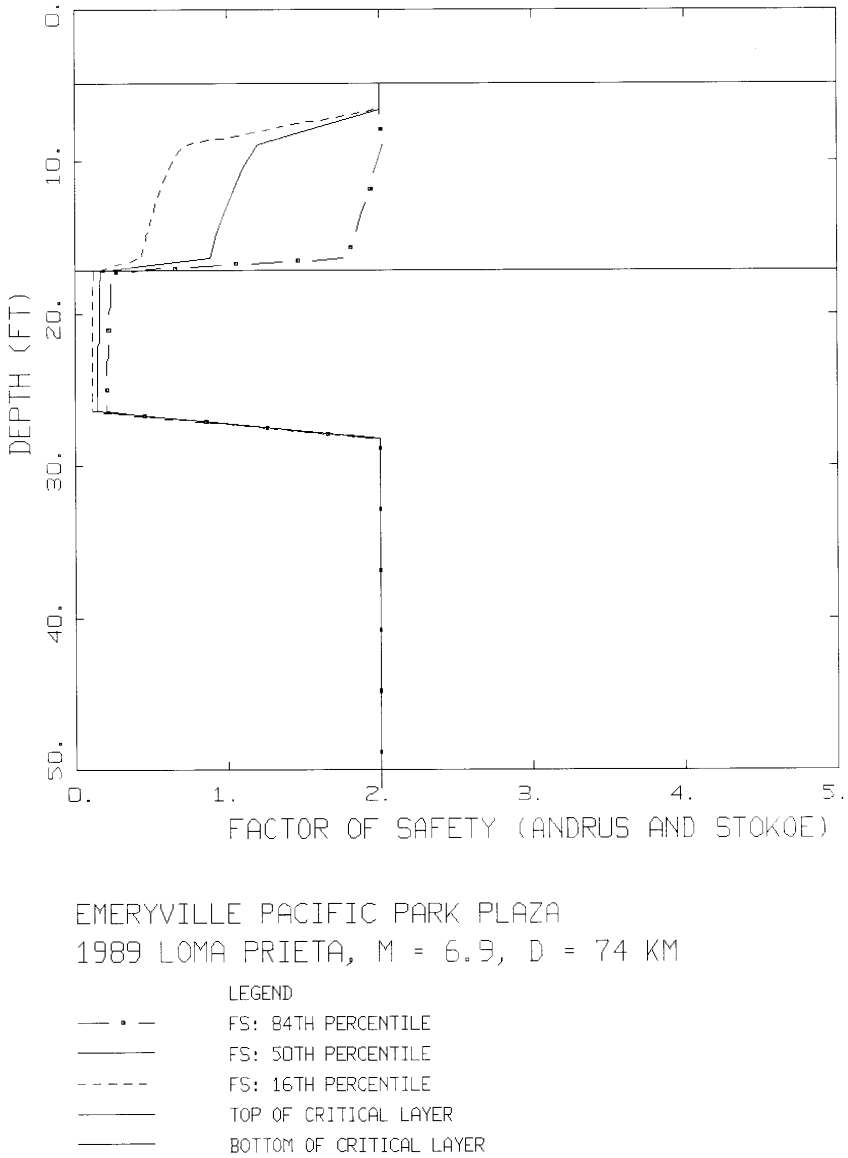


Figure 5k. Variation of the factor of safety (FS) using the Andrus and Stokoe (2004) shear-wave velocity based approach verses depth computed for a suite of random profiles at the Emeryville Pacific Park Plaza site. Average horizontal spectrum (Figure 5a) based on recorded motions used as control motions. Critical layer indicated with horizontal lines.

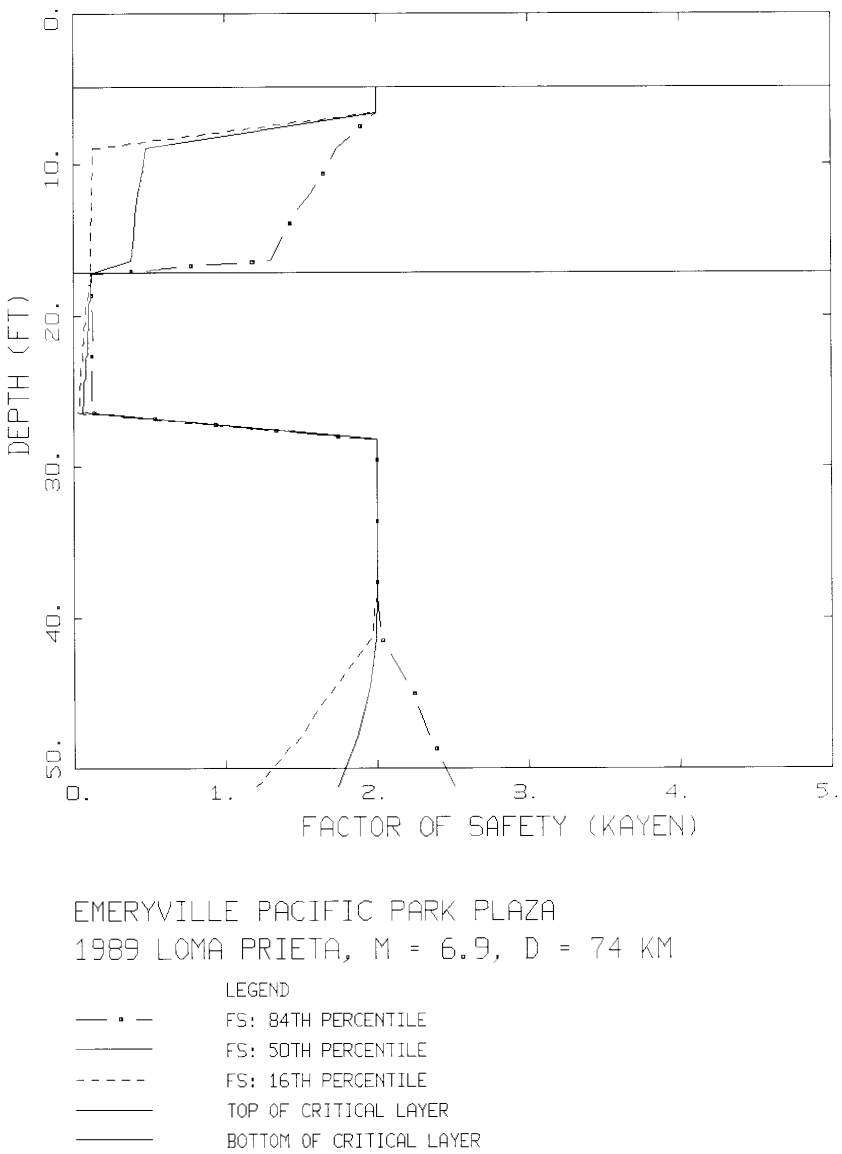


Figure 5l. Variation of the factor of safety using the Kayen and Mitchell (1997) Arias Intensity based approach verses depth computed for a suite of random profiles at the Emeryville Pacific Park Plaza site. Average horizontal spectrum (Figure 5a) based on recorded motions used as control motions. Critical layer indicated with horizontal lines.

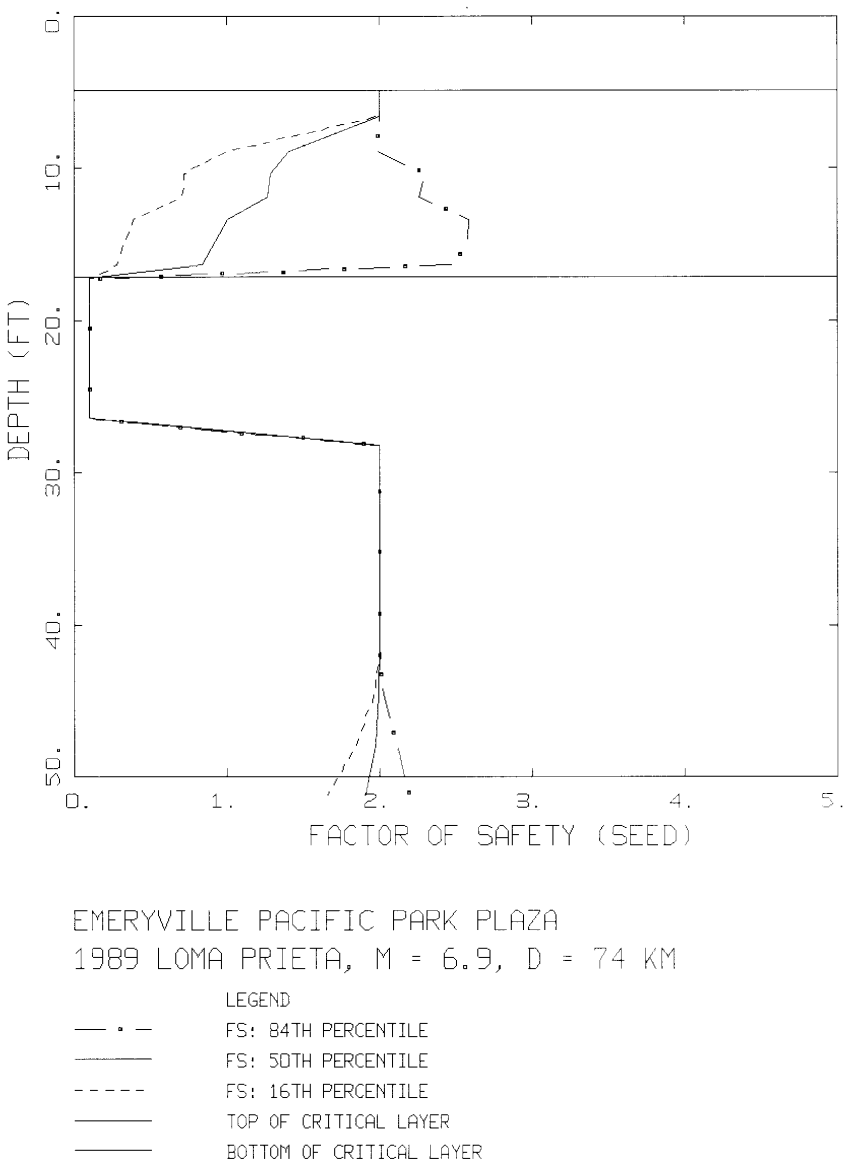


Figure 5m. Variation of the factor of the factor of safety using the Seed et al., (2002) SPT based approach verses depth computed for a suite of random profiles at the Emeryville Pacific Park Plaza site. Average horizontal spectrum (Figure 5a) based on recorded motions used as control motions. Critical layer indicated with horizontal lines.

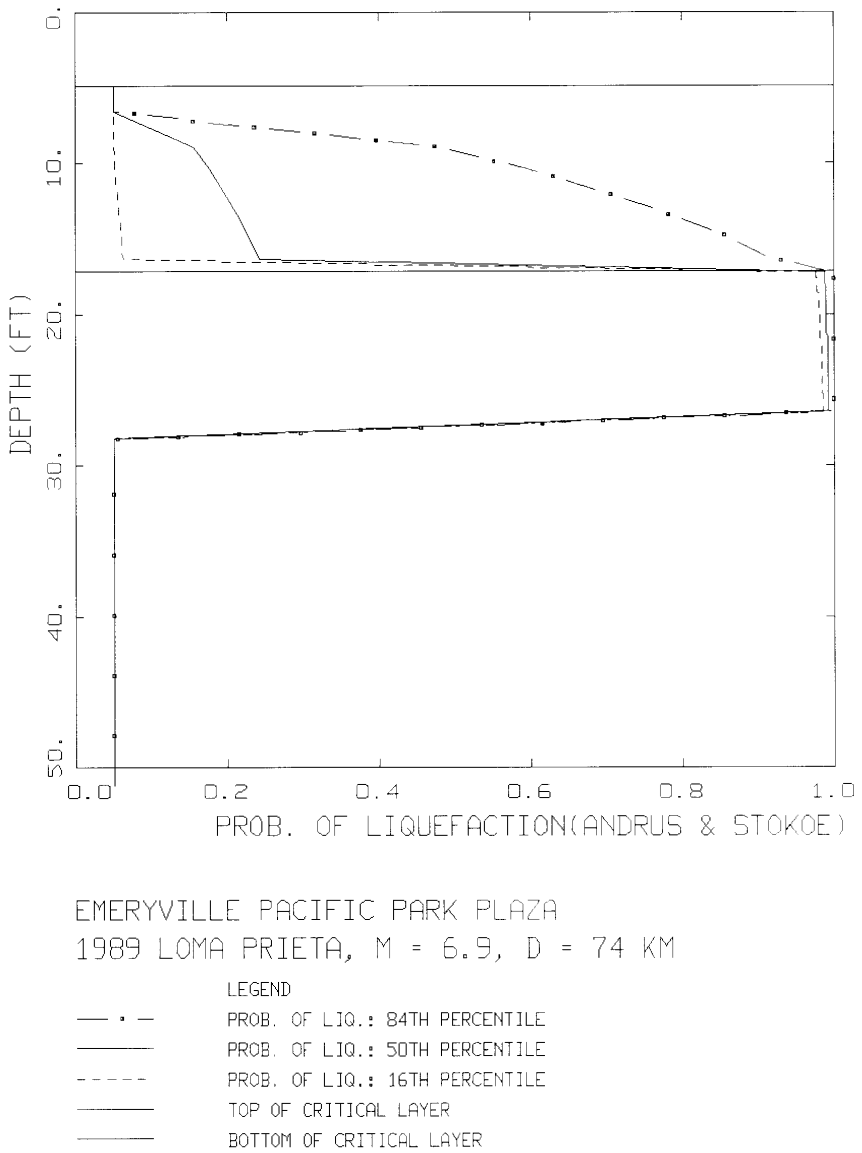


Figure 5n. Variation of the probability of liquefaction using the Andrus and Stokoe (2004) shear-wave velocity based approach verses depth computed for a suite of random profiles at the Emeryville Pacific Park Plaza site. Average horizontal spectrum (Figure 5a) based on recorded motions used as control motions. Critical layer indicated with horizontal lines.

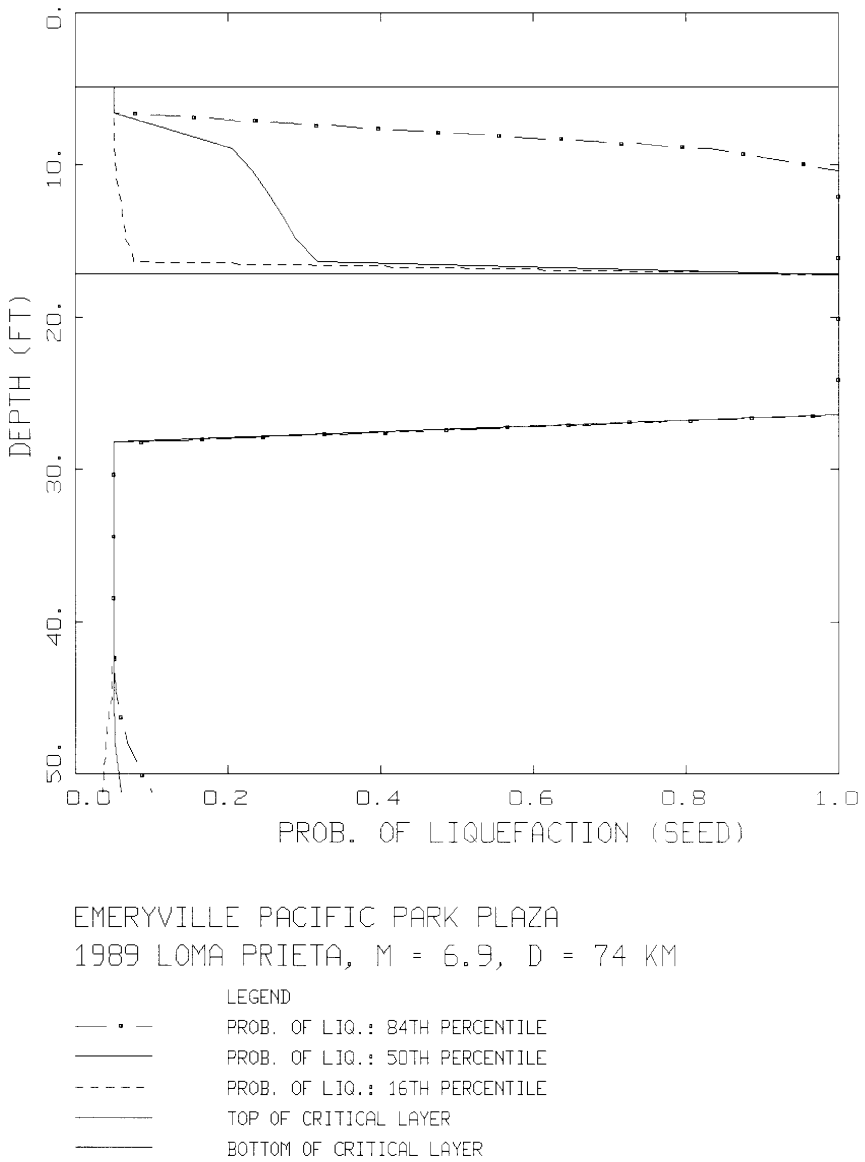


Figure 5o. Variation probability of liquefaction using the Seed et al. (2002) SPT based approach verses depth computed for a suite of random profiles at the Emeryville Pacific Park Plaza site. Average horizontal spectrum (Figure 5a) based on recorded motions used as control motions. Critical layer indicated with horizontal lines.

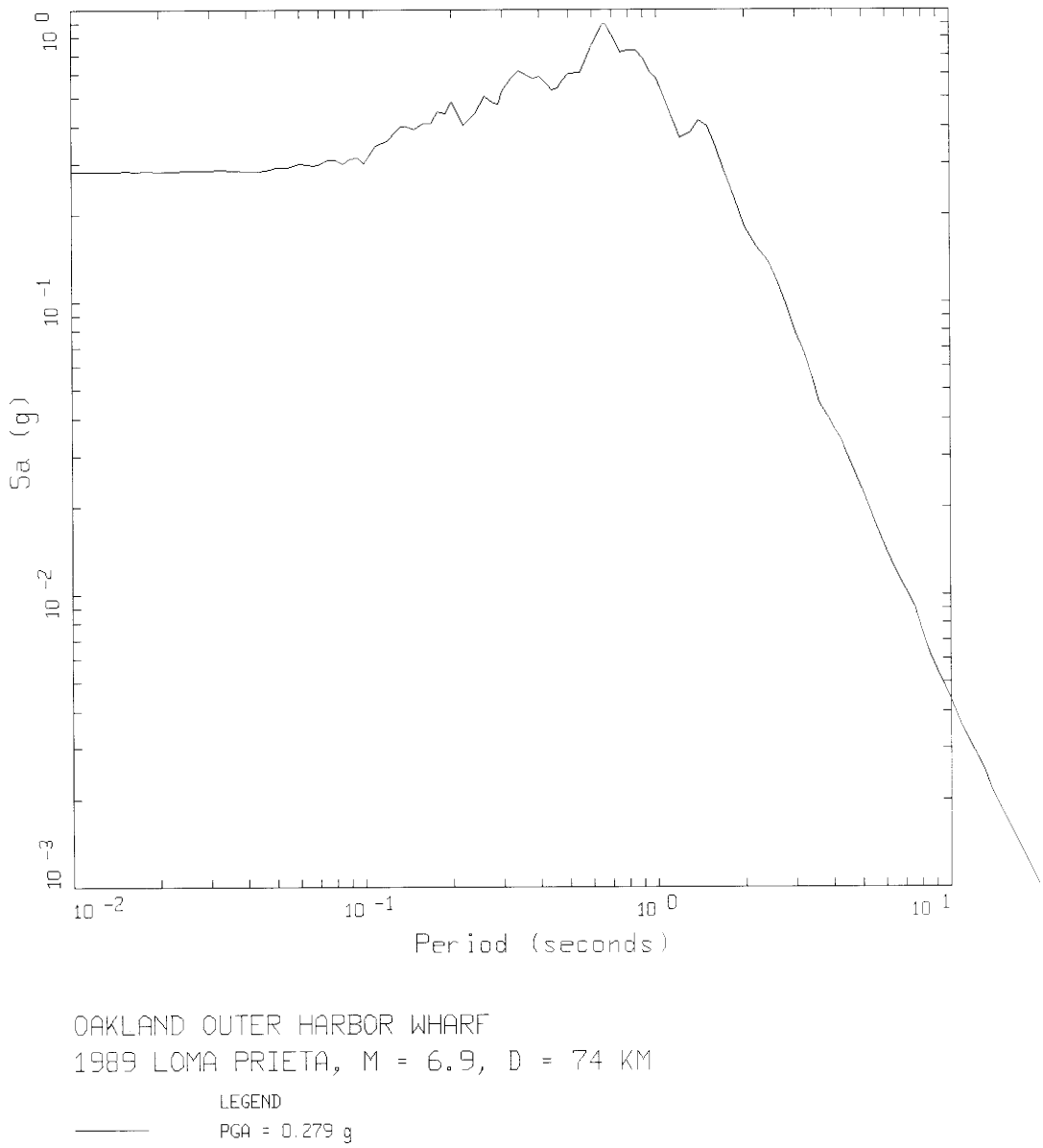


Figure 6a. Average horizontal component response spectra computed from recorded motions: Oakland Outer Harbor Wharf site, Loma Prieta earthquake.

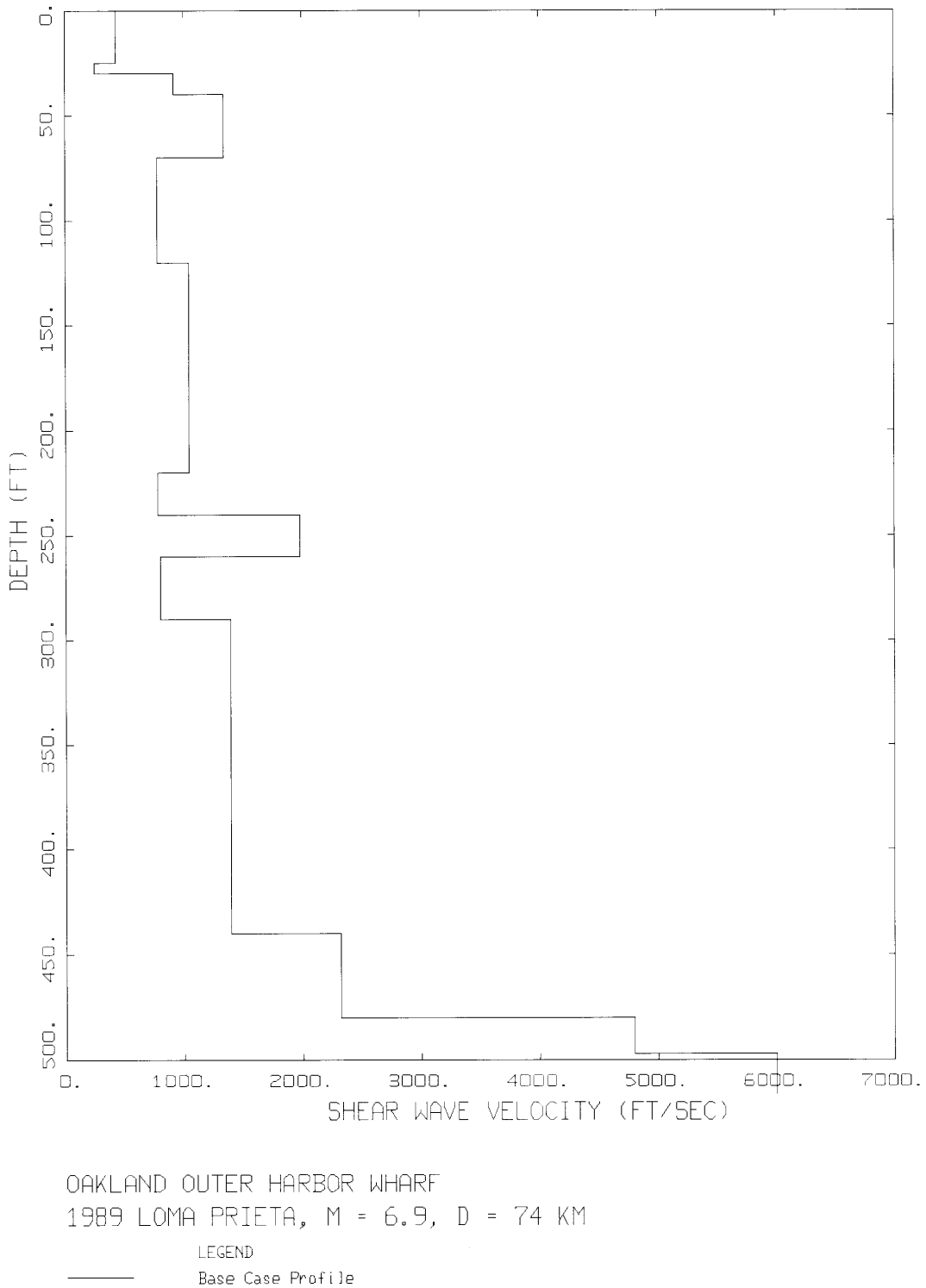


Figure 6b. Shear-wave velocity profile (measured) at the Oakland Outer Harbor Wharf site site to a depth of 500 ft.

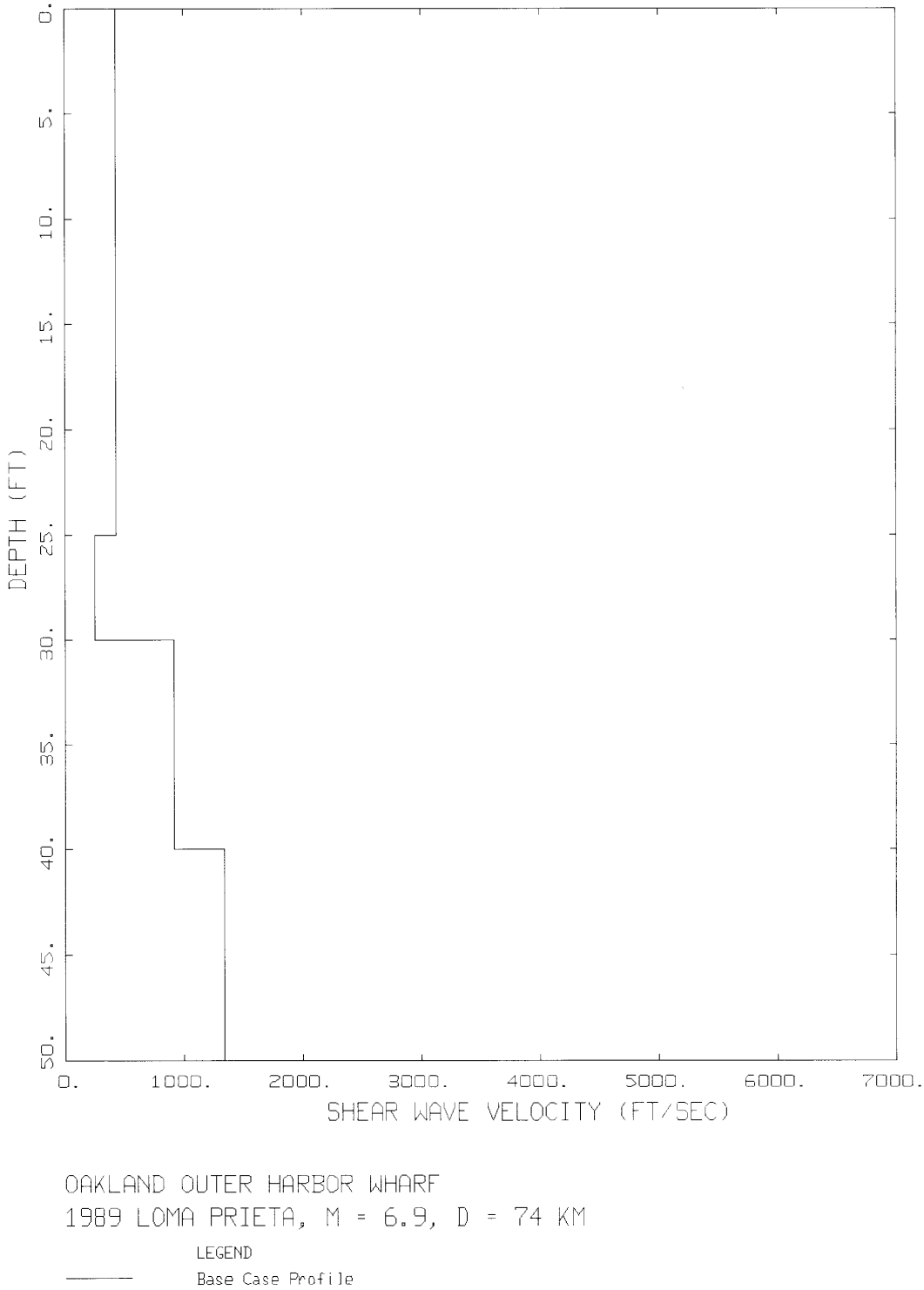


Figure 6c. Shear-wave velocity profile (measured) at the Oakland Outer Harbor Wharf site to a depth of 50 ft.

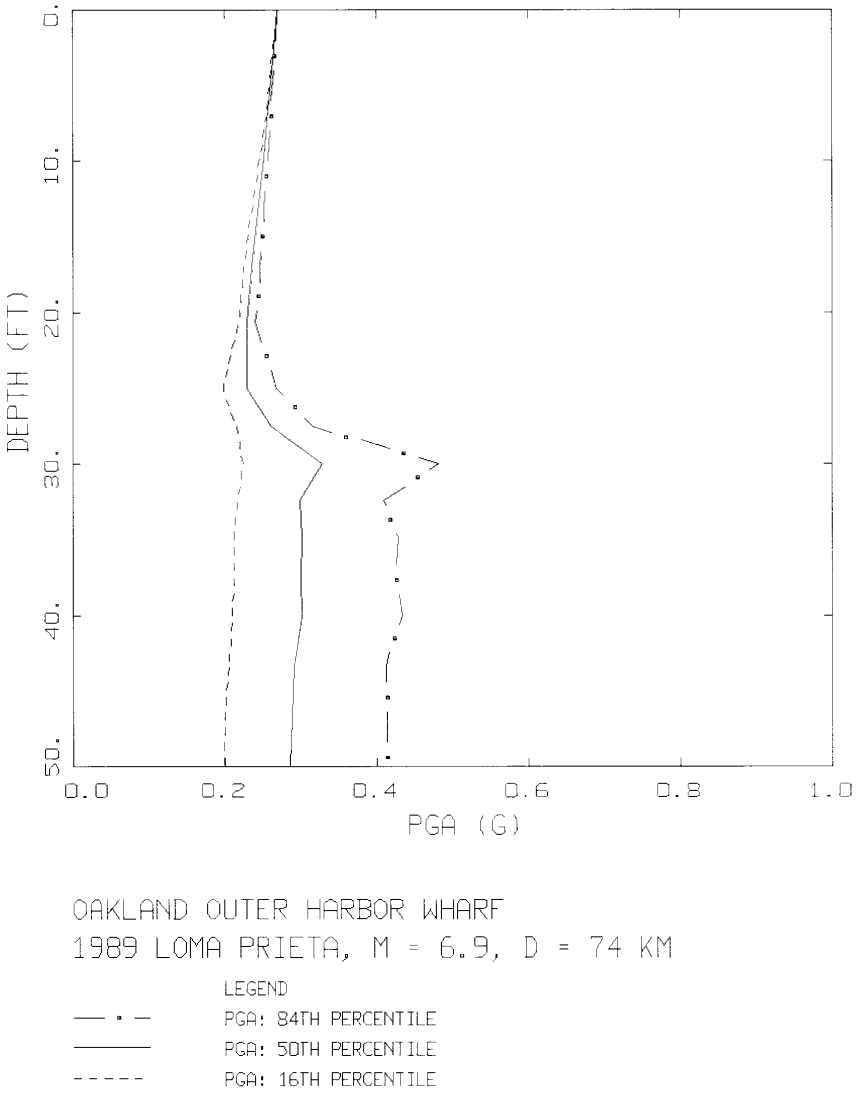


Figure 6d. Variation of peak acceleration(g) (Average horizontal component) verses depth computed for a suite of random profiles at the Oakland Outer Harbor Wharf site. Average horizontal spectrum (Figure 6a) based on recorded motions used as control motions.

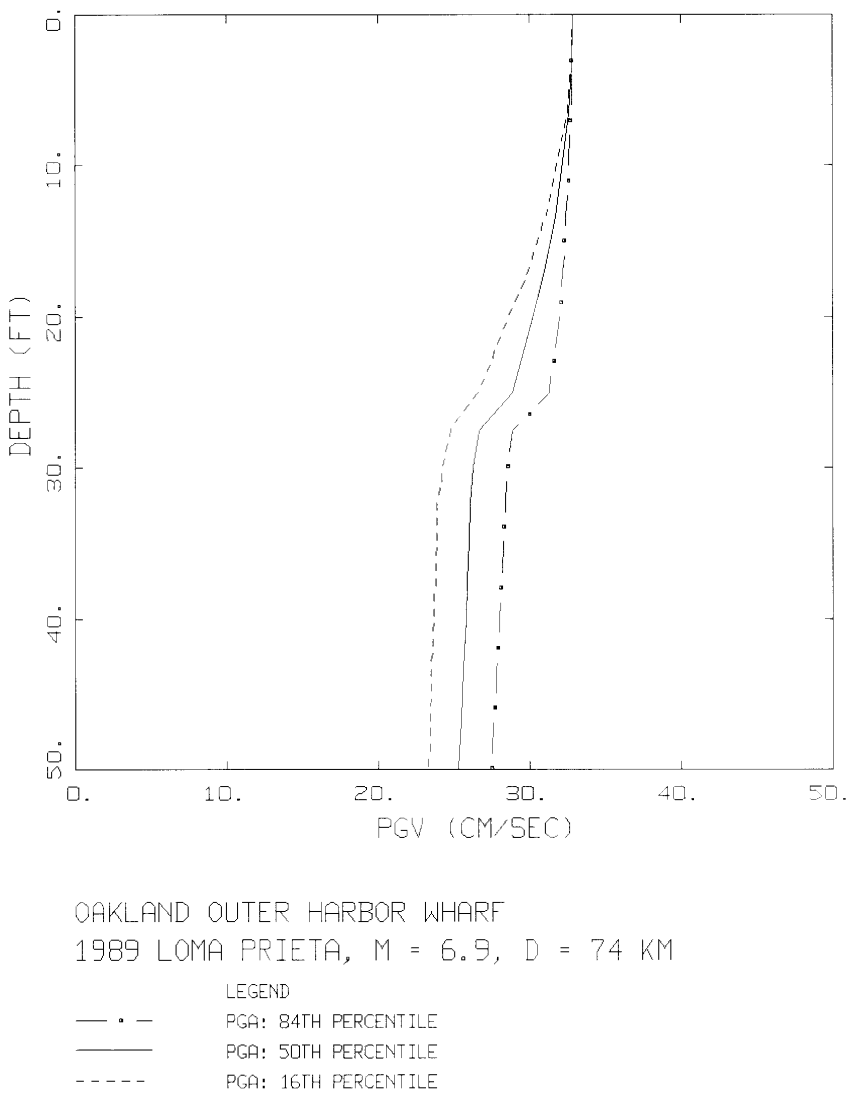


Figure 6e. Variation of peak particle velocity (cm/sec) verses depth computed for a suite of random profiles at the Oakland Outer Harbor Wharf site. Average horizontal spectrum (Figure 6a) based on recorded motions used as control motions.

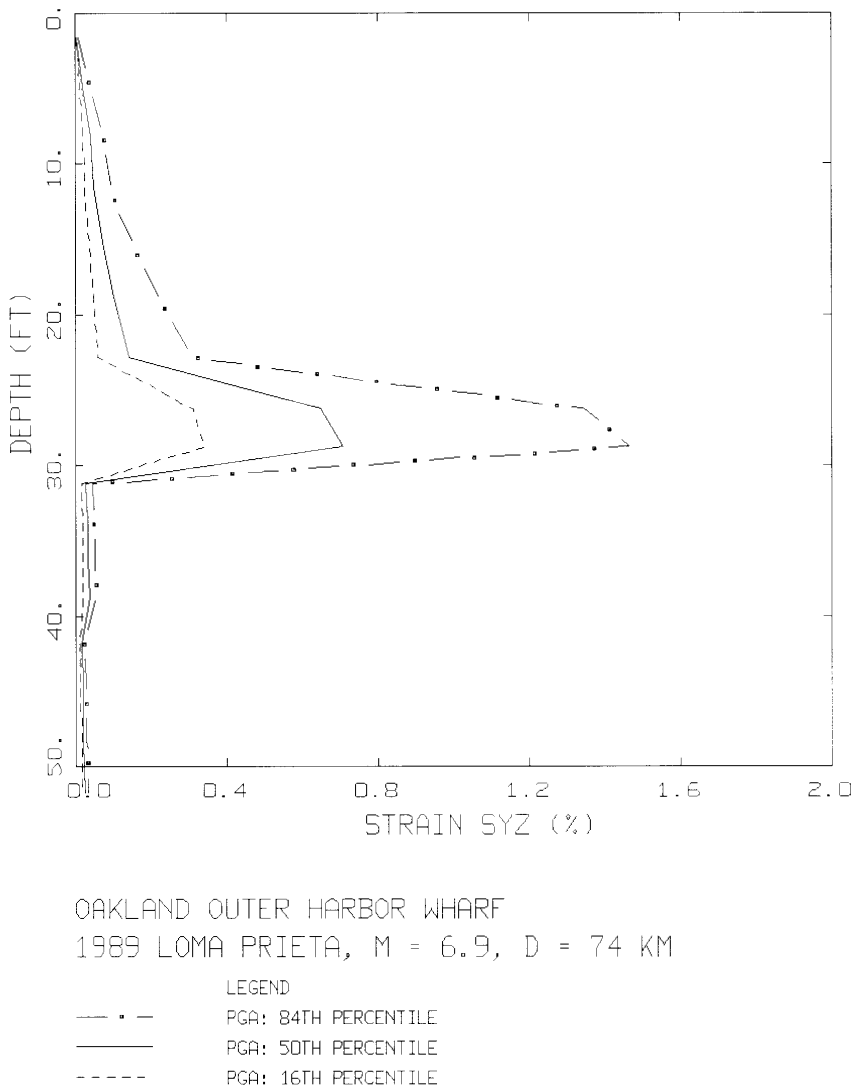


Figure 6f. Variation of peak shear strain(%) verses depth computed for a suite of random profiles at the Oakland Outer Harbor Wharf site. Average horizontal spectrum (Figure 6a) based on recorded motions used as control motions.

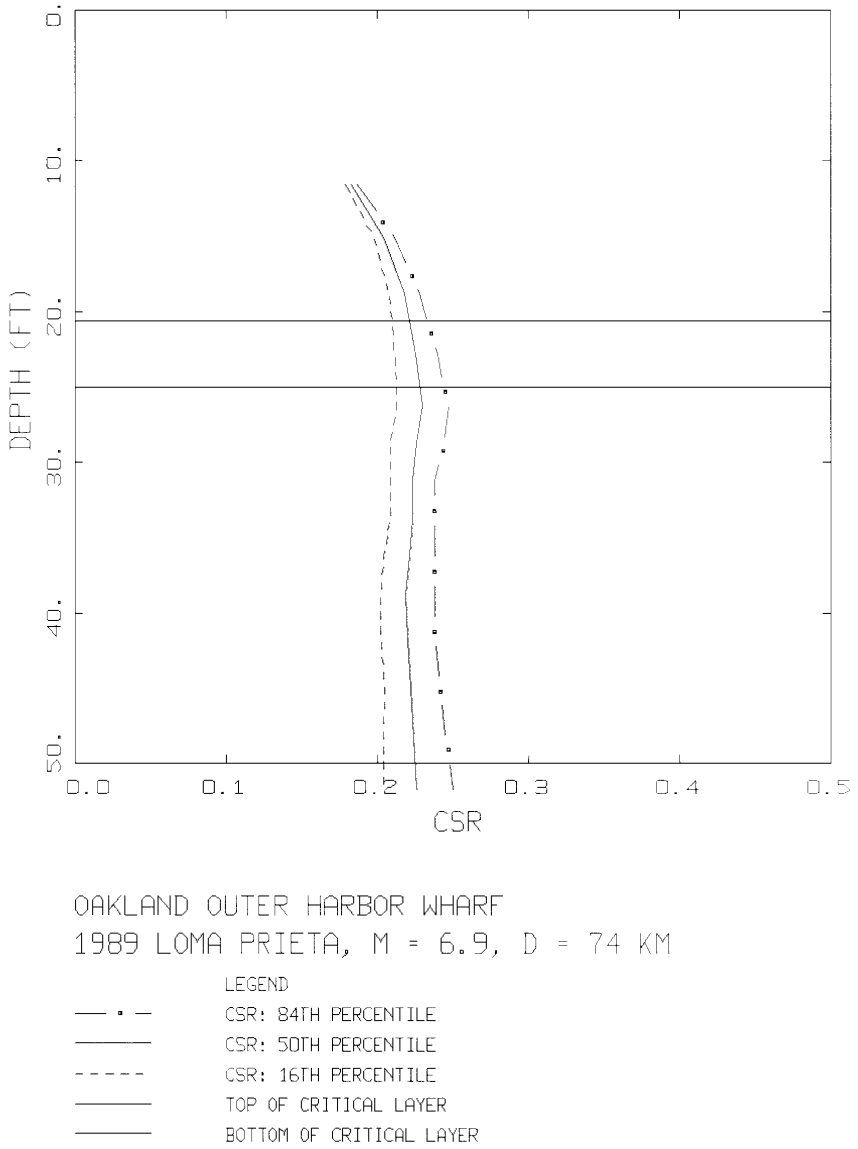


Figure 6g. Variation of CSR verses depth computed for a suite of random profiles for at Oakland Outer Harbor Wharf site. Average horizontal spectrum (Figure 6a) based on recorded motions used as control motions. Critical layer indicated with horizontal lines.

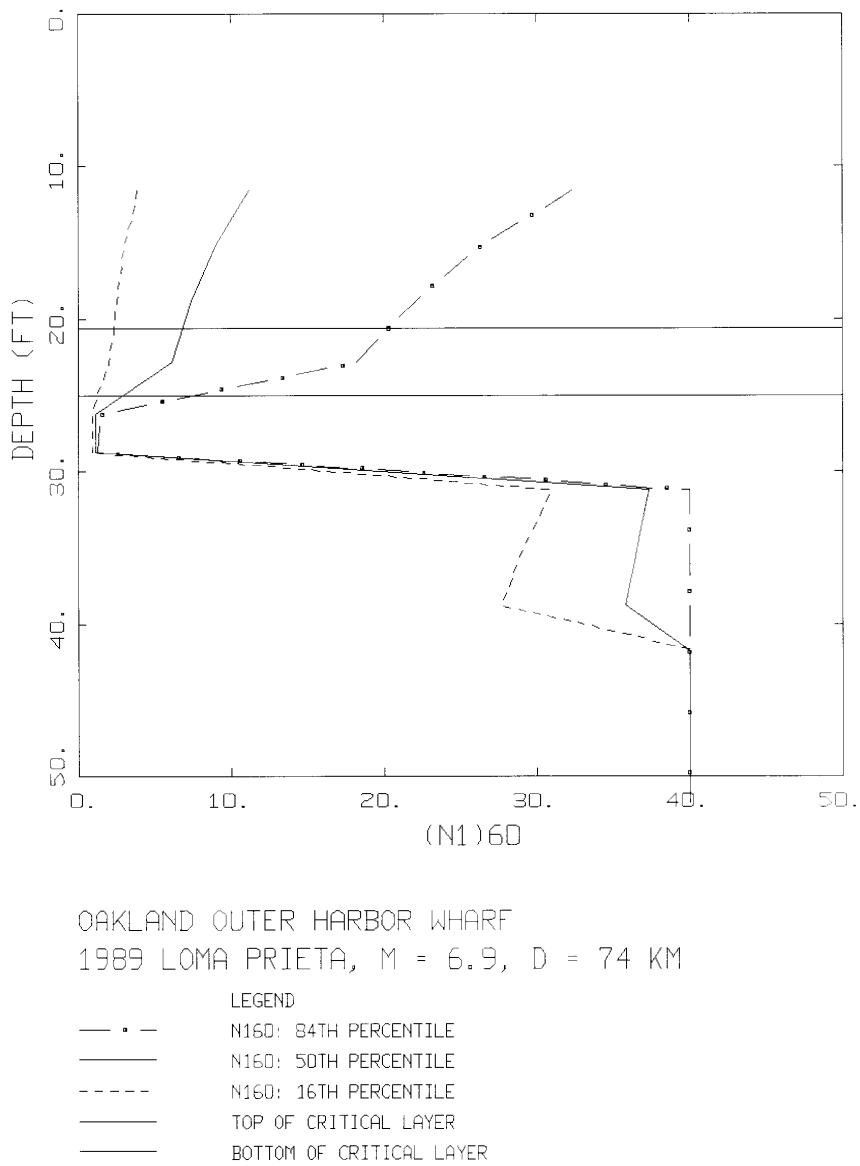


Figure 6h. Variation of peak $(N_1)_{60}$ verses depth computed for a suite of random profiles at the Oakland Outer Harbor Wharf site using the shear-wave velocity correlation model of Iwasaki et al., (1987). Average horizontal spectrum (Figure 6a) based on recorded motions used as control motions. Critical layer indicated with horizontal lines.

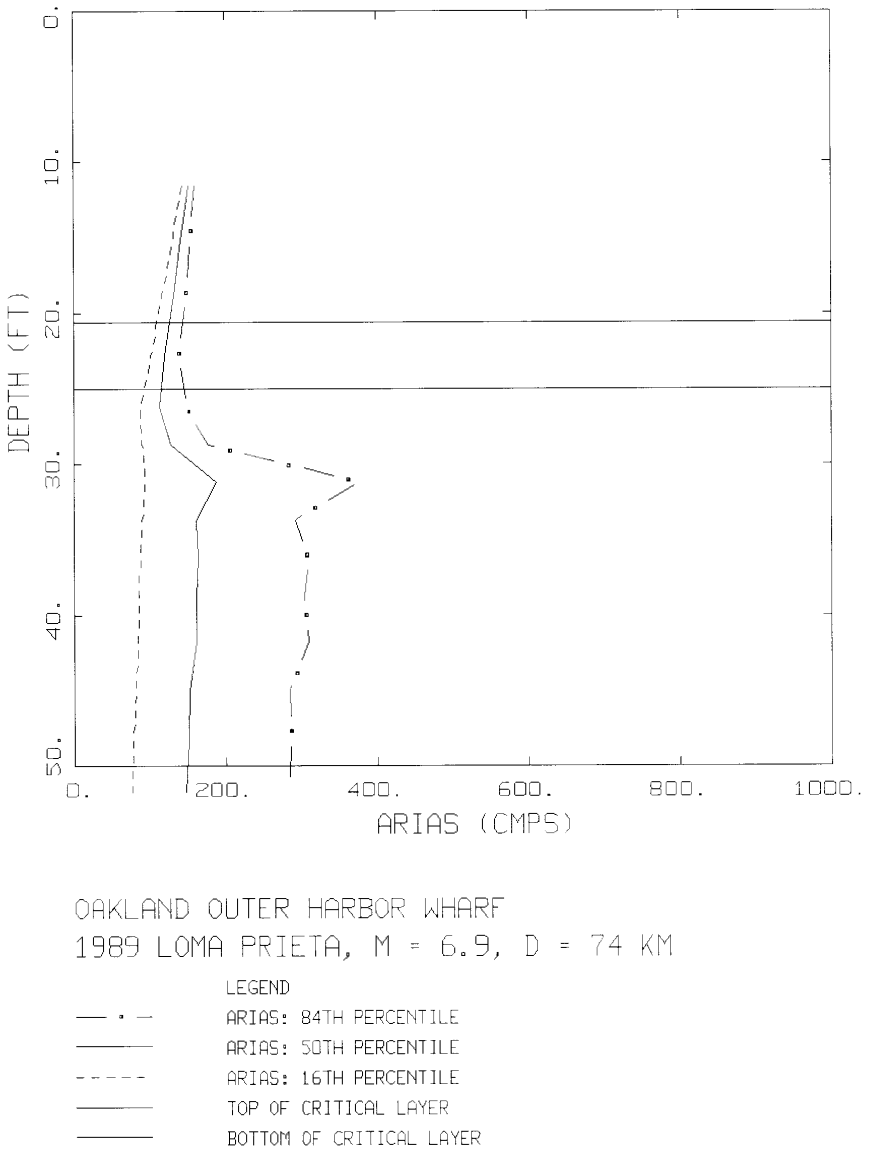


Figure 6i. Variation of Arias Intensity (cm/sec) verses depth computed for a suite of random profiles at the Oakland Outer Harbor Wharf site. Average horizontal spectrum (Figure 6a) based on recorded motions used as control motions. Critical layer indicated with horizontal lines.

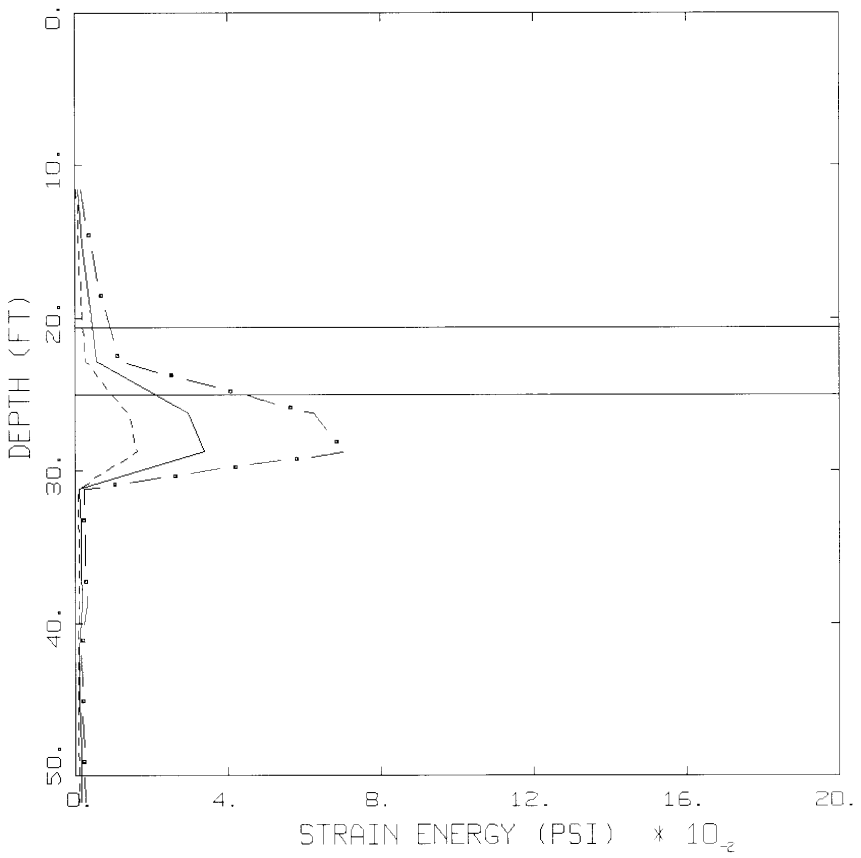


OAKLAND OUTER HARBOR WHARF
1989 LOMA PRIETA, M = 6.9, D = 74 KM

LEGEND

| | |
|---|---|
| —— · — | STRAIN ENERGY: 84TH PERCENTILE |
| ——— | STRAIN ENERGY: 50TH PERCENTILE |
| - - - - - | STRAIN ENERGY: 16TH PERCENTILE |
| ——— | TOP OF CRITICAL LAYER |
| ——— | BOTTOM OF CRITICAL LAYER |

Figure 6j Variation of strain energy (PSI) verses depth computed for a suite of random profiles at the Oakland Outer Harbor Wharf site. Average horizontal spectrum (Figure 6a) based on recorded motions used as control motions. Critical layer indicated with horizontal lines.

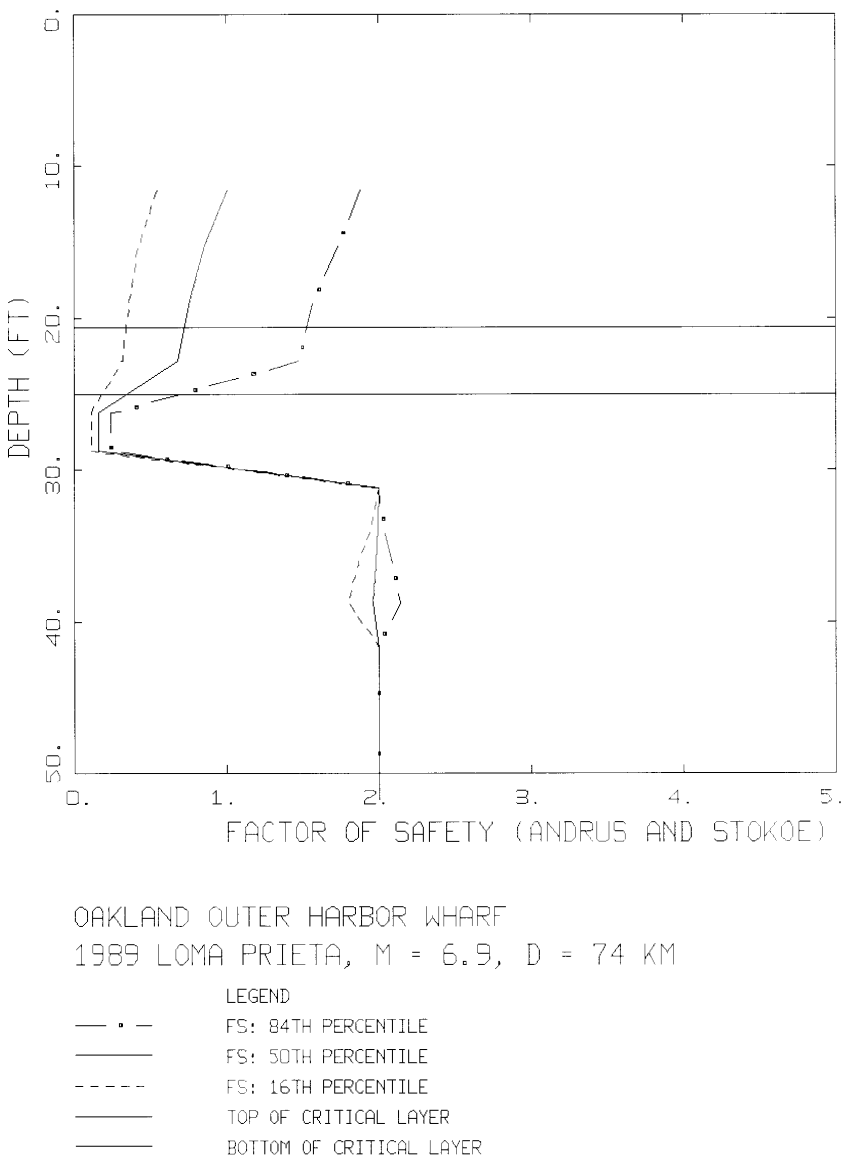


Figure 6k. Variation of the factor of safety (FS) using the Andrus and Stokoe (2004) shear-wave velocity based approach verses depth computed for a suite of random profiles at the Oakland Outer Harbor Wharf site. Average horizontal spectrum (Figure 6a) based on recorded motions used as control motions. Critical layer indicated with horizontal lines.

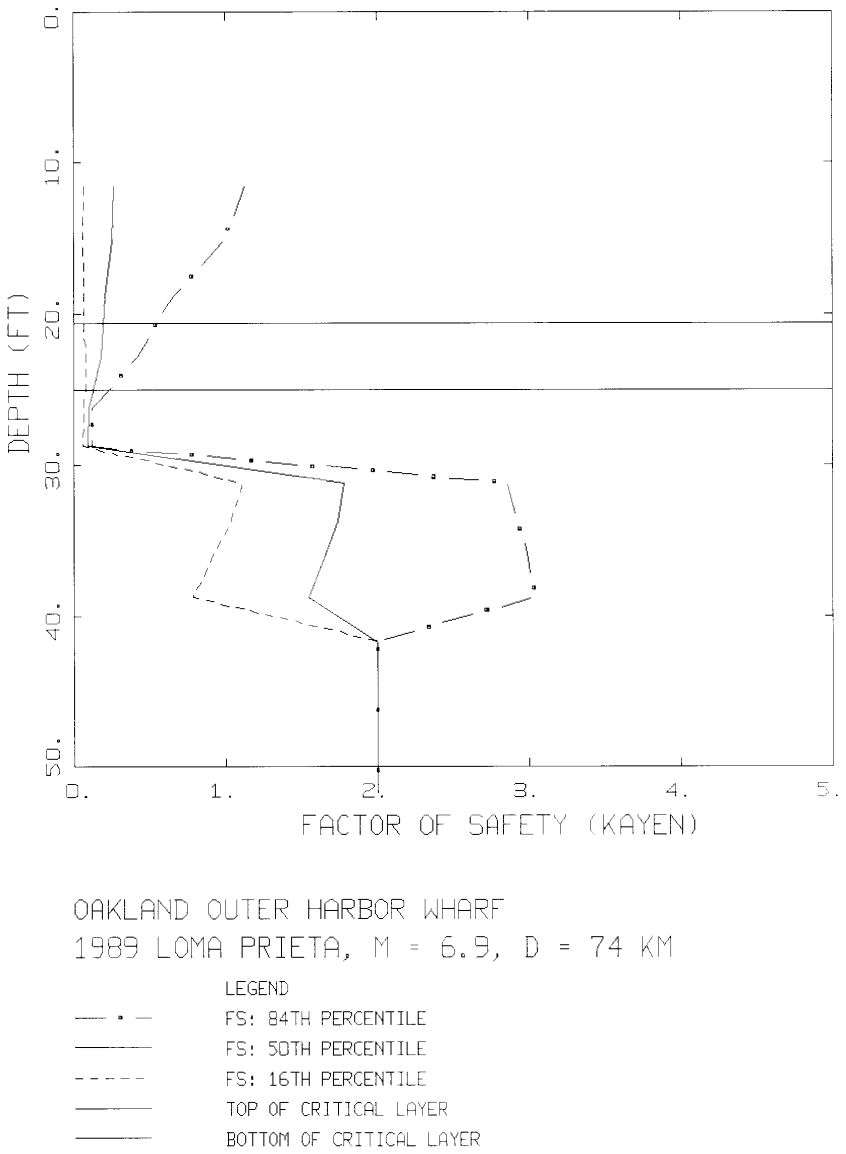


Figure 6l. Variation of the factor of safety using the Kayen and Mitchell (1997) Arias Intensity based approach verses depth computed for a suite of random profiles at the Oakland Outer Harbor Wharf site. Average horizontal spectrum (Figure 6a) based on recorded motions used as control motions. Critical layer indicated with horizontal lines.

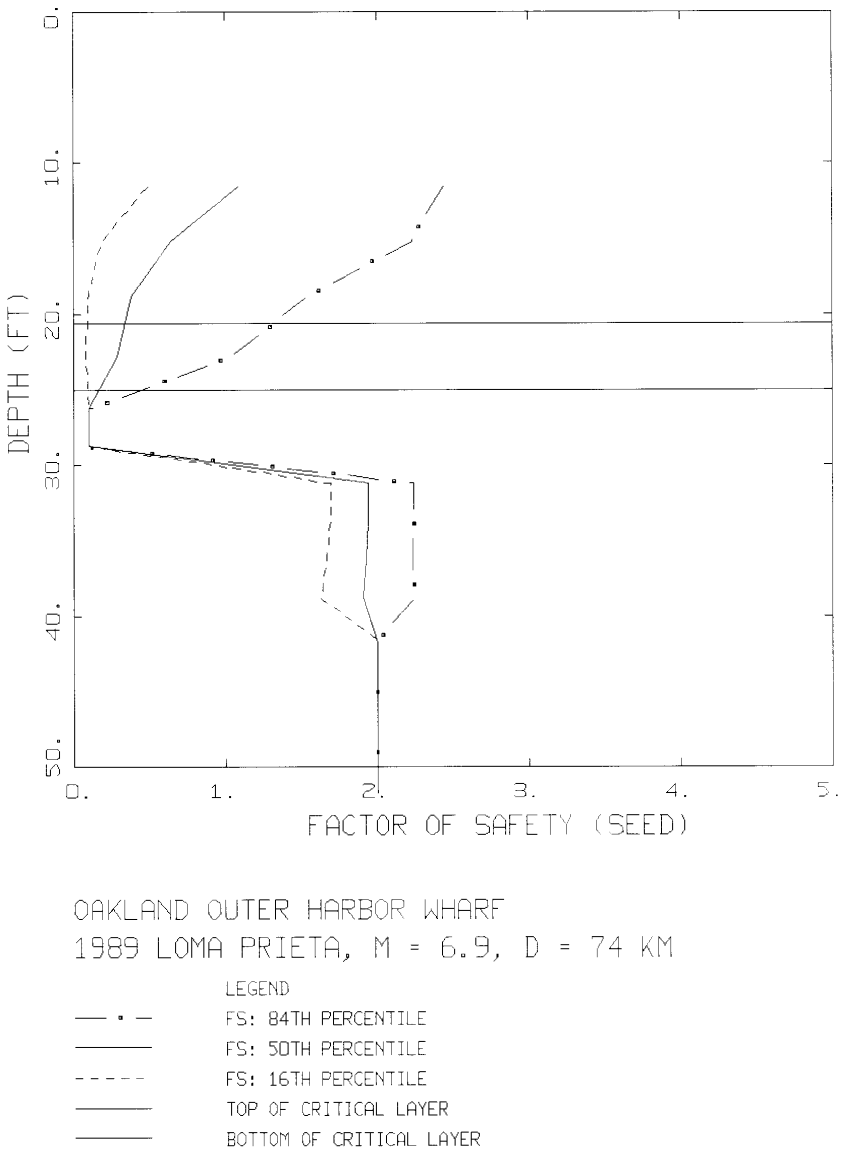


Figure 6m. Variation of the factor of the factor of safety using the Seed et al., (2002) SPT based approach verses depth computed for a suite of random profiles at the Oakland Outer Harbor Wharf site. Average horizontal spectrum (Figure 6a) based on recorded motions used as control motions. Critical layer indicated with horizontal lines.

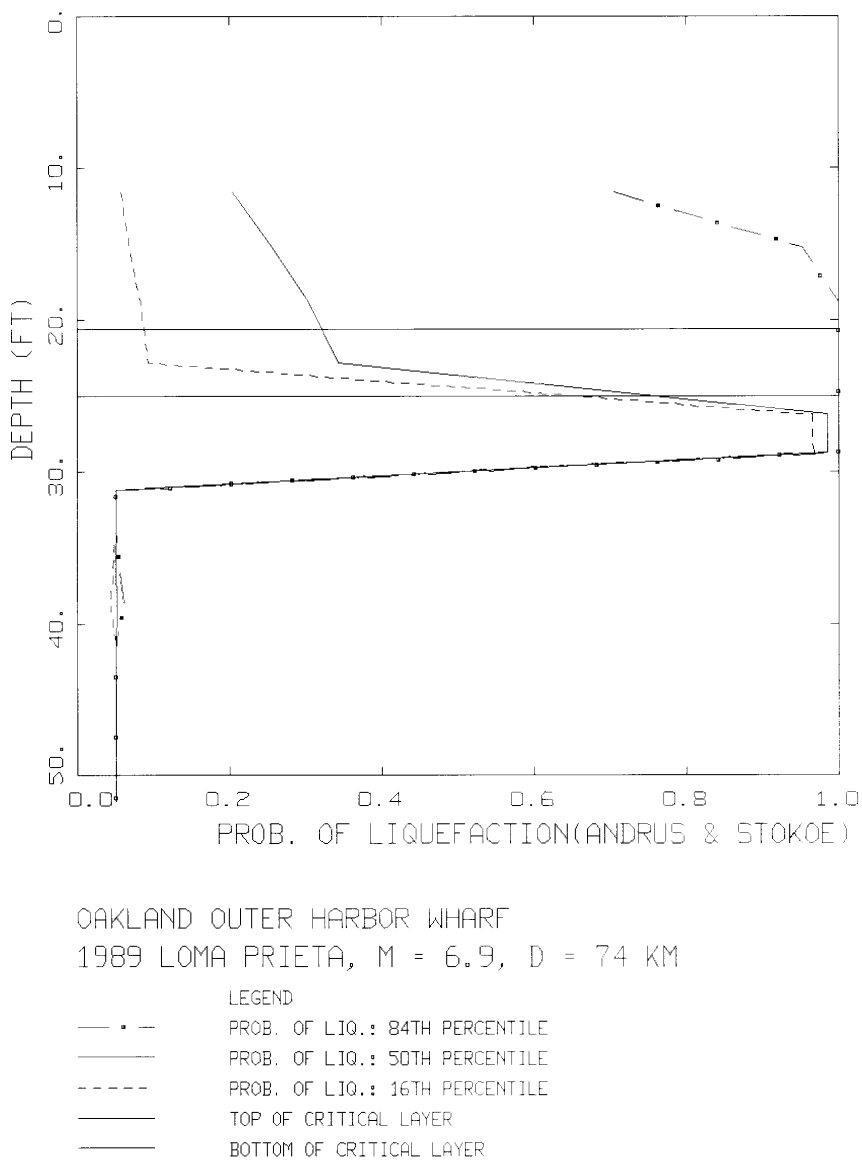


Figure 6n. Variation of the probability of liquefaction using the Andrus and Stokoe (2004) shear-wave velocity based approach verses depth computed for a suite of random profiles at the Oakland Outer Harbor Wharf site. Average horizontal spectrum (Figure 6a) based on recorded motions used as control motions. Critical layer indicated with horizontal lines.

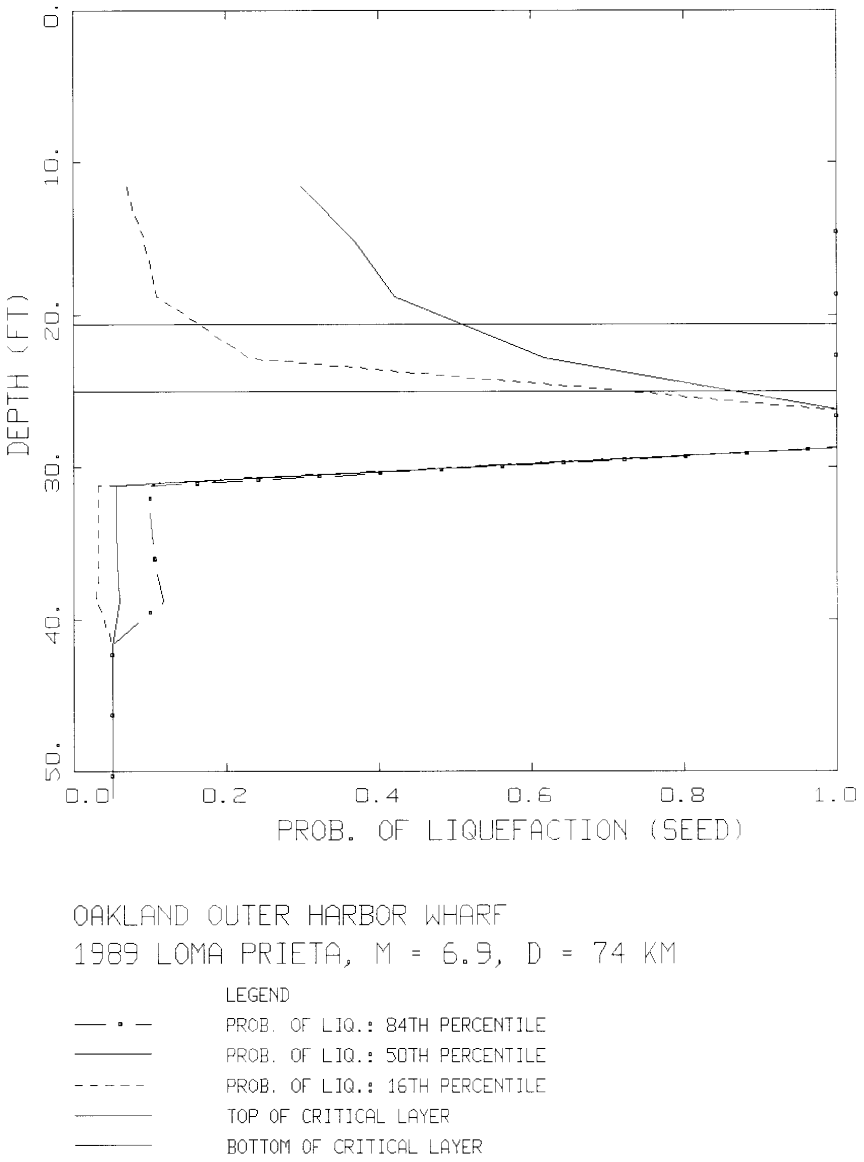


Figure 6o. Variation probability of liquefaction using the Seed et al. (2002) SPT based approach verses depth computed for a suite of random profiles at the Oakland Outer Harbor Wharf site. Average horizontal spectrum (Figure 6a) based on recorded motions used as control motions. Critical layer indicated with horizontal lines.

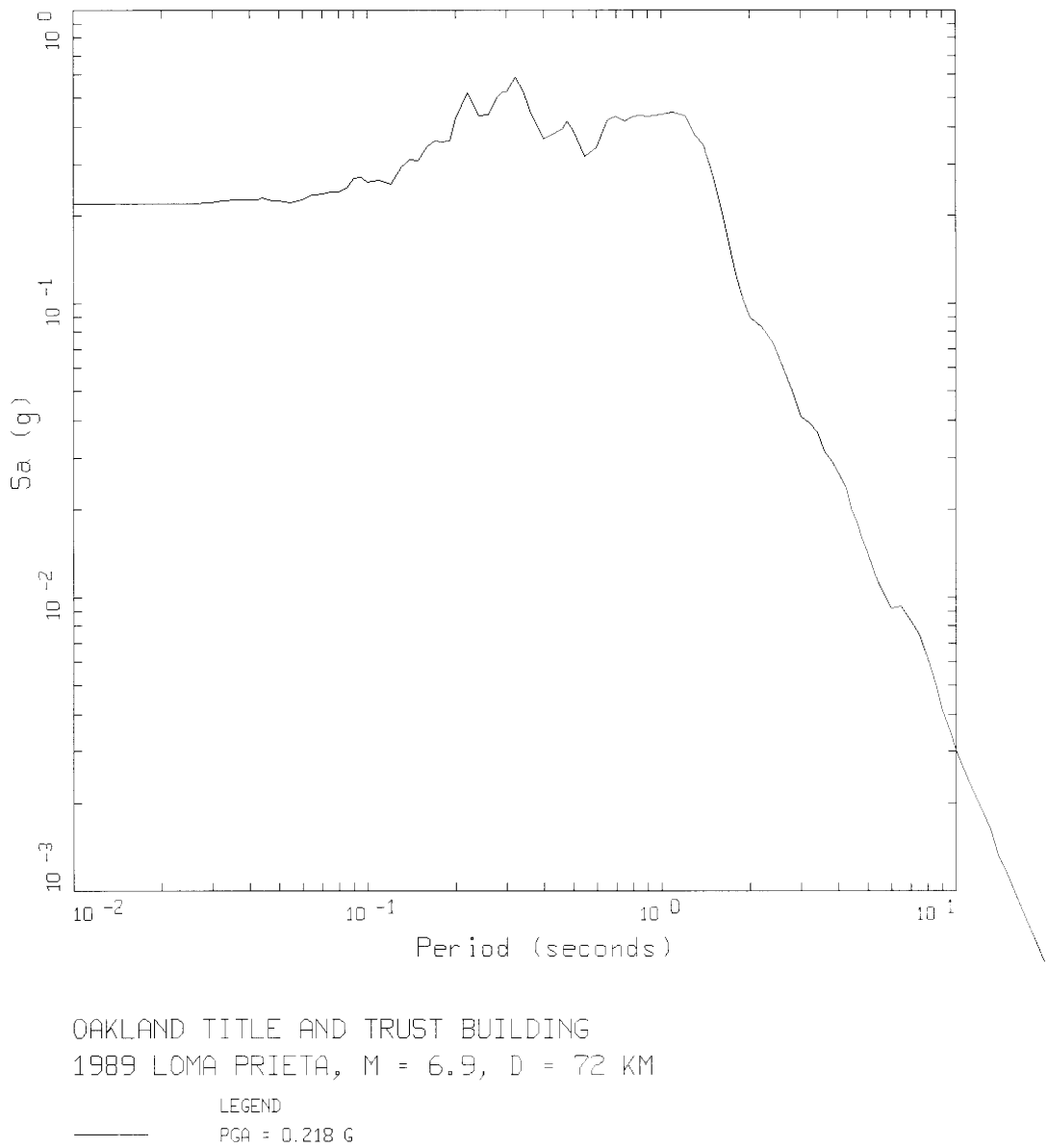


Figure 7a. Average horizontal component response spectra computed from recorded motions: Oakland Title and Trust site, Loma Prieta earthquake.

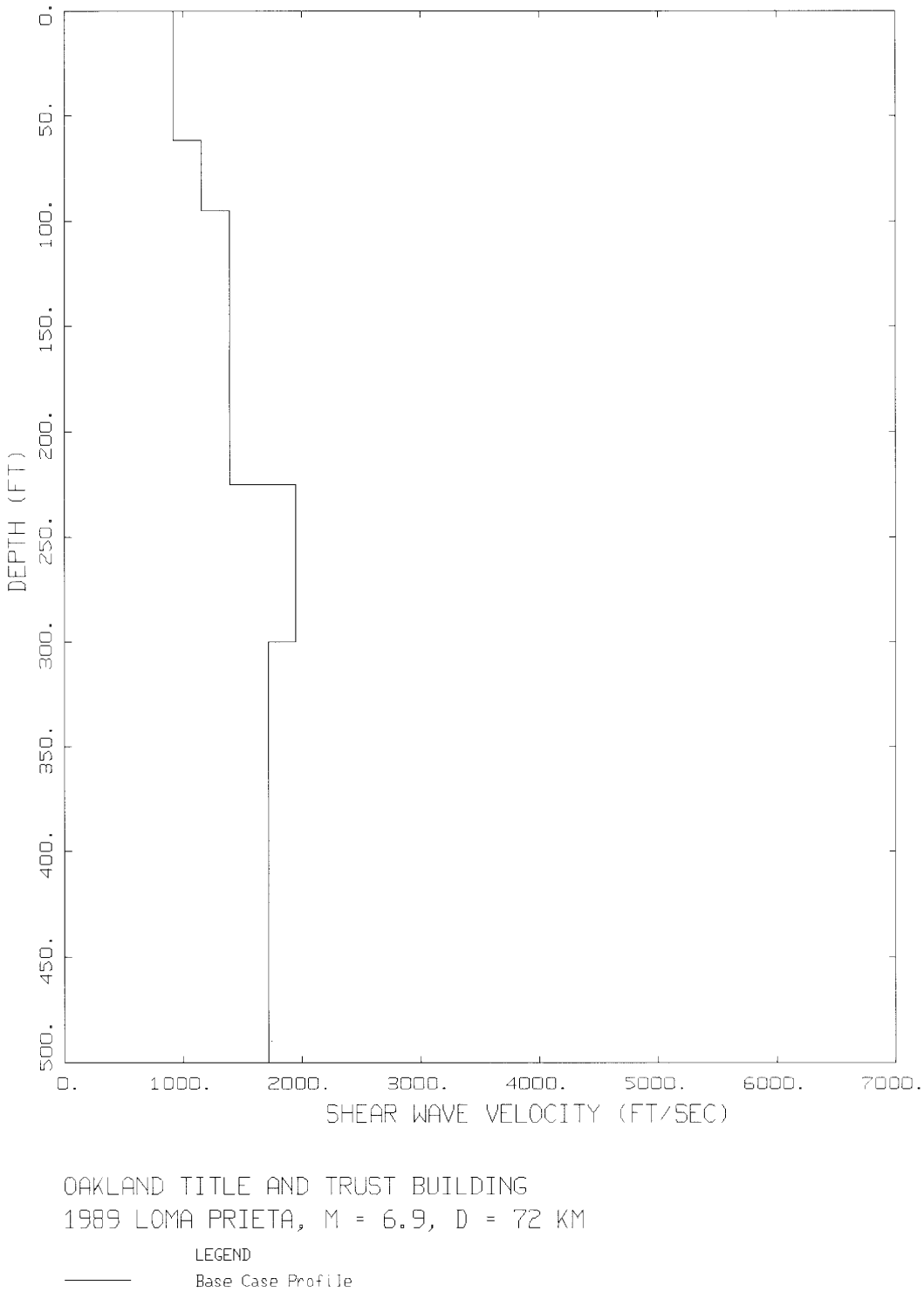


Figure 7b. Shear-wave velocity profile (measured) at the Oakland Title and Trust site to a depth of 500 ft.

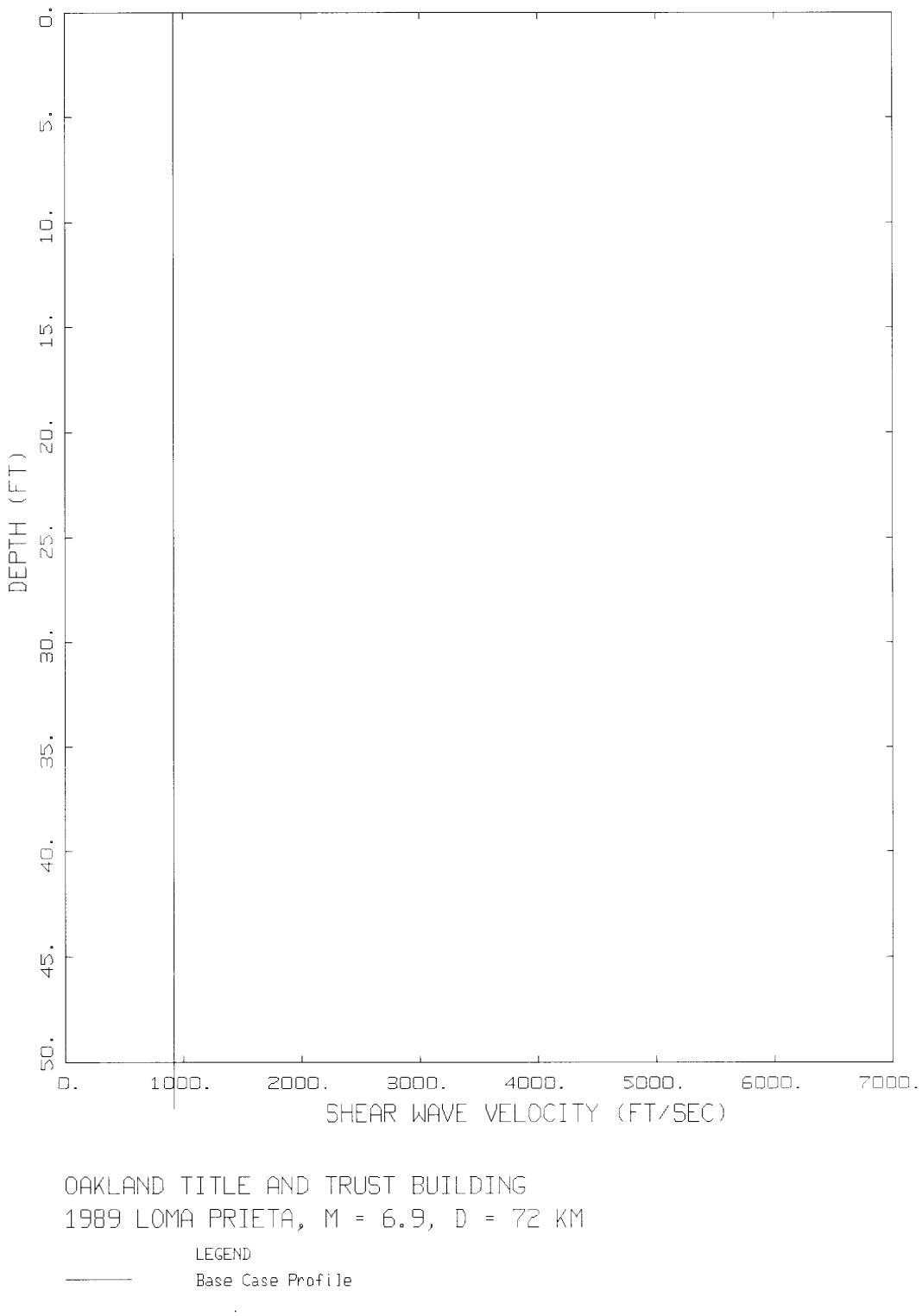


Figure 7c. Shear-wave velocity profile (measured) at the Oakland Title and Trust site to a depth of 50 ft.

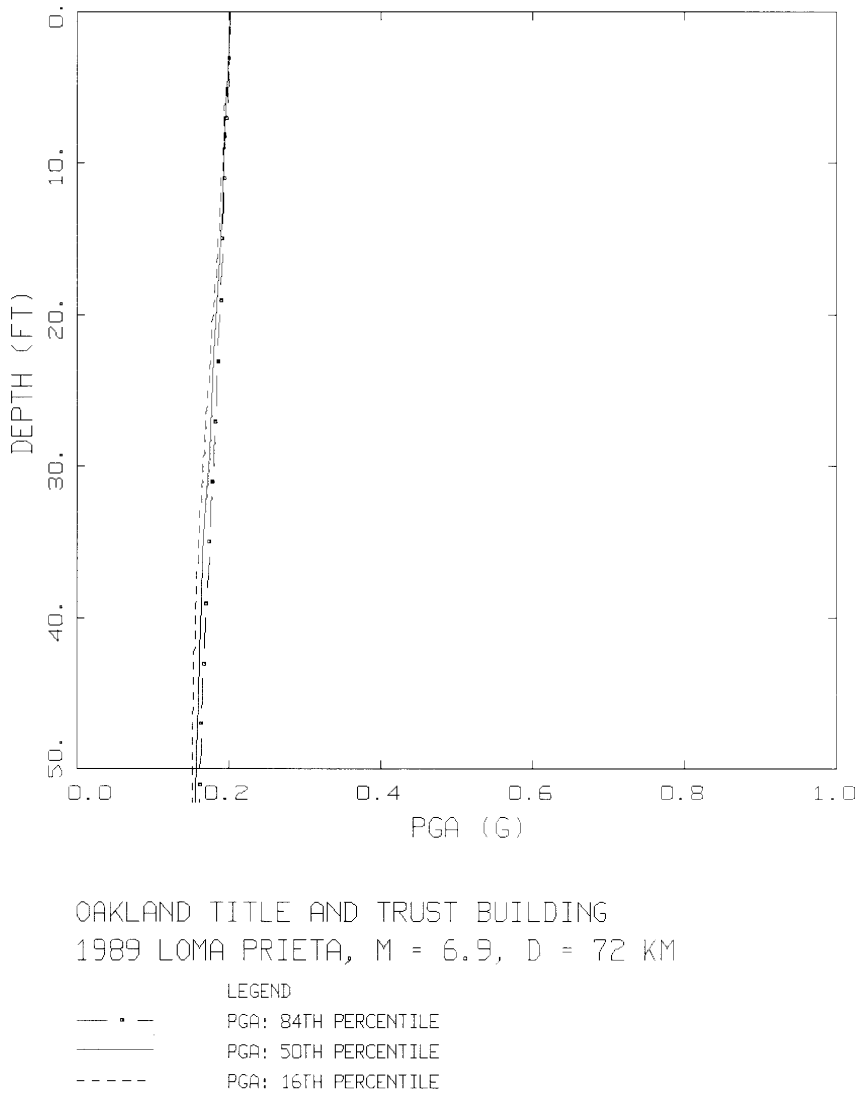


Figure 7d. Variation of peak acceleration(g) (Average horizontal component) verses depth computed for a suite of random profiles at the Oakland Title and Trust site. Average horizontal spectrum (Figure 7a) based on recorded motions used as control motions.

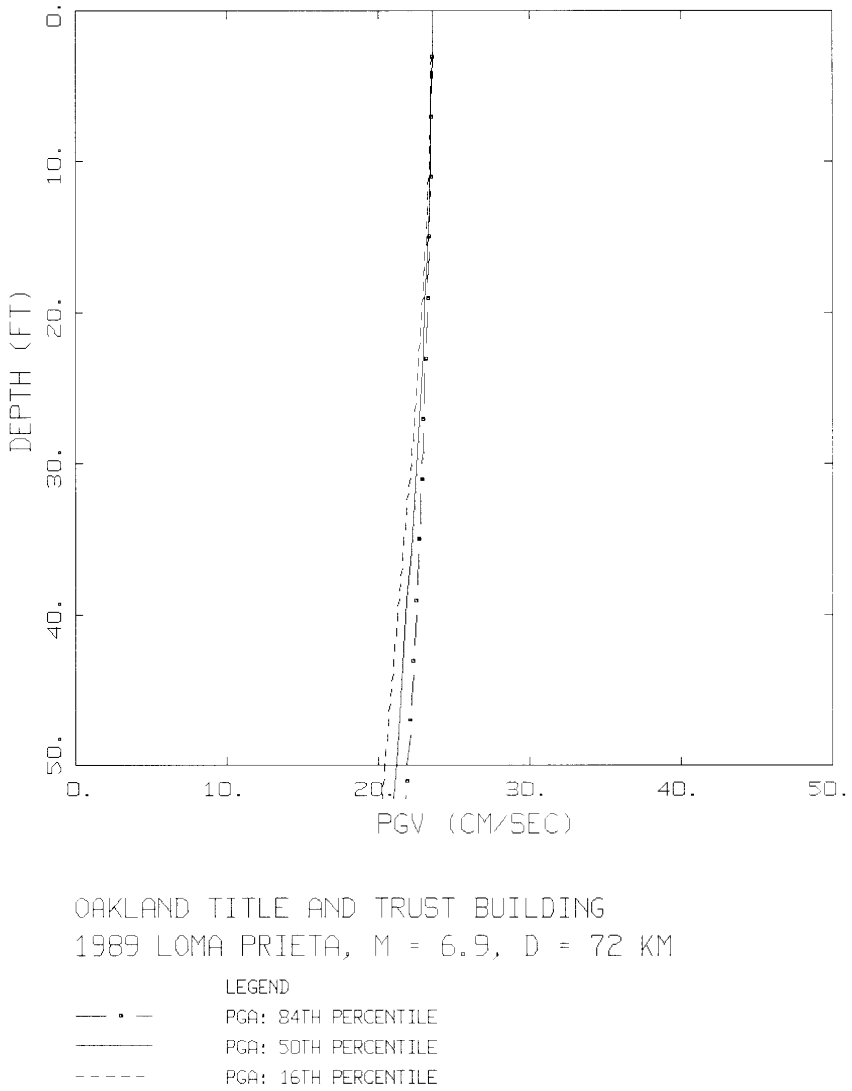


Figure 7e. Variation of peak particle velocity (cm/sec) verses depth computed for a suite of random profiles at the Oakland Title and Trust site. Average horizontal spectrum (Figure 7a) based on recorded motions used as control motions.

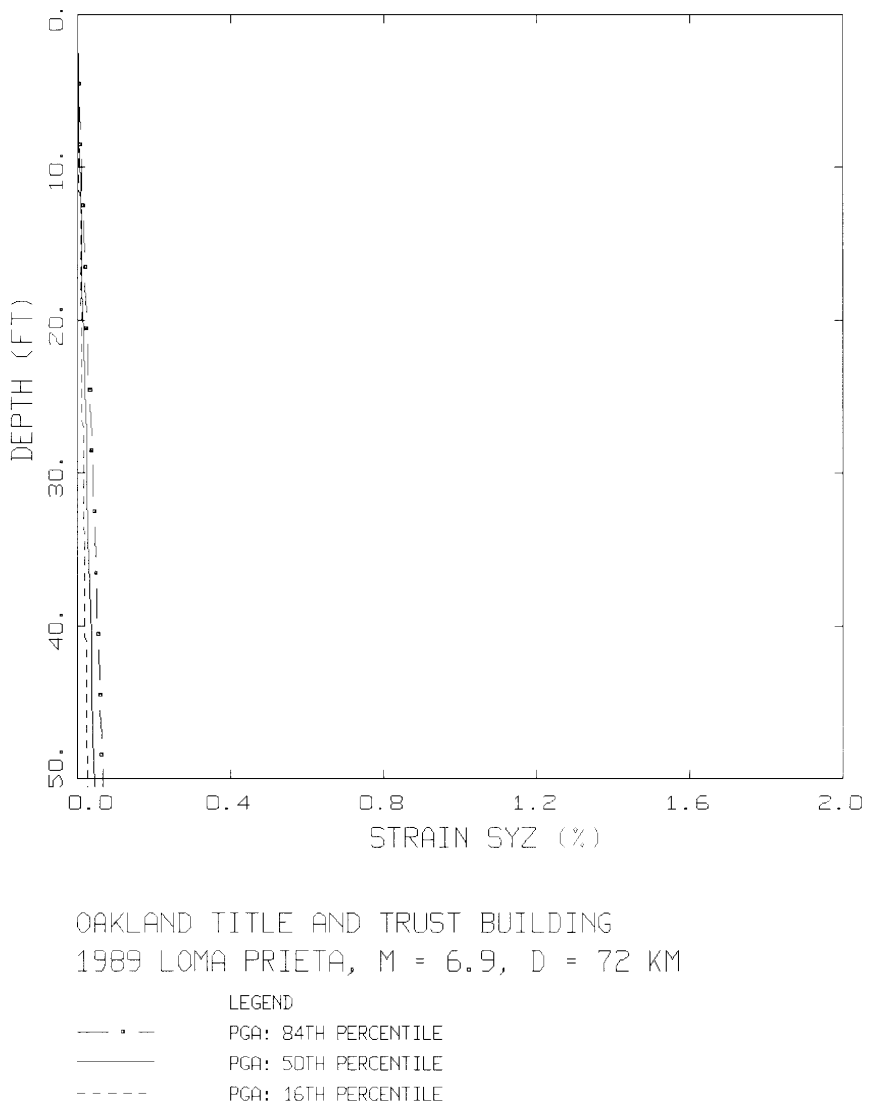


Figure 7f. Variation of peak shear strain(%) verses depth computed for a suite of random profiles at the Oakland Title and Trust site. Average horizontal spectrum (Figure 7a) based on recorded motions used as control motions.

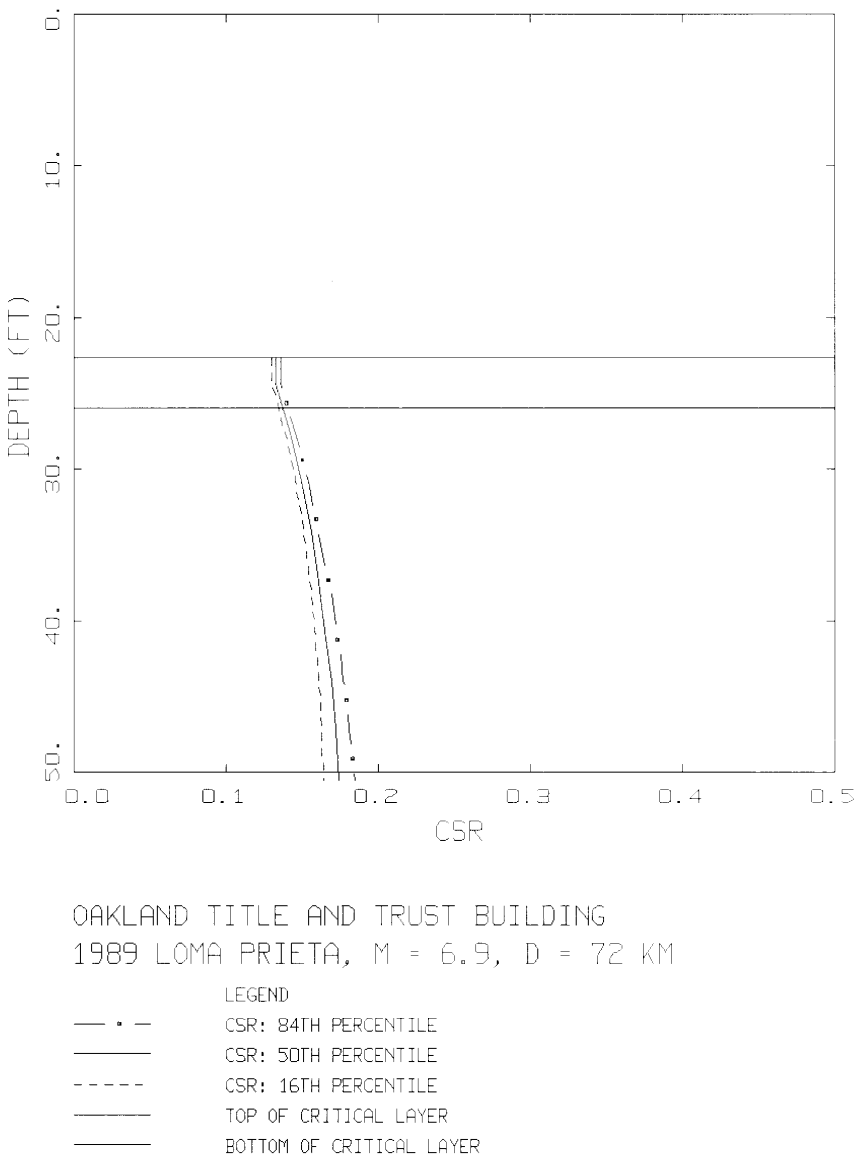


Figure 7g. Variation of CSR verses depth computed for a suite of random profiles for at Oakland Title and Trust site. Average horizontal spectrum (Figure 7a) based on recorded motions used as control motions. Critical layer indicated with horizontal lines.

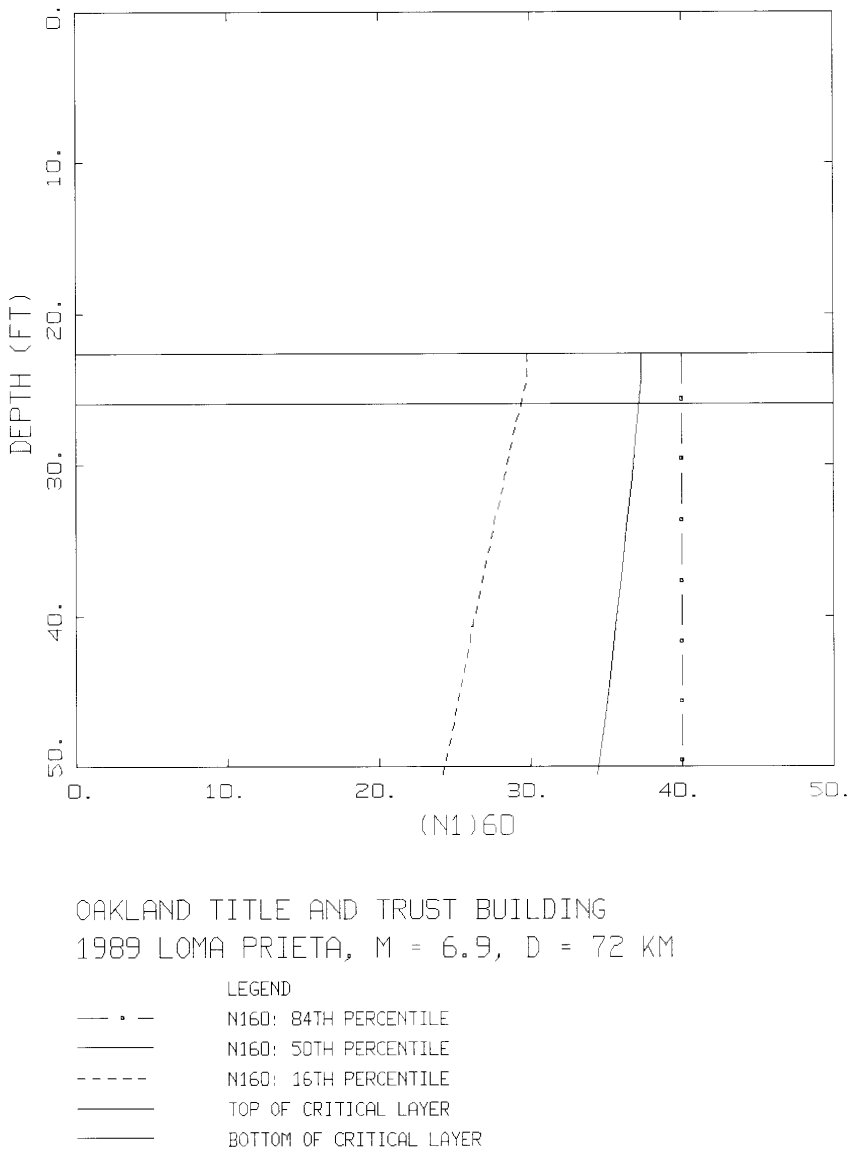


Figure 7h. Variation of peak $(N_1)_{60}$ verses depth computed for a suite of random profiles at the Oakland Title and Trust site using the shear-wave velocity correlation model of Iwasaki et al., (1987). Average horizontal spectrum (Figure 7a) based on recorded motions used as control motions. Critical layer indicated with horizontal lines.

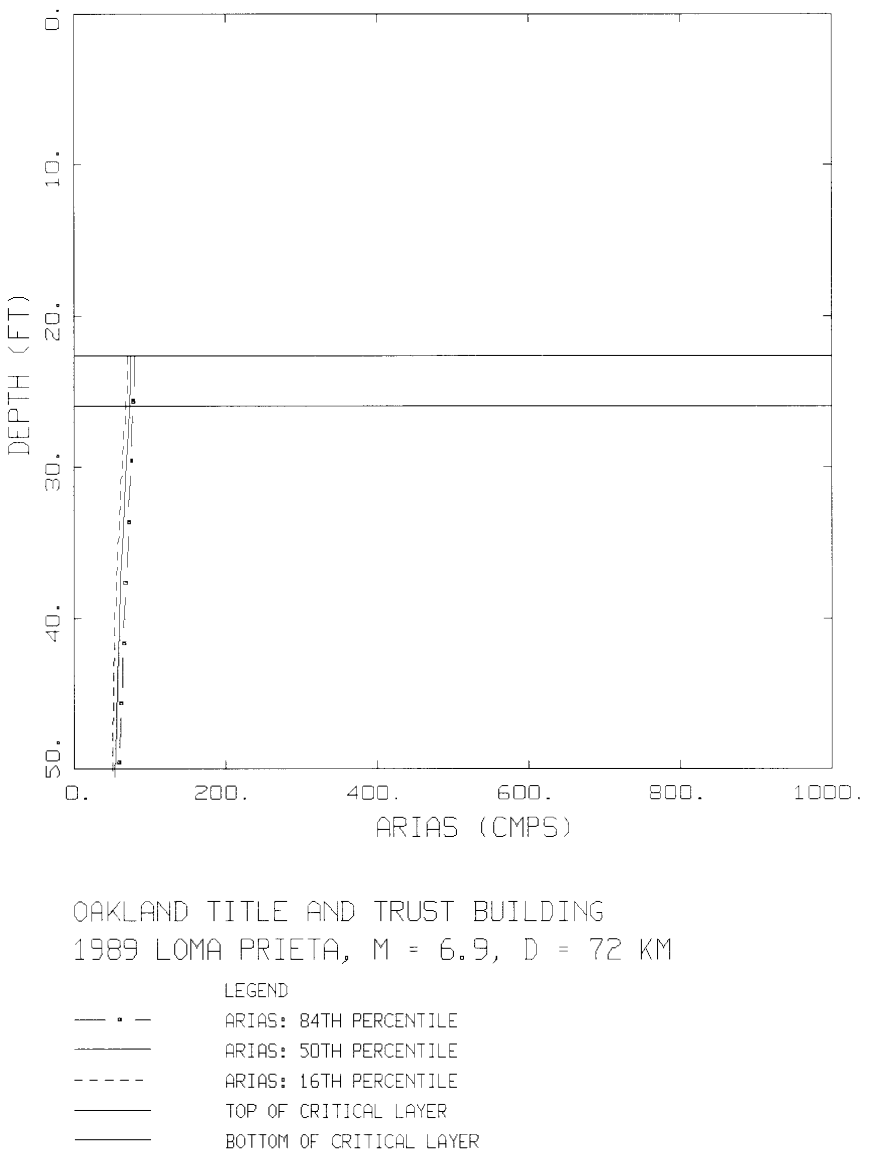


Figure 7i. Variation of Arias Intensity (cm/sec) verses depth computed for a suite of random profiles at the Oakland Title and Trust site. Average horizontal spectrum (Figure 7a) based on recorded motions used as control motions. Critical layer indicated with horizontal lines.

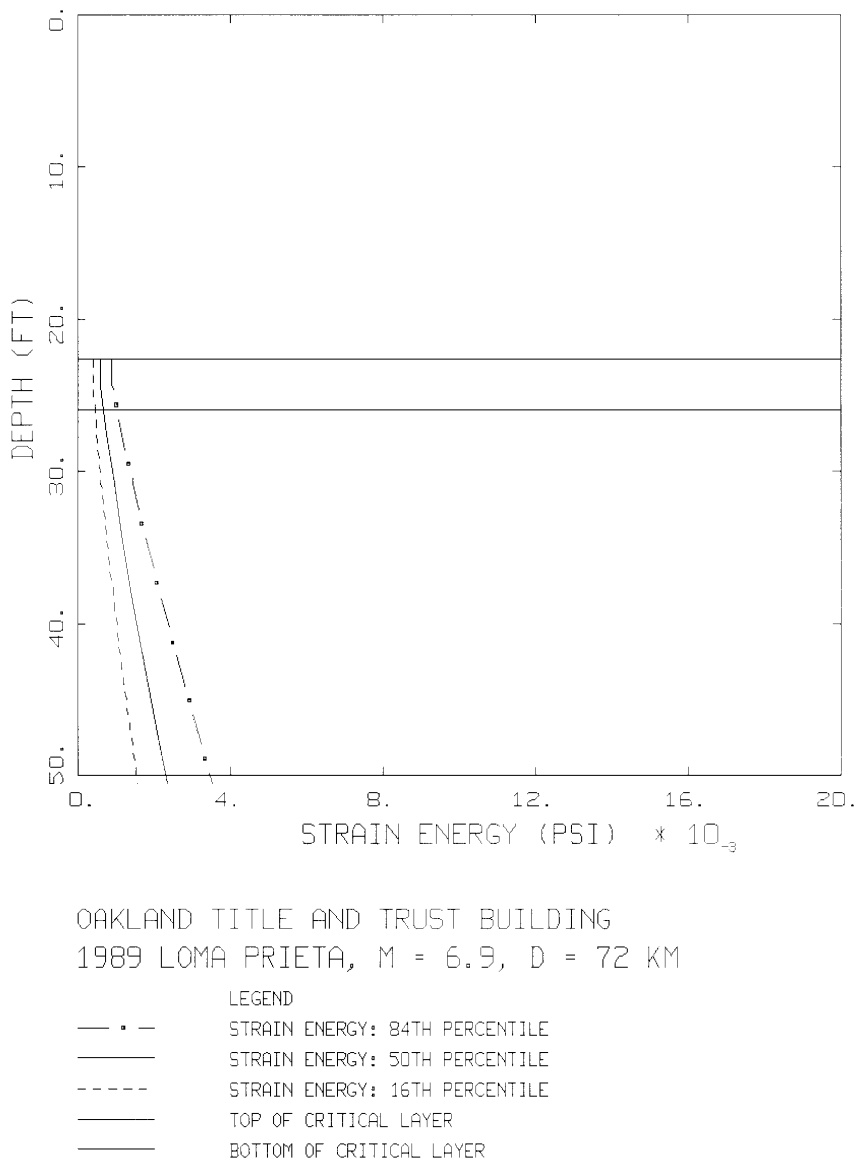


Figure 7j Variation of strain energy (PSI) verses depth computed for a suite of random profiles at the Oakland Title and Trust site. Average horizontal spectrum (Figure 7a) based on recorded motions used as control motions. Critical layer indicated with horizontal lines.

Figure 7k. Variation of the factor of safety (FS) using the Andrus and Stokoe (2004) shear-wave velocity based approach verses depth computed for a suite of random profiles at the Oakland Title and Trust site. Average horizontal spectrum (Figure 7a) based on recorded motions used as control motions. Critical layer indicated with horizontal lines.

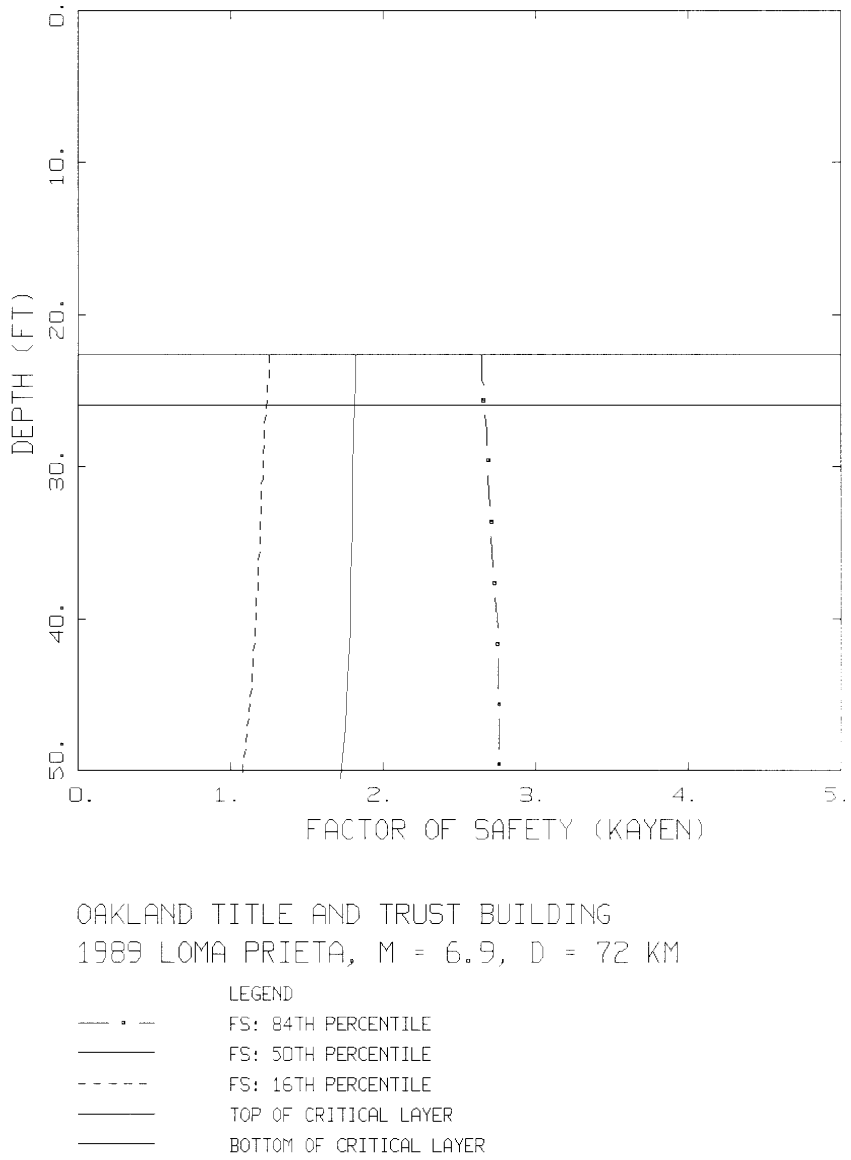


Figure 7l. Variation of the factor of safety using the Kayen and Mitchell (1997) Arias Intensity based approach verses depth computed for a suite of random profiles at the Oakland Title and Trust site. Average horizontal spectrum (Figure 7a) based on recorded motions used as control motions. Critical layer indicated with horizontal lines.

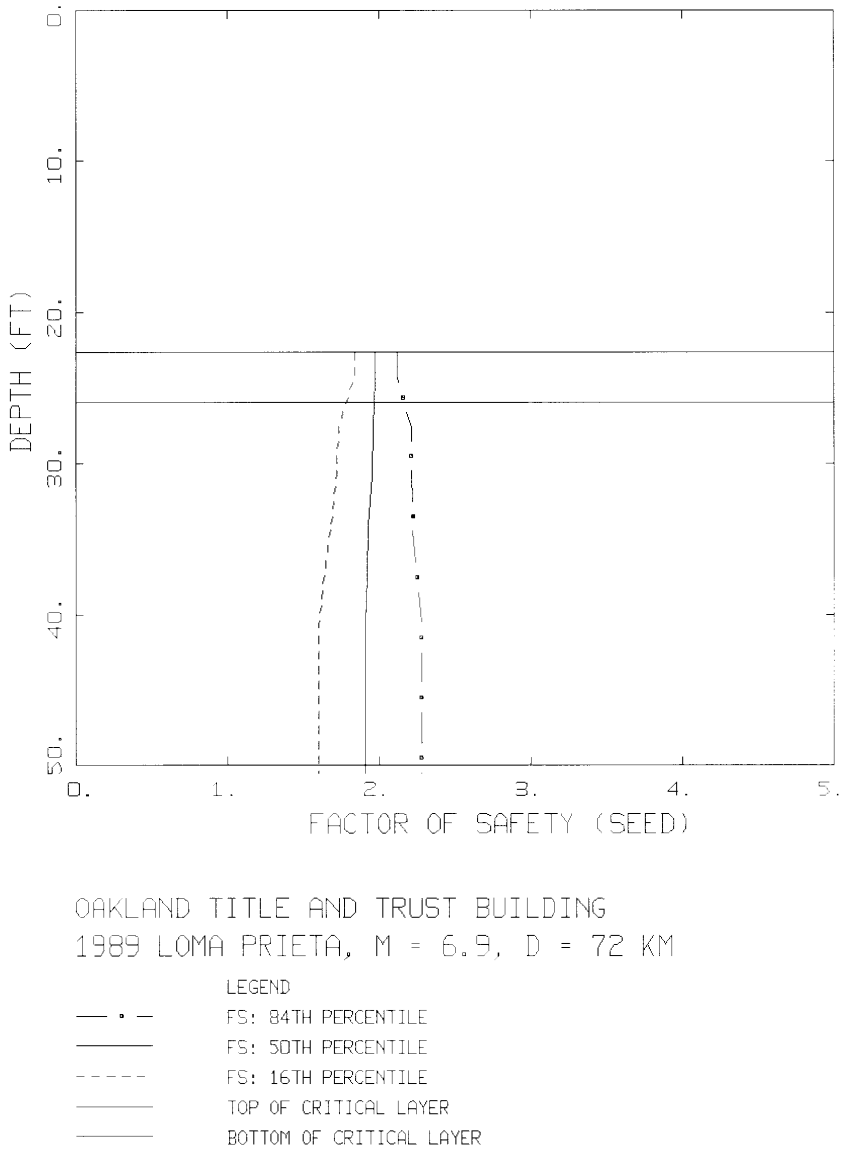


Figure 7m. Variation of the factor of the factor of safety using the Seed et al., (2002) SPT based approach verses depth computed for a suite of random profiles at the Oakland Title and Trust site. Average horizontal spectrum (Figure 7a) based on recorded motions used as control motions. Critical layer indicated with horizontal lines.

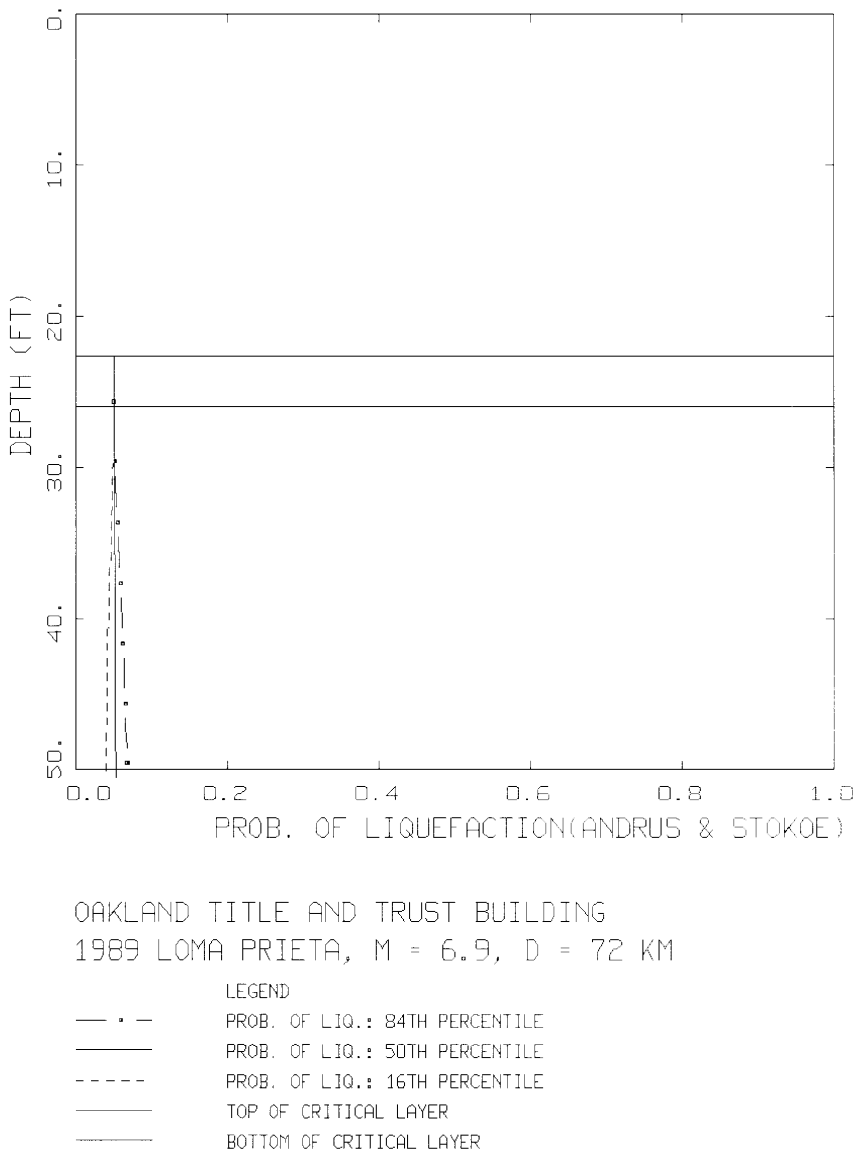


Figure 7n. Variation of the probability of liquefaction using the Andrus and Stokoe (2004) shear-wave velocity based approach verses depth computed for a suite of random profiles at the Oakland Title and Trust site. Average horizontal spectrum (Figure 7a) based on recorded motions used as control motions. Critical layer indicated with horizontal lines.

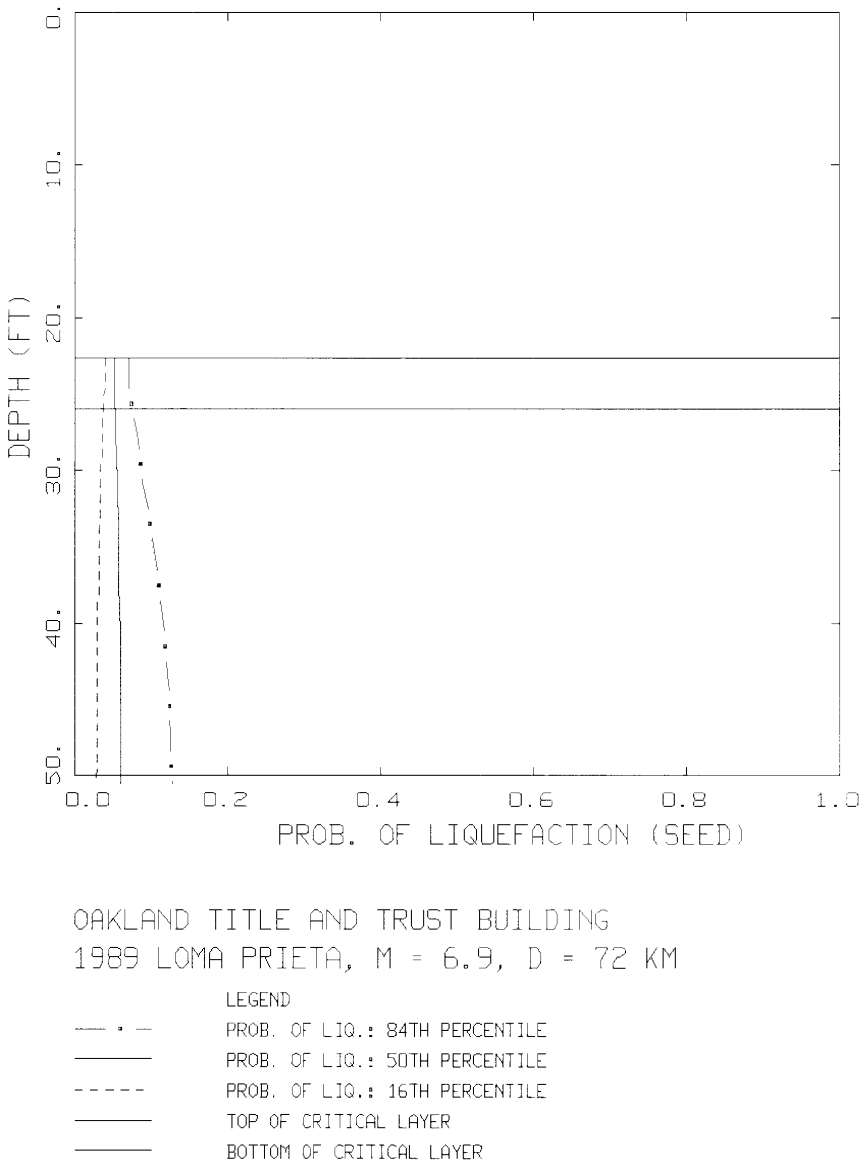


Figure 7o. Variation probability of liquefaction using the Seed et al. (2002) SPT based approach verses depth computed for a suite of random profiles at the Oakland Title and Trust site. Average horizontal spectrum (Figure 7a) based on recorded motions used as control motions. Critical layer indicated with horizontal lines.

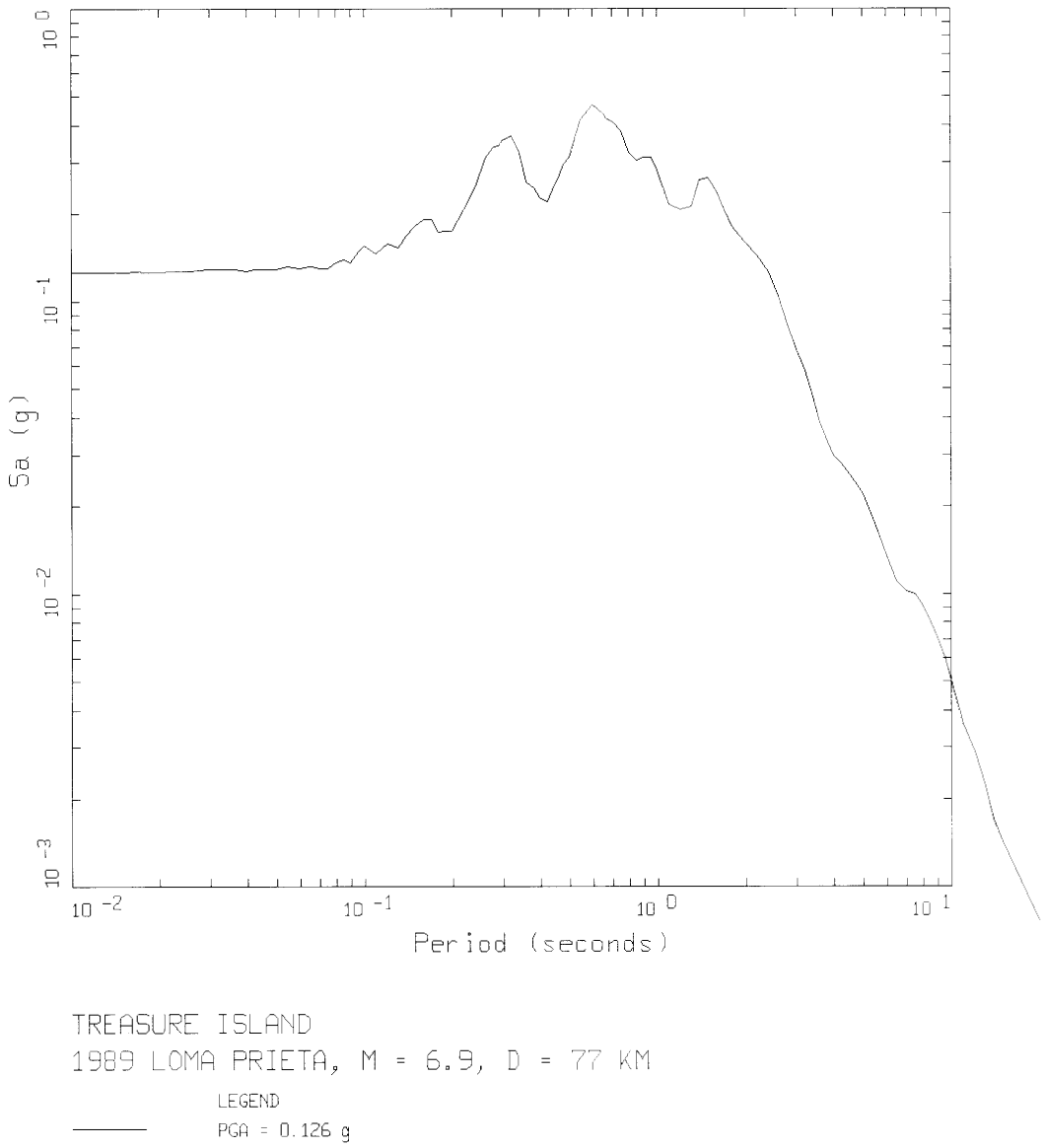


Figure 8a. Average horizontal component response spectra computed from recorded motions: Treasure Island site, Loma Prieta earthquake.

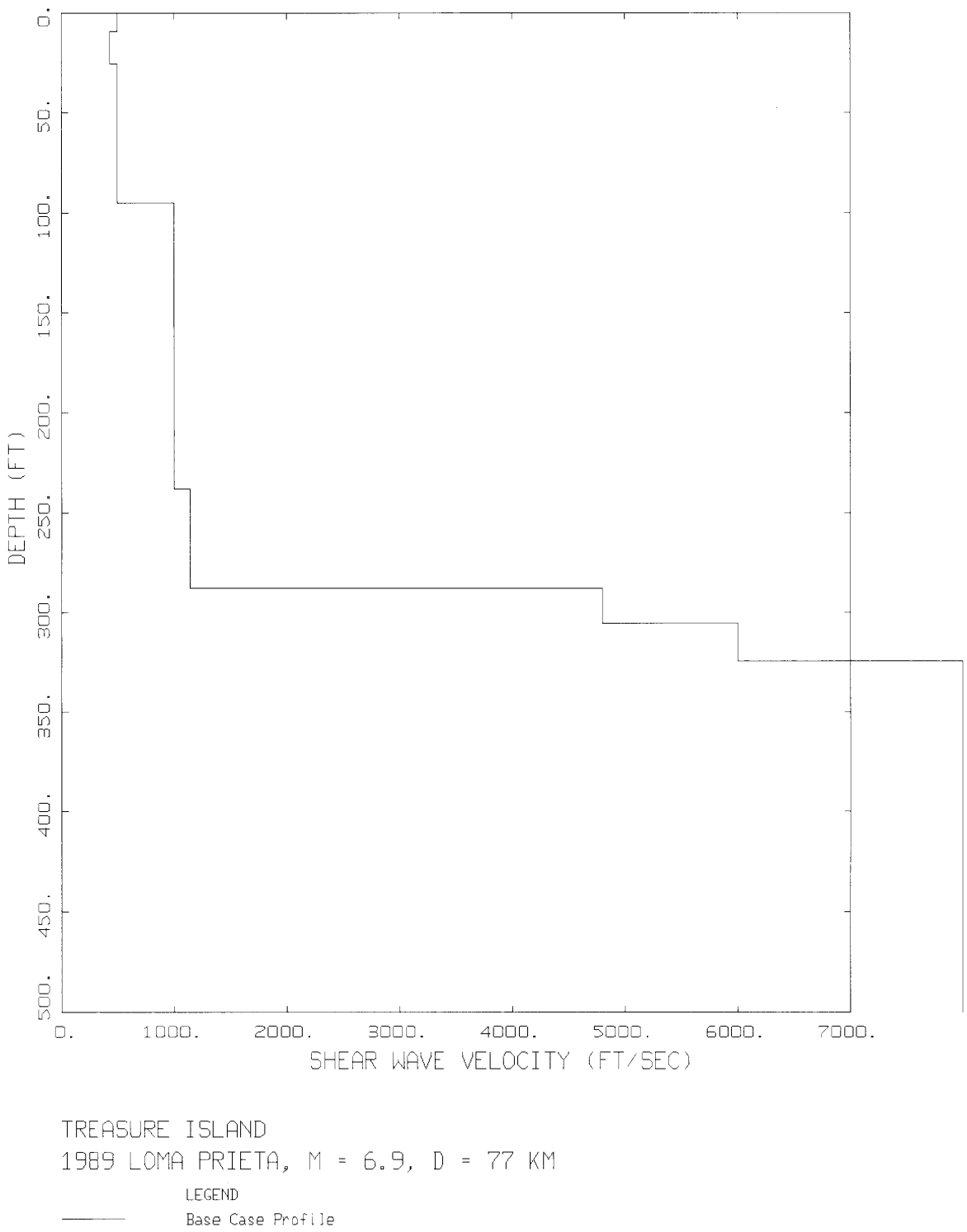


Figure 8b. Shear-wave velocity profile (measured) at the Treasure Island site to a depth of 500 ft.

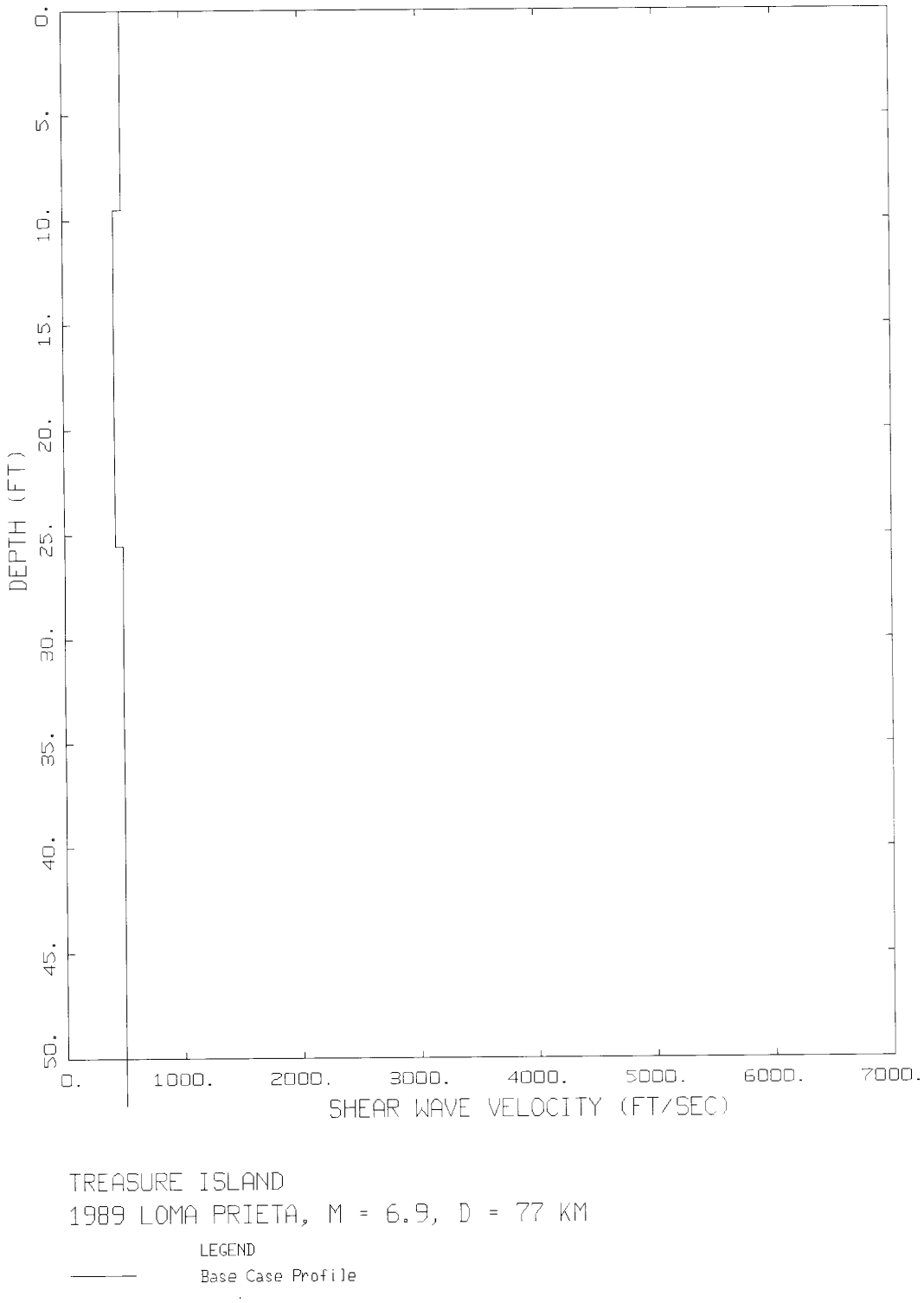


Figure 8c. Shear-wave velocity profile (measured) at the Treasure Island site to a depth of 50 ft.

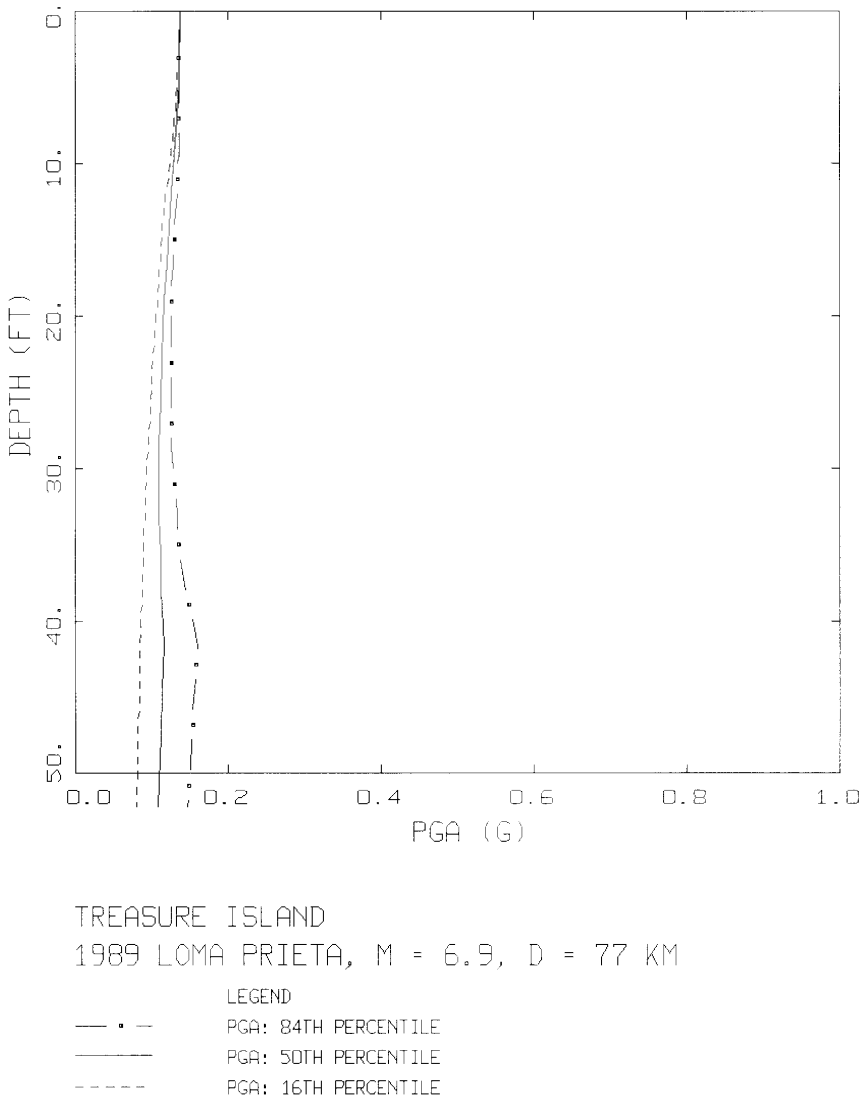


Figure 8d. Variation of peak acceleration(g) (Average horizontal component) verses depth computed for a suite of random profiles at the Treasure Island site. Average horizontal spectrum (Figure 8a) based on recorded motions used as control motions.

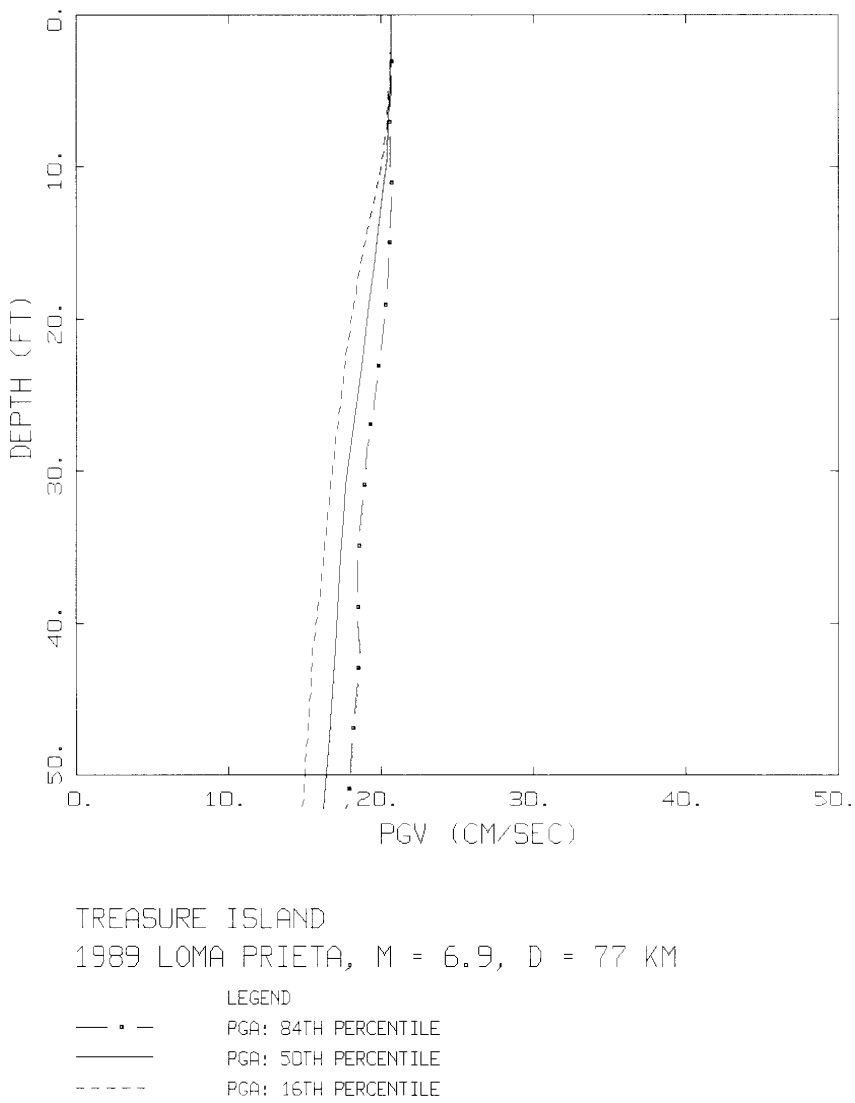


Figure 8e. Variation of peak particle velocity (cm/sec) verses depth computed for a suite of random profiles at the Treasure Island site. Average horizontal spectrum (Figure 8a) based on recorded motions used as control motions.

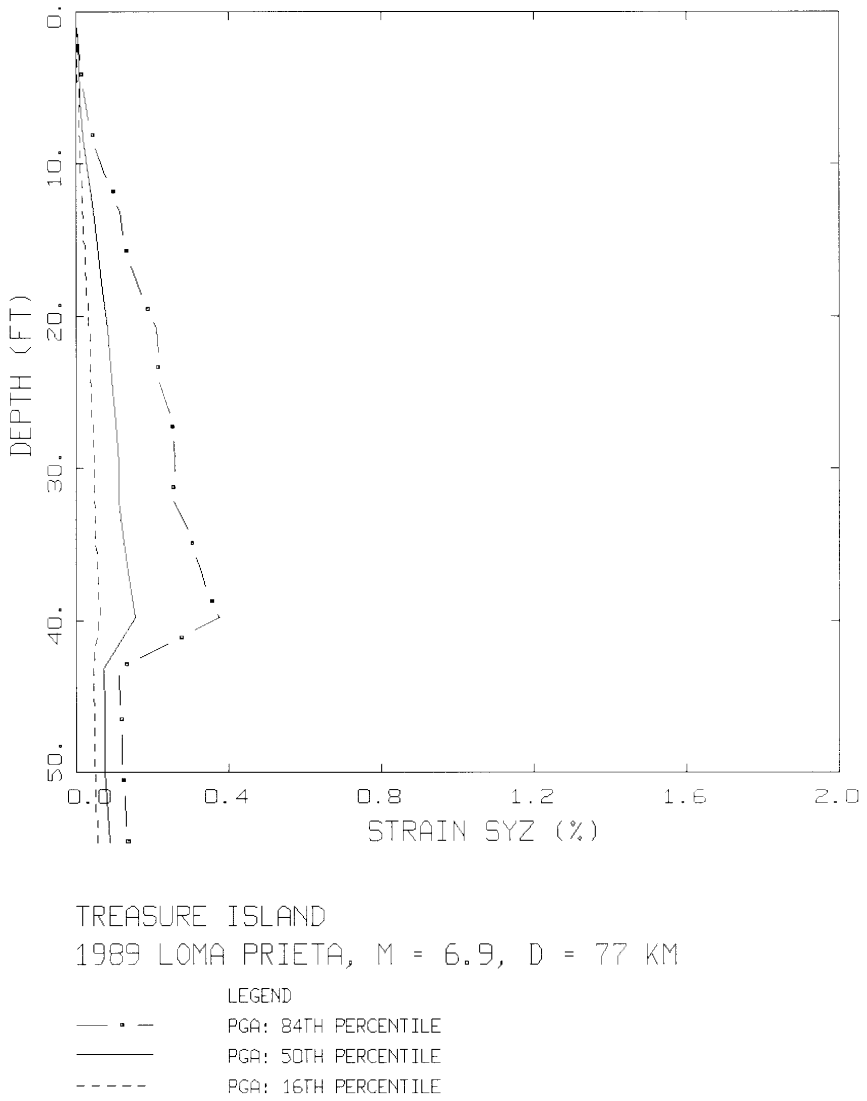


Figure 8f. Variation of peak shear strain(%) verses depth computed for a suite of random profiles at the Treasure Island. Average horizontal spectrum (Figure 8a) based on recorded motions used as control motions.

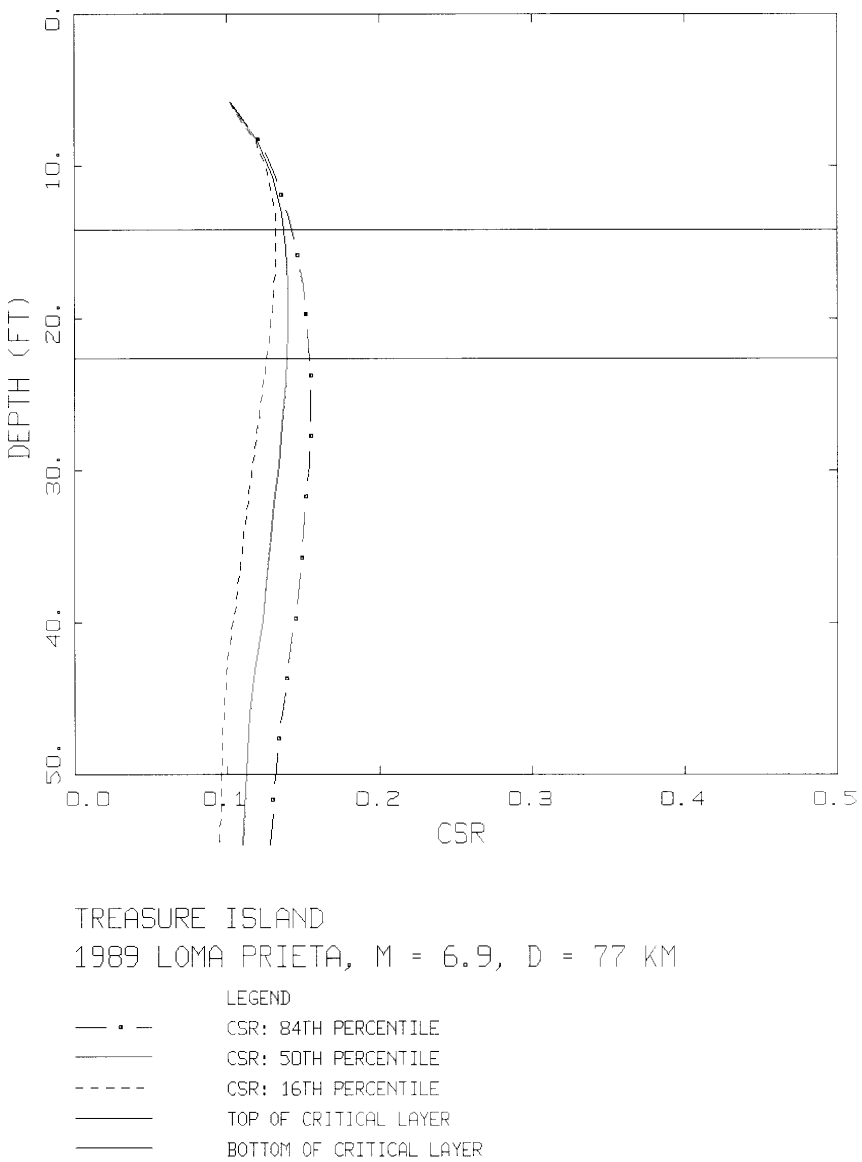


Figure 8g. Variation of CSR verses depth computed for a suite of random profiles for at Treasure Island site Average horizontal spectrum (Figure 8a) based on recorded motions used as control motions. Critical layer indicated with horizontal lines.

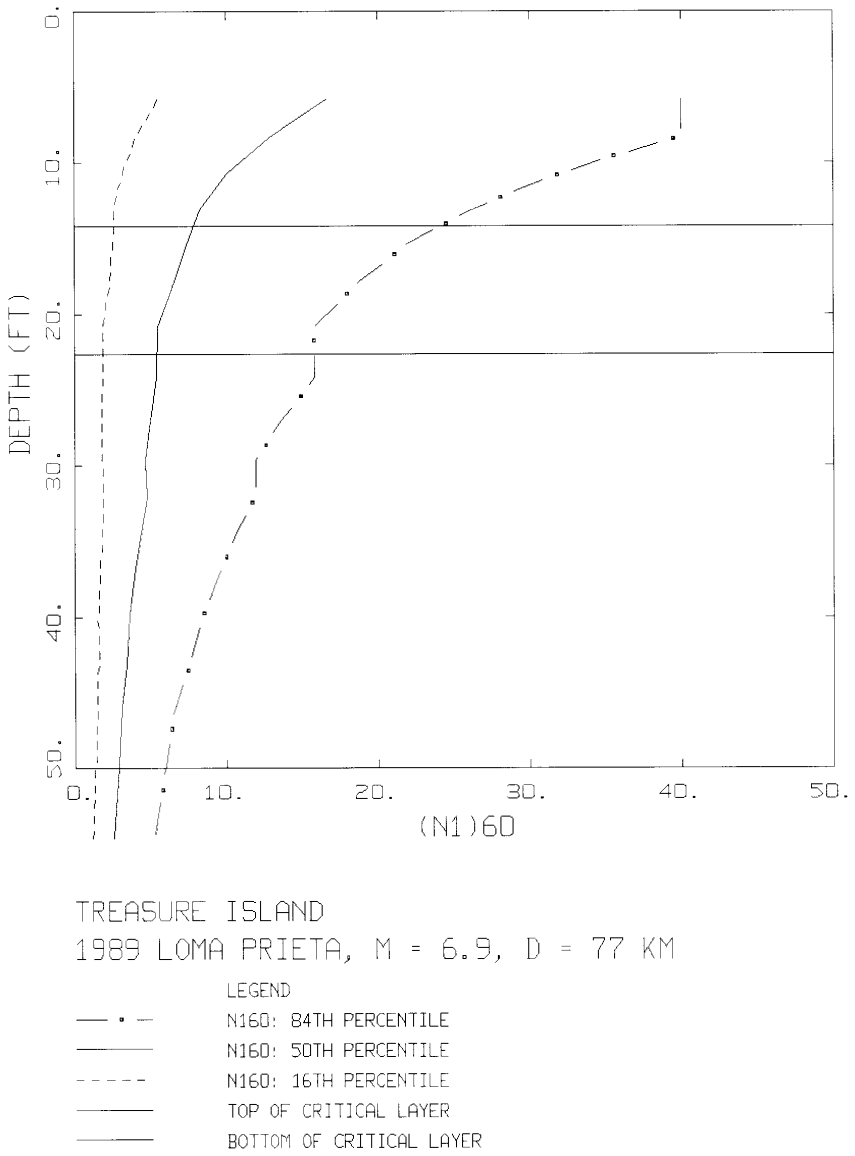


Figure 8h. Variation of peak $(N_1)_{60}$ verses depth computed for a suite of random profiles at the Treasure Island site using the shear-wave velocity correlation model of Iwasaki et al., (1987). Average horizontal spectrum (Figure 8a) based on recorded motions used as control motions. Critical layer indicated with horizontal lines.

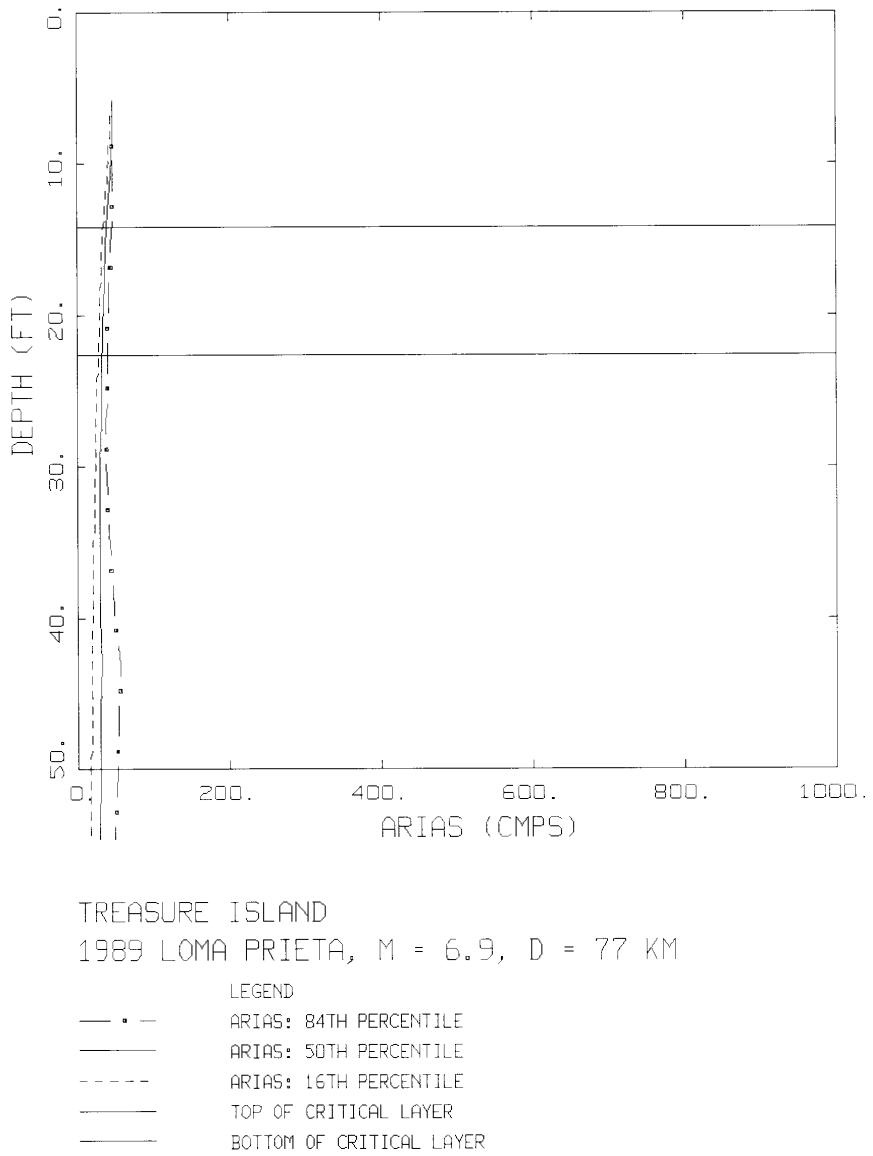


Figure 8i. Variation of Arias Intensity (cm/sec) verses depth computed for a suite of random profiles at the Treasure Island site. Average horizontal spectrum (Figure 8a) based on recorded motions used as control motions. Critical layer indicated with horizontal lines.

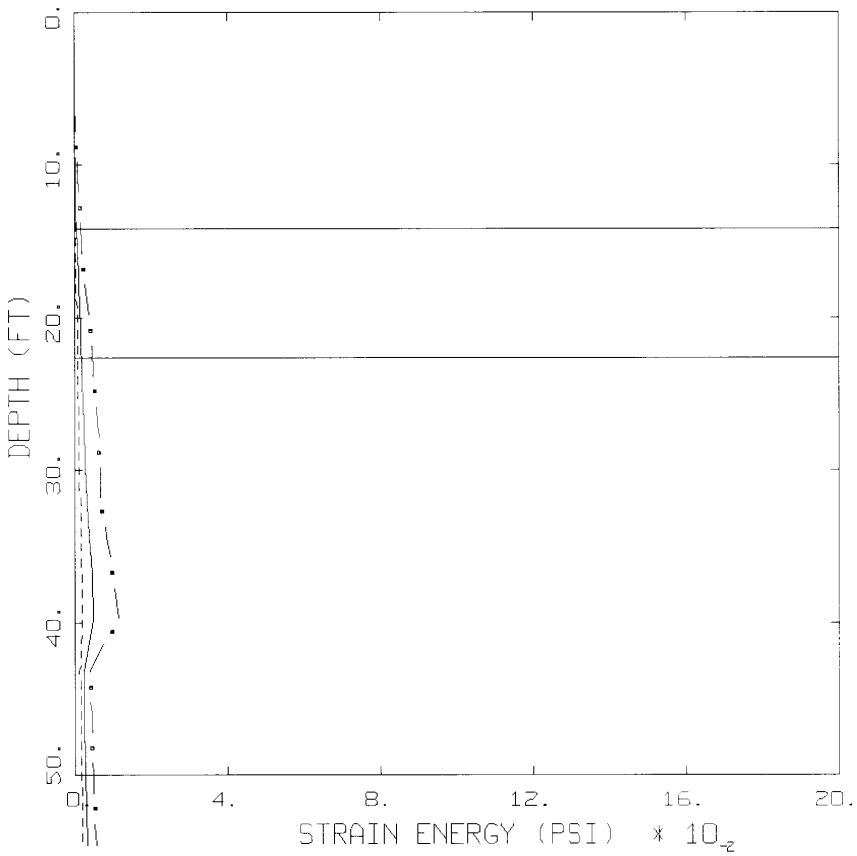


TREASURE ISLAND
1989 LOMA PRIETA, M = 6.9, D = 77 KM

LEGEND

| | |
|---|---|
| —— · — | STRAIN ENERGY: 84TH PERCENTILE |
| ——— | STRAIN ENERGY: 50TH PERCENTILE |
| - - - - - | STRAIN ENERGY: 16TH PERCENTILE |
| ——— | TOP OF CRITICAL LAYER |
| ——— | BOTTOM OF CRITICAL LAYER |

Figure 8j Variation of strain energy (PSI) verses depth computed for a suite of random profiles at the Treasure Island site. Average horizontal spectrum (Figure 8a) based on recorded motions used as control motions. Critical layer indicated with horizontal lines.

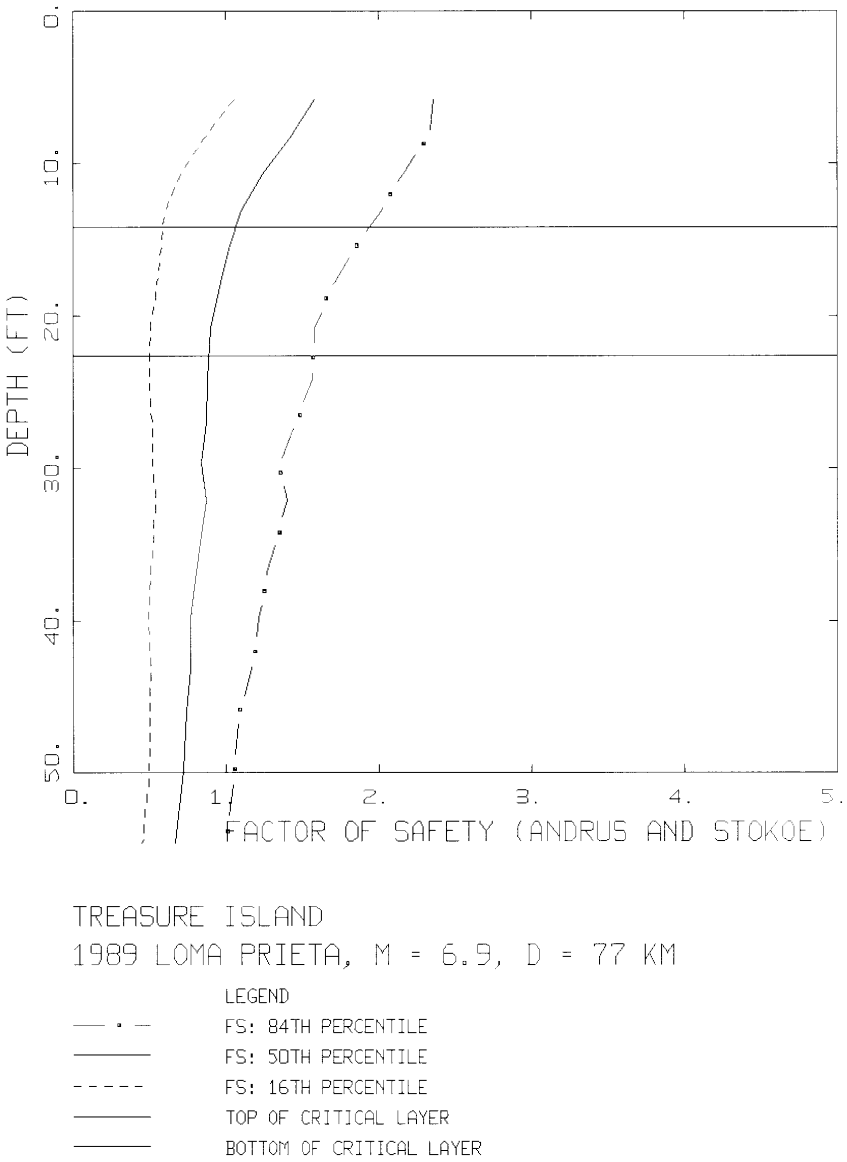


Figure 8k. Variation of the factor of safety (FS) using the Andrus and Stokoe (2004) shear-wave velocity based approach verses depth computed for a suite of random profiles at the Treasure Island site. Average horizontal spectrum (Figure 8a) based on recorded motions used as control motions. Critical layer indicated with horizontal lines.

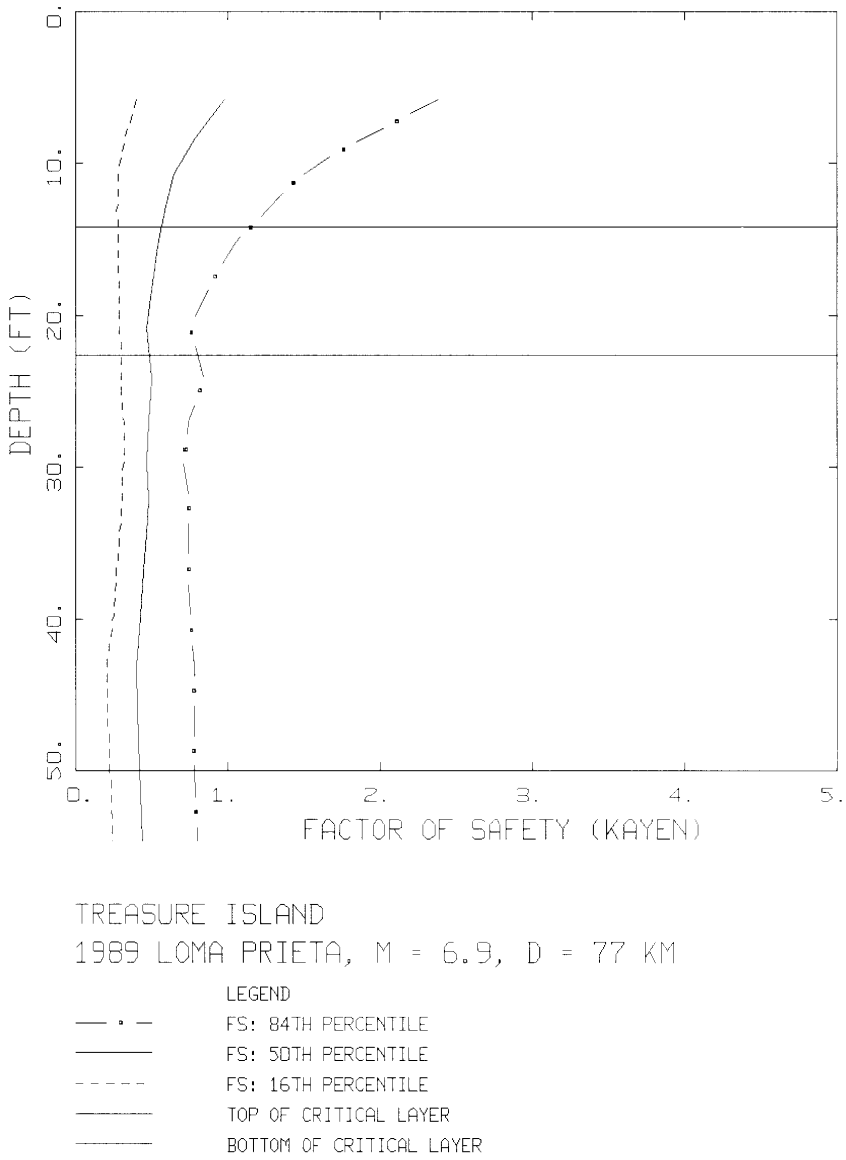


Figure 8l. Variation of the factor of safety using the Kayen and Mitchell (1998) Arias Intensity based approach verses depth computed for a suite of random profiles at the Treasure Island site. Average horizontal spectrum (Figure 8a) based on recorded motions used as control motions. Critical layer indicated with horizontal lines.

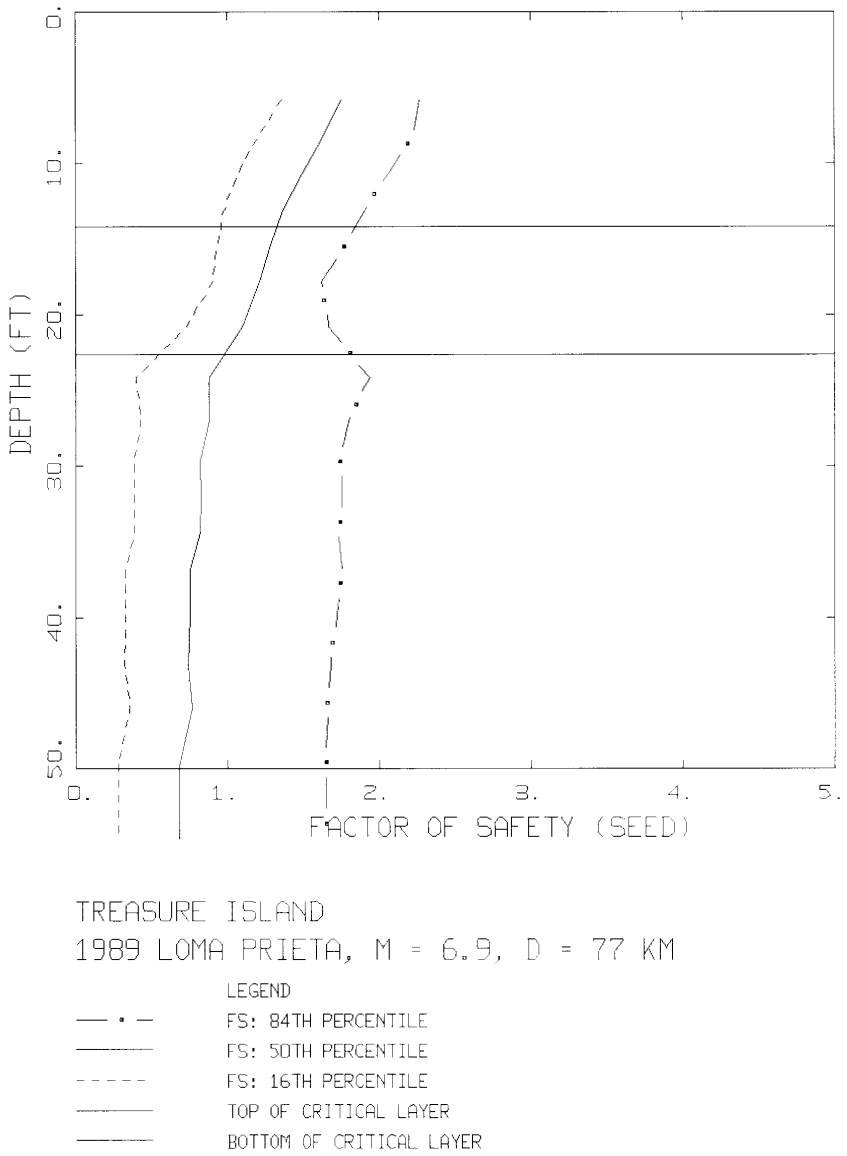


Figure 8m. Variation of the factor of the factor of safety using the Seed et al., (2002) SPT based approach verses depth computed for a suite of random profiles at the Treasure Island site. Average horizontal spectrum (Figure 8a) based on recorded motions used as control motions. Critical layer indicated with horizontal lines.

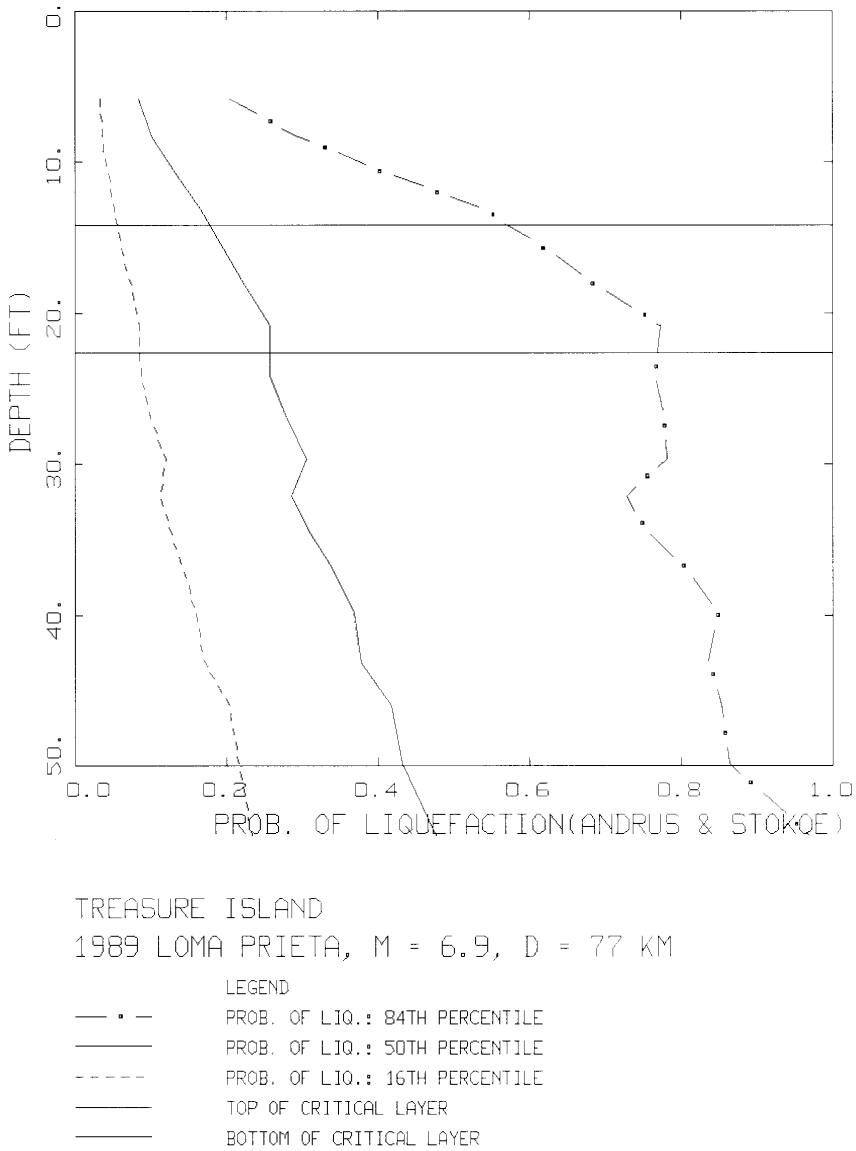


Figure 8n. Variation of the probability of liquefaction using the Andrus and Stokoe (2004) shear-wave velocity based approach verses depth computed for a suite of random profiles at the Treasure Island site. Average horizontal spectrum (Figure 8a) based on recorded motions used as control motions. Critical layer indicated with horizontal lines.

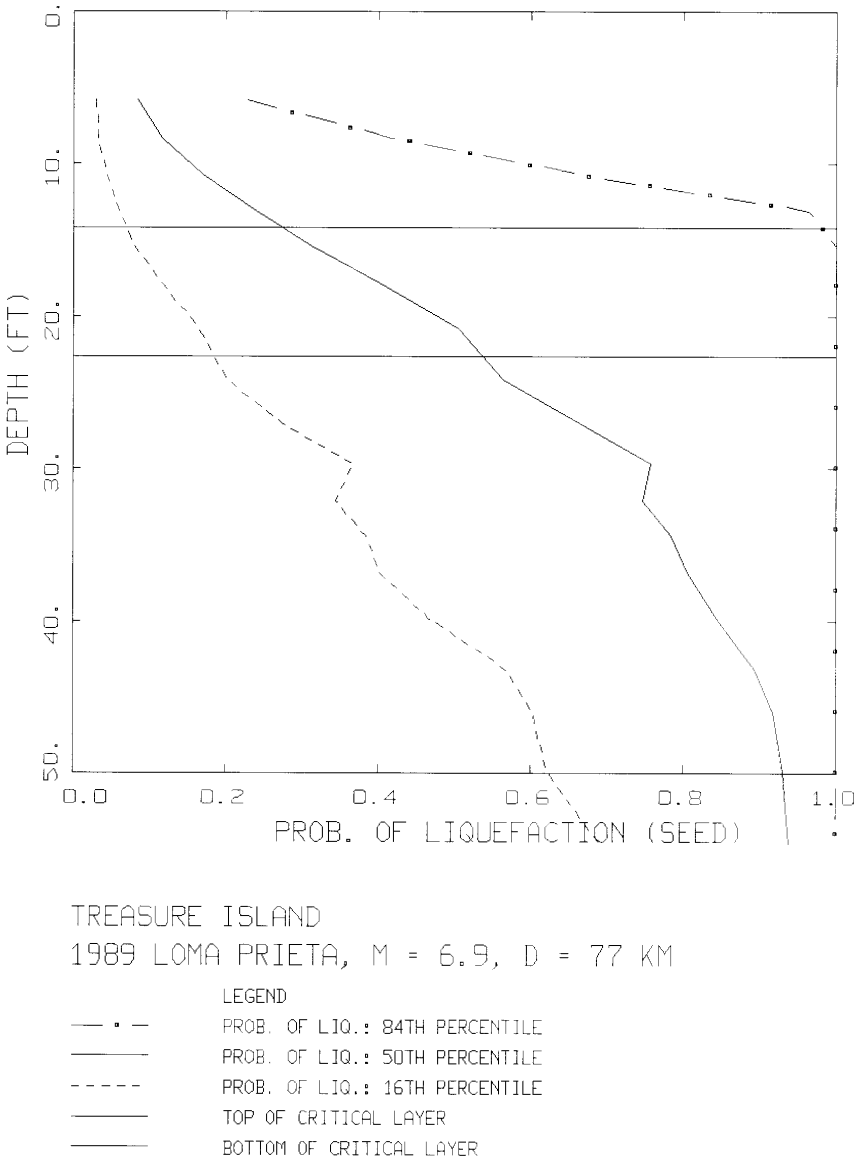


Figure 8o. Variation probability of liquefaction using the Seed et al. (2002) SPT based approach verses depth computed for a suite of random profiles at the Treasure Island site. Average horizontal spectrum (Figure 8a) based on recorded motions used as control motions. Critical layer indicated with horizontal lines.

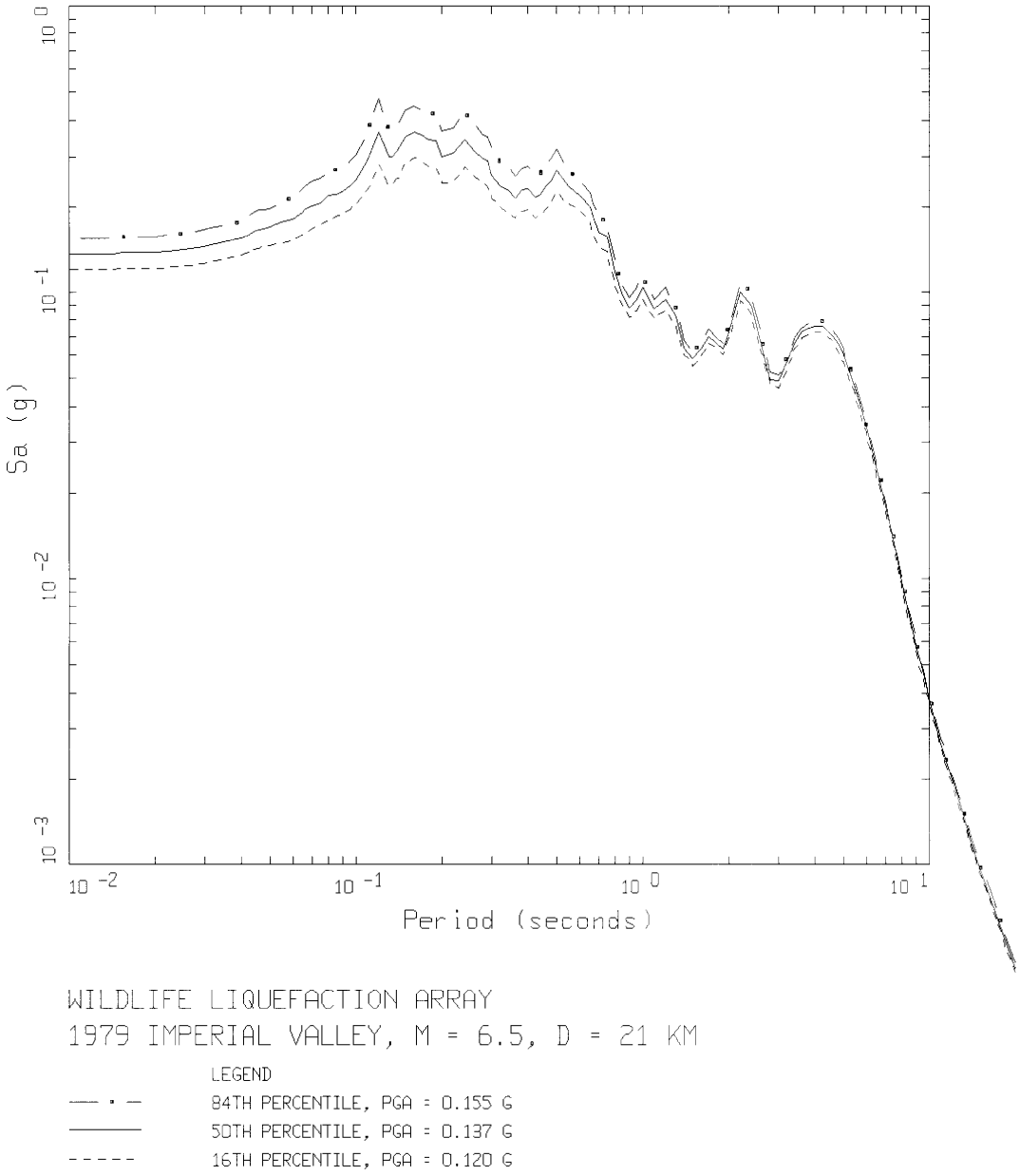


Figure 9a. Average horizontal component response spectra computed from simulated motions: Wildlife Liquefaction Array, 1979 Imperial Valley earthquake.

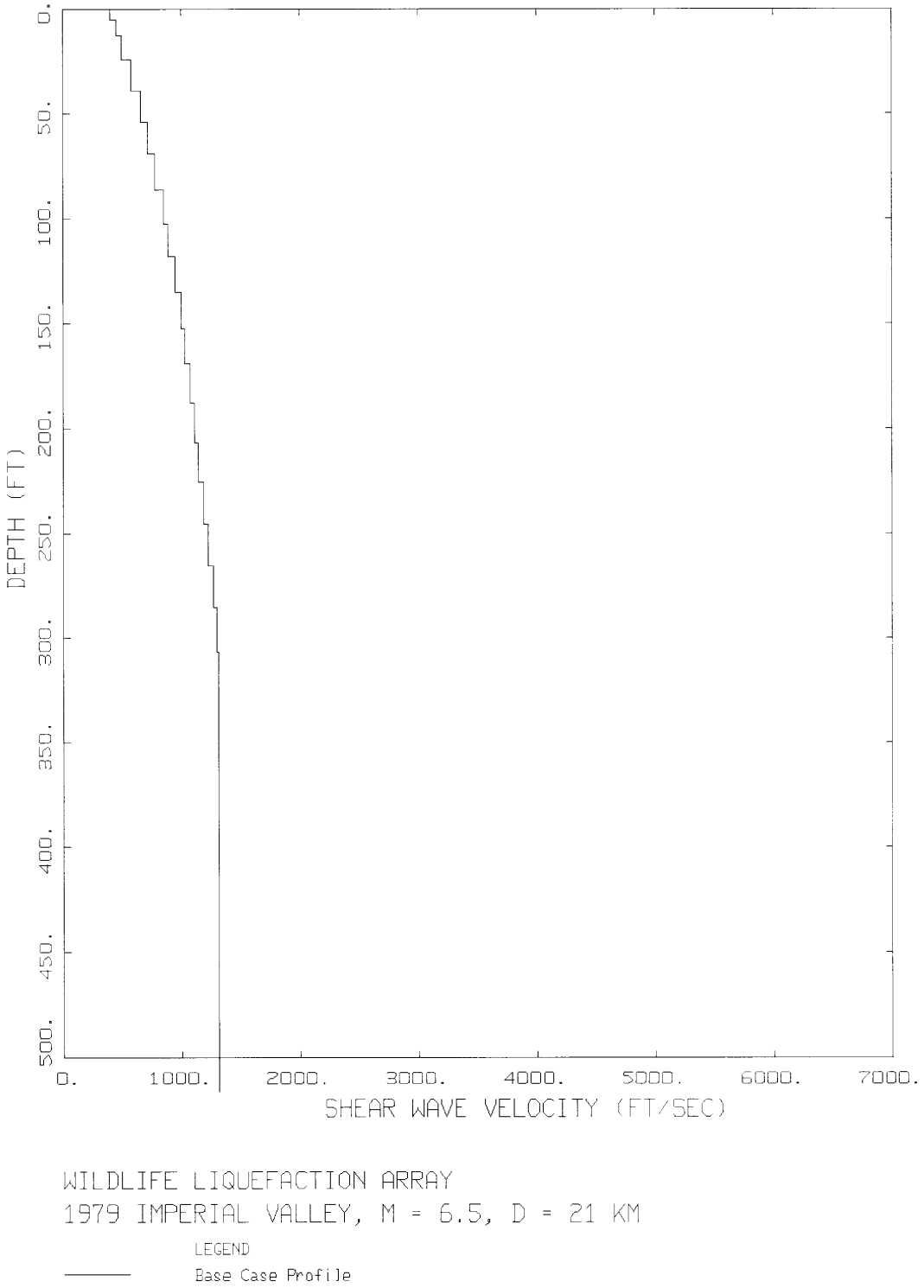


Figure 9b. Shear-wave velocity profile (assumed) at the Wildlife Liquefaction Array to a depth of 500 ft.

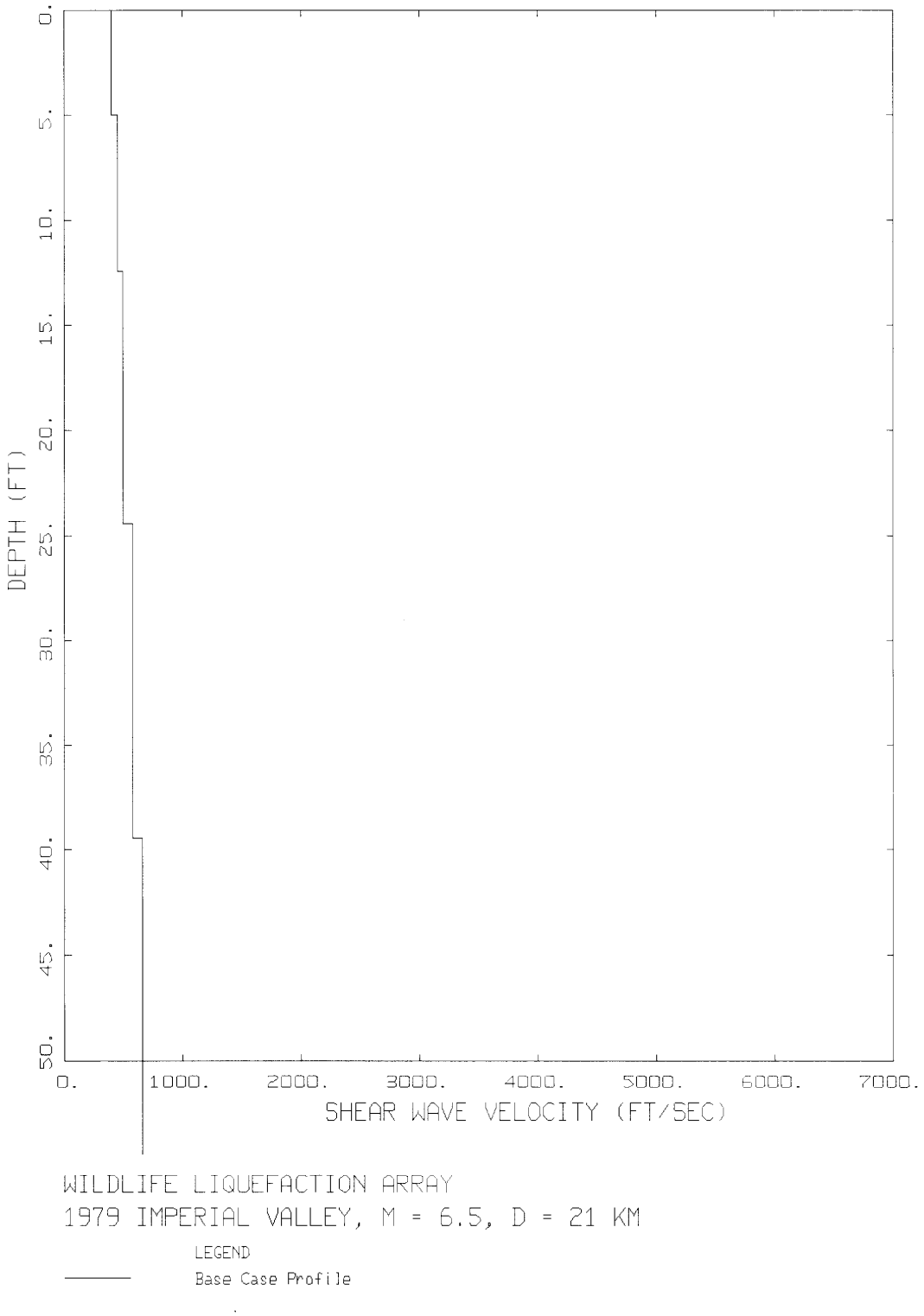


Figure 9c. Shear-wave velocity profile (assumed) at the Wildlife Liquefaction Array to a depth of 50 ft.

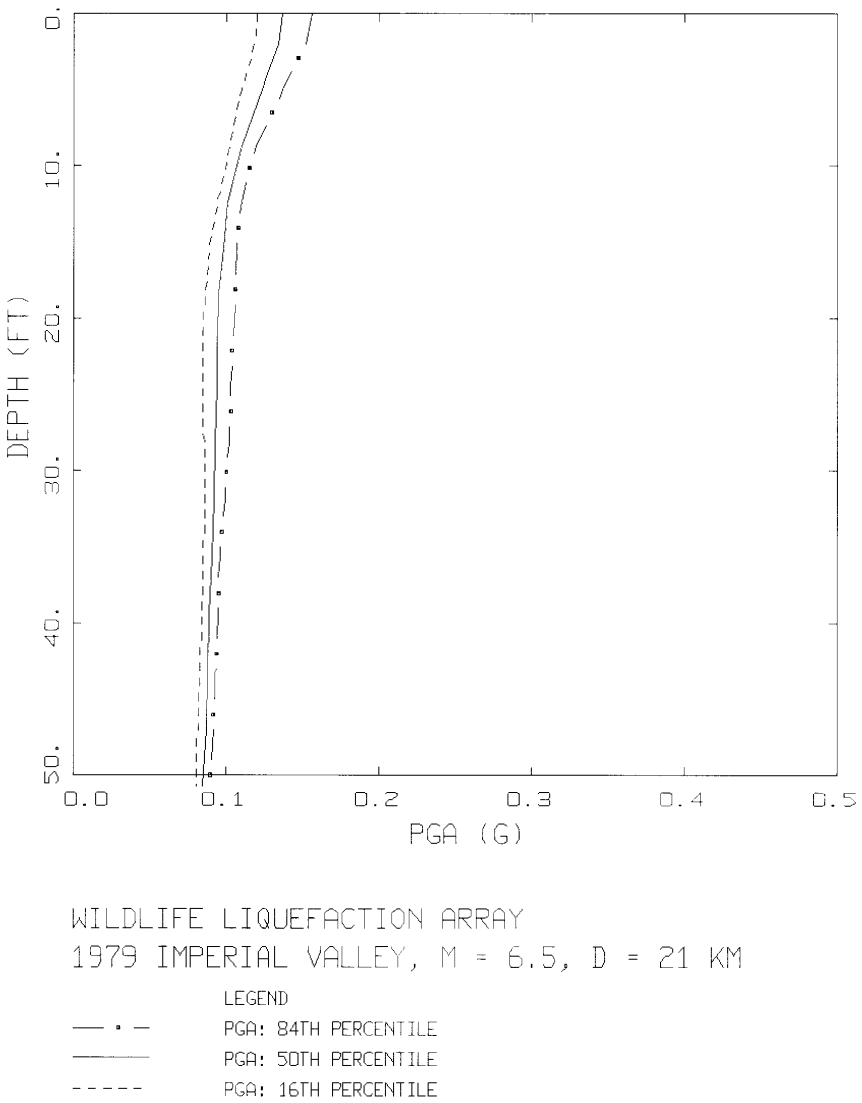


Figure 9d. Variation of peak acceleration(g) (Average horizontal component) verses depth computed for a suite of random profiles at the Wildlife Liquefaction Array. Average horizontal spectrum (Figure 9a) based on simulated motions used as control motions.

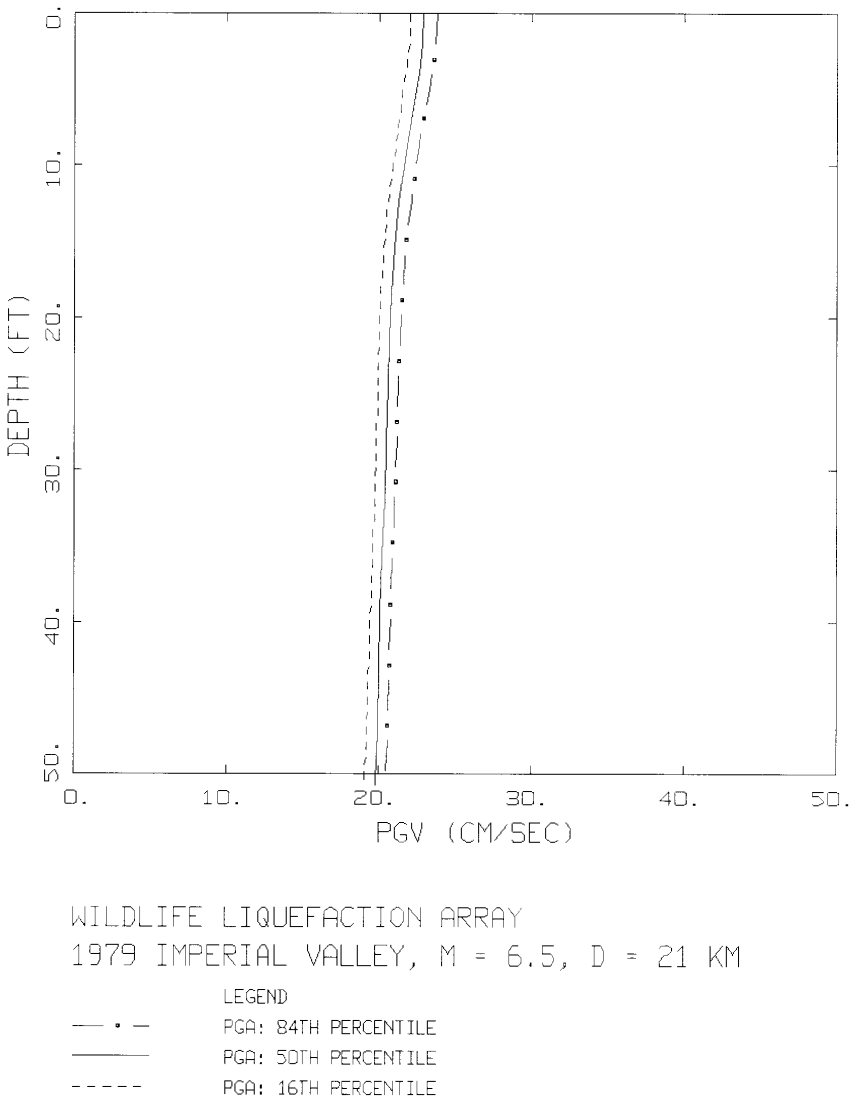


Figure 9e. Variation of peak particle velocity (cm/sec) verses depth computed for a suite of random profiles at the Wildlife Liquefaction Array. Average horizontal spectrum (Figure 9a) based on simulated motions used as control motions.

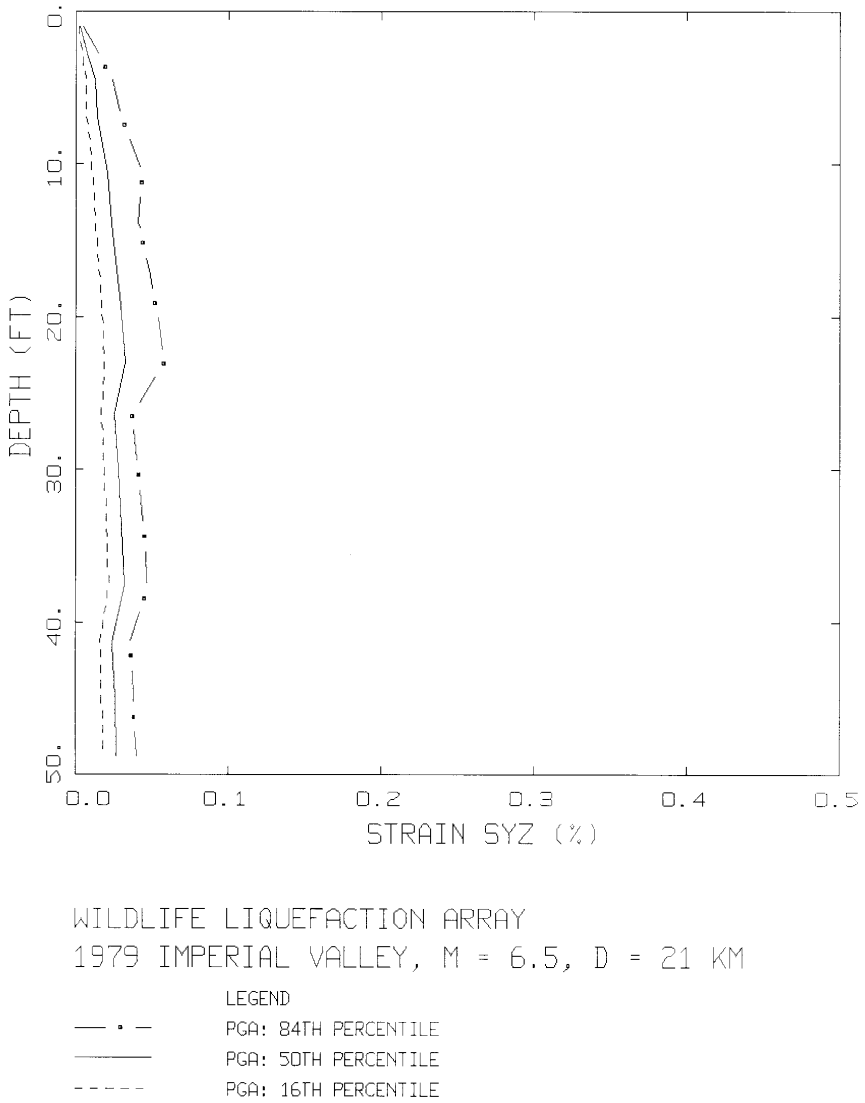


Figure 9f. Variation of peak shear strain(%) verses depth computed for a suite of random profiles at the Wildlife Liquefaction Array. Average horizontal spectrum (Figure 9a) based on simulated motions used as control motions.

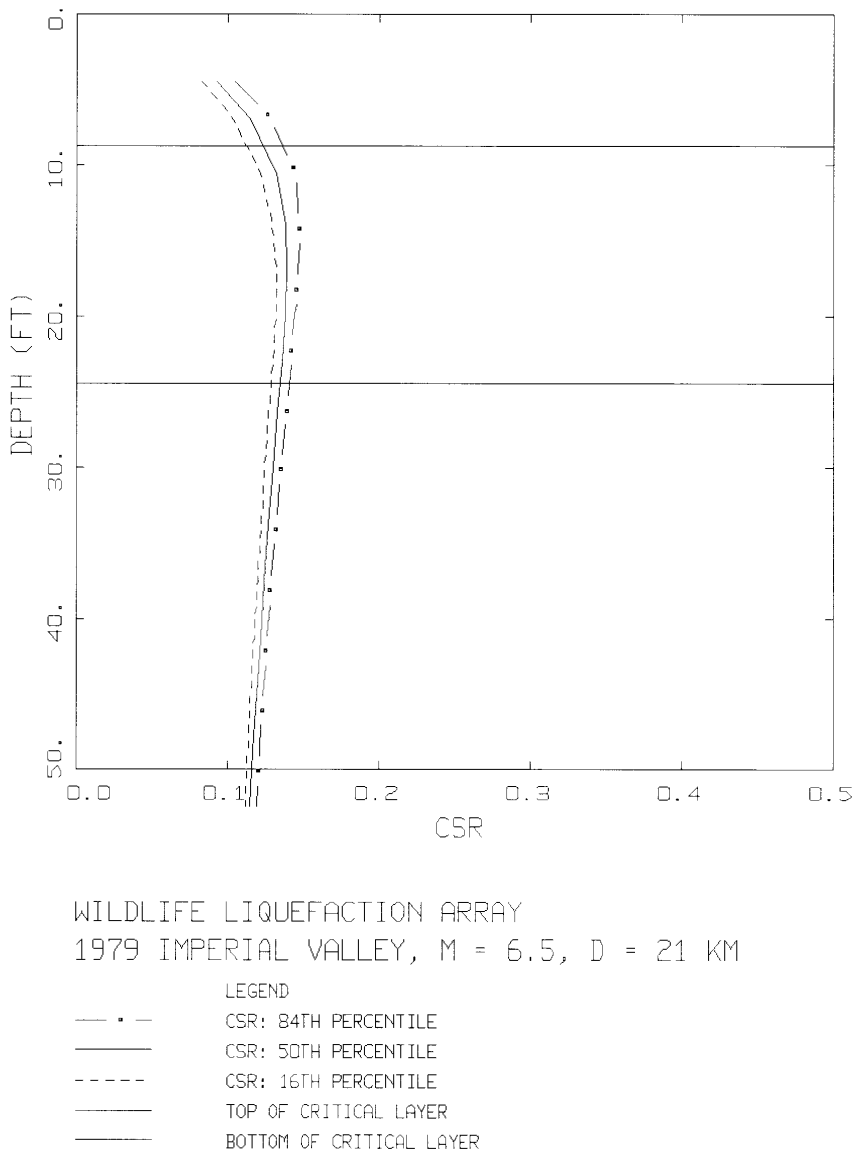


Figure 9g. Variation of CSR verses depth computed for a suite of random profiles for at Wildlife Liquefaction Array. Average horizontal spectrum (Figure 9a) based on simulated motions used as control motions. Critical layer indicated with horizontal lines.

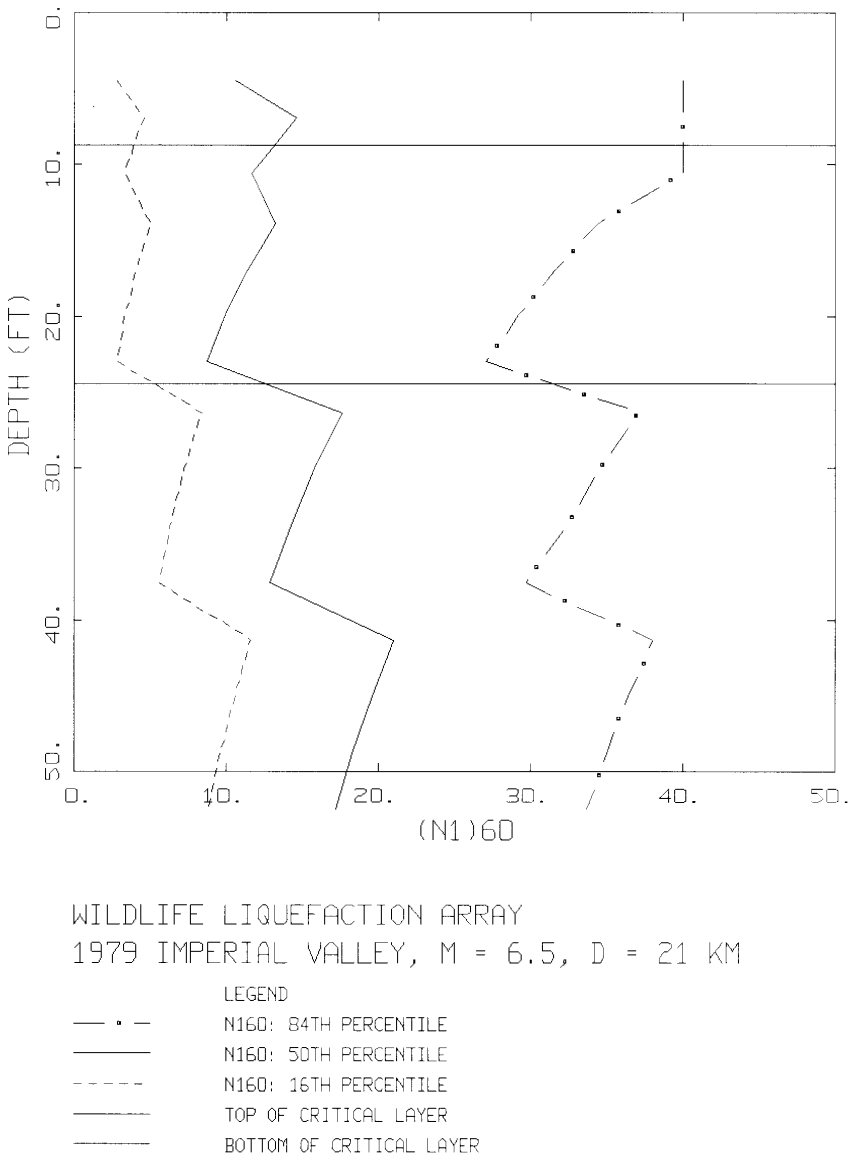


Figure 9h. Variation of peak $(N_1)_{60}$ verses depth computed for a suite of random profiles at the Wildlife Liquefaction Array using the shear-wave velocity correlation model of Iwasaki et al., (1987). Average horizontal spectrum (Figure 9a) based on simulated motions used as control motions. Critical layer indicated with horizontal lines.

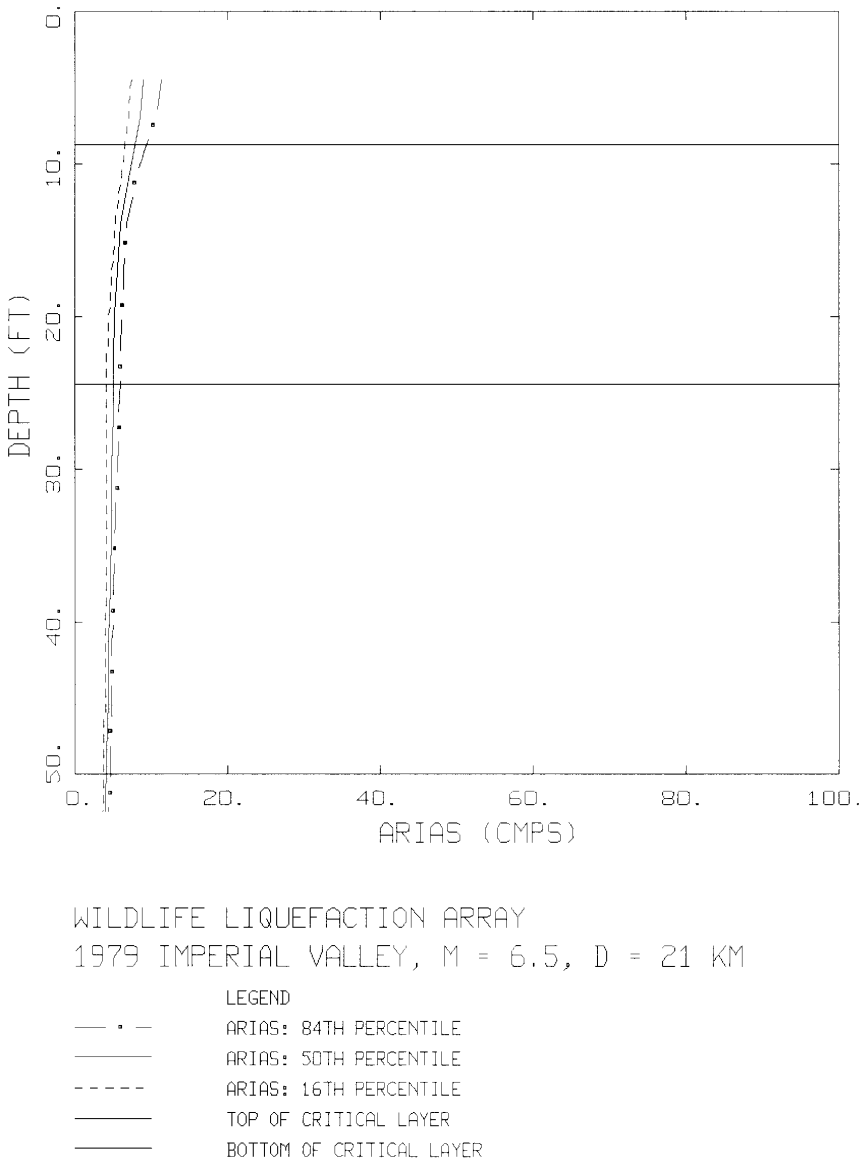


Figure 9i. Variation of Arias Intensity (cm/sec) verses depth computed for a suite of random profiles at the Wildlife Liquefaction Array. Average horizontal spectrum (Figure 9a) based on simulated motions used as control motions. Critical layer indicated with horizontal lines.

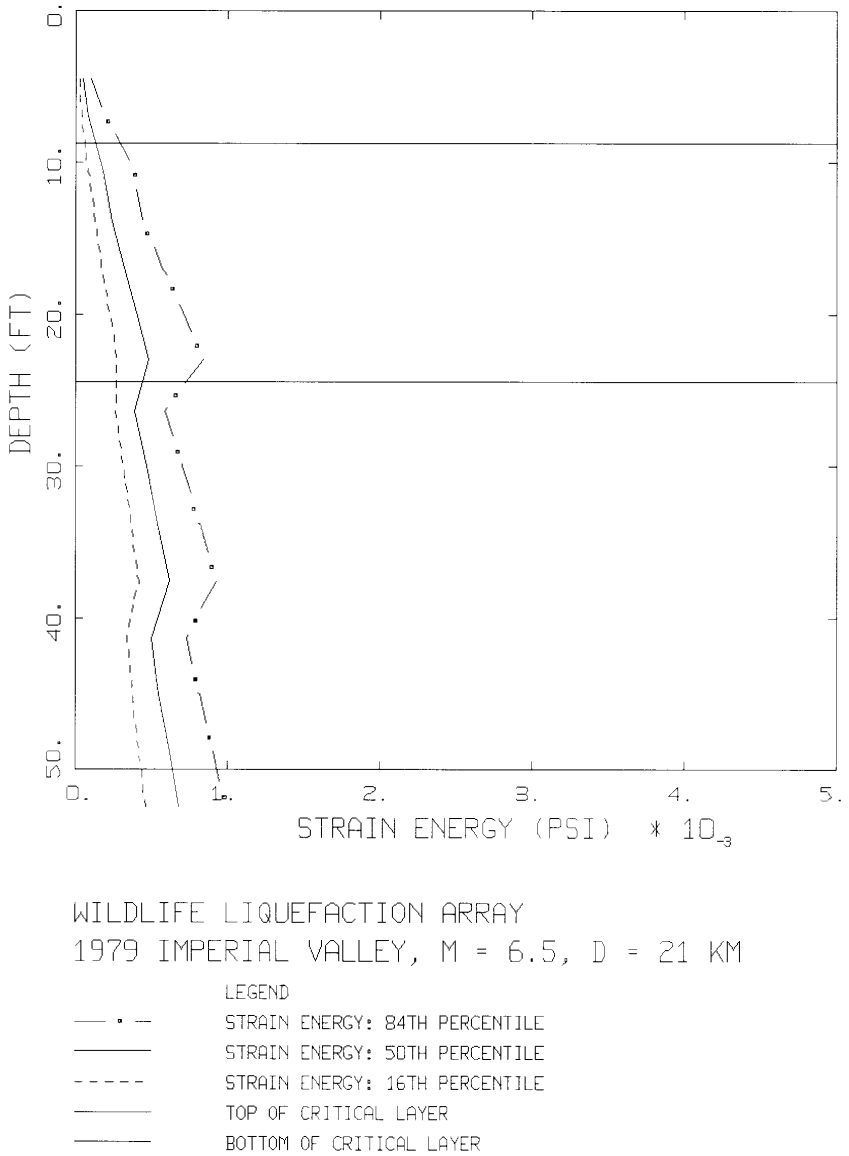


Figure 9j Variation of strain energy (PSI) verses depth computed for a suite of random profiles at the Wildlife Liquefaction Array. Average horizontal spectrum (Figure 9a) based on simulated motions used as control motions. Critical layer indicated with horizontal lines.

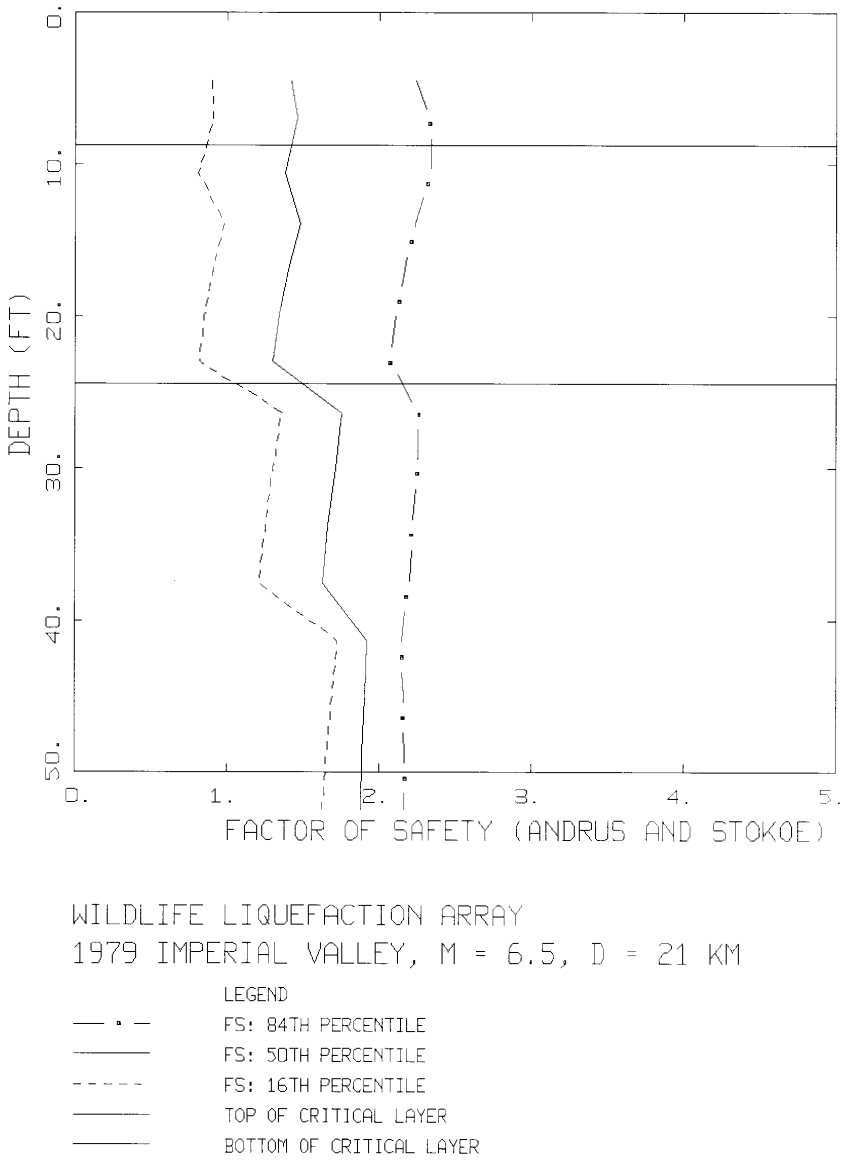


Figure 9k. Variation of the factor of safety (FS) using the Andrus and Stokoe (2004) shear-wave velocity based approach verses depth computed for a suite of random profiles at the Wildlife Liquefaction Array. Average horizontal spectrum (Figure 9a) based on simulated motions used as control motions. Critical layer indicated with horizontal lines.

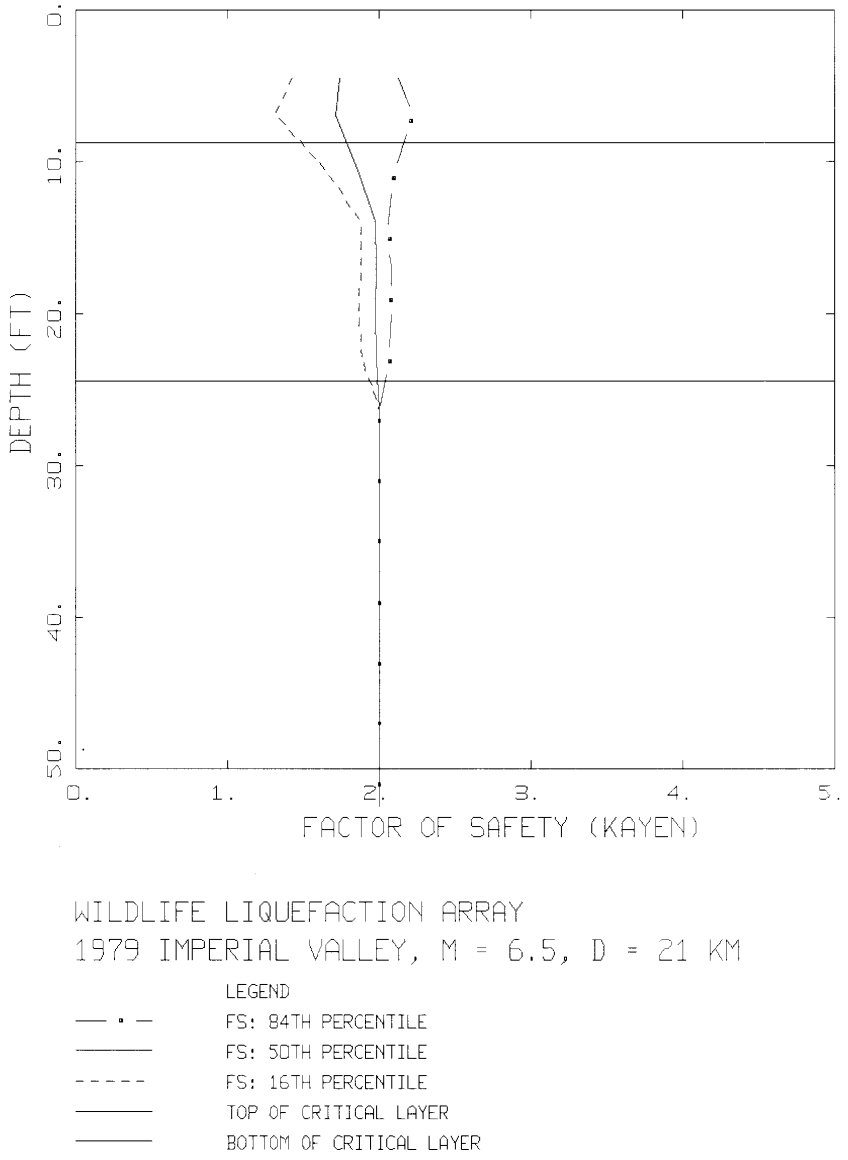


Figure 9l. Variation of the factor of safety using the Kayen and Mitchell (1999) Arias Intensity based approach verses depth computed for a suite of random profiles at the Wildlife Liquefaction Array. Average horizontal spectrum (Figure 9a) based on simulated motions used as control motions. Critical layer indicated with horizontal lines

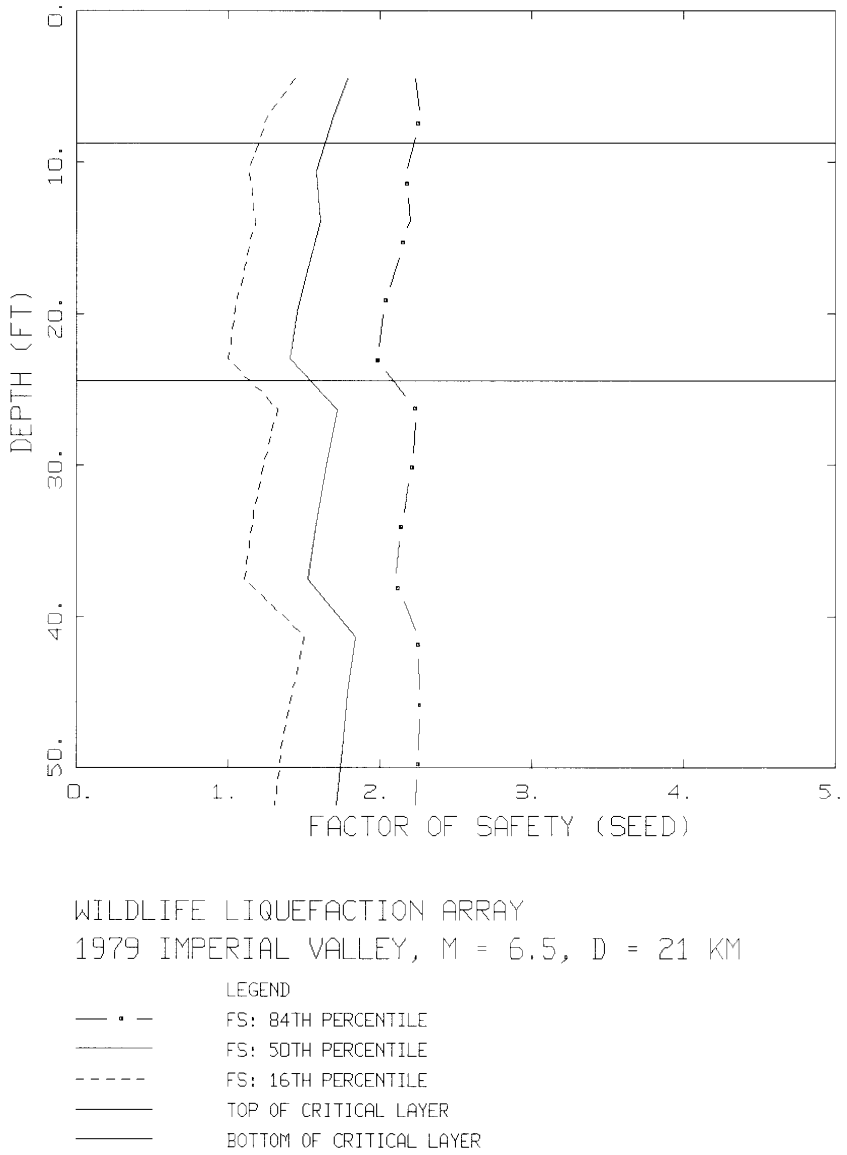


Figure 9m. Variation of the factor of the factor of safety using the Seed et al., (2002) SPT based approach verses depth computed for a suite of random profiles at the Wildlife Liquefaction Array. Average horizontal spectrum (Figure 9a) based on simulated motions used as control motions. Critical layer indicated with horizontal lines.

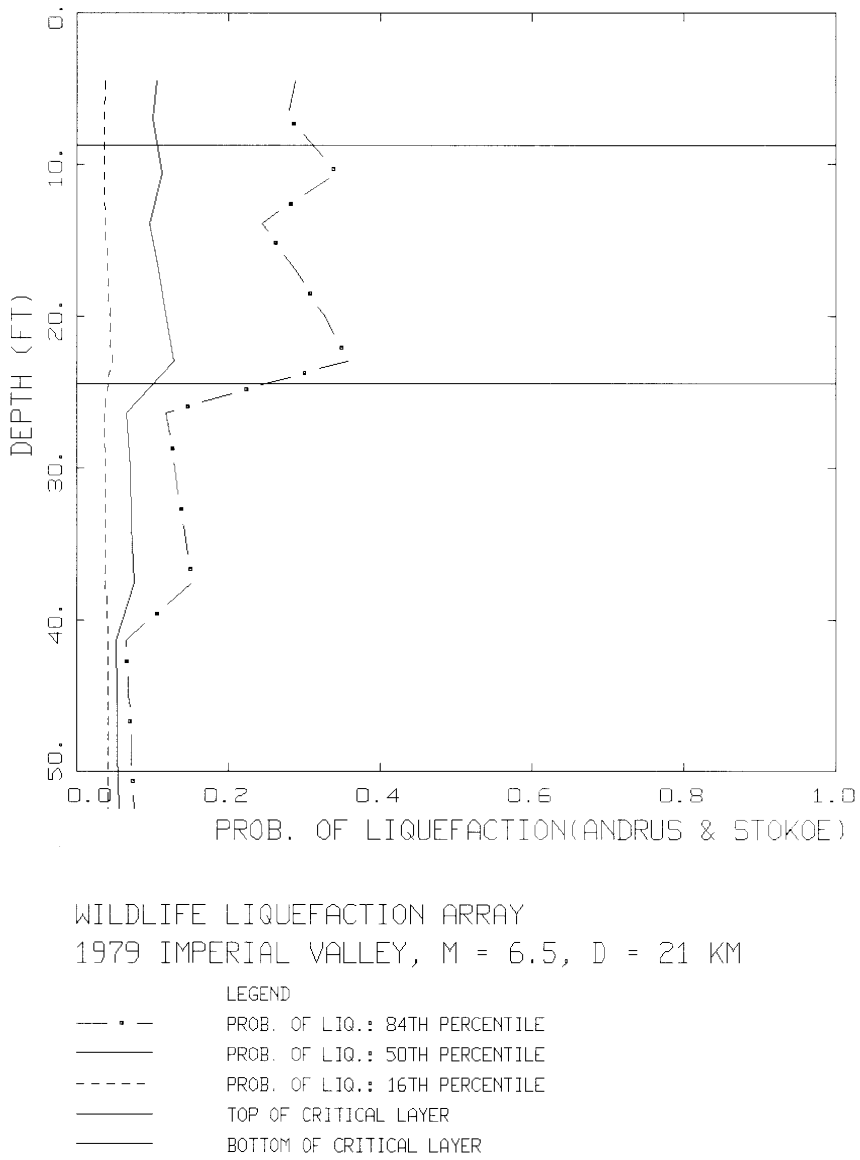


Figure 9n. Variation of the probability of liquefaction using the Andrus and Stokoe (2004) shear-wave velocity based approach verses depth computed for a suite of random profiles at the Wildlife Liquefaction Array. Average horizontal spectrum (Figure 9a) based on simulated motions used as control motions. Critical layer indicated with horizontal lines.

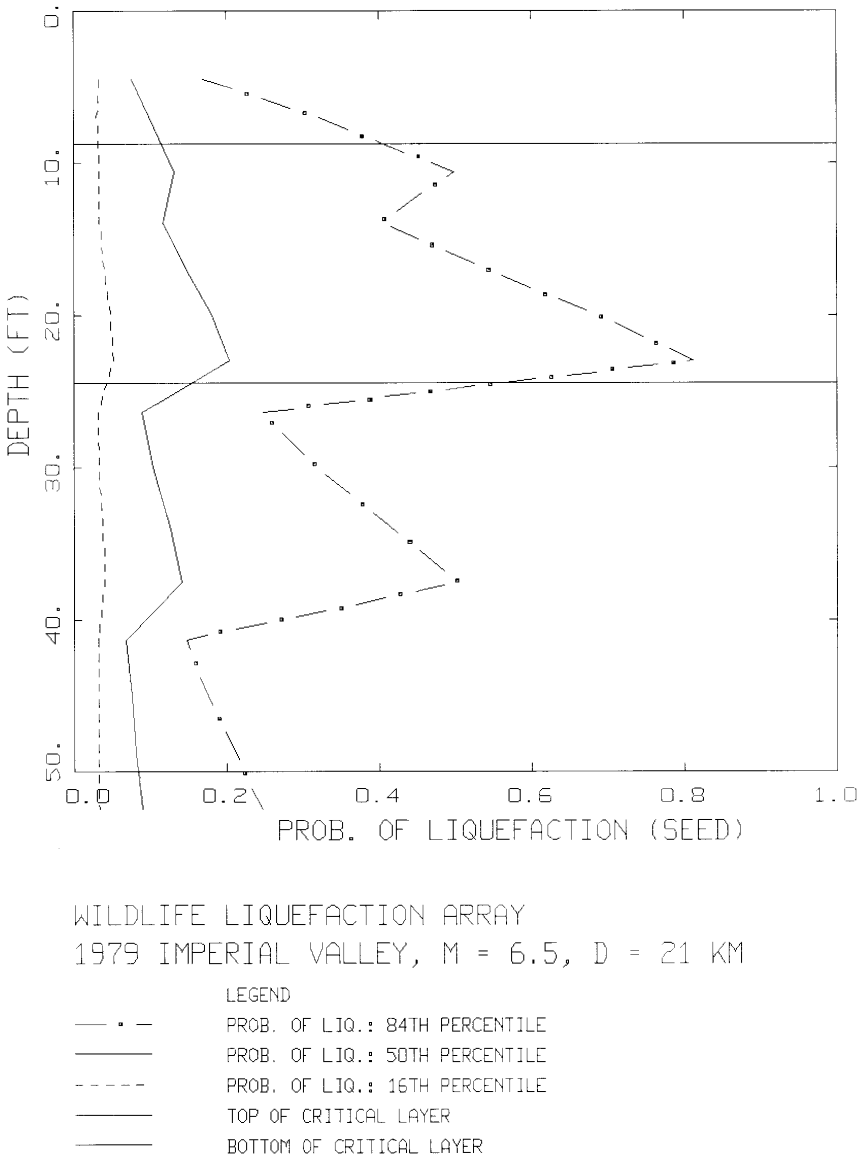


Figure 9o. Variation probability of liquefaction using the Seed et al. (2002) SPT based approach verses depth computed for a suite of random profiles at the Wildlife Liquefaction Array. Average horizontal spectrum (Figure 9a) based on simulated motions used as control motions. Critical layer indicated with horizontal lines.

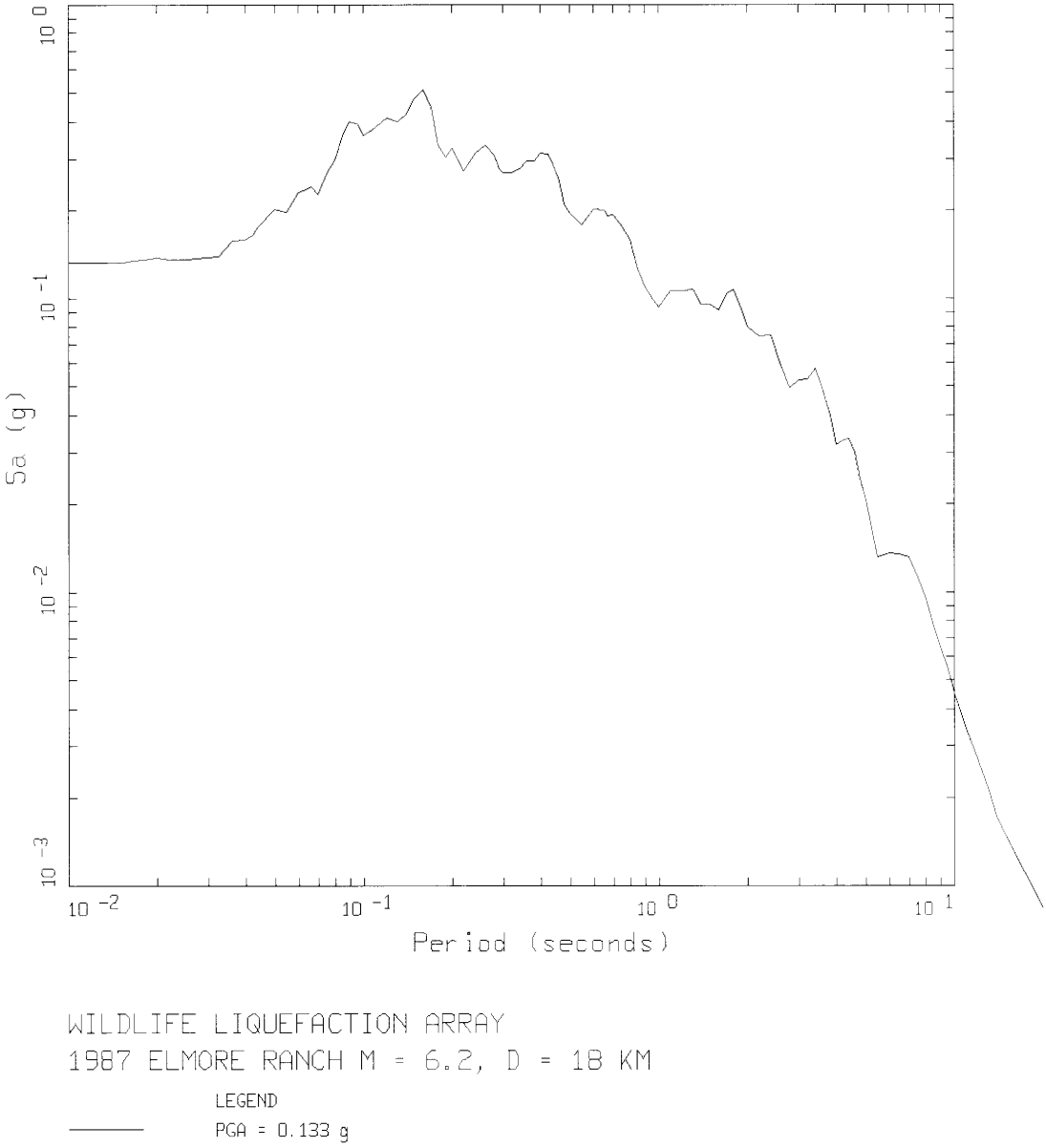


Figure 10a. Average horizontal component response spectra computed from recorded motions: Wildlife Liquefaction Array, 1987 Elmore Ranch earthquake.

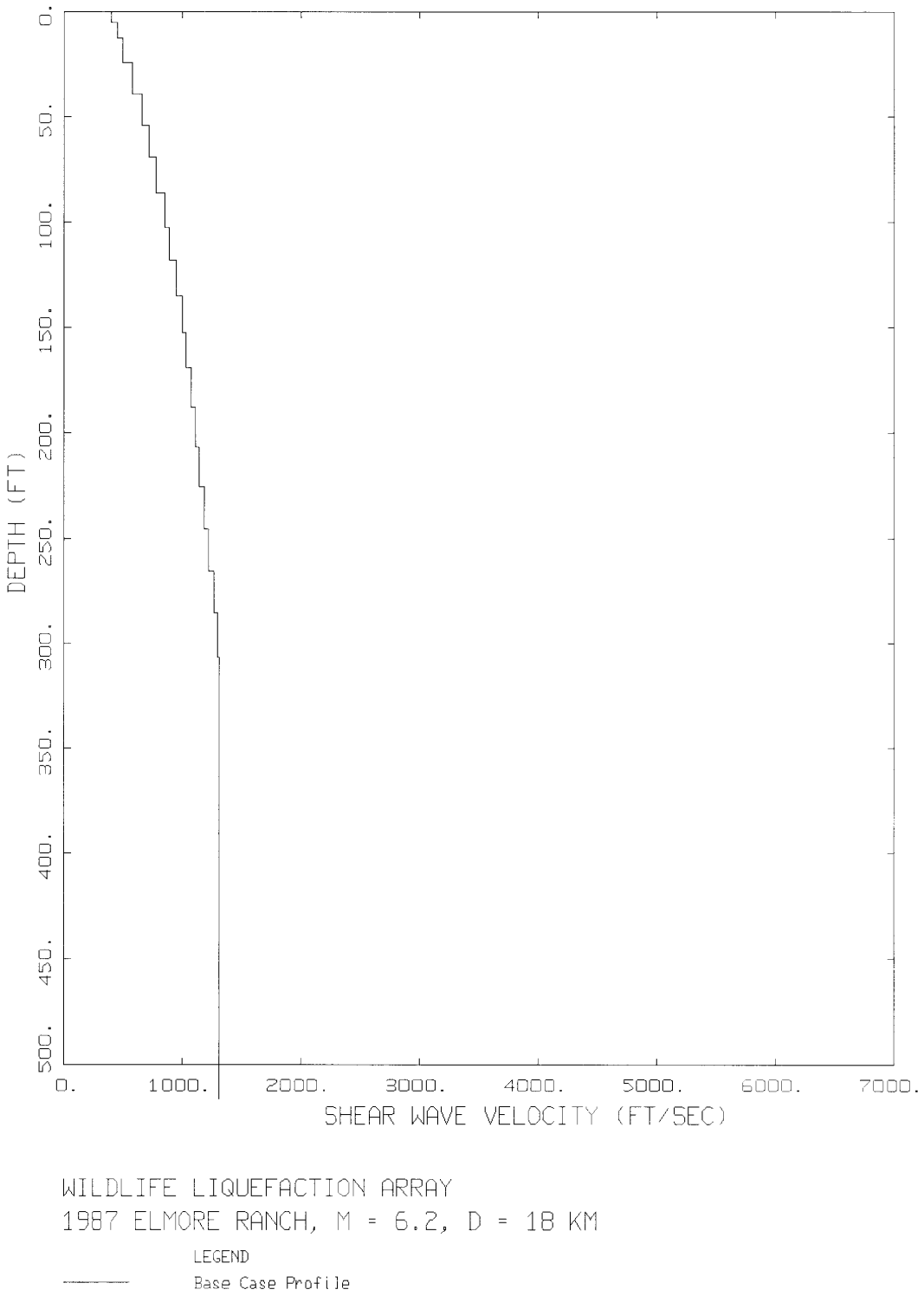


Figure 10b. Shear-wave velocity profile (assumed) at the Wildlife Liquefaction Array to a depth of 500 ft.

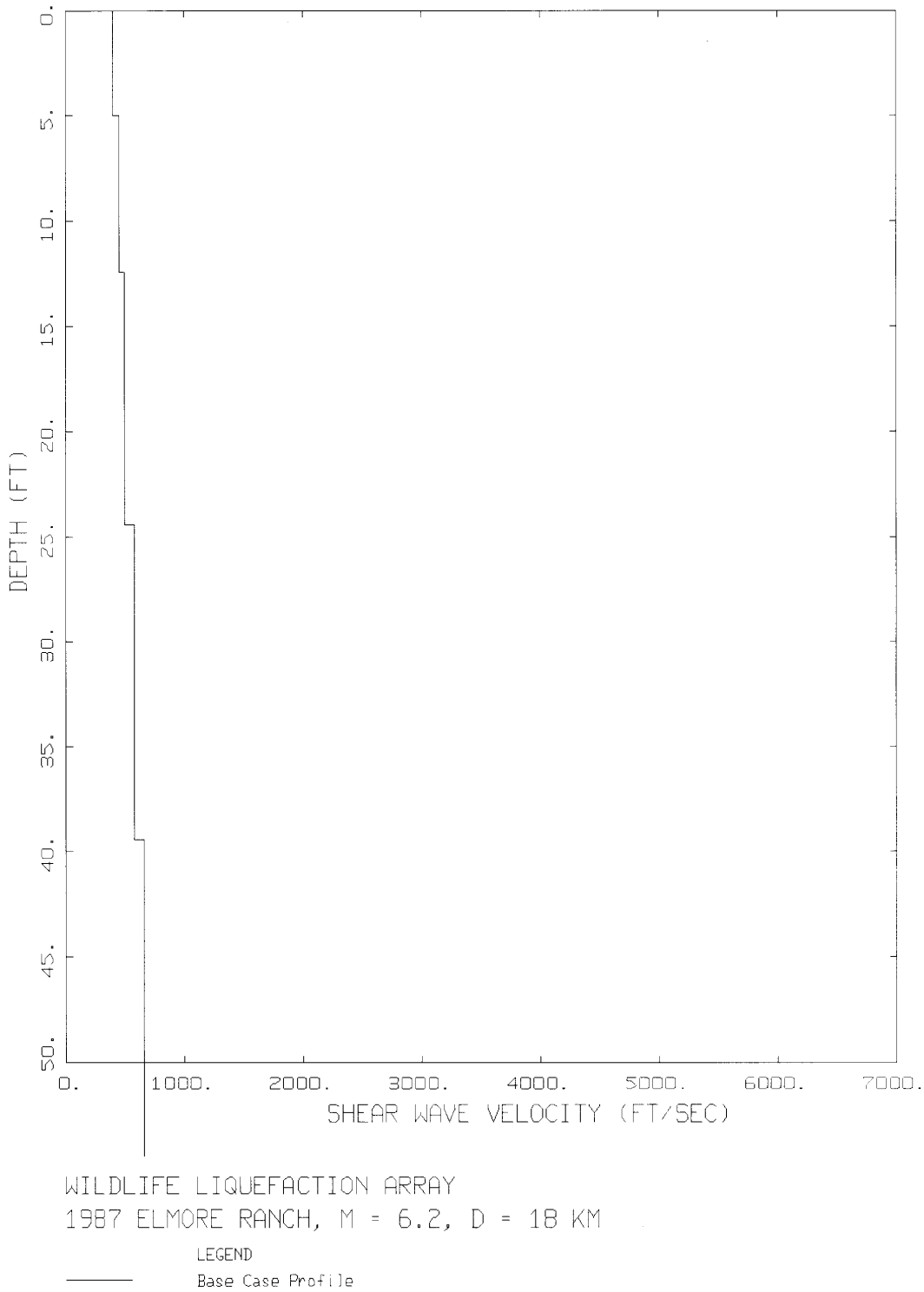


Figure 10c. Shear-wave velocity profile (assumed) at the Wildlife Liquefaction Array to a depth of 50 ft.

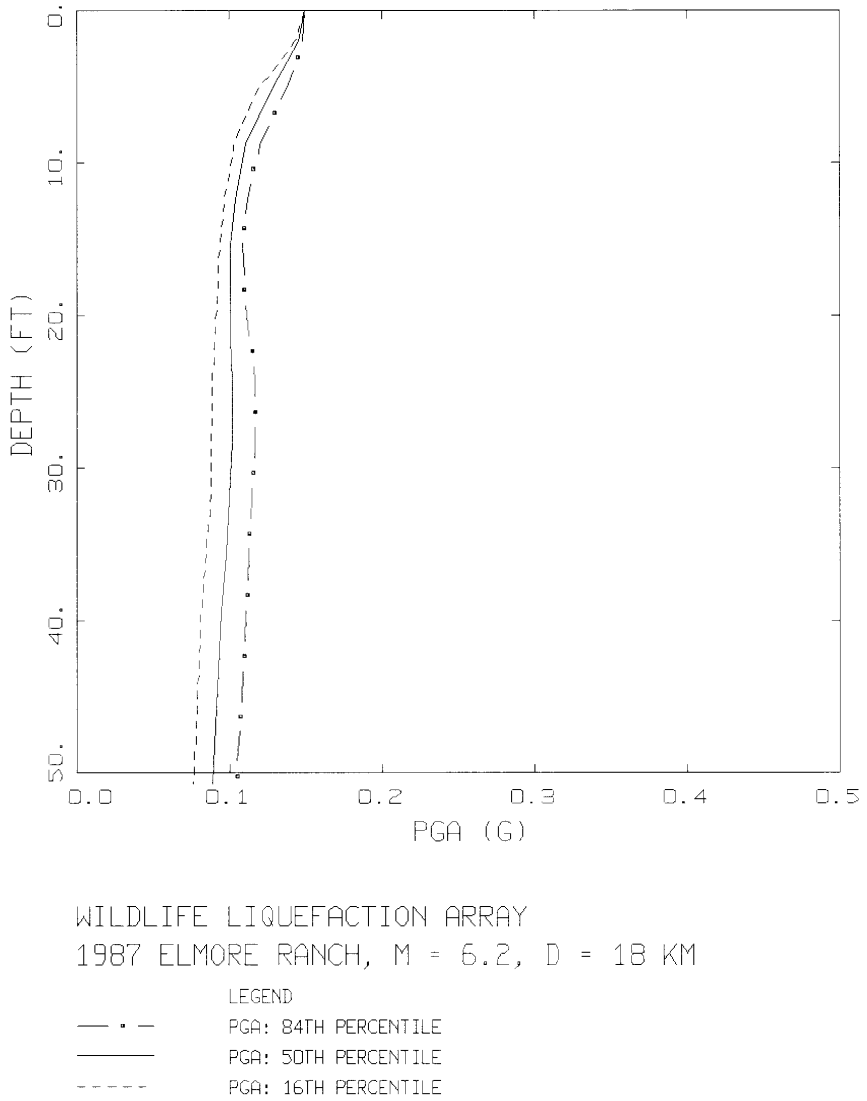


Figure 10d. Variation of peak acceleration(g) (Average horizontal component) verses depth computed for a suite of random profiles at the Wildlife Liquefaction Array. Average horizontal spectrum (Figure 10a) based on recorded motions used as control motions.

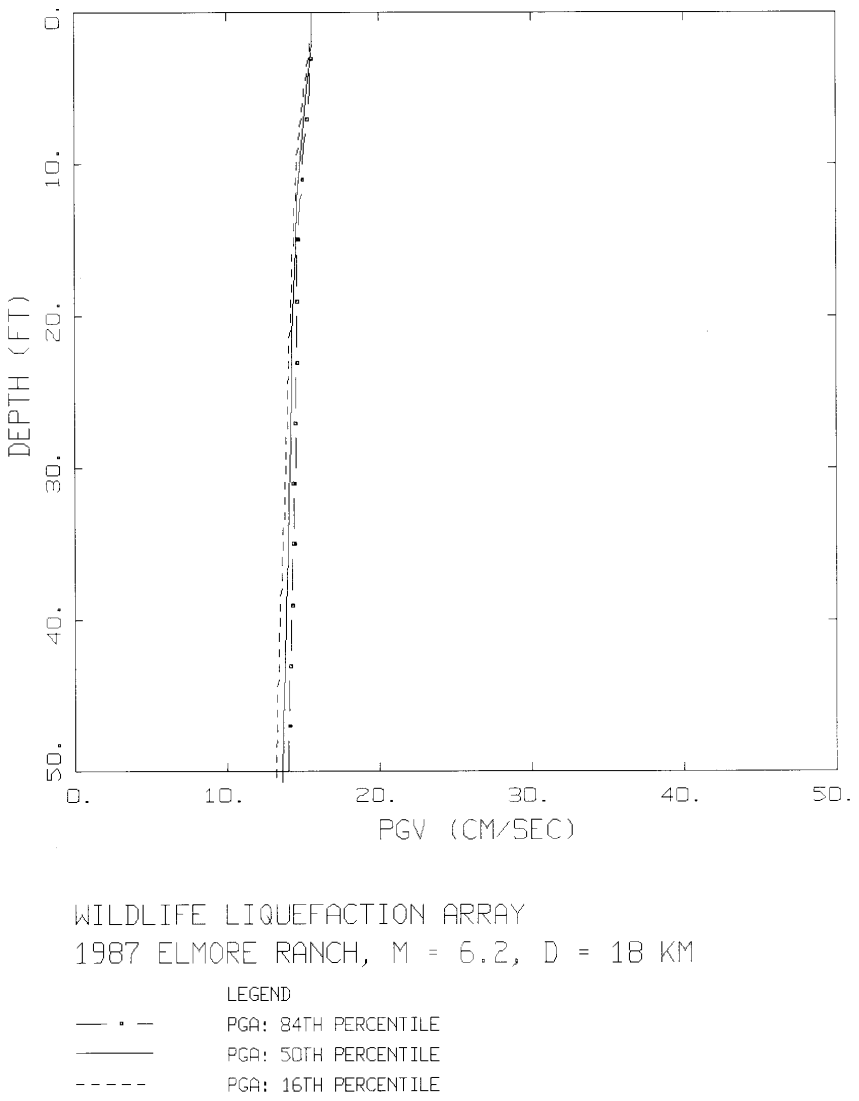


Figure 10e. Variation of peak particle velocity (cm/sec) verses depth computed for a suite of random profiles at the Wildlife Liquefaction Array. Average horizontal spectrum (Figure 10a) based on recorded motions used as control motions.

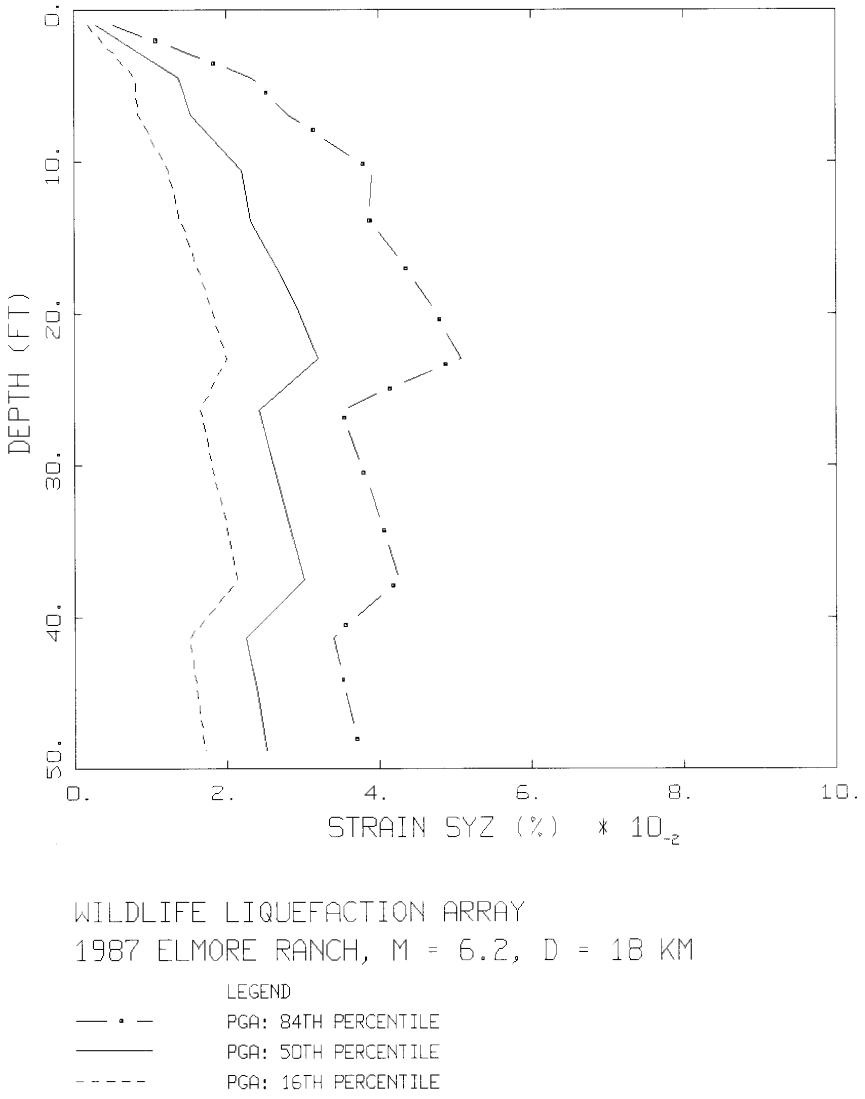


Figure 10f. Variation of peak shear strain(%) verses depth computed for a suite of random profiles at the Wildlife Liquefaction Array. Average horizontal spectrum (Figure 10a) based on recorded motions used as control motions.

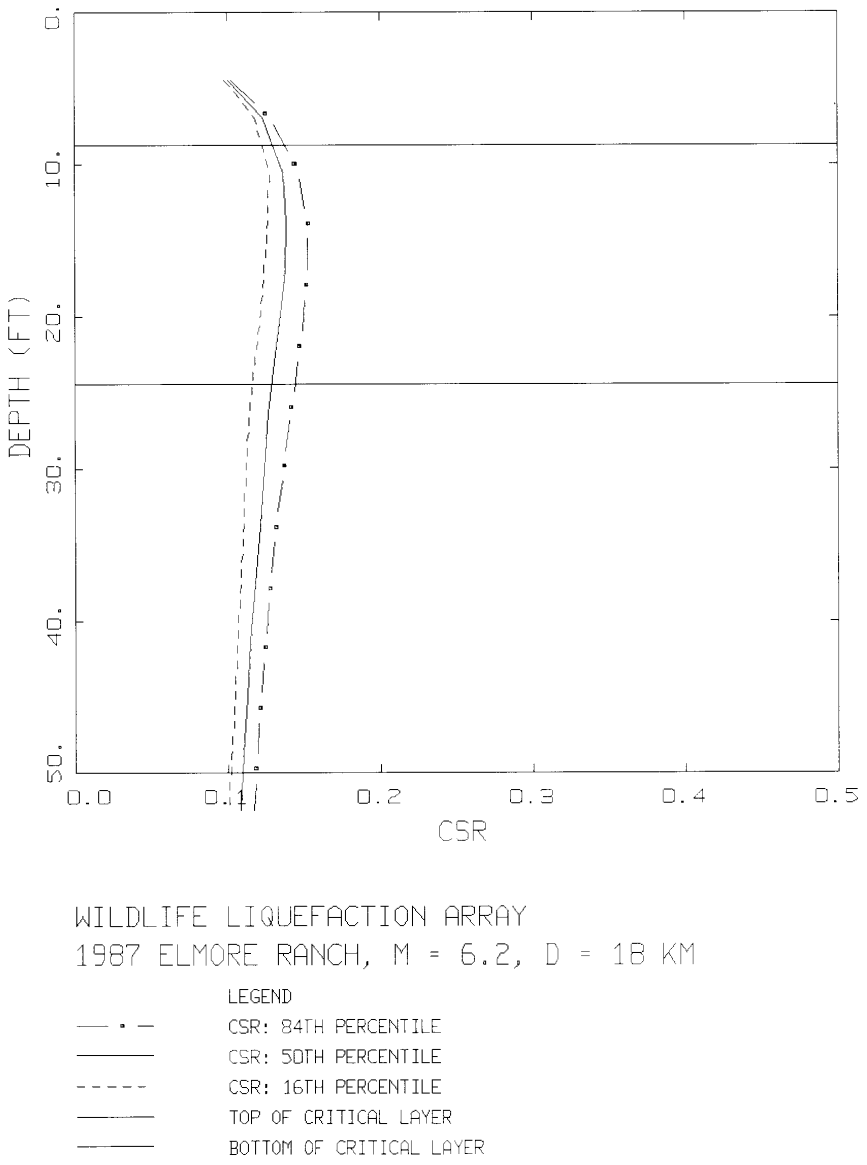


Figure 10g. Variation of CSR verses depth computed for a suite of random profiles for at Wildlife Liquefaction Array. Average horizontal spectrum (Figure 10a) based on recorded motions used as control motions. Critical layer indicated with horizontal lines.

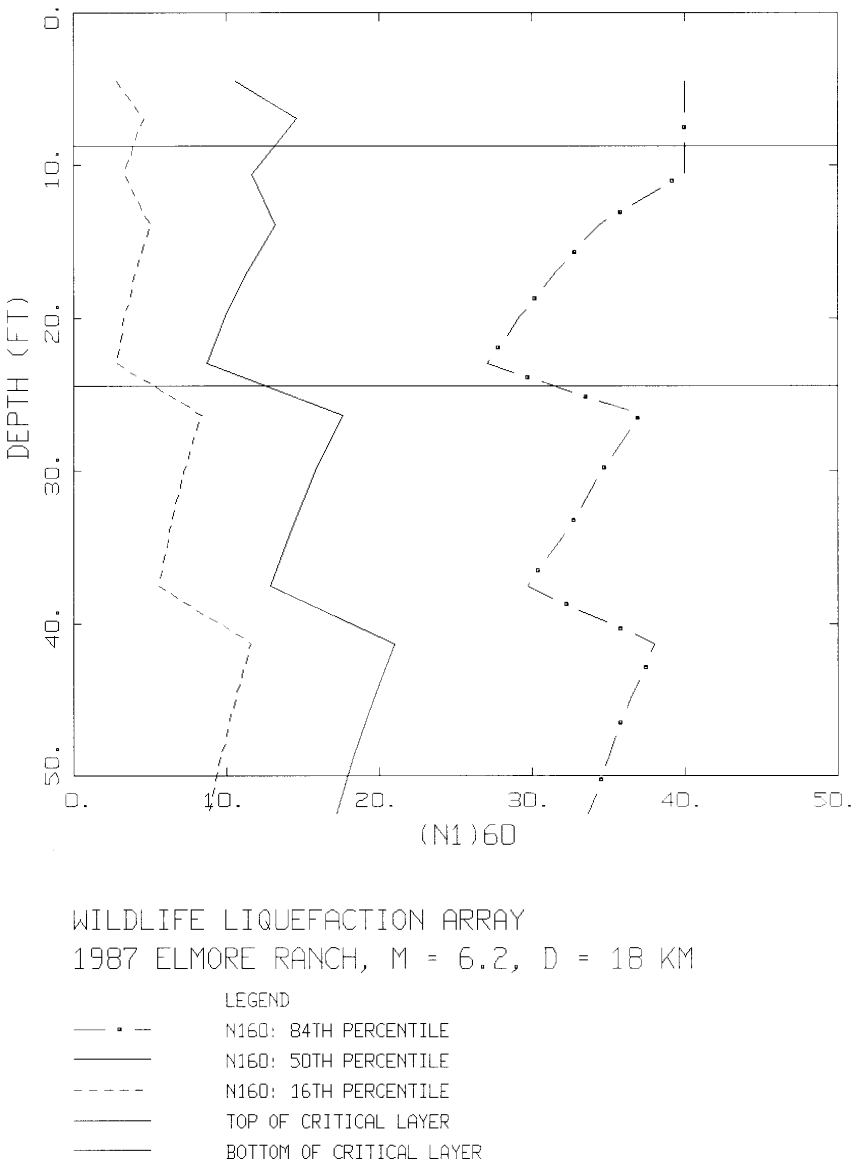


Figure 10h. Variation of peak $(N_1)_{60}$ verses depth computed for a suite of random profiles at the Wildlife Liquefaction Array using the shear-wave velocity correlation model of Iwasaki et al., (1988). Average horizontal spectrum (Figure 10a) based on recorded motions used as control motions. Critical layer indicated with horizontal lines.

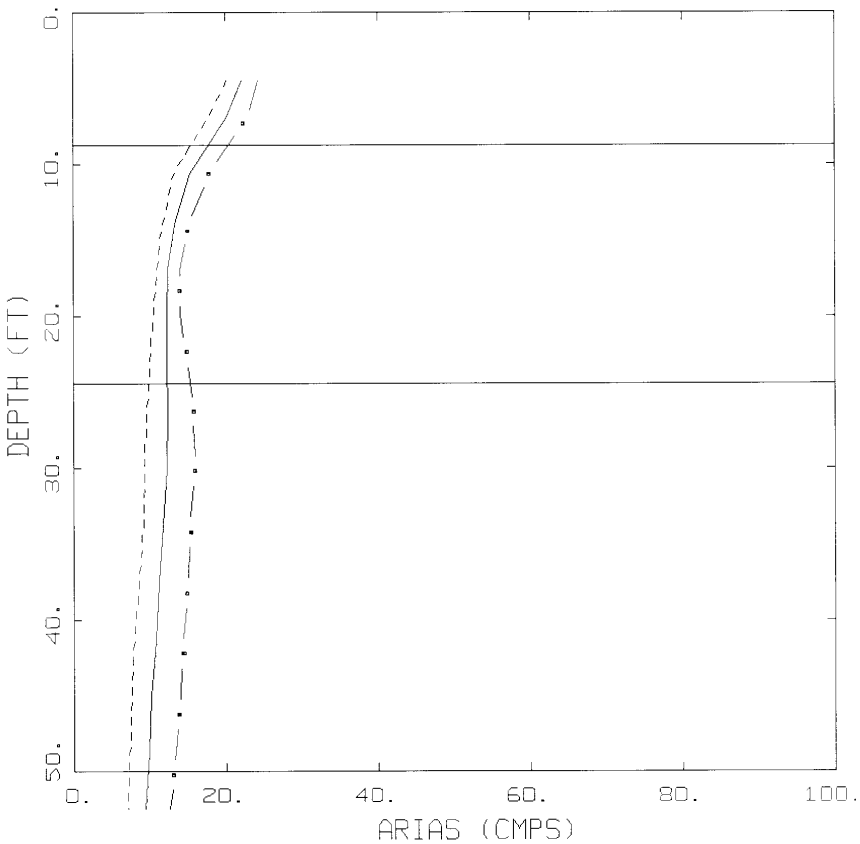


WILDLIFE LIQUEFACTION ARRAY
1987 ELMORE RANCH, M = 6.2, D = 18 KM

LEGEND

| | |
|---|---|
| — · — | ARIAS: 84TH PERCENTILE |
| ——— | ARIAS: 50TH PERCENTILE |
| - - - - - | ARIAS: 16TH PERCENTILE |
| ——— | TOP OF CRITICAL LAYER |
| ——— | BOTTOM OF CRITICAL LAYER |

Figure 10i. Variation of Arias Intensity (cm/sec) verses depth computed for a suite of random profiles at the Wildlife Liquefaction Array. Average horizontal spectrum (Figure 10a) based on recorded motions used as control motions. Critical layer indicated with horizontal lines.

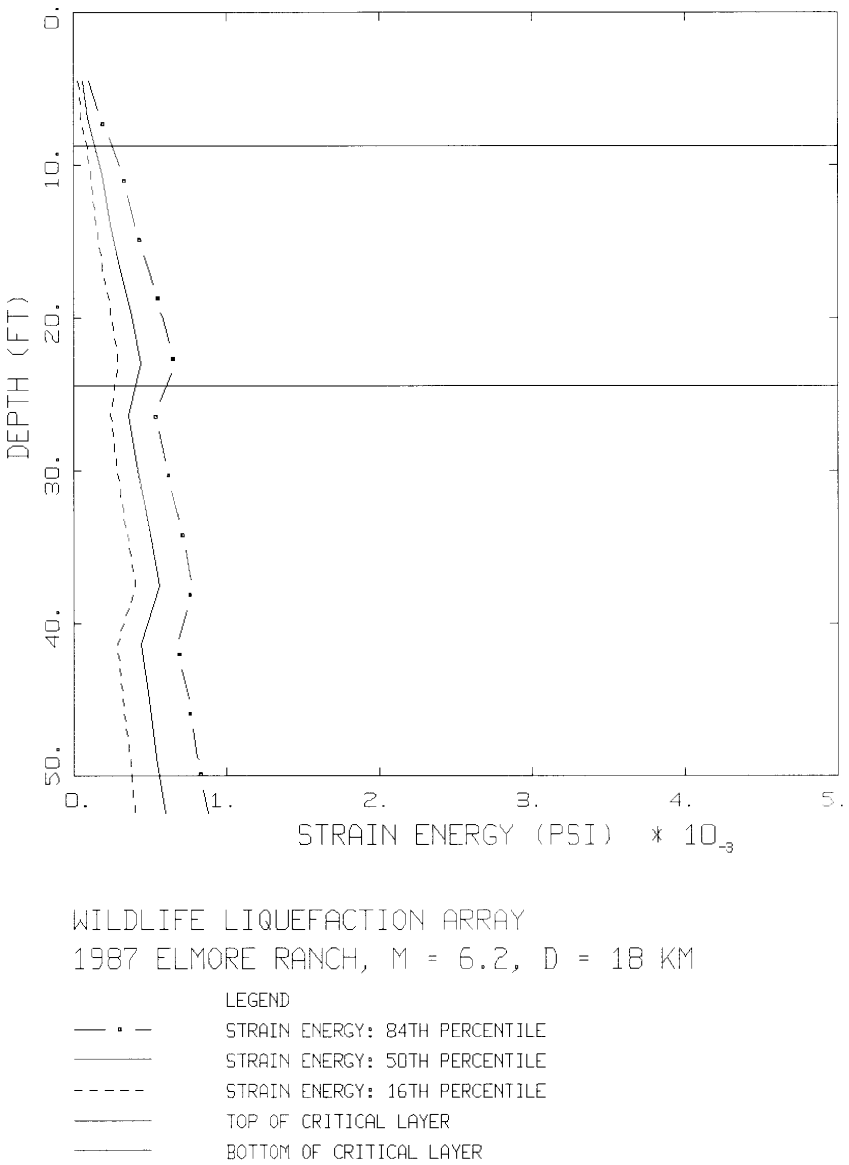


Figure 10j Variation of strain energy (PSI) verses depth computed for a suite of random profiles at the Wildlife Liquefaction Array. Average horizontal spectrum (Figure 10a) based on recorded motions used as control motions. Critical layer indicated with horizontal lines.

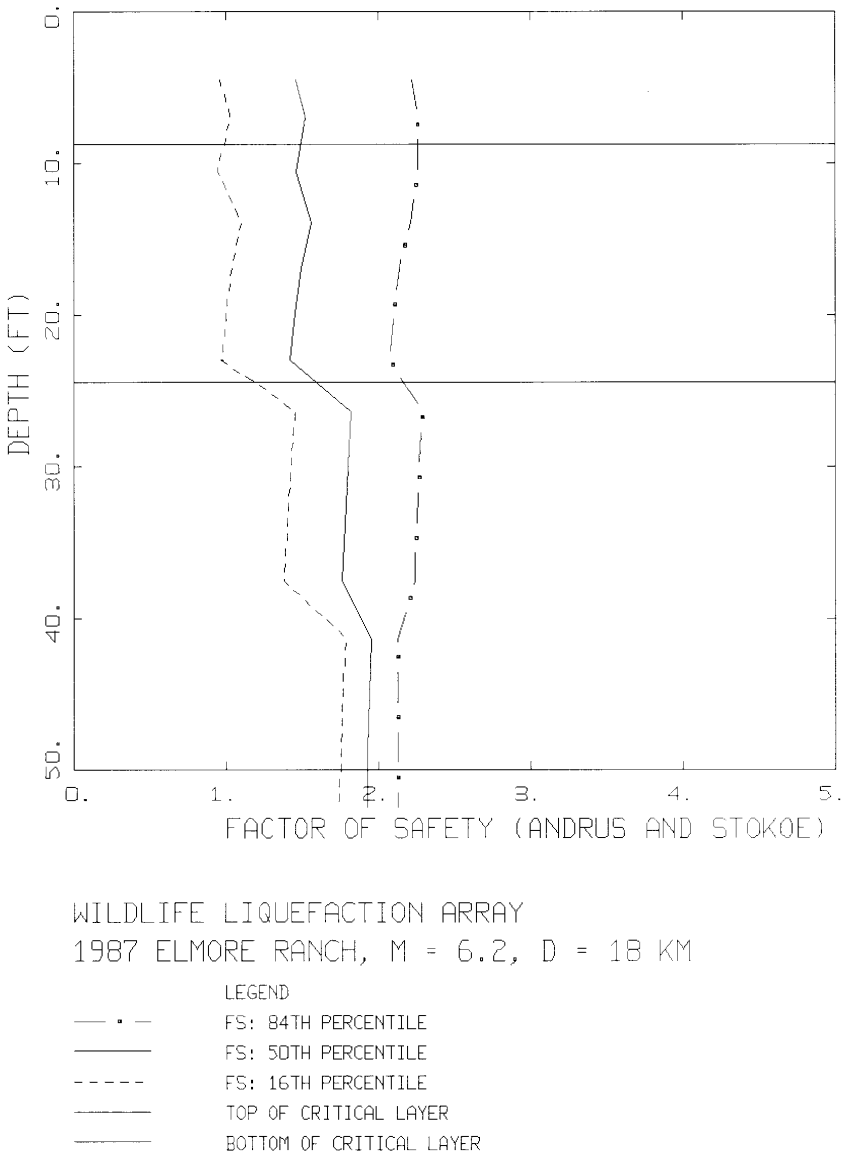


Figure 10k. Variation of the factor of safety (FS) using the Andrus and Stokoe (2004) shear-wave velocity based approach verses depth computed for a suite of random profiles at the Wildlife Liquefaction Array. Average horizontal spectrum (Figure 10a) based on recorded motions used as control motions. Critical layer indicated with horizontal lines.

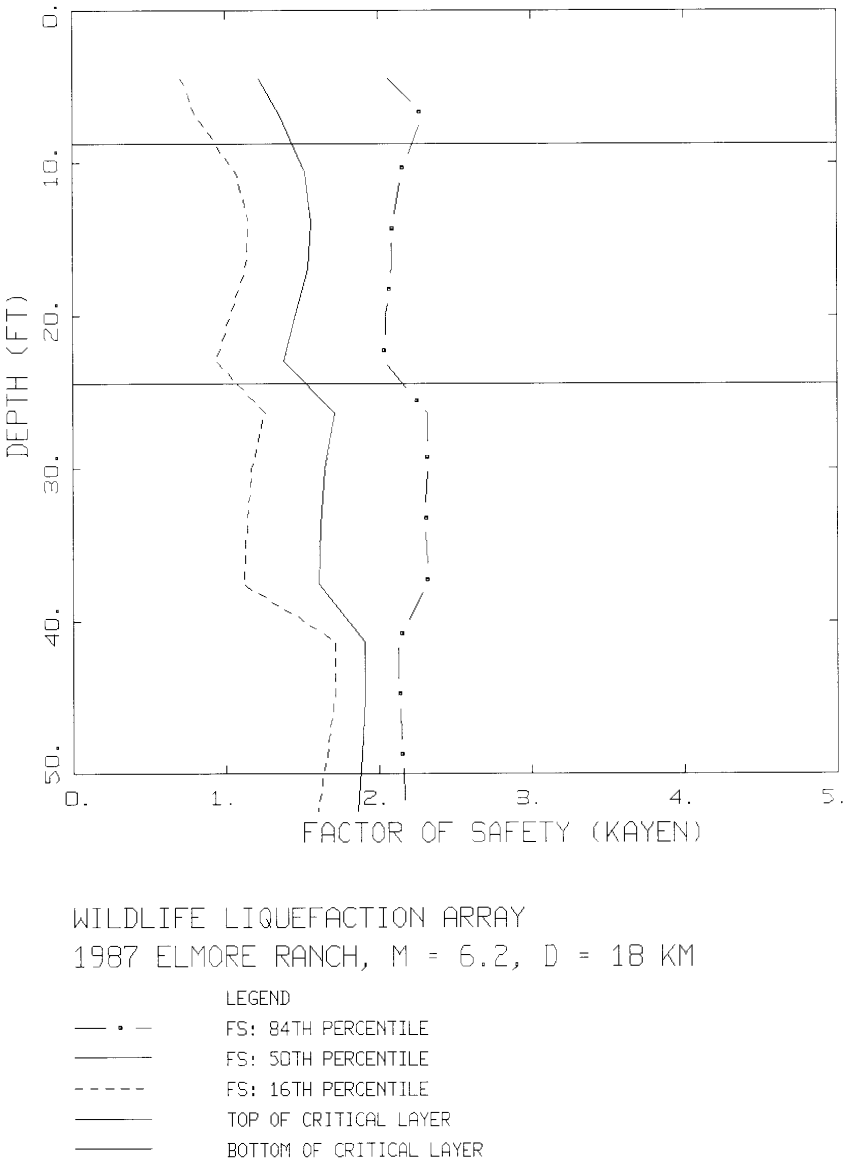


Figure 10l. Variation of the factor of safety using the Kayen and Mitchell (1999) Arias Intensity based approach verses depth computed for a suite of random profiles at the Wildlife Liquefaction Array. Average horizontal spectrum (Figure 10a) based on recorded motions used as control motions. Critical layer indicated with horizontal lines.

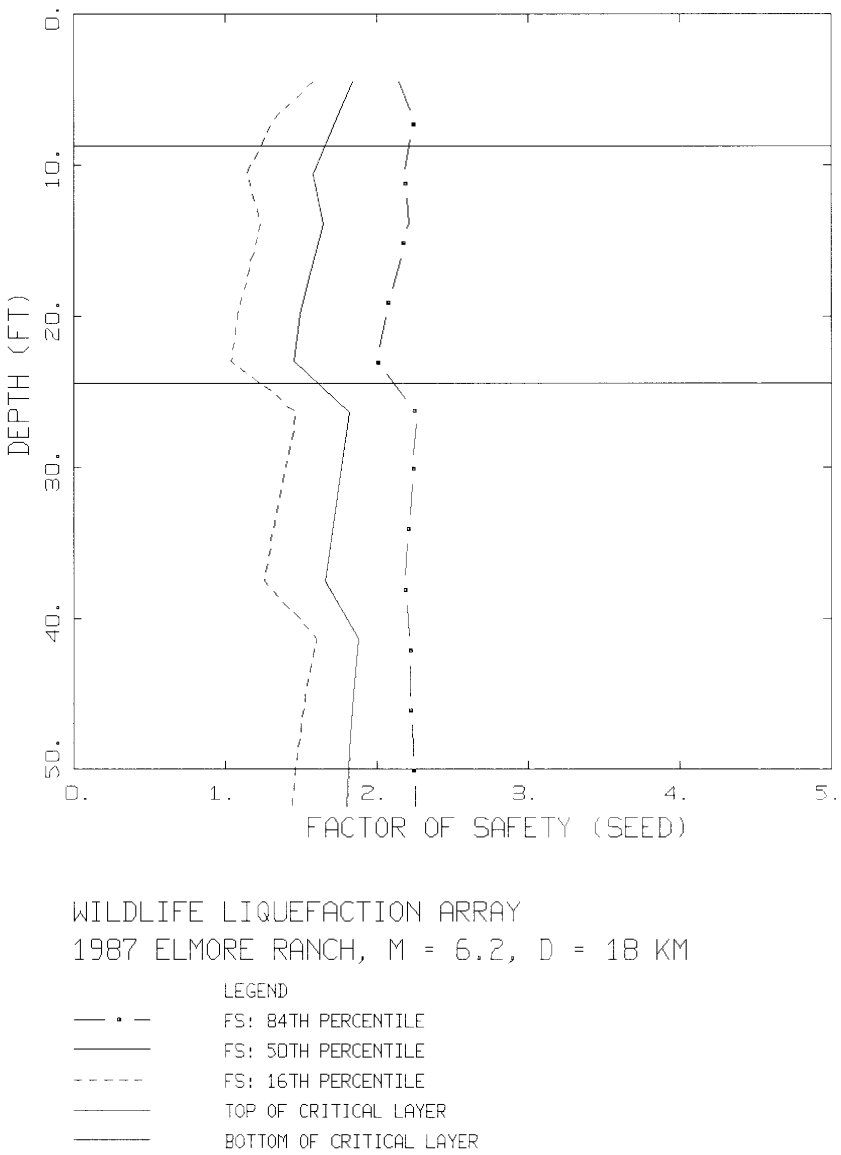


Figure 10m. Variation of the factor of the factor of safety using the Seed et al., (2002) SPT based approach verses depth computed for a suite of random profiles at the Wildlife Liquefaction Array. Average horizontal spectrum (Figure 10a) based on recorded motions used as control motions. Critical layer indicated with horizontal lines.

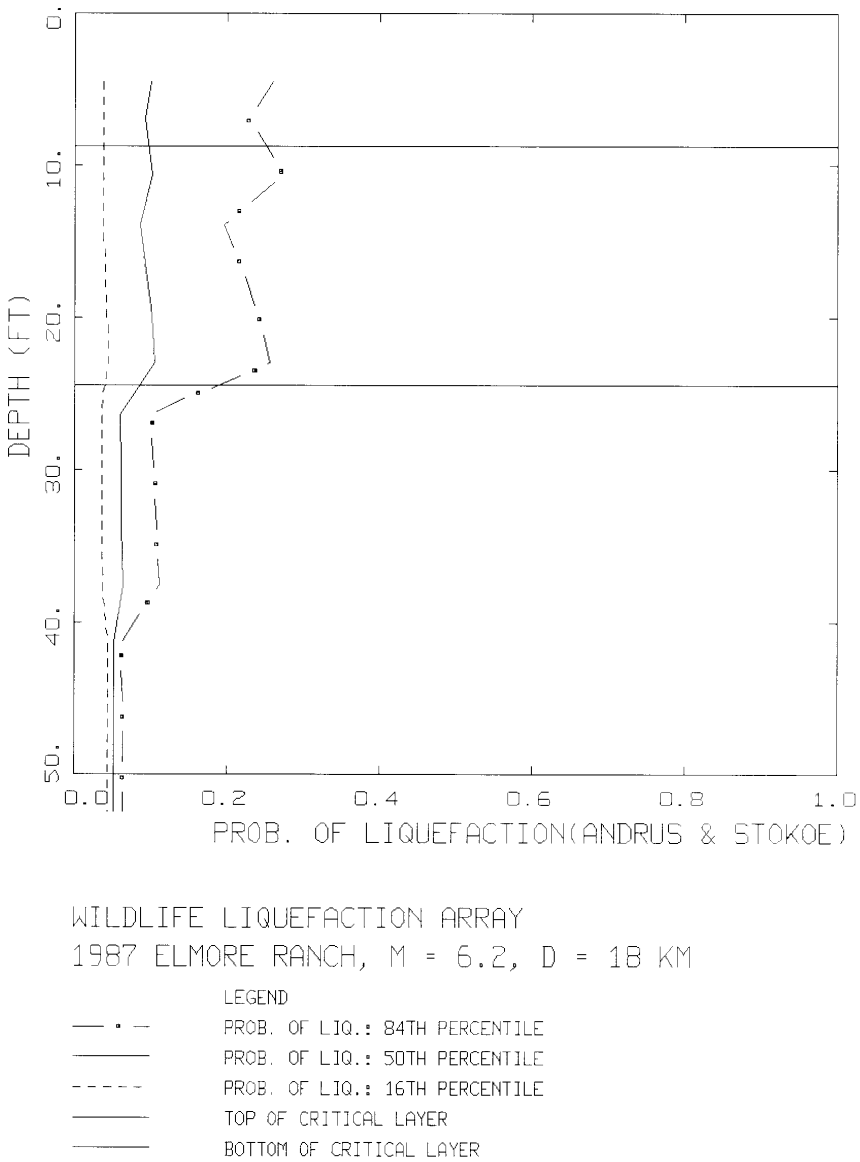


Figure 10n. Variation of the probability of liquefaction using the Andrus and Stokoe (2004) shear-wave velocity based approach verses depth computed for a suite of random profiles at the Wildlife Liquefaction Array. Average horizontal spectrum (Figure 10a) based on recorded motions used as control motions. Critical layer indicated with horizontal lines.

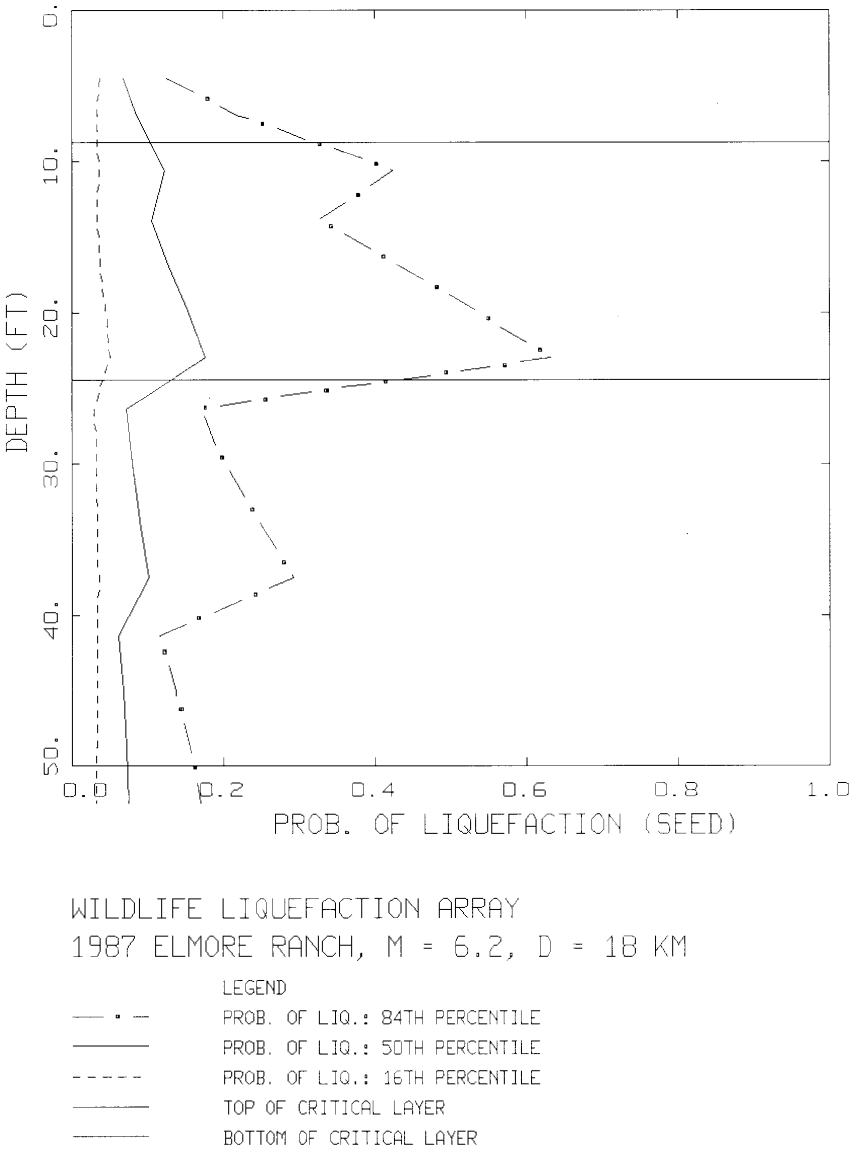


Figure 10o. Variation probability of liquefaction using the Seed et al. (2002) SPT based approach verses depth computed for a suite of random profiles at the Wildlife Liquefaction Array. Average horizontal spectrum (Figure 10a) based on recorded motions used as control motions. Critical layer indicated with horizontal lines.

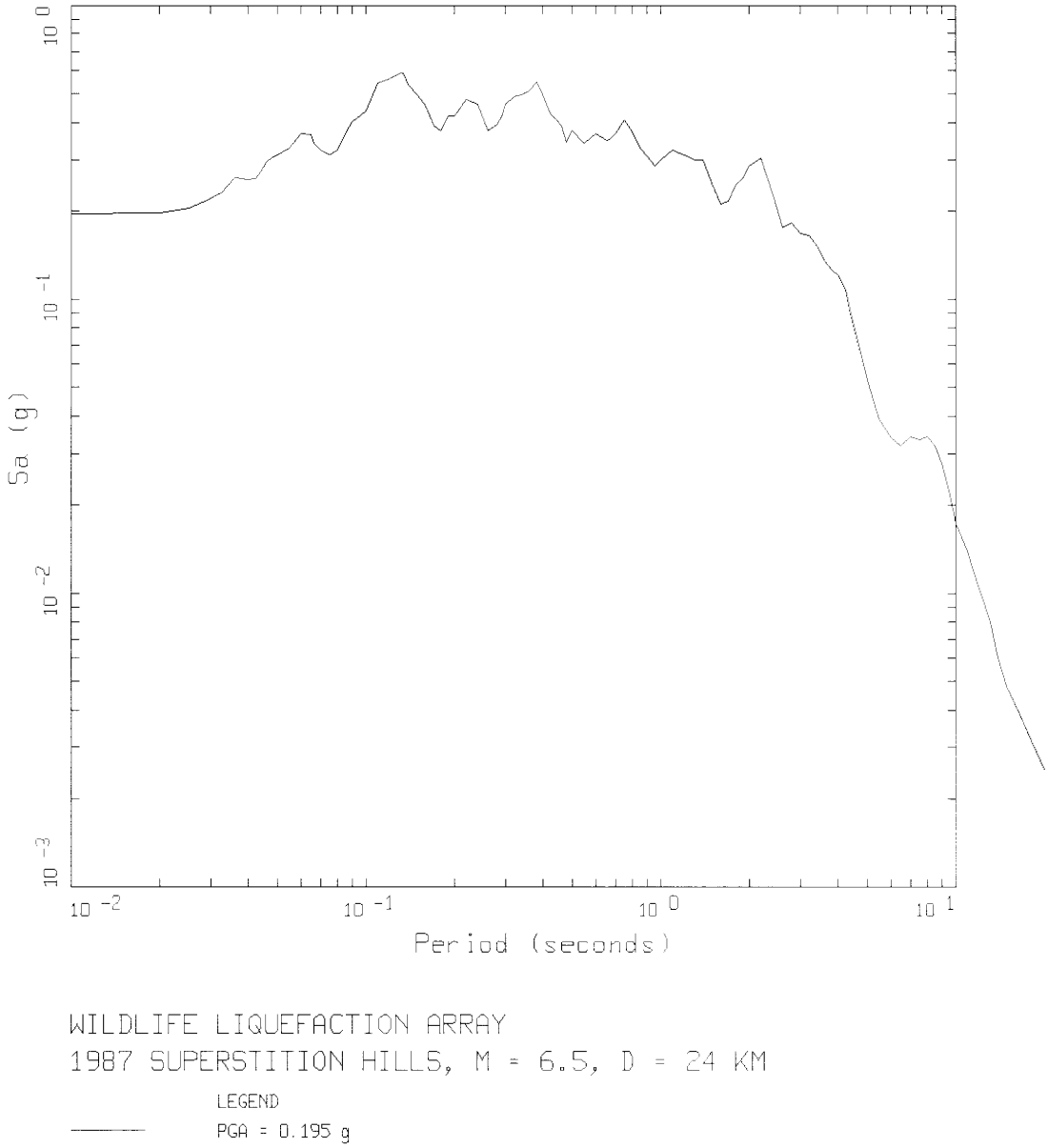


Figure 11a. Average horizontal component response spectra computed from recorded motions: Wildlife Liquefaction Array, 1987 Superstition Hills earthquake.

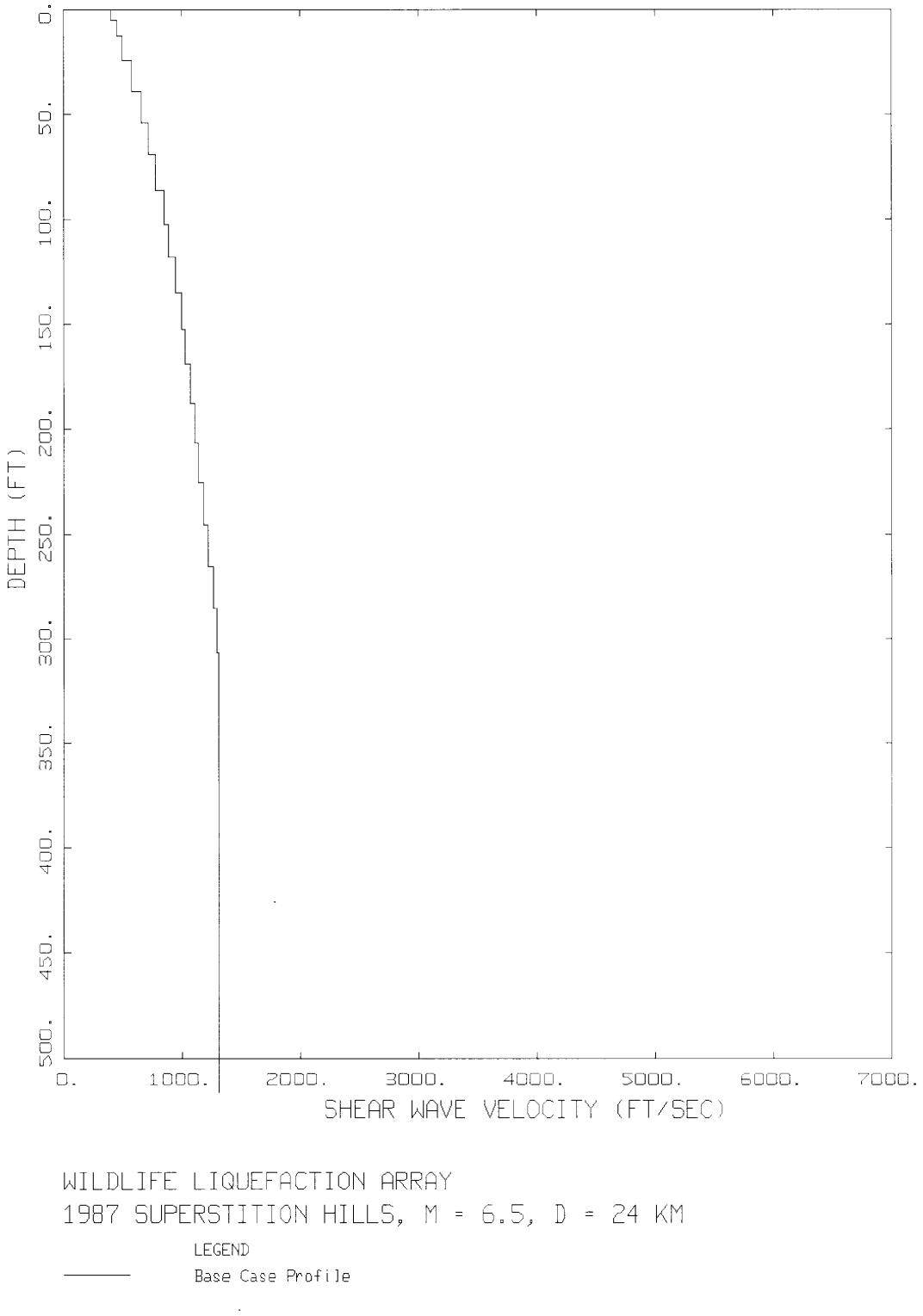


Figure 11b. Shear-wave velocity profile (assumed) at the Wildlife Liquefaction Array to a depth of 500 ft.

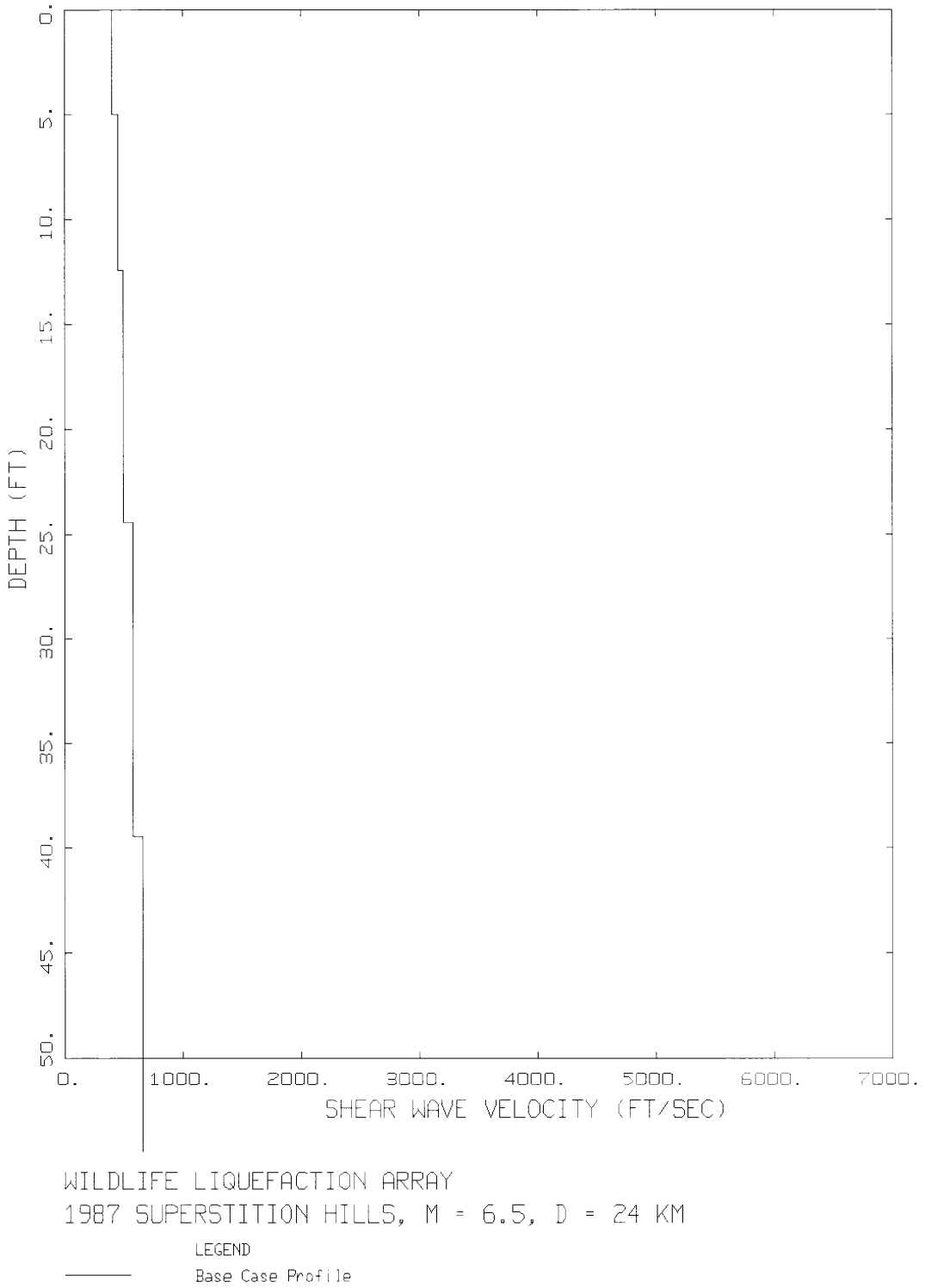


Figure 11c. Shear-wave velocity profile (assumed) at the Wildlife Liquefaction Array to a depth of 50 ft.

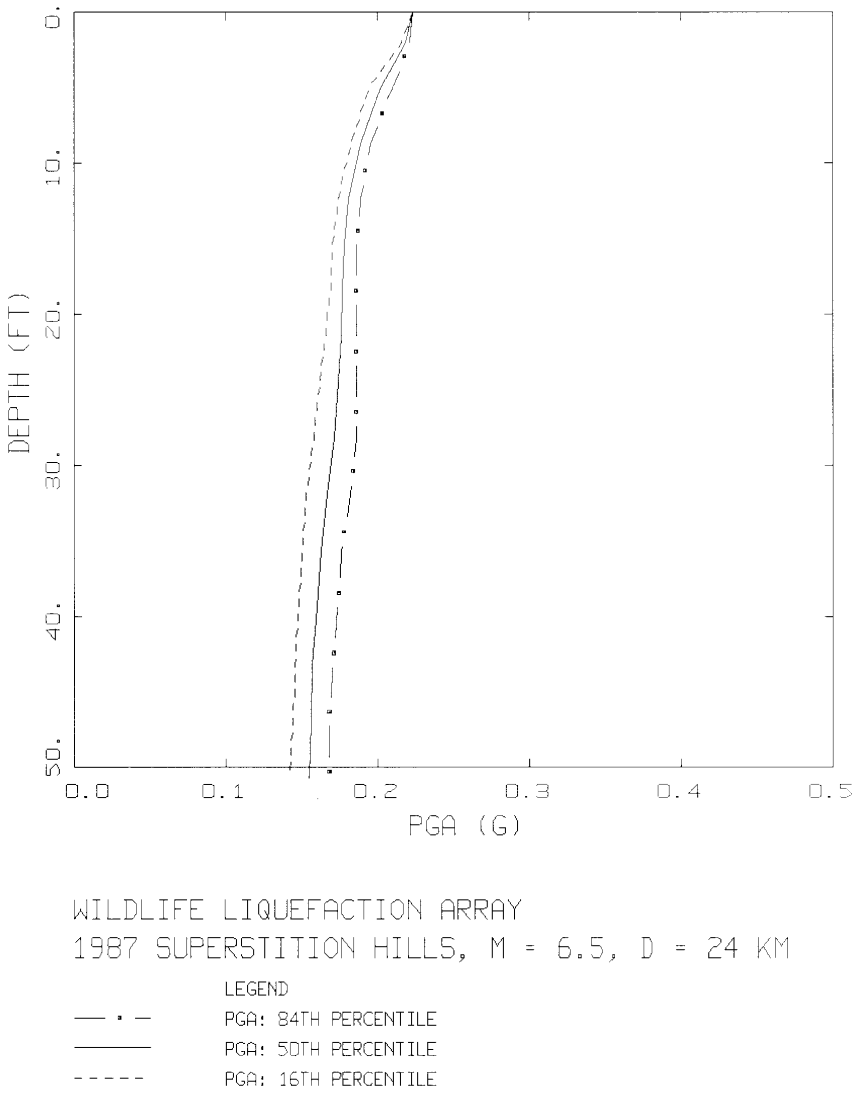


Figure 11d. Variation of peak acceleration(g) (Average horizontal component) verses depth computed for a suite of random profiles at the Wildlife Liquefaction Array. Average horizontal spectrum (Figure 11a) based on recorded motions used as control motions.

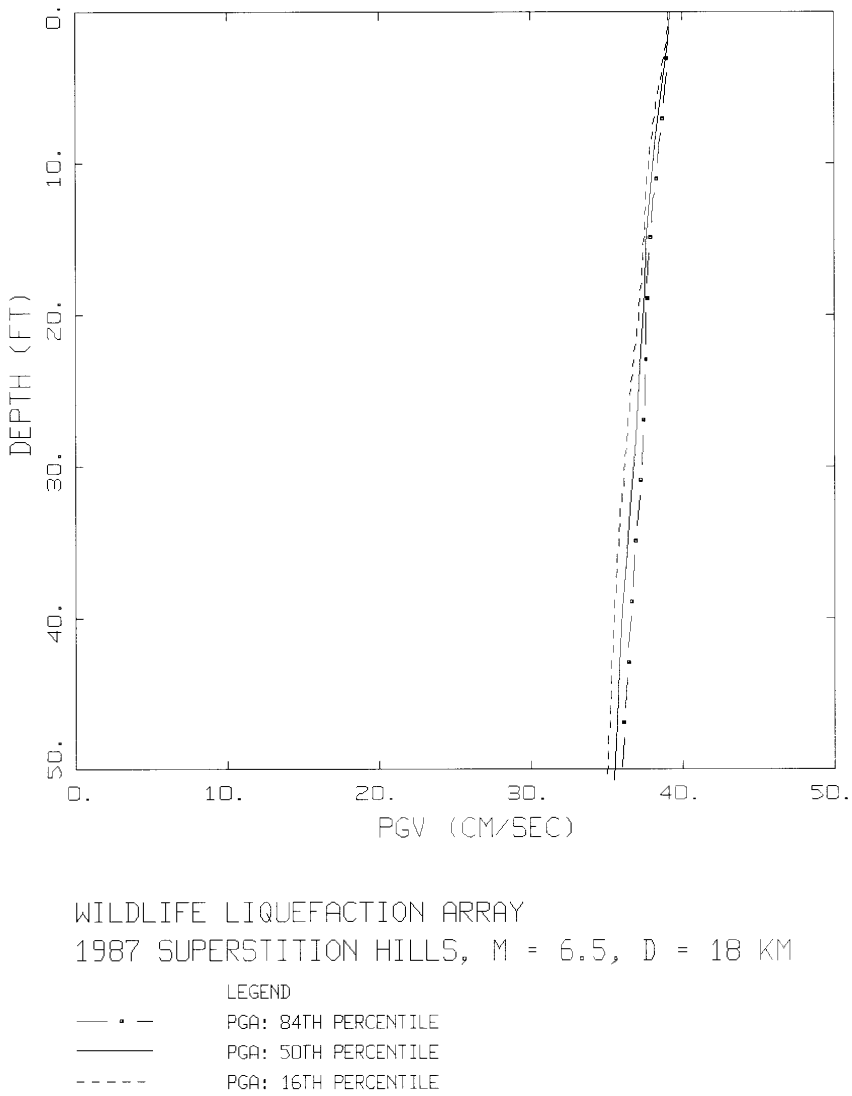


Figure 11e. Variation of peak particle velocity (cm/sec) verses depth computed for a suite of random profiles at the Wildlife Liquefaction Array. Average horizontal spectrum (Figure 11a) based on recorded motions used as control motions.

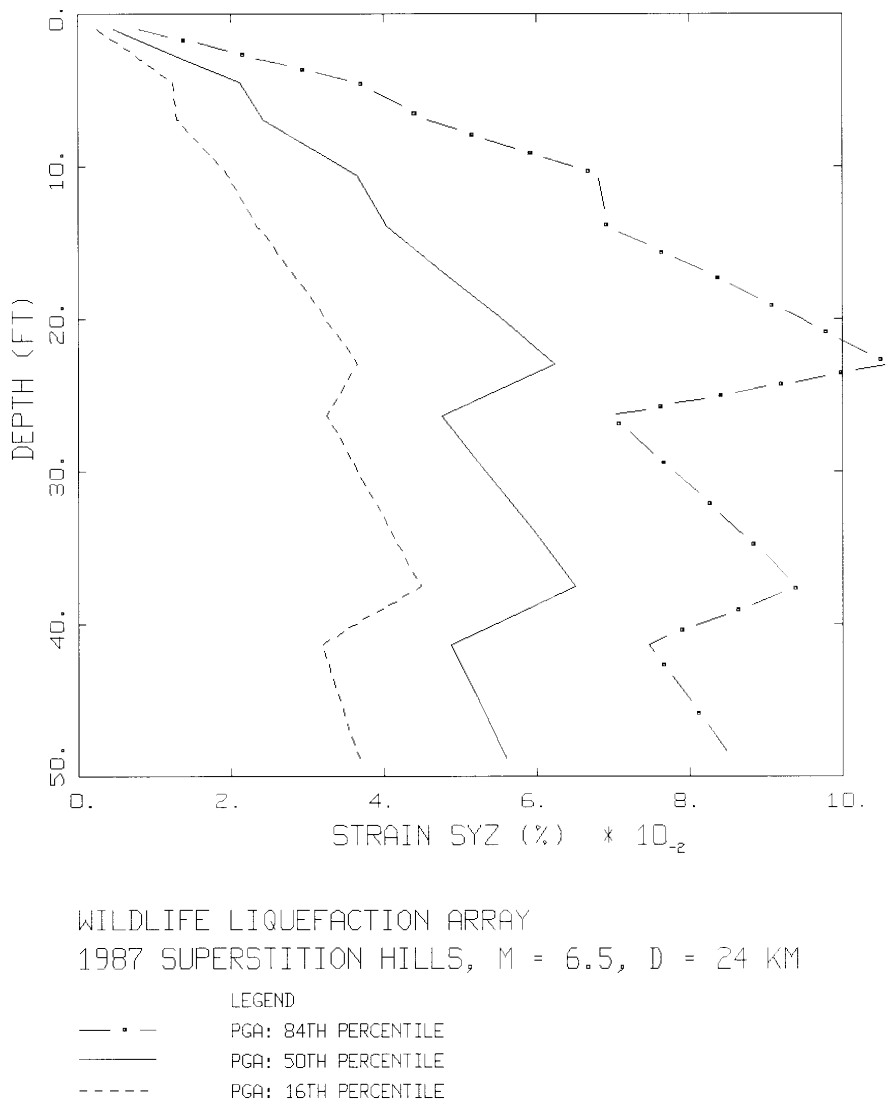


Figure 11f. Variation of peak shear strain(%) verses depth computed for a suite of random profiles at the Wildlife Liquefaction Array. Average horizontal spectrum (Figure 11a) based on recorded motions used as control motions.

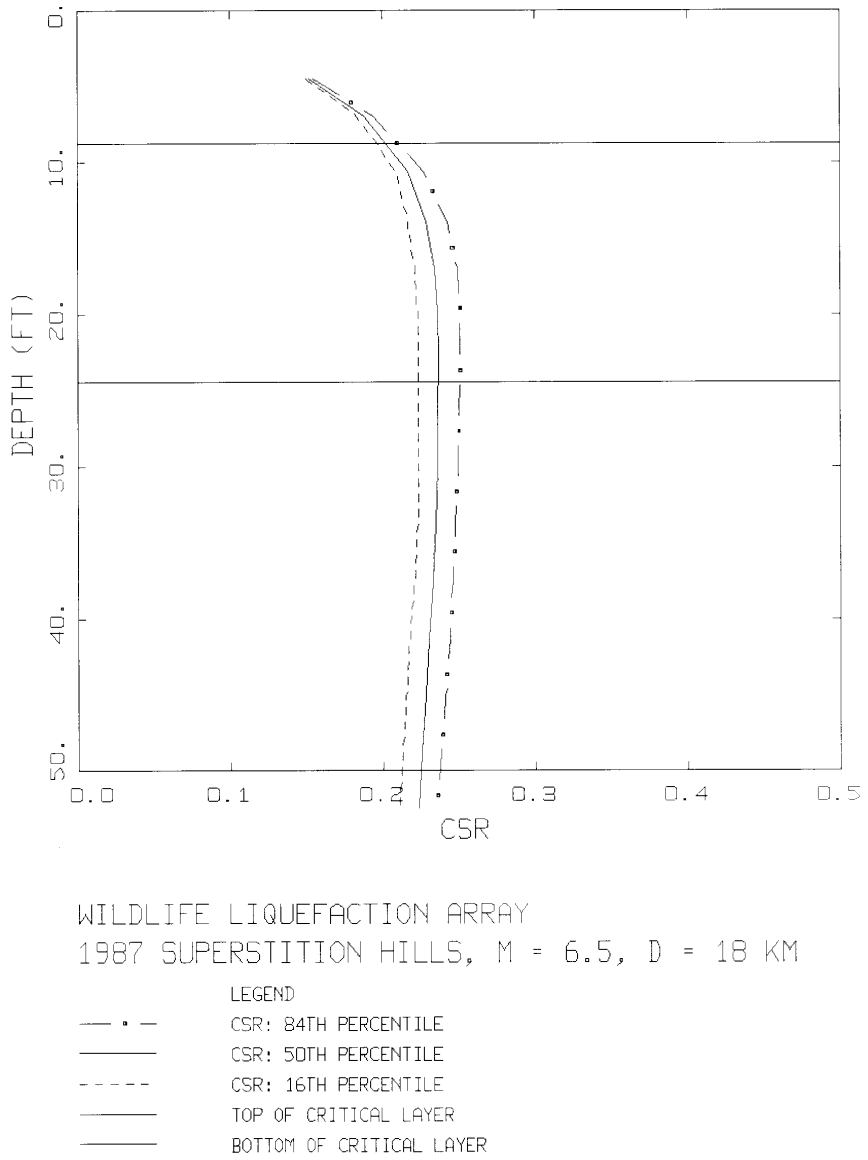


Figure 11g. Variation of CSR verses depth computed for a suite of random profiles for at Wildlife Liquefaction Array. Average horizontal spectrum (Figure 11a) based on recorded motions used as control motions. Critical layer indicated with horizontal lines.

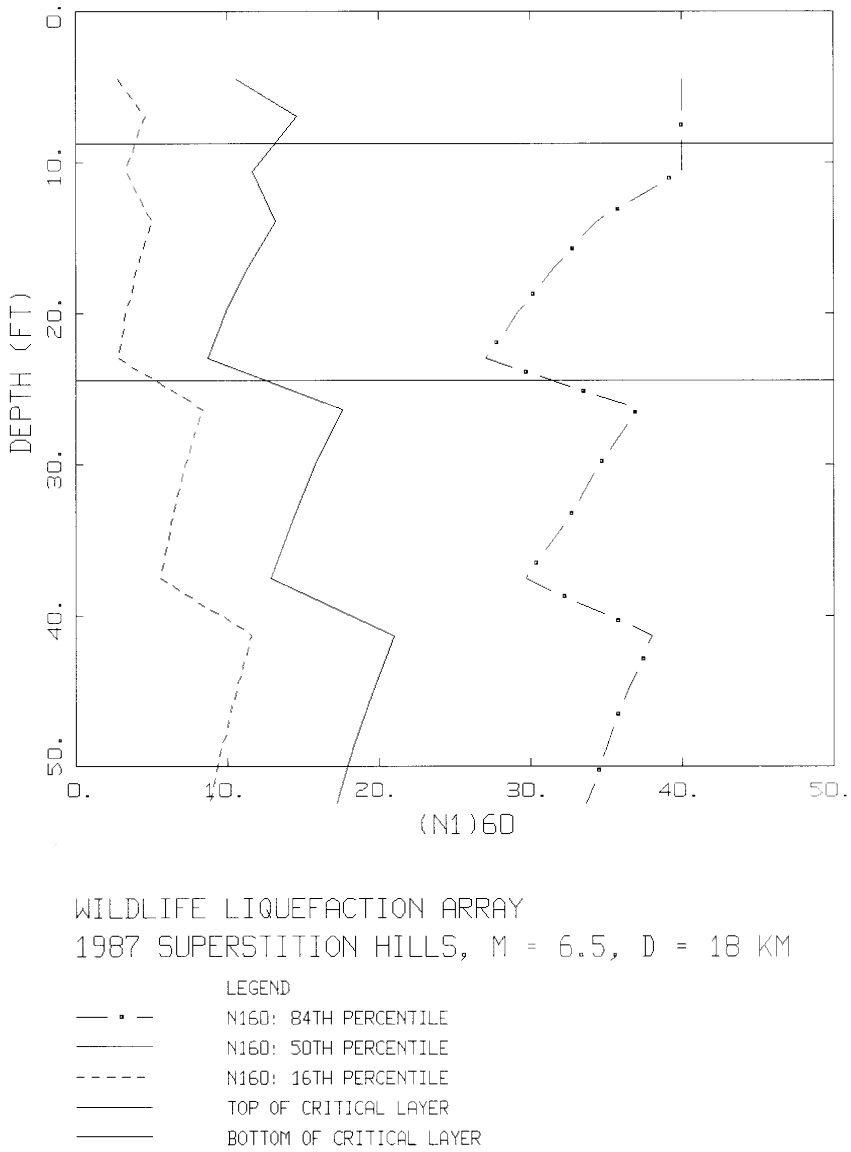


Figure 11h. Variation of peak $(N_1)_{60}$ verses depth computed for a suite of random profiles at the Wildlife Liquefaction Array using the shear-wave velocity correlation model of Iwasaki et al., (1987). Average horizontal spectrum (Figure 11a) based on recorded motions used as control motions. Critical layer indicated with horizontal lines.

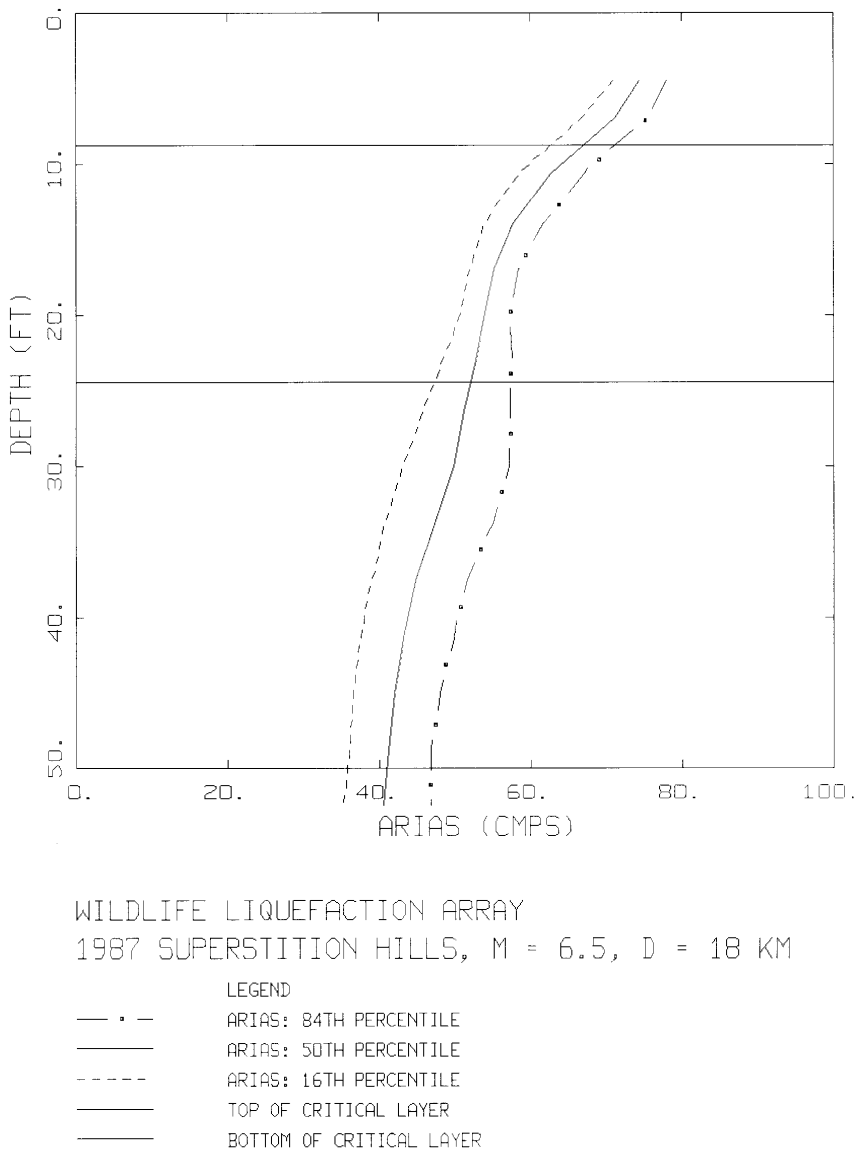


Figure 11i. Variation of Arias Intensity (cm/sec) verses depth computed for a suite of random profiles at the Wildlife Liquefaction Array. Average horizontal spectrum (Figure 11a) based on recorded motions used as control motions. Critical layer indicated with horizontal lines.

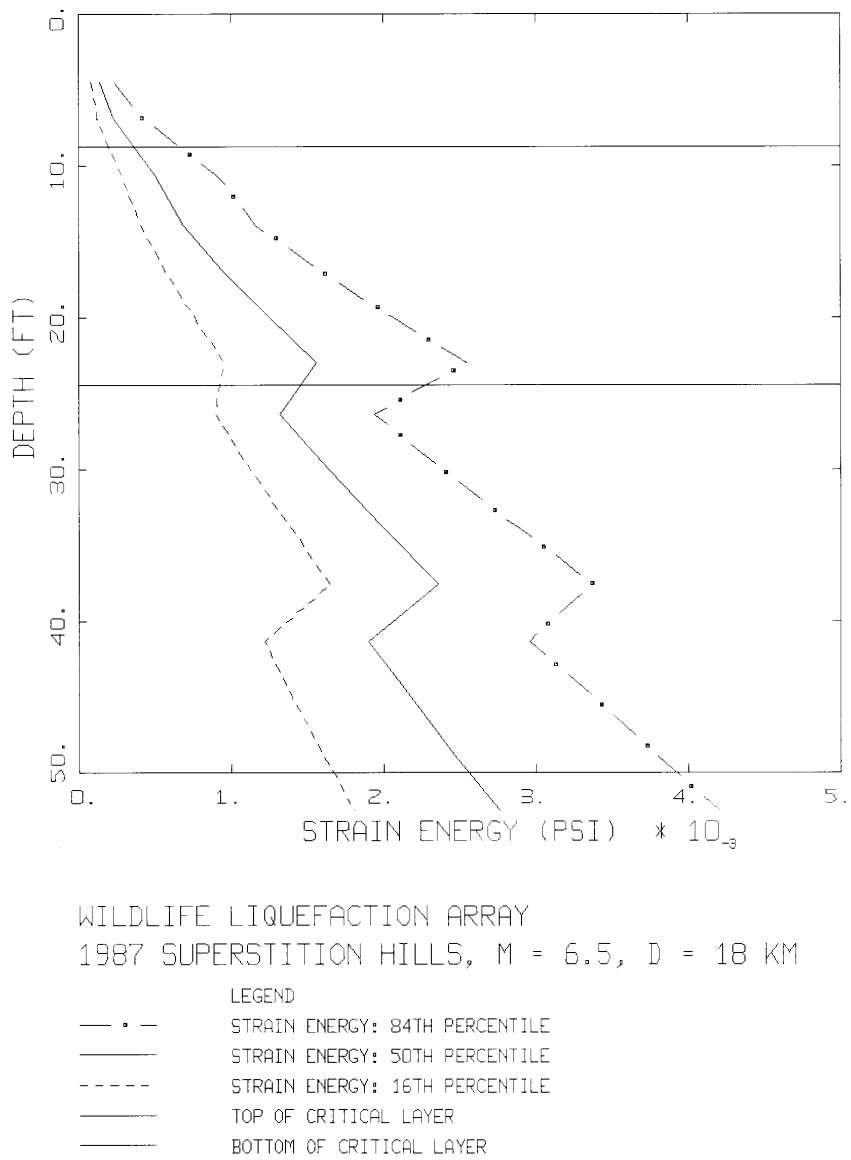


Figure 11j Variation of strain energy (PSI) verses depth computed for a suite of random profiles at the Wildlife Liquefaction Array. Average horizontal spectrum (Figure 11a) based on recorded motions used as control motions. Critical layer indicated with horizontal lines.

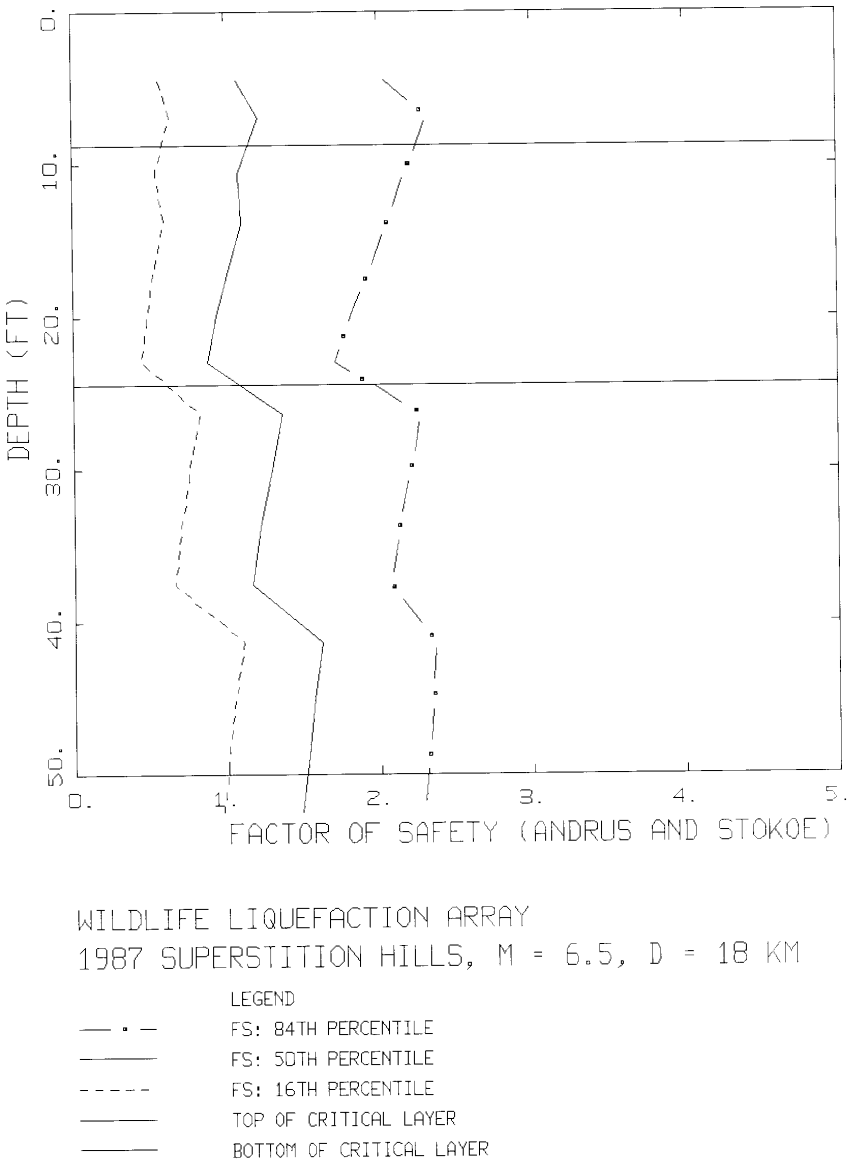


Figure 11k. Variation of the factor of safety (FS) using the Andrus and Stokoe (2004) shear-wave velocity based approach verses depth computed for a suite of random profiles at the Wildlife Liquefaction Array. Average horizontal spectrum (Figure 11a) based on recorded motions used as control motions. Critical layer indicated with horizontal lines.

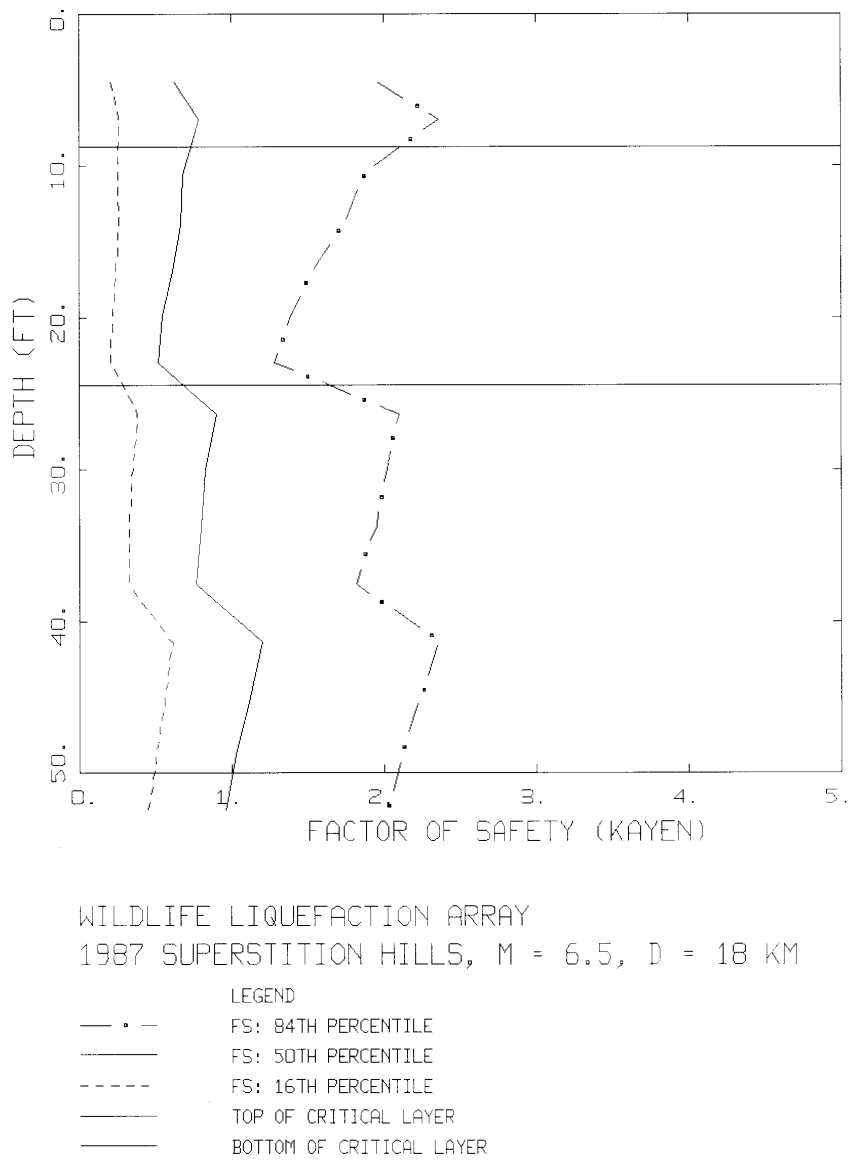


Figure 11l. Variation of the factor of safety using the Kayen and Mitchell (1979) Arias Intensity based approach verses depth computed for a suite of random profiles at the Wildlife Liquefaction Array. Average horizontal spectrum (Figure 11a) based on recorded motions used as control motions. Critical layer indicated with horizontal lines.

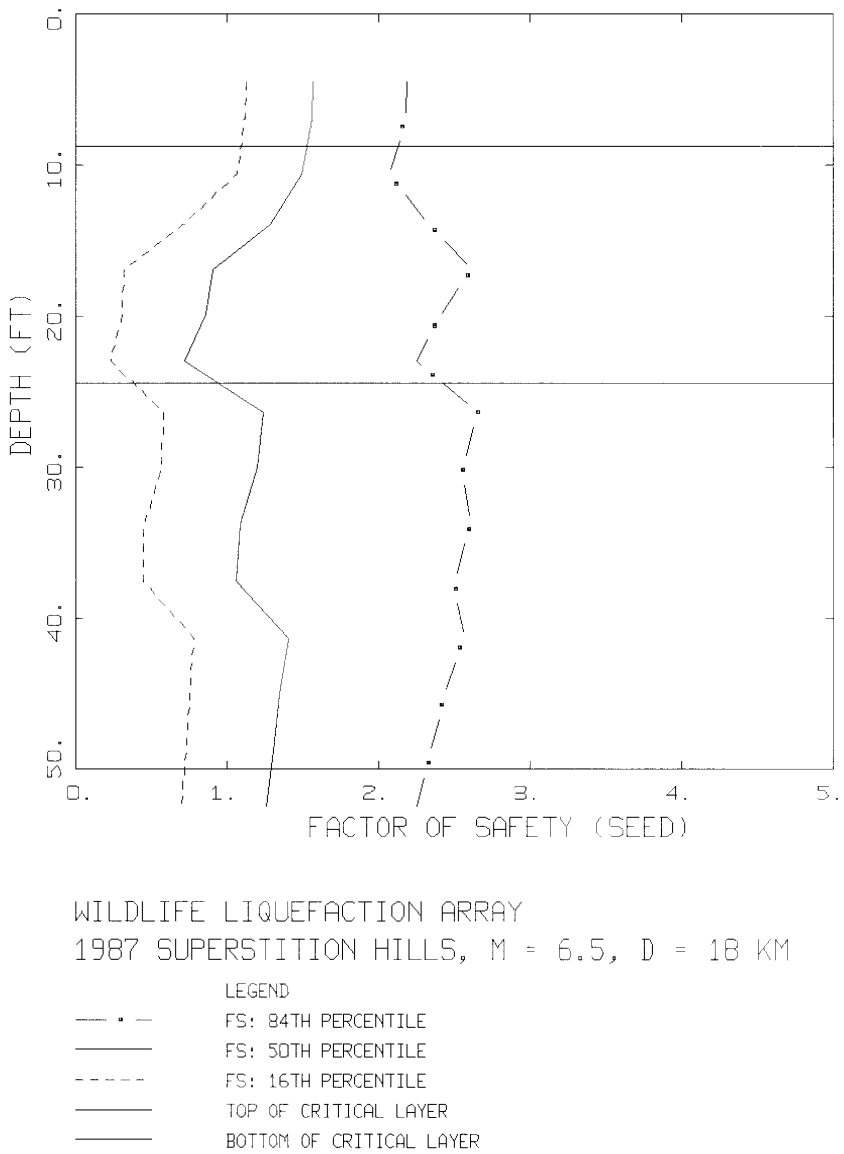


Figure 11m. Variation of the factor of the factor of safety using the Seed et al., (2002) SPT based approach verses depth computed for a suite of random profiles at the Wildlife Liquefaction Array. Average horizontal spectrum (Figure 11a) based on recorded motions used as control motions. Critical layer indicated with horizontal lines.

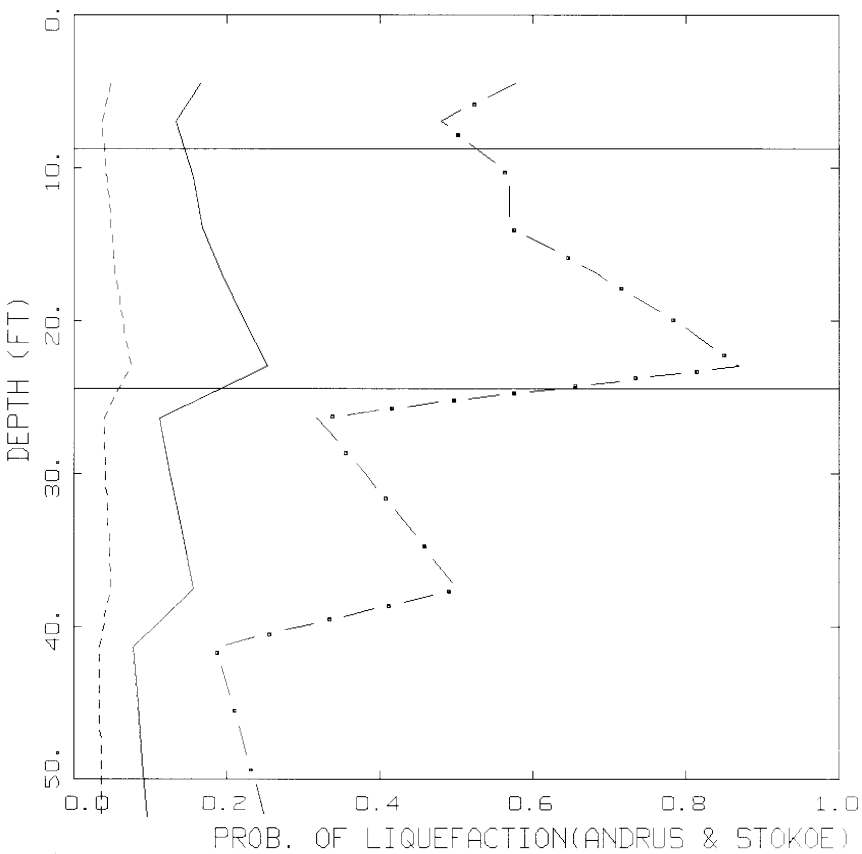


WILDLIFE LIQUEFACTION ARRAY
1987 SUPERSTITION HILLS, M = 6.5, D = 18 KM

LEGEND

| | |
|---|---|
| —— • —— | PROB. OF LIQ.: 84TH PERCENTILE |
| ——— | PROB. OF LIQ.: 50TH PERCENTILE |
| - - - - - | PROB. OF LIQ.: 16TH PERCENTILE |
| ——— | TOP OF CRITICAL LAYER |
| ——— | BOTTOM OF CRITICAL LAYER |

Figure 11n. Variation of the probability of liquefaction using the Andrus and Stokoe (2004) shear-wave velocity based approach verses depth computed for a suite of random profiles at the Wildlife Liquefaction Array. Average horizontal spectrum (Figure 11a) based on recorded motions used as control motions. Critical layer indicated with horizontal lines.

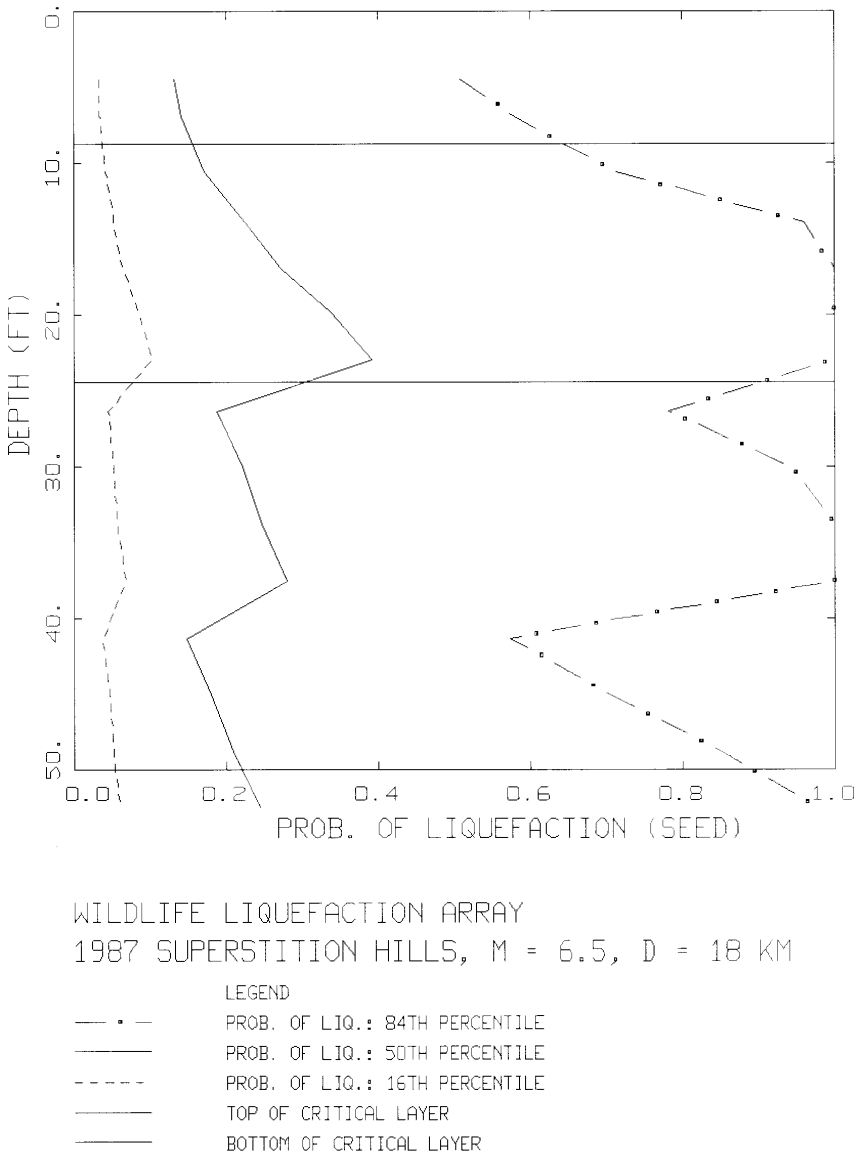


Figure 11o. Variation probability of liquefaction using the Seed et al. (2002) SPT based approach verses depth computed for a suite of random profiles at the Wildlife Liquefaction Array. Average horizontal spectrum (Figure 11a) based on recorded motions used as control motions. Critical layer indicated with horizontal lines.

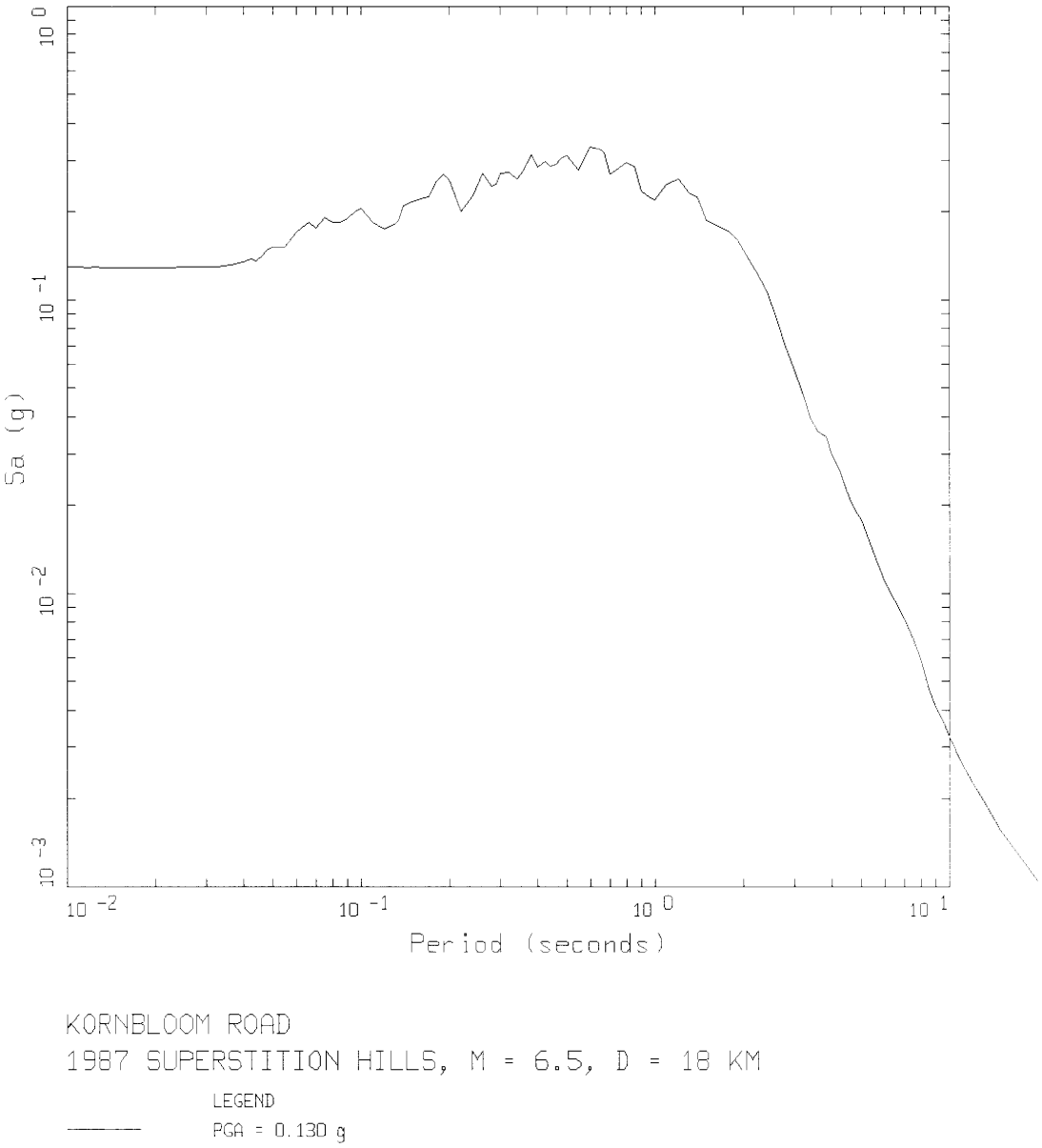


Figure 12a. Average horizontal component response spectra computed from recorded motions: Kornbloom Road site, 1987 Superstition Hills earthquake.

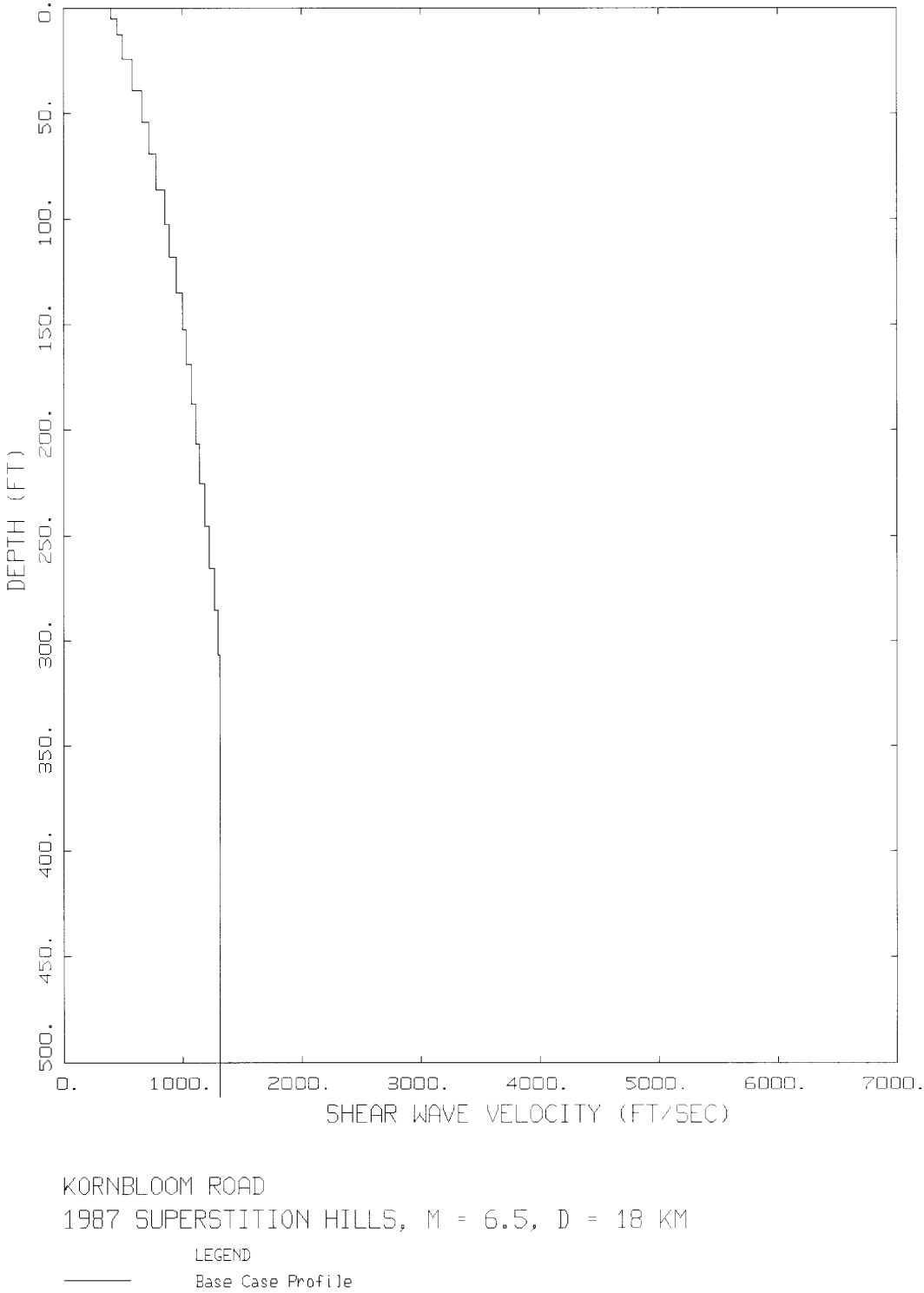


Figure 12b. Shear-wave velocity profile (assumed) at the Kornbloom Road site to a depth of 500 ft.

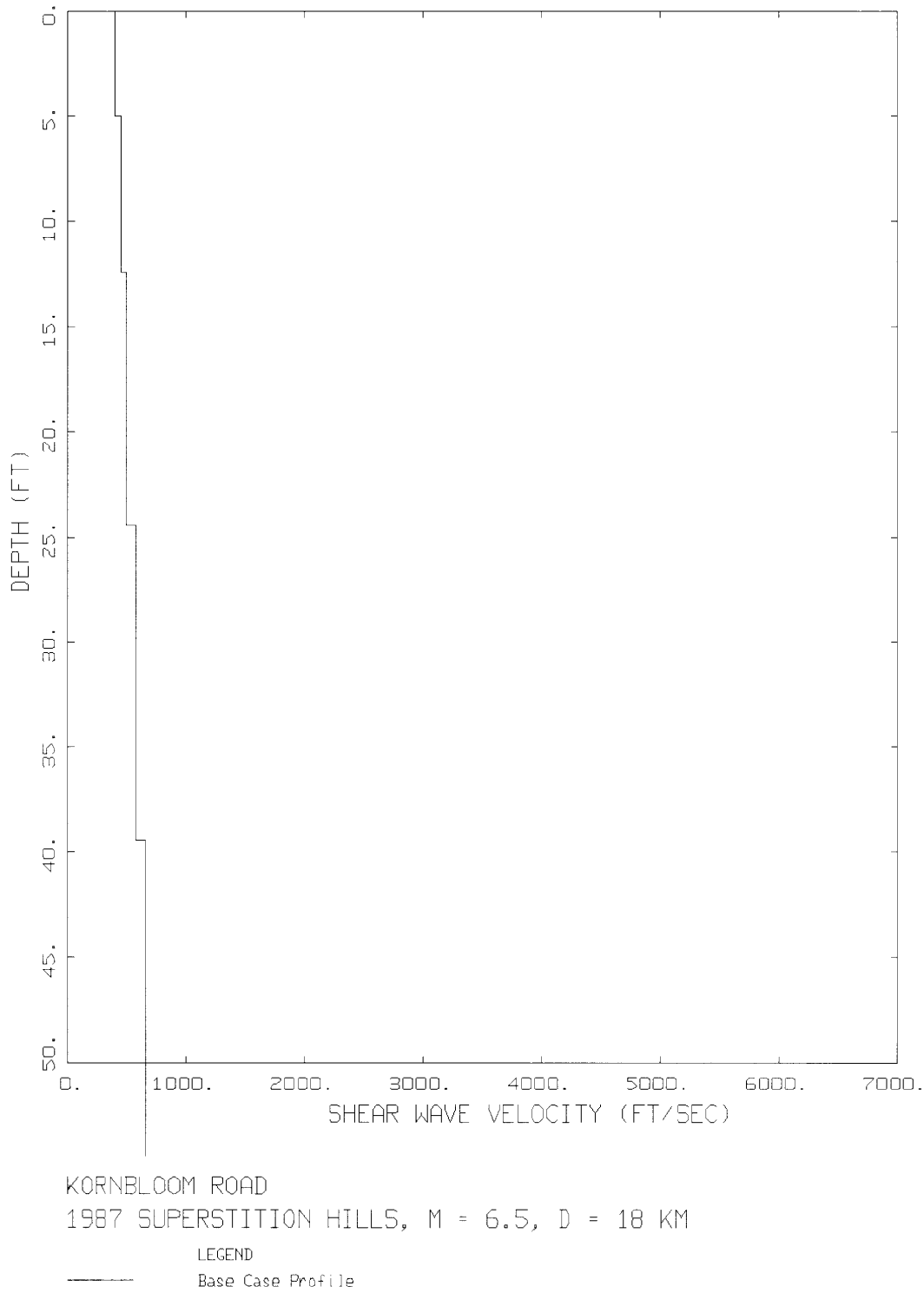


Figure 12c. Shear-wave velocity profile (assumed) at the Kornbloom Road site to a depth of 50 ft.

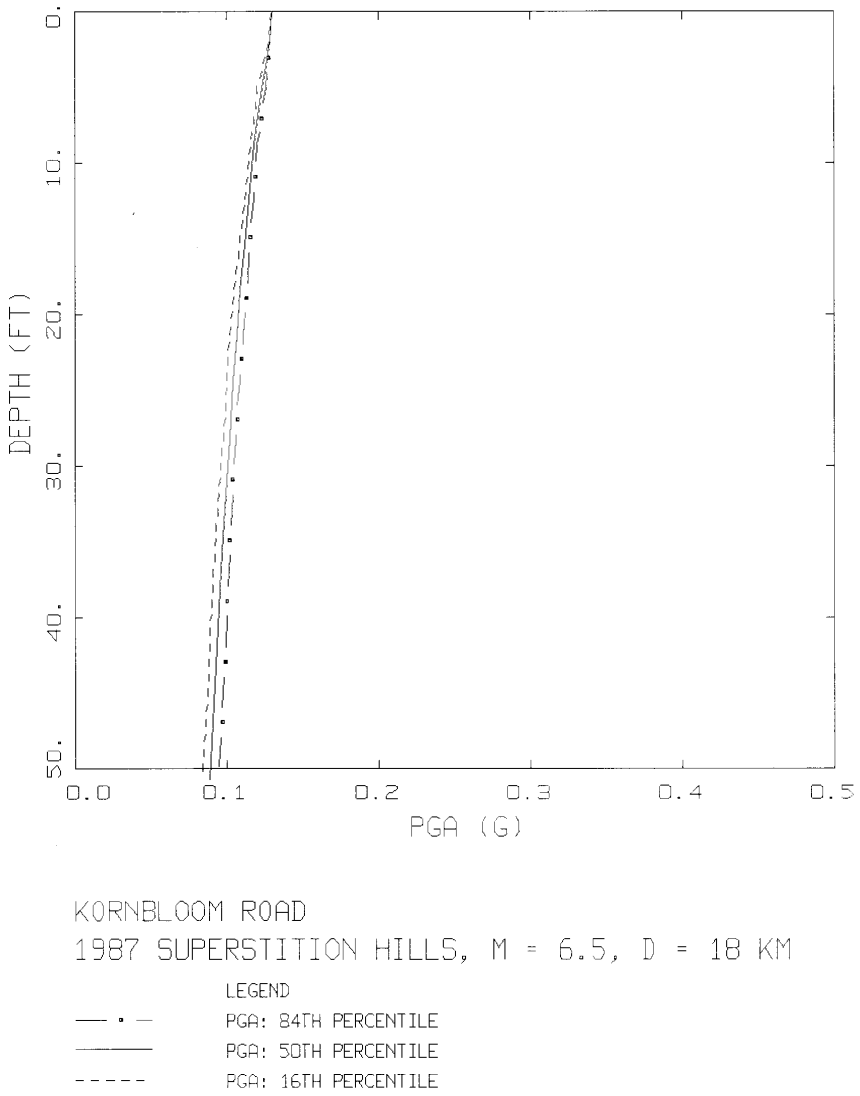


Figure 12d. Variation of peak acceleration(g) (Average horizontal component) verses depth computed for a suite of random profiles at the Kornbloom Road site. Average horizontal spectrum (Figure 12a) based on recorded motions used as control motions.

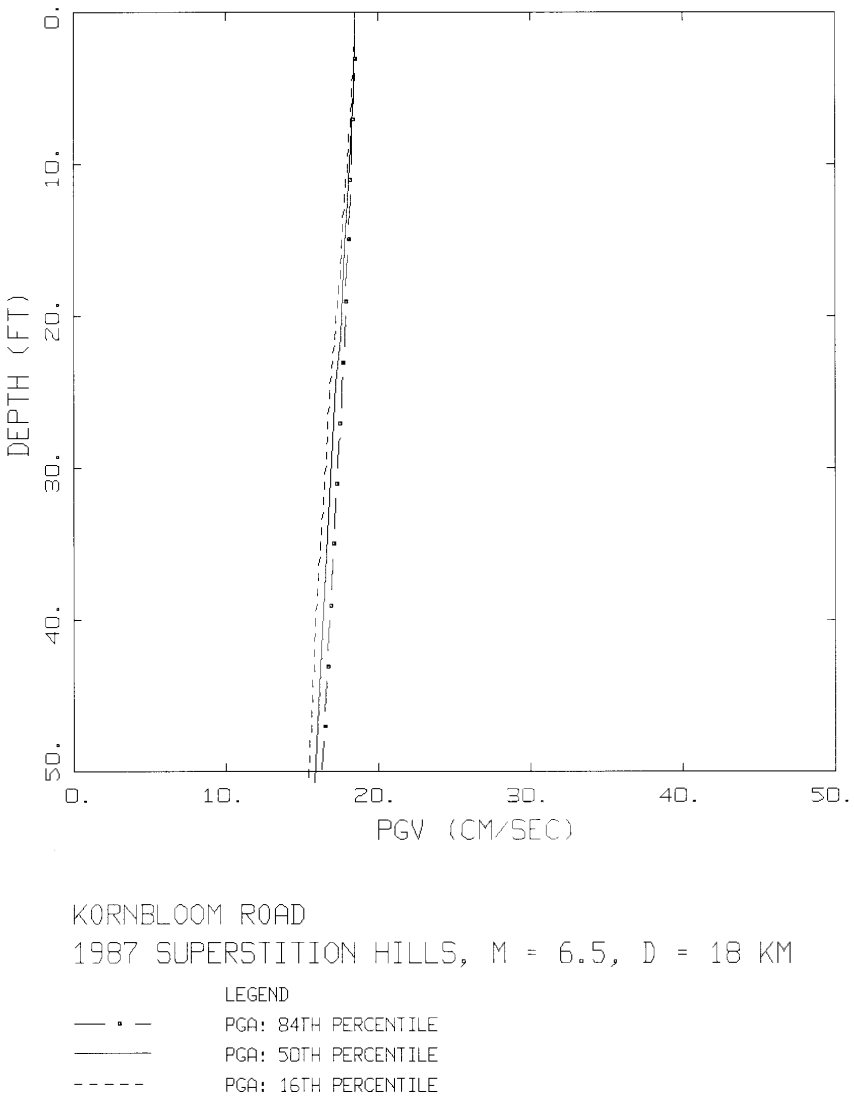


Figure 12e. Variation of peak particle velocity (cm/sec) verses depth computed for a suite of random profiles at the Kornbloom Road site. Average horizontal spectrum (Figure 12a) based on recorded motions used as control motions.

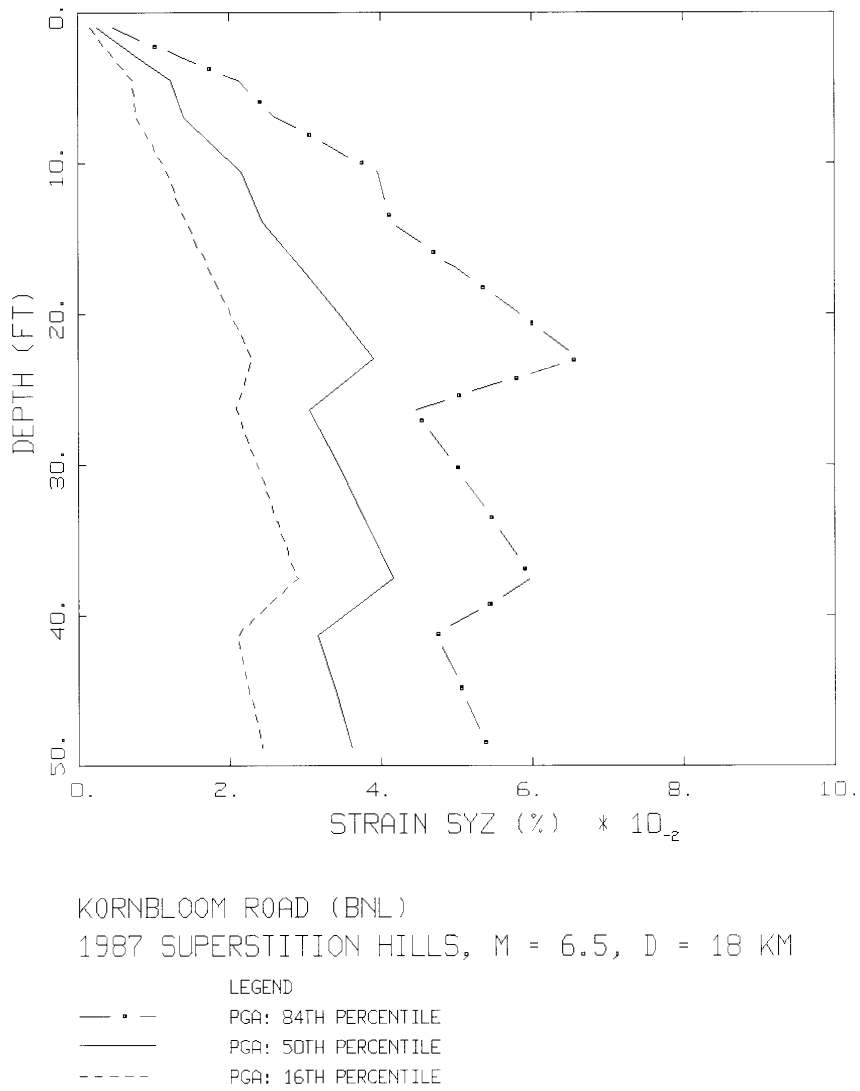


Figure 12f. Variation of peak shear strain(%) verses depth computed for a suite of random profiles at the Kornbloom Road site. Average horizontal spectrum (Figure 12a) based on recorded motions used as control motions.

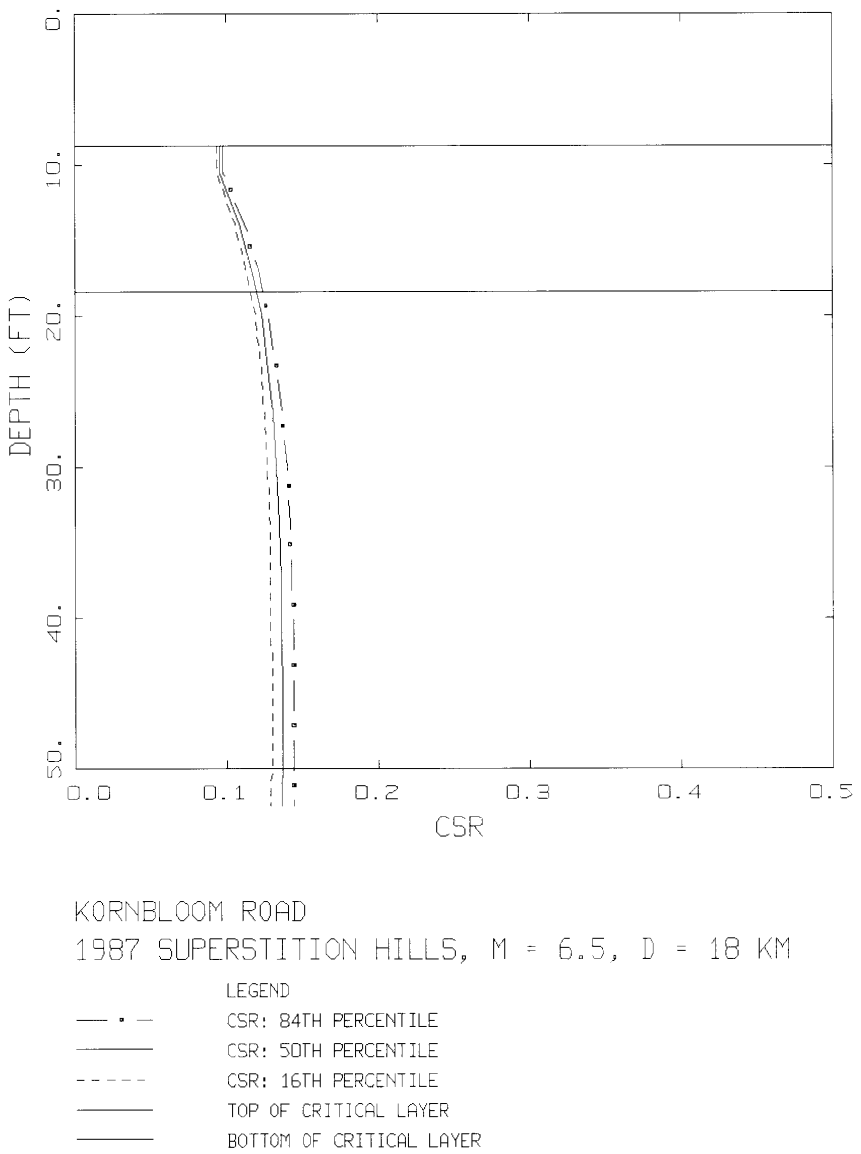


Figure 12g. Variation of CSR verses depth computed for a suite of random profiles for at Kornbloom Road site. Average horizontal spectrum (Figure 12a) based on recorded motions used as control motions. Critical layer indicated with horizontal lines.

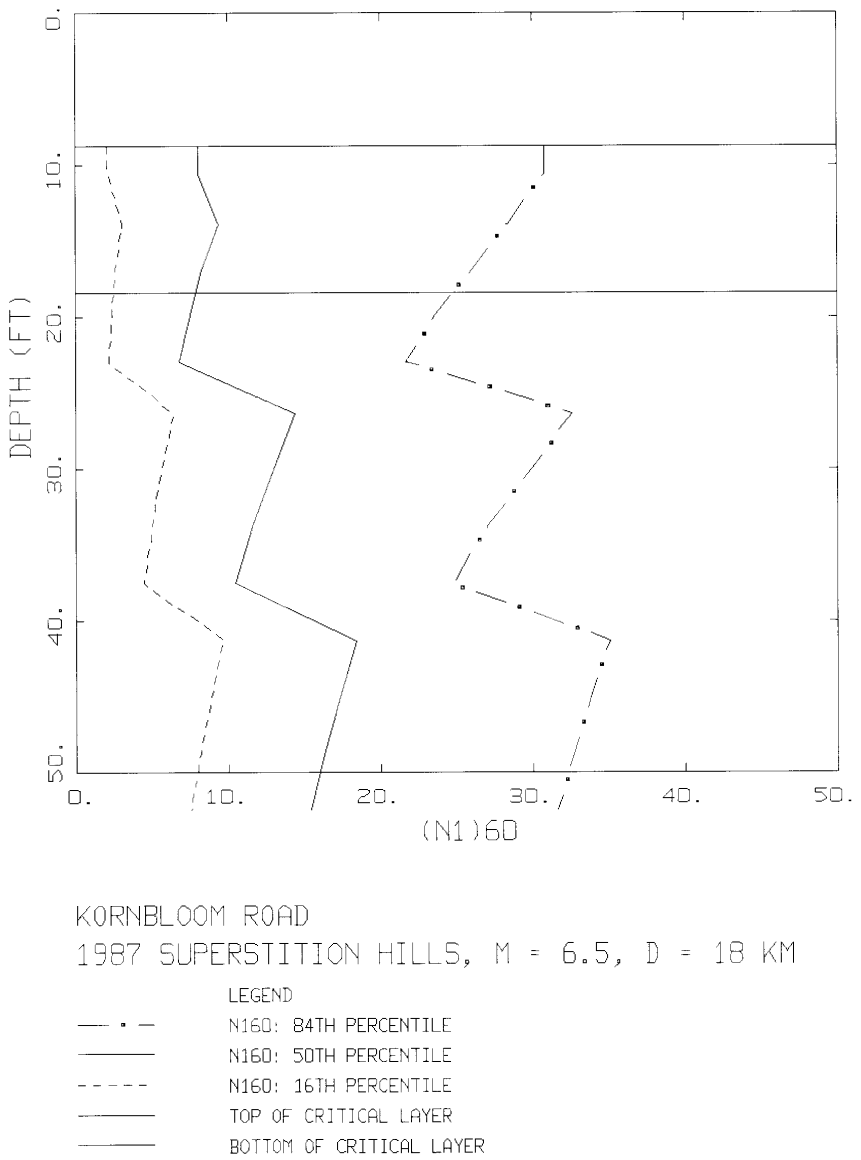


Figure 12h. Variation of peak $(N_1)_{60}$ verses depth computed for a suite of random profiles at the Kornbloom Road site using the shear-wave velocity correlation model of Iwasaki et al., (1987). Average horizontal spectrum (Figure 12a) based on recorded motions used as control motions. Critical layer indicated with horizontal lines.

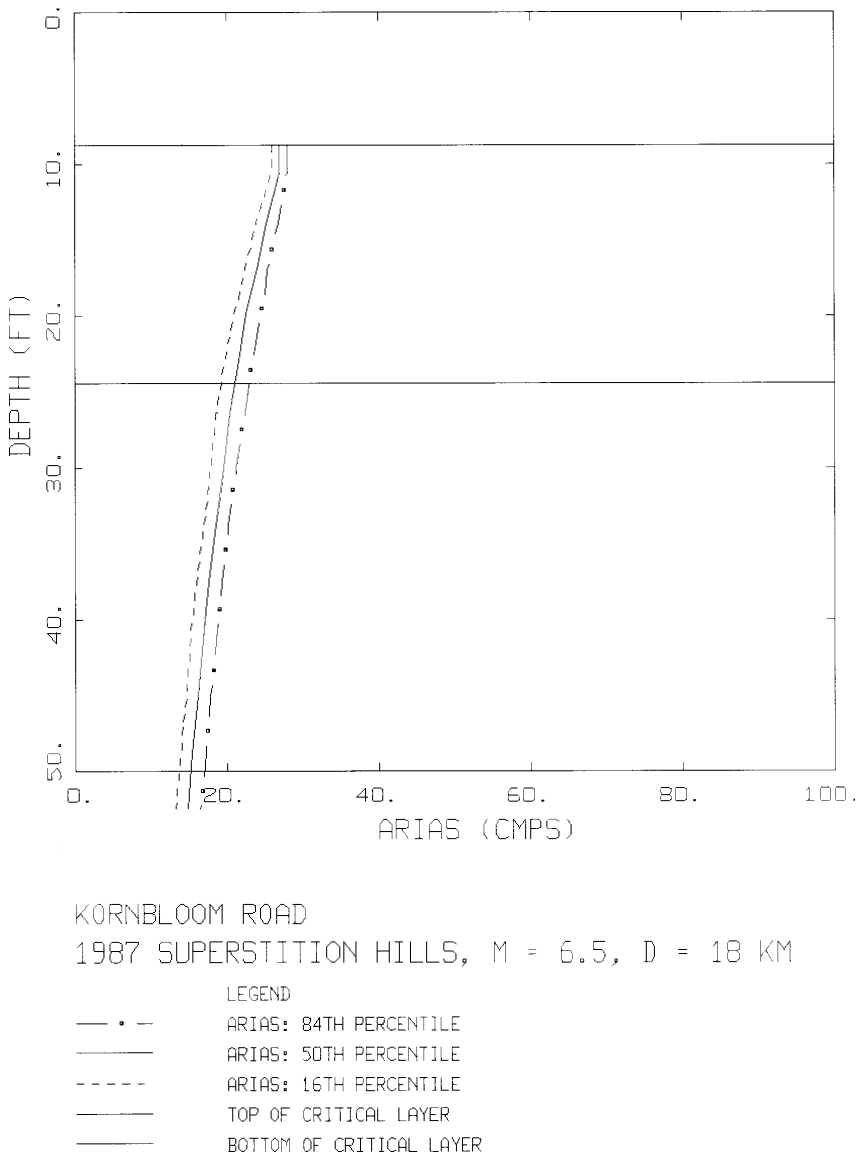


Figure 12i. Variation of Arias Intensity (cm/sec) verses depth computed for a suite of random profiles at the Kornbloom Road site. Average horizontal spectrum (Figure 12a) based on recorded motions used as control motions. Critical layer indicated with horizontal lines.

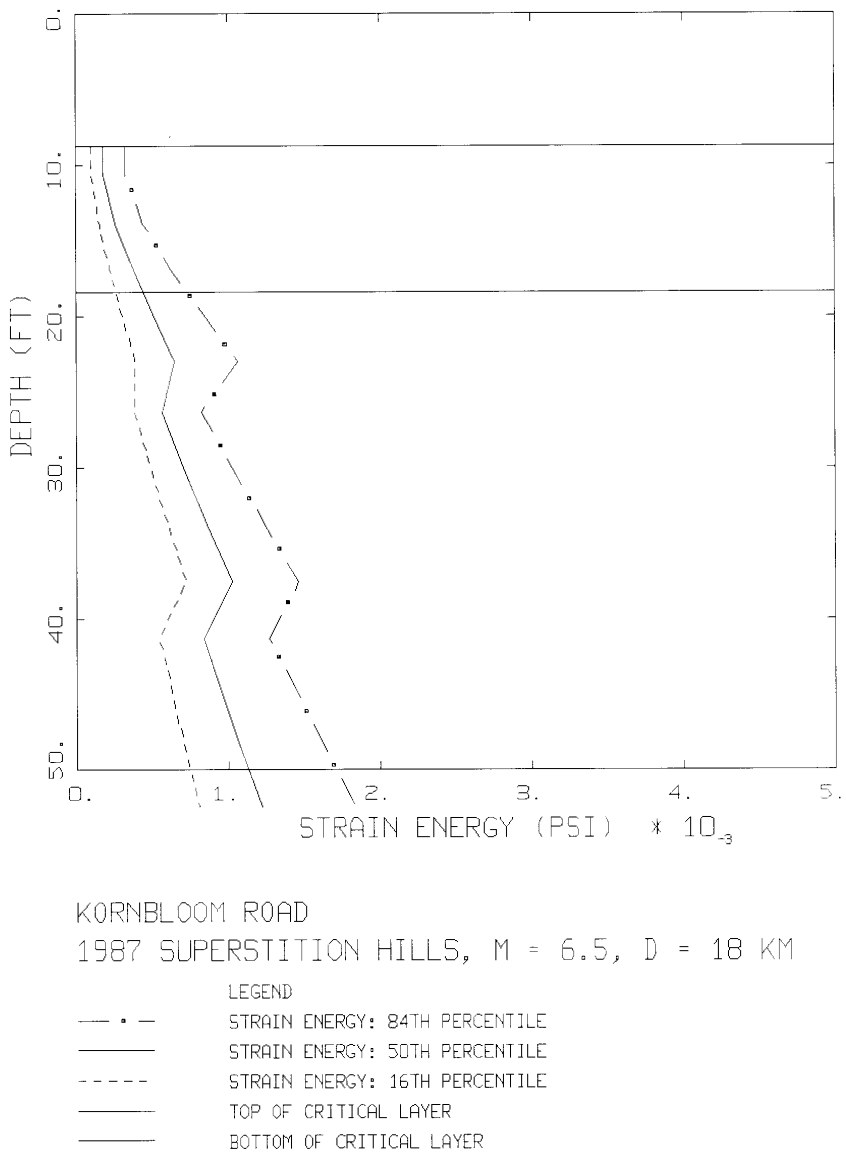


Figure 12j Variation of strain energy (PSI) verses depth computed for a suite of random profiles at the Kornbloom Road site. Average horizontal spectrum (Figure 12a) based on recorded motions used as control motions. Critical layer indicated with horizontal lines.

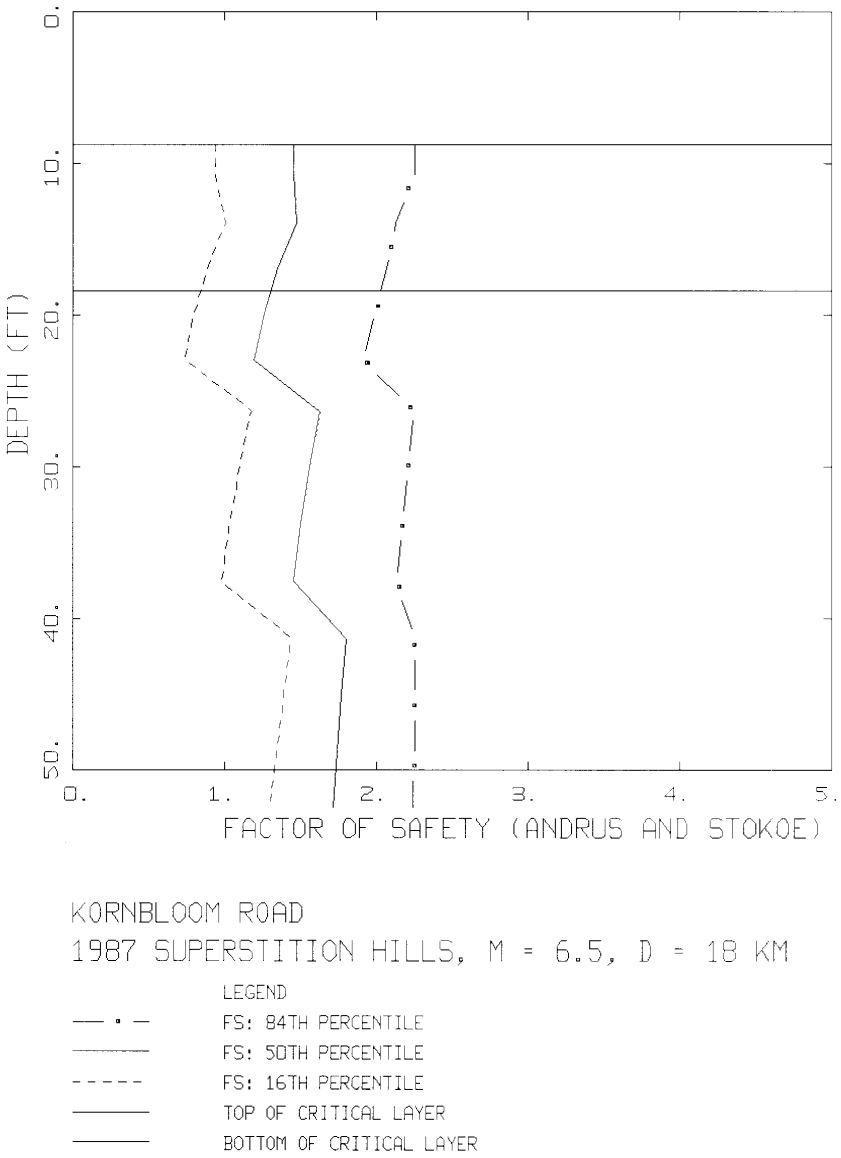


Figure 12k. Variation of the factor of safety (FS) using the Andrus and Stokoe (2004) shear-wave velocity based approach verses depth computed for a suite of random profiles at the Kornbloom Road site. Average horizontal spectrum (Figure 12a) based on recorded motions used as control motions. Critical layer indicated with horizontal lines.

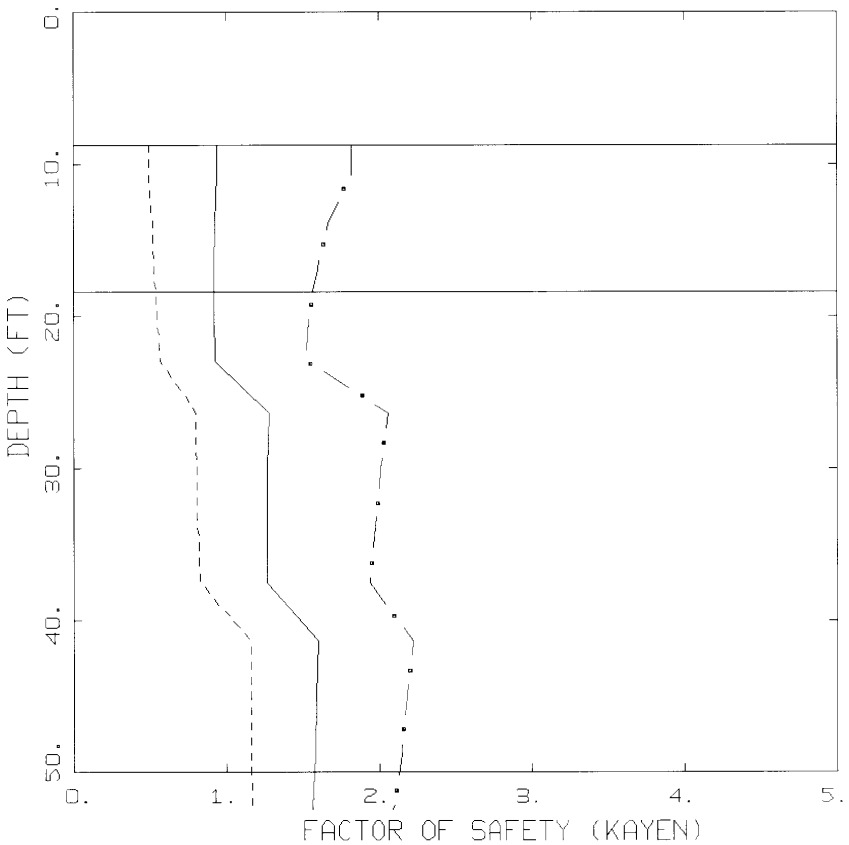


KORNBLOOM ROAD
1987 SUPERSTITION HILLS, M = 6.5, D = 18 KM

LEGEND
FS: 84TH PERCENTILE
FS: 50TH PERCENTILE
FS: 16TH PERCENTILE
TOP OF CRITICAL LAYER
BOTTOM OF CRITICAL LAYER

Figure 12l. Variation of the factor of safety using the Kayen and Mitchell (1979) Arias Intensity based approach verses depth computed for a suite of random profiles at the Kornbloom Road site. Average horizontal spectrum (Figure 12a) based on recorded motions used as control motions. Critical layer indicated with horizontal lines.

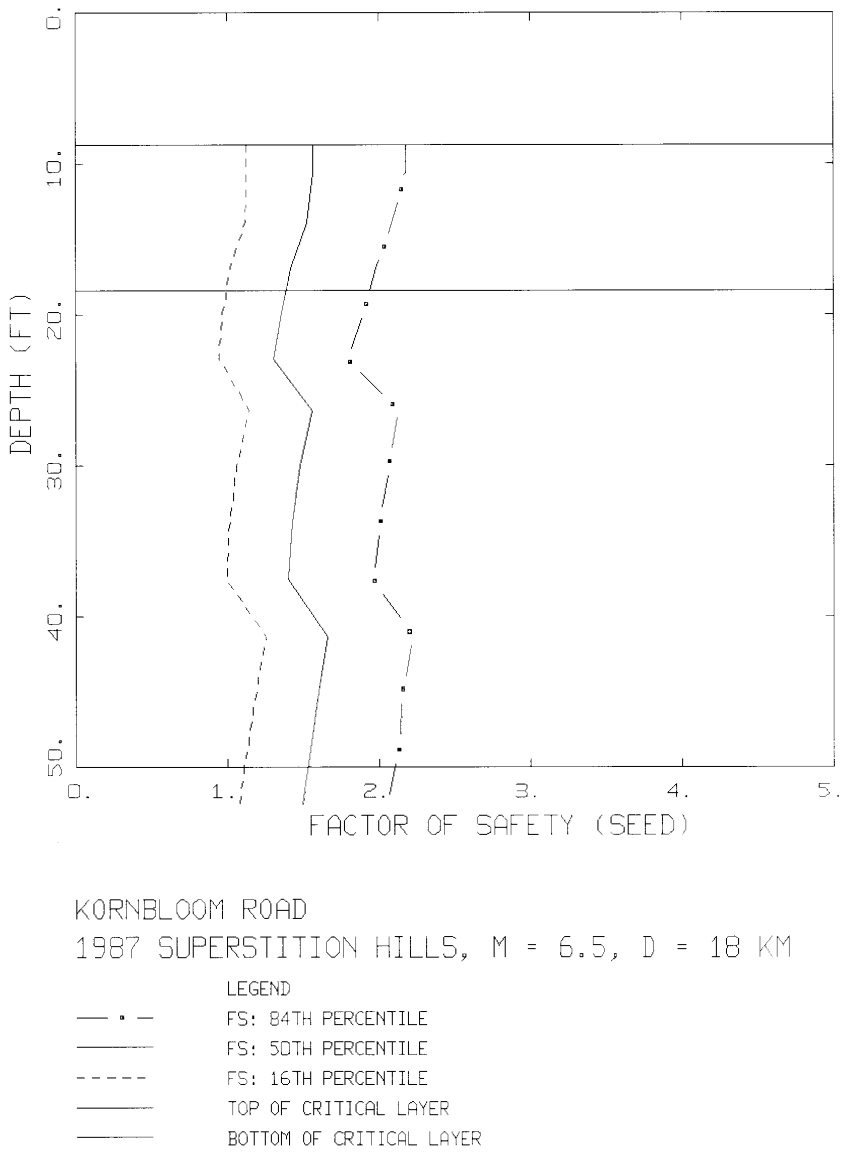


Figure 12m. Variation of the factor of the factor of safety using the Seed et al., (2002) SPT based approach verses depth computed for a suite of random profiles at the Kornbloom Road site. Average horizontal spectrum (Figure 12a) based on recorded motions used as control motions. Critical layer indicated with horizontal lines.

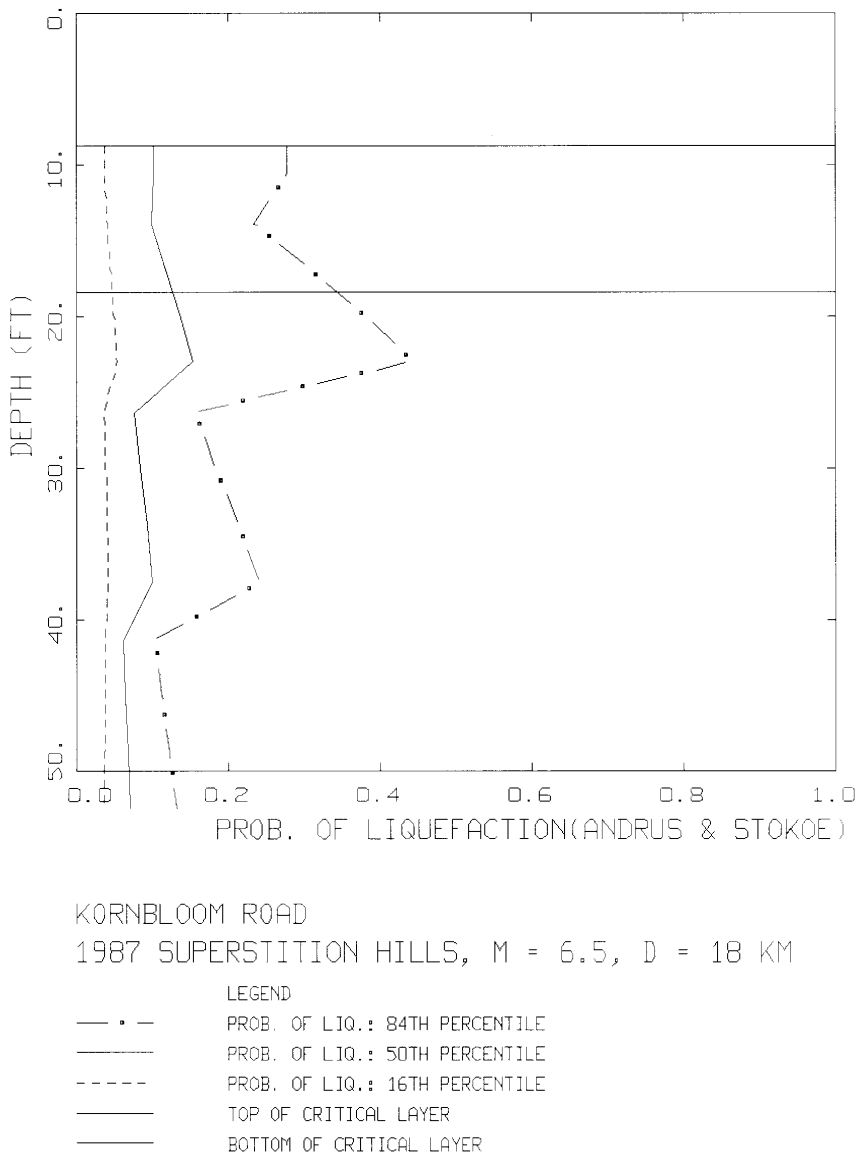


Figure 12n. Variation of the probability of liquefaction using the Andrus and Stokoe (2004) shear-wave velocity based approach verses depth computed for a suite of random profiles at the Kornbloom Road site. Average horizontal spectrum (Figure 12a) based on recorded motions used as control motions. Critical layer indicated with horizontal lines.

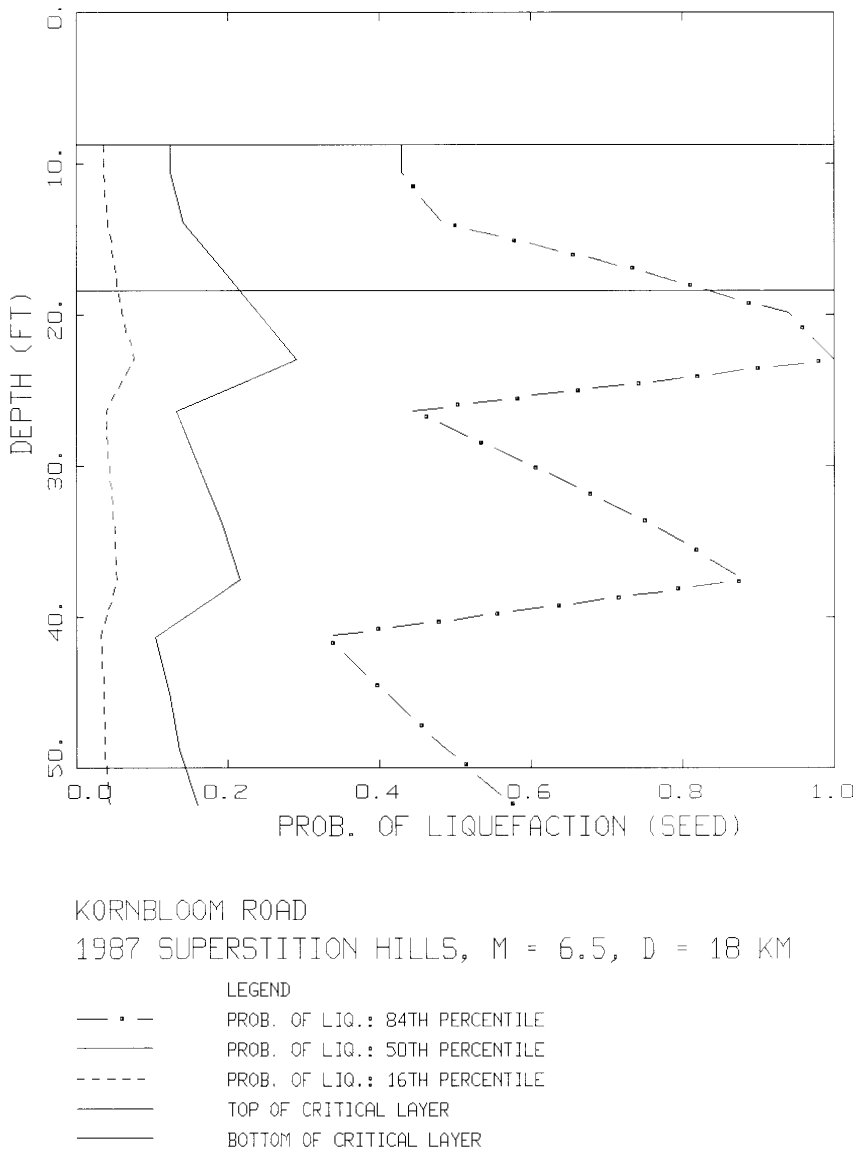


Figure 12o. Variation probability of liquefaction using the Seed et al. (2002) SPT based approach verses depth computed for a suite of random profiles at the Kornbloom Road site. Average horizontal spectrum (Figure 12a) based on recorded motions used as control motions. Critical layer indicated with horizontal lines.

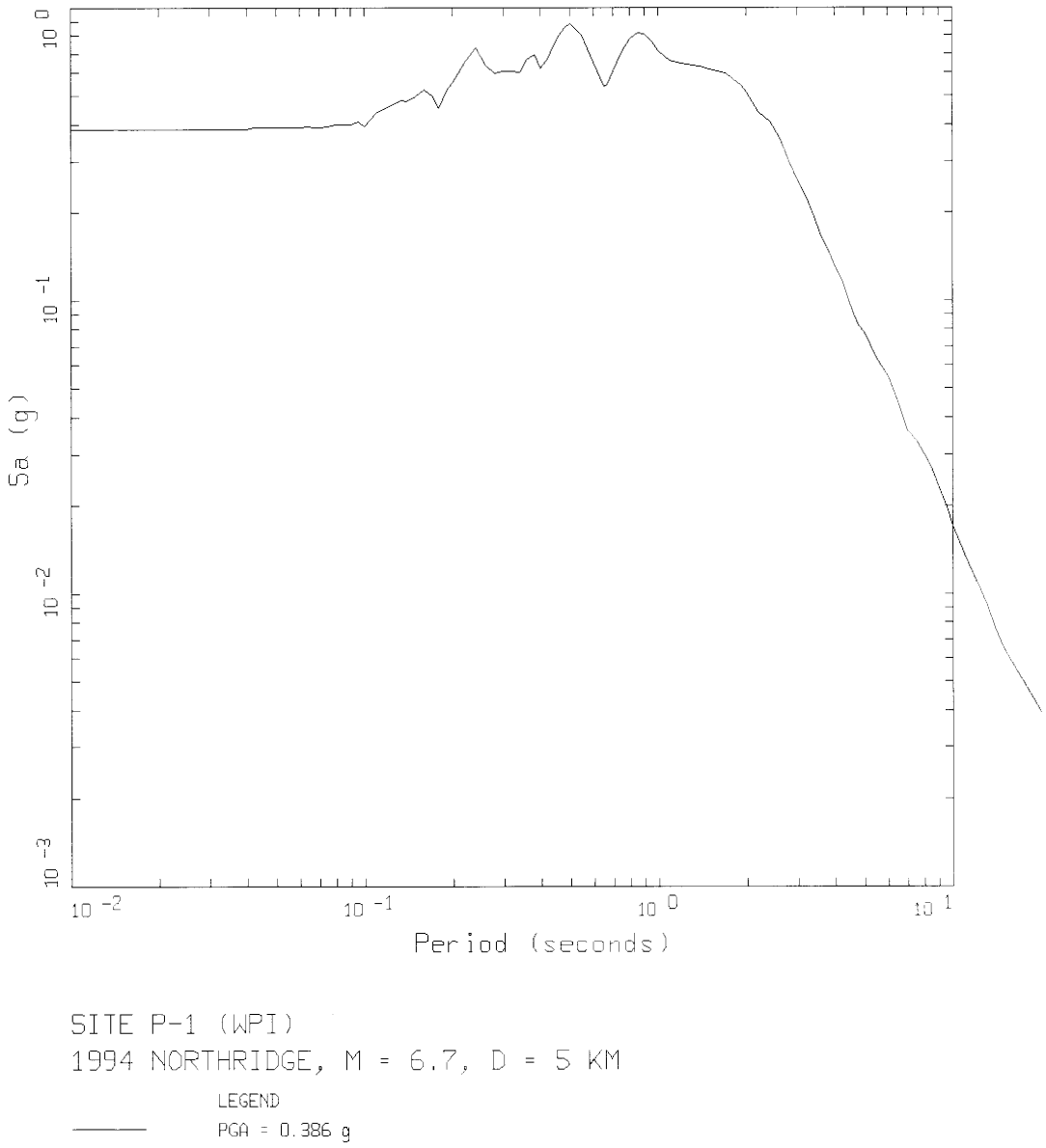


Figure 13a. Average horizontal component response spectra computed from measured motions: West Pico Canyon, P-1 site, 1994 Northridge earthquake.

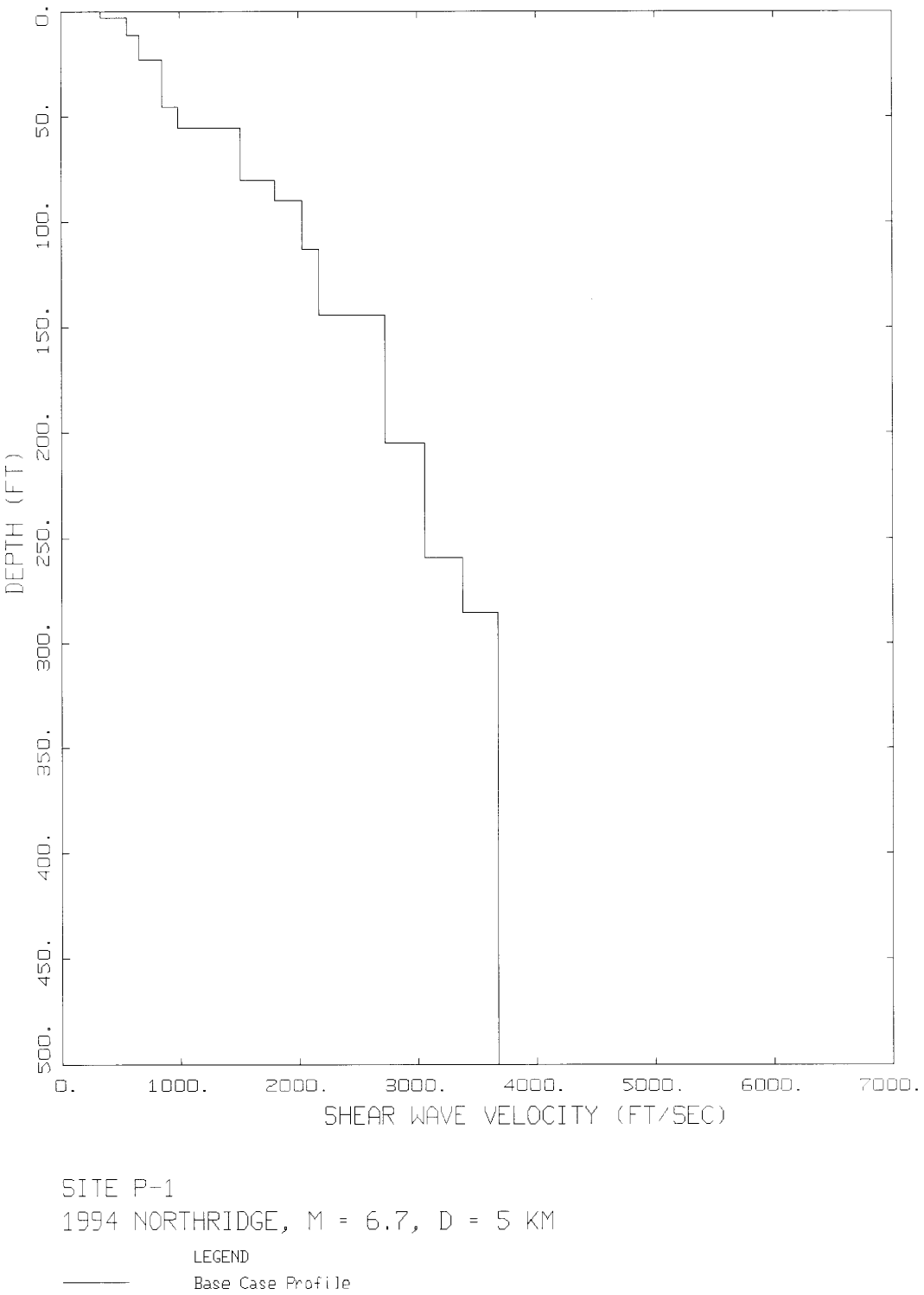


Figure 13b. Shear-wave velocity profile (measured) at the West Pico Canyon, P-1 site to a depth of 500 ft.

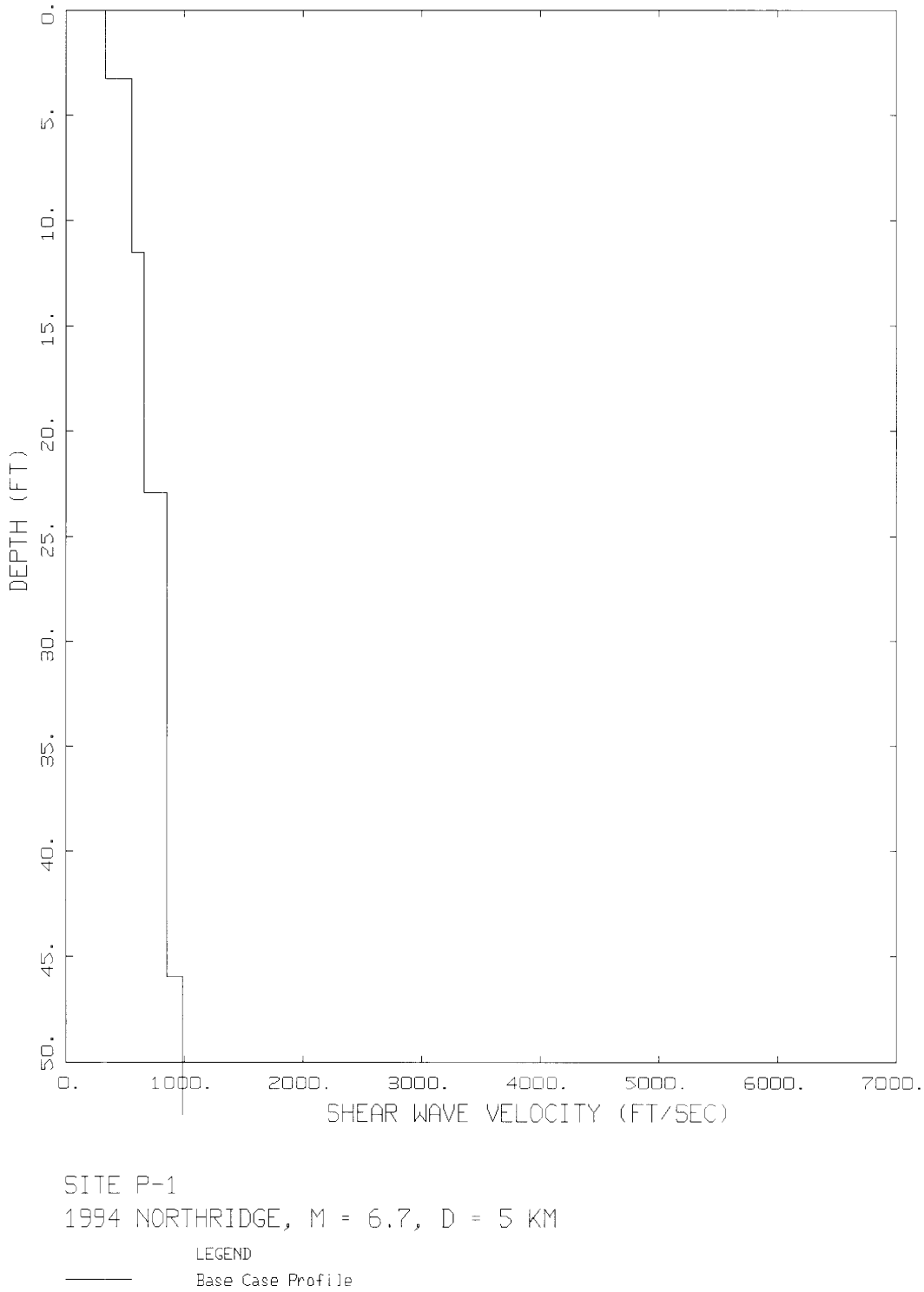


Figure 13c. Shear-wave velocity profile (measured) at the West Pico Canyon, P-1 site to a depth of 50 ft.

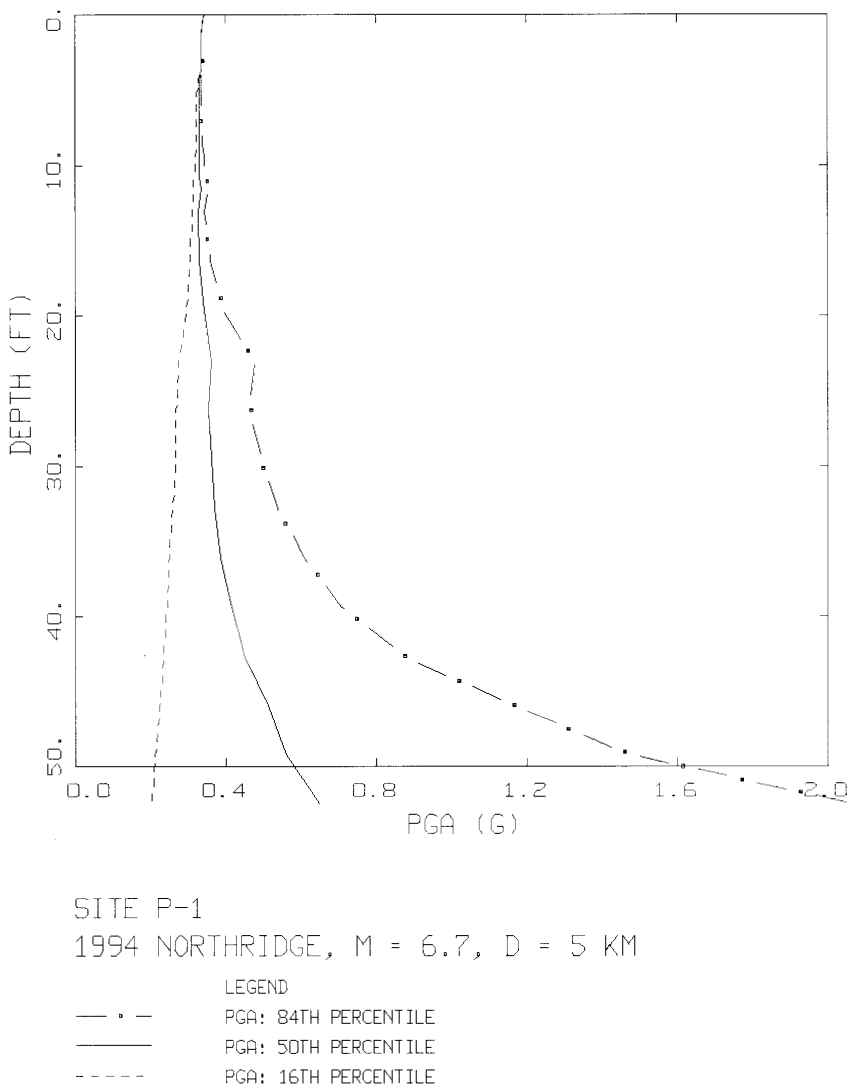


Figure 13d. Variation of peak acceleration(g) (Average horizontal component) verses depth computed for a suite of random profiles at the West Pico Canyon, P-1 site. Average horizontal spectrum (Figure 13a) based on recorded motions used as control motions.

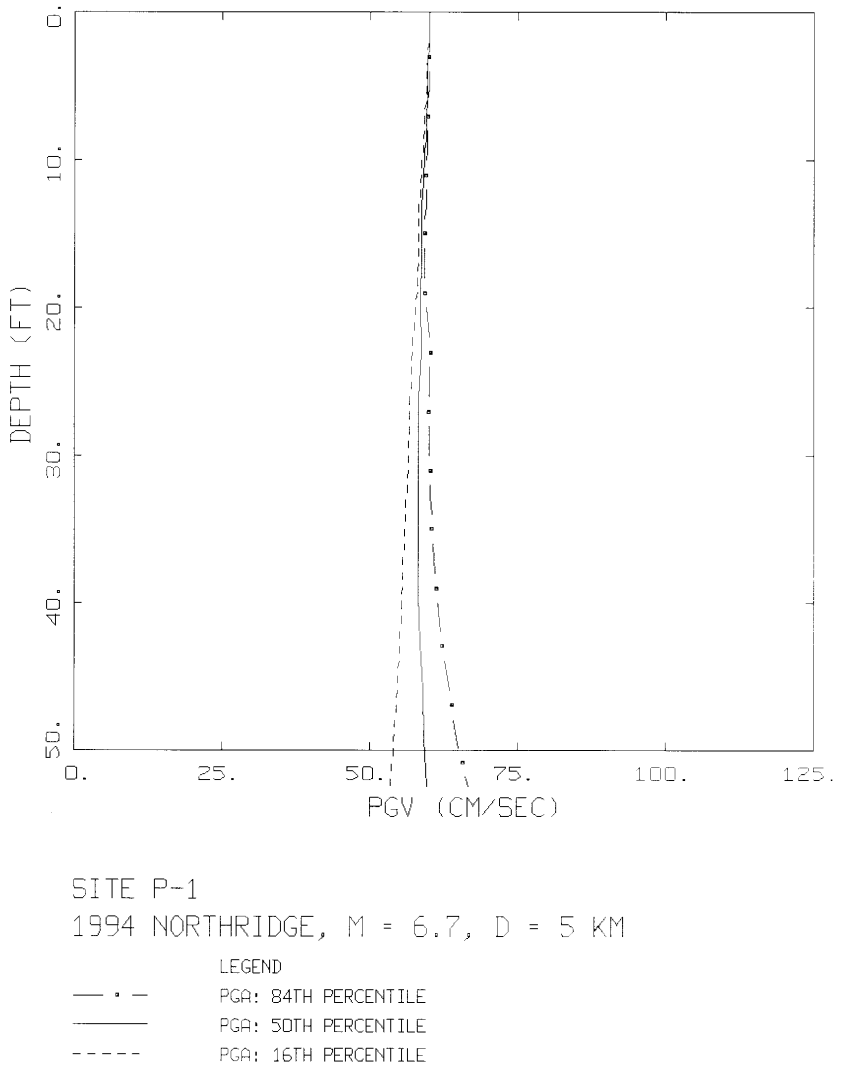


Figure 13e. Variation of peak particle velocity (cm/sec) verses depth computed for a suite of random profiles at the West Pico Canyon, P-1 site. Average horizontal spectrum (Figure 13a) based on recorded motions used as control motions.

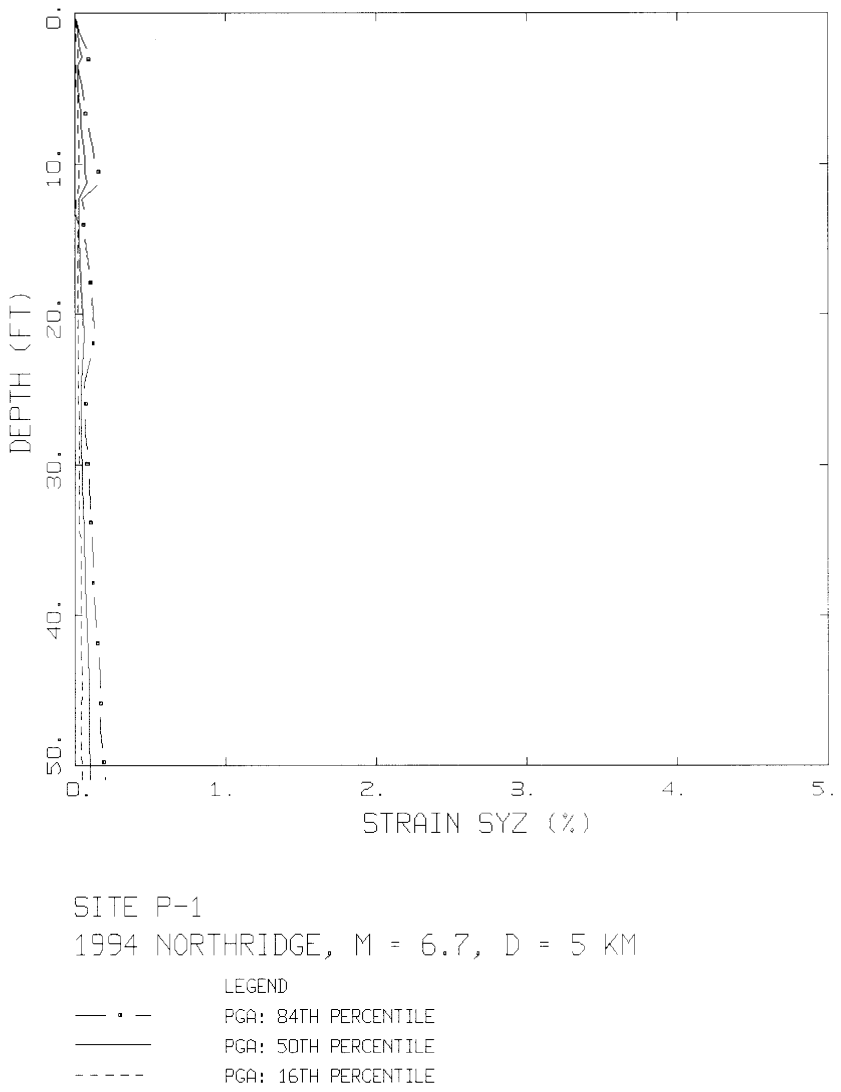


Figure 13f. Variation of peak shear strain(%) verses depth computed for a suite of random profiles at the West Pico Canyon, P-1 site. Average horizontal spectrum (Figure 13a) based on recorded motions used as control motions.

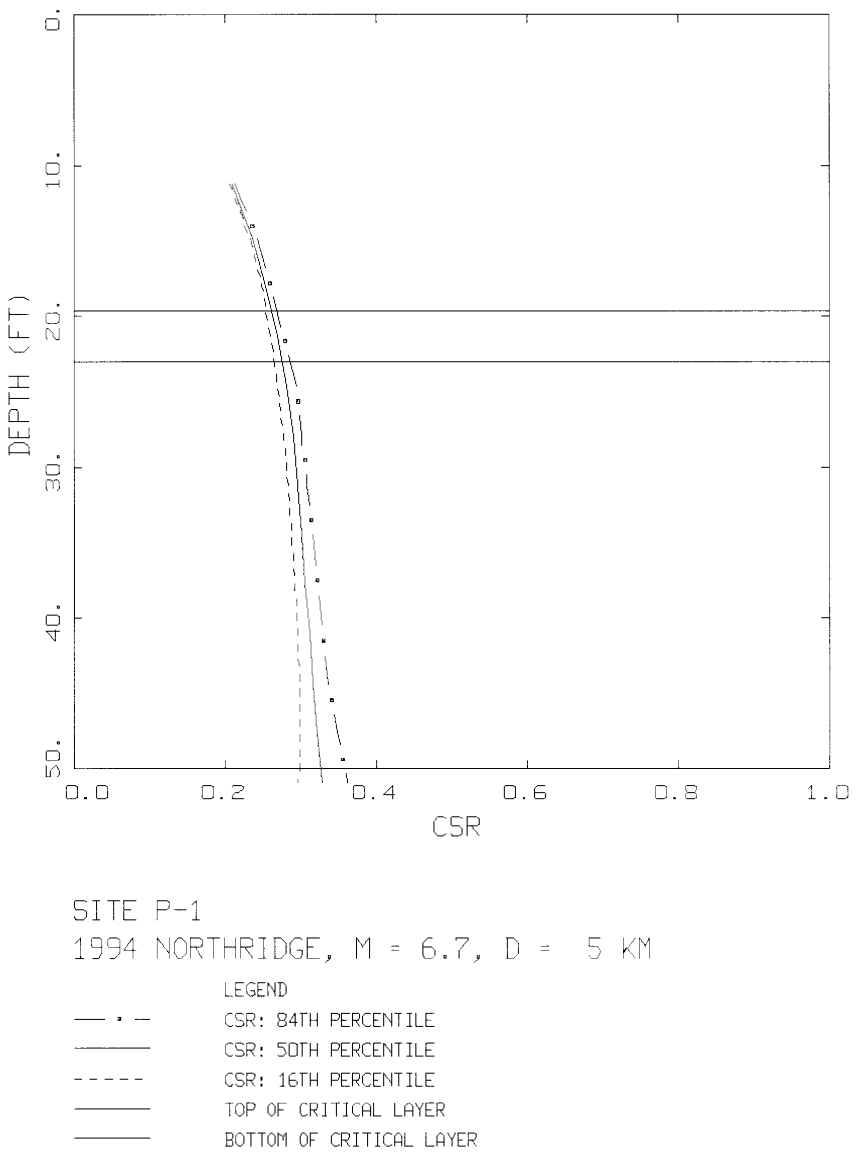


Figure 13g. Variation of CSR verses depth computed for a suite of random profiles for at West Pico Canyon, P-1 site. Average horizontal spectrum (Figure 13a) based on recorded motions used as control motions. Critical layer indicated with horizontal lines.

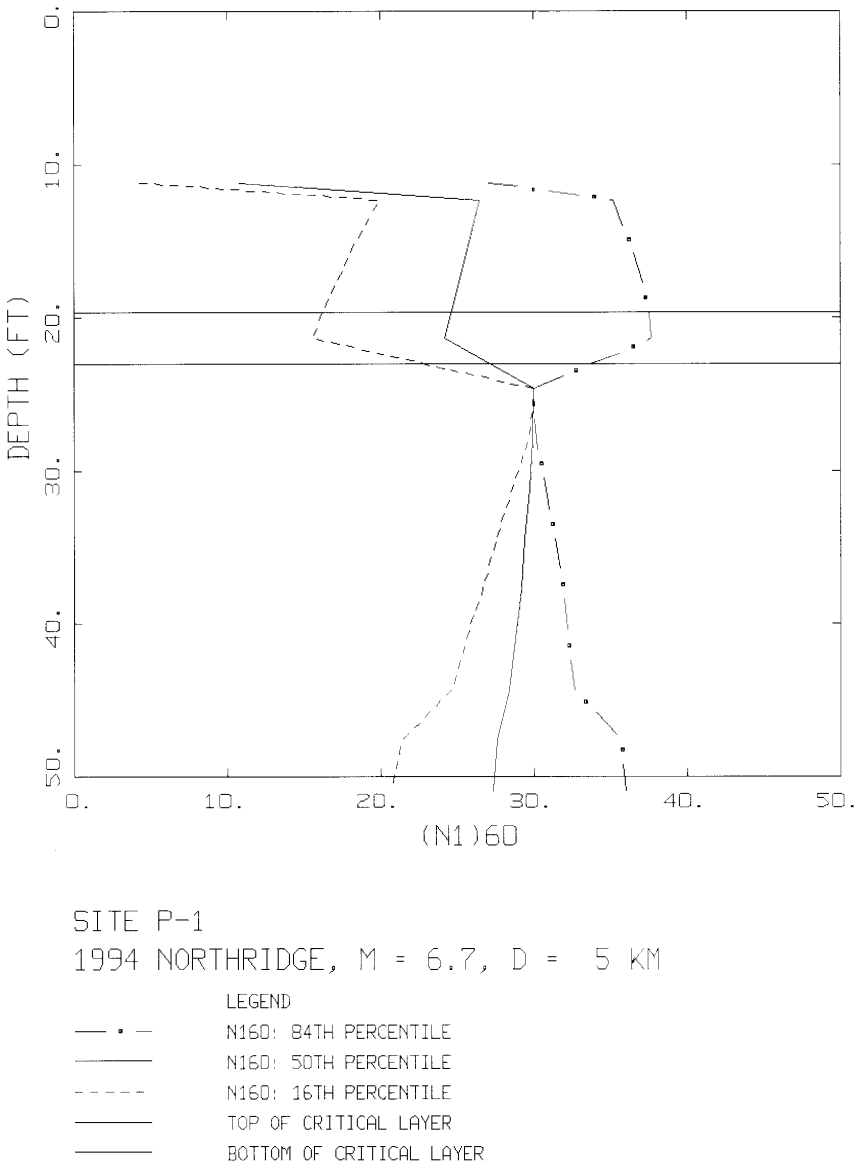


Figure 13h. Variation of peak $(N_1)_{60}$ verses depth computed for a suite of random profiles at the West Pico Canyon, P-1 site using the shear-wave velocity correlation model of Iwasaki et al., (1987). Average horizontal spectrum (Figure 13a) based on recorded motions used as control motions. Critical layer indicated with horizontal lines.

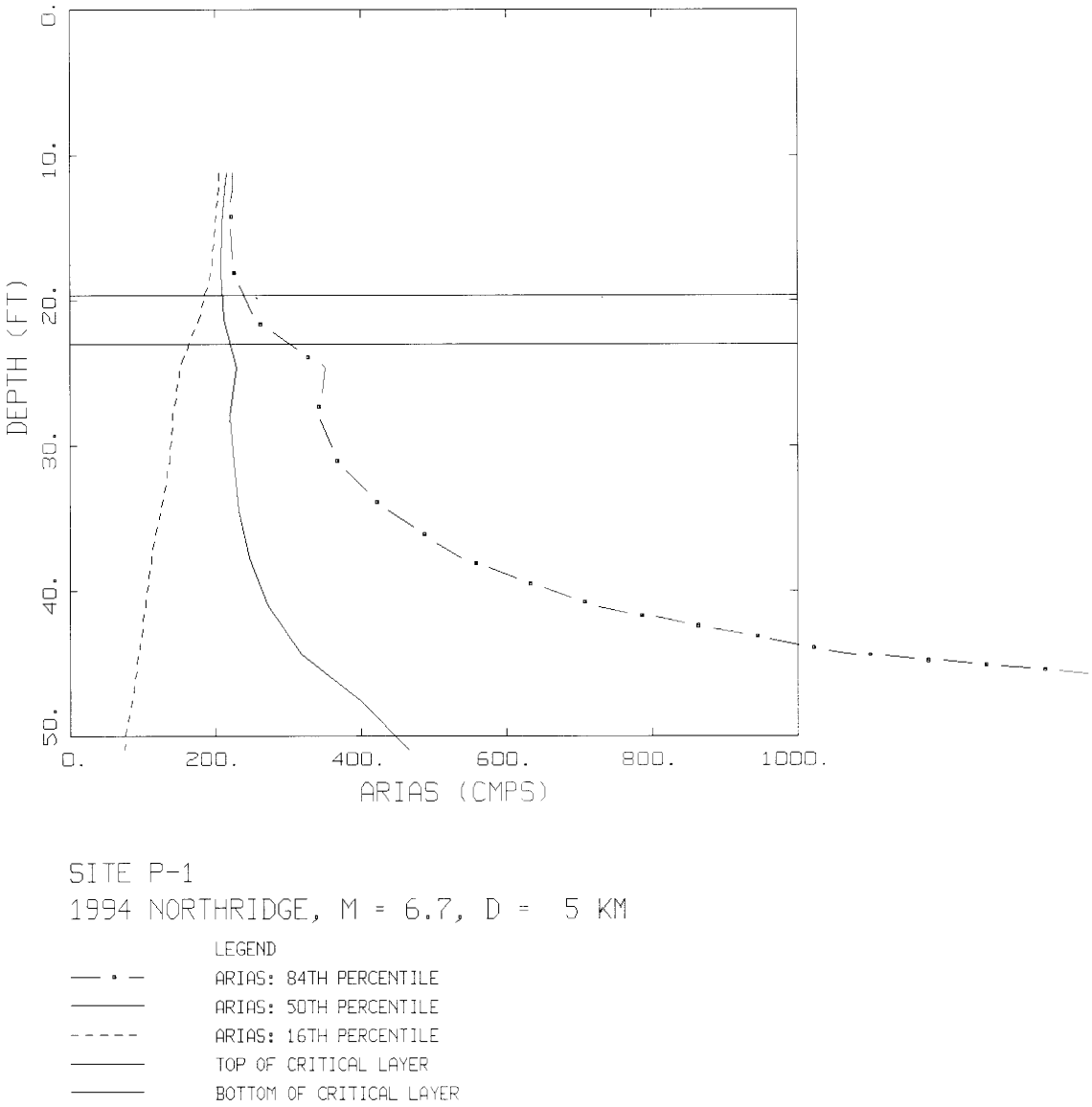


Figure 13i. Variation of Arias Intensity (cm/sec) verses depth computed for a suite of random profiles at the West Pico Canyon, P-1 site. Average horizontal spectrum (Figure 13a) based on recorded motions used as control motions. Critical layer indicated with horizontal lines.

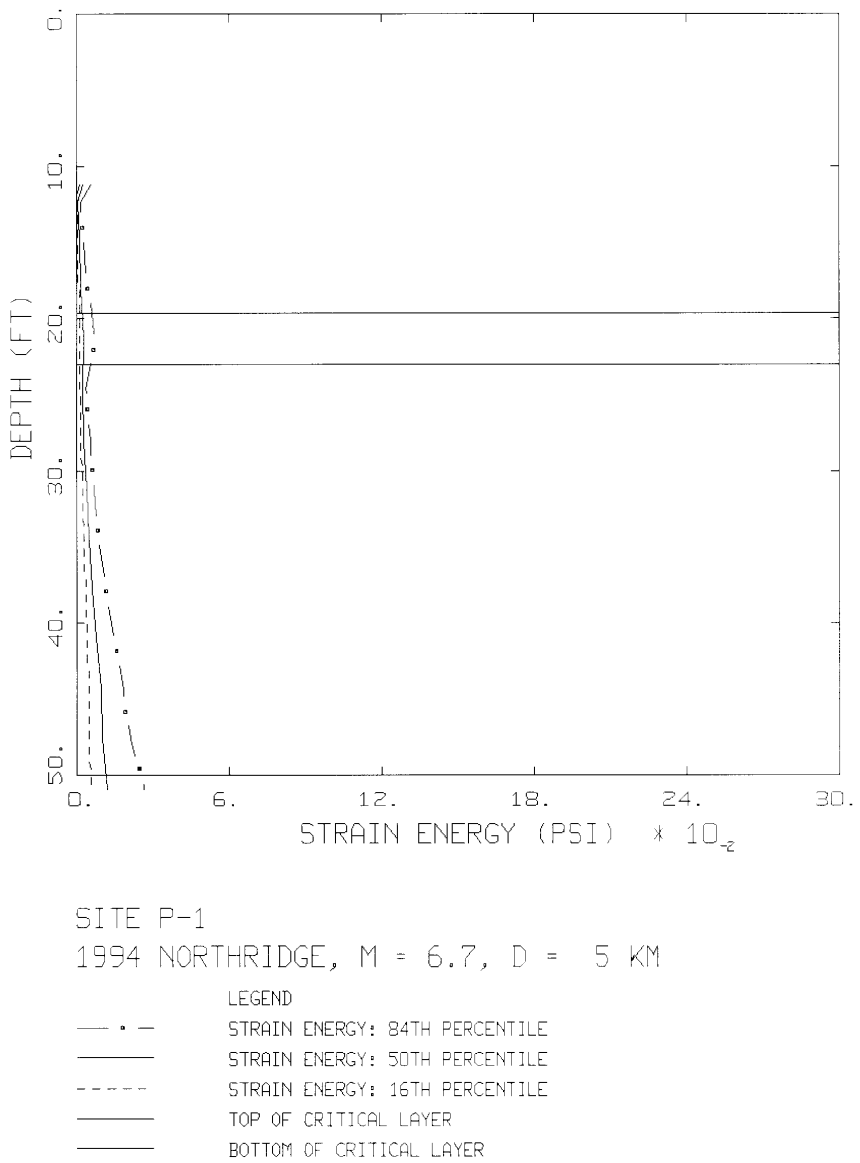


Figure 13j Variation of strain energy (PSI) verses depth computed for a suite of random profiles at the West Pico Canyon, P-1 site. Average horizontal spectrum (Figure 13a) based on recorded motions used as control motions. Critical layer indicated with horizontal lines.

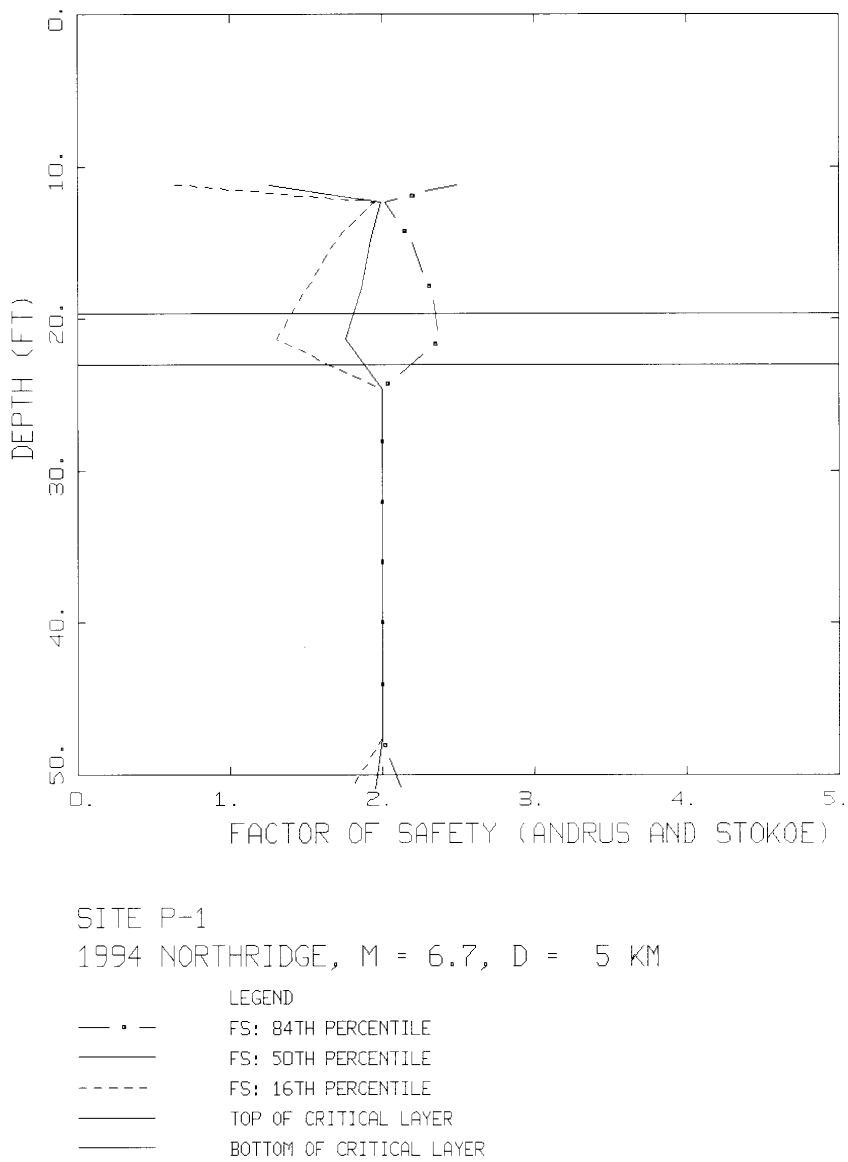


Figure 13k. Variation of the factor of safety (FS) using the Andrus and Stokoe (2001) shear-wave velocity based approach verses depth computed for a suite of random profiles at the West Pico Canyon, P-1 site. Average horizontal spectrum (Figure 13a) based on recorded motions used as control motions. Critical layer indicated with horizontal lines.

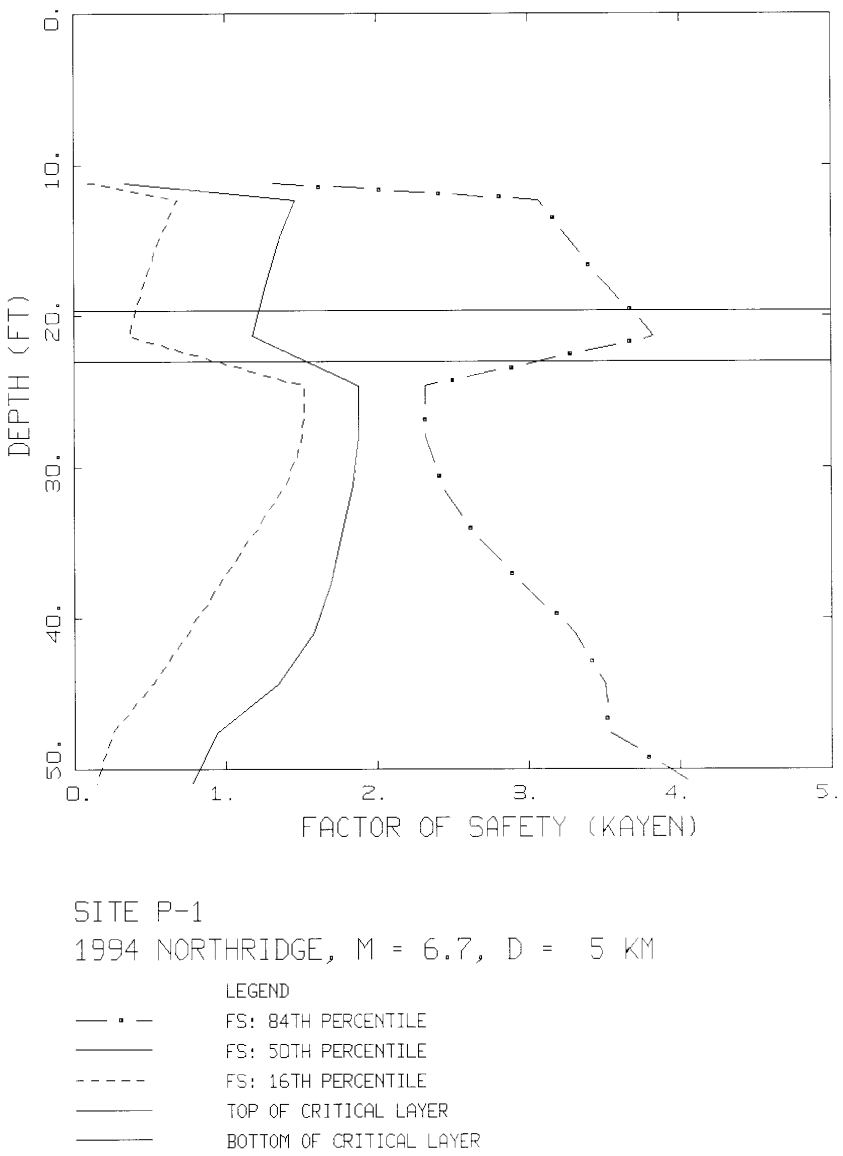


Figure 13l. Variation of the factor of safety using the Kayen and Mitchell (1979) Arias Intensity based approach verses depth computed for a suite of random profiles at the West Pico Canyon, P-1 site. Average horizontal spectrum (Figure 13a) based on recorded motions used as control motions. Critical layer indicated with horizontal lines.

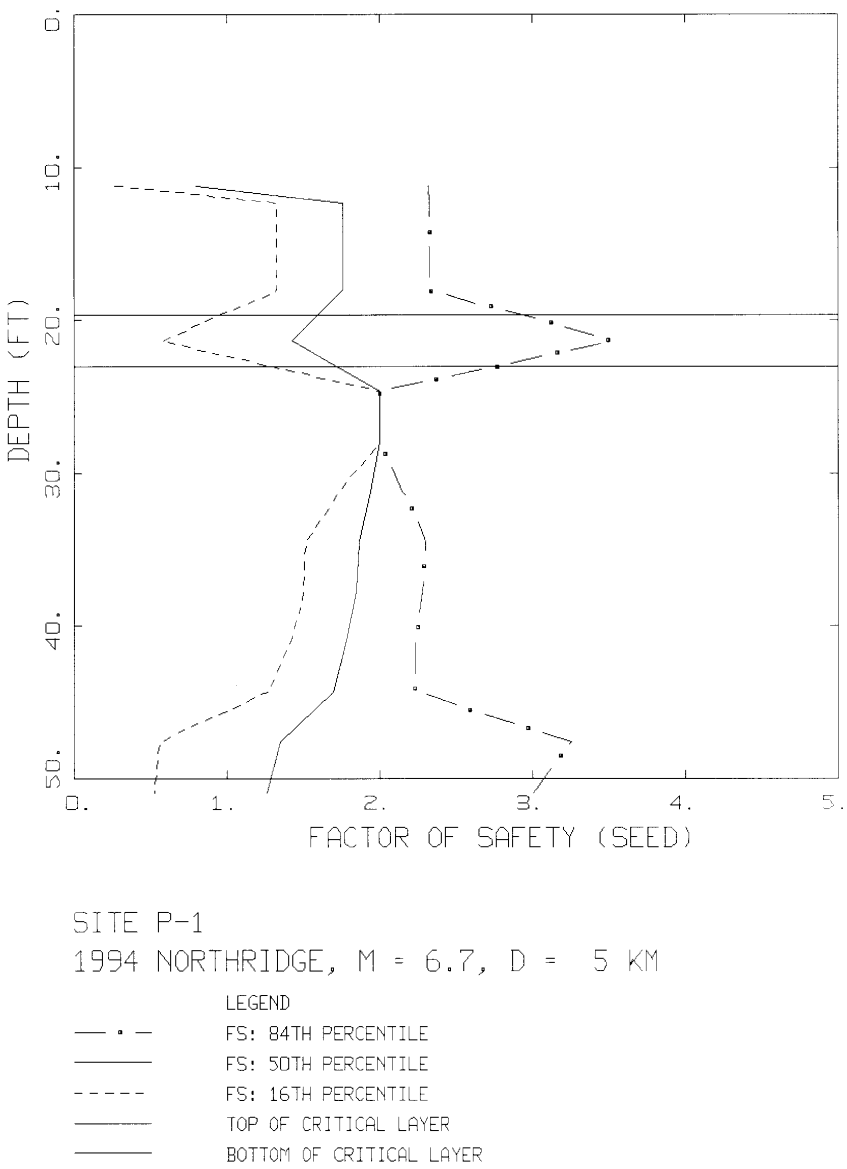


Figure 13m. Variation of the factor of the factor of safety using the Seed et al., (2002) SPT based approach verses depth computed for a suite of random profiles at the West Pico Canyon, P-1 site. Average horizontal spectrum (Figure 13a) based on recorded motions used as control motions. Critical layer indicated with horizontal lines.

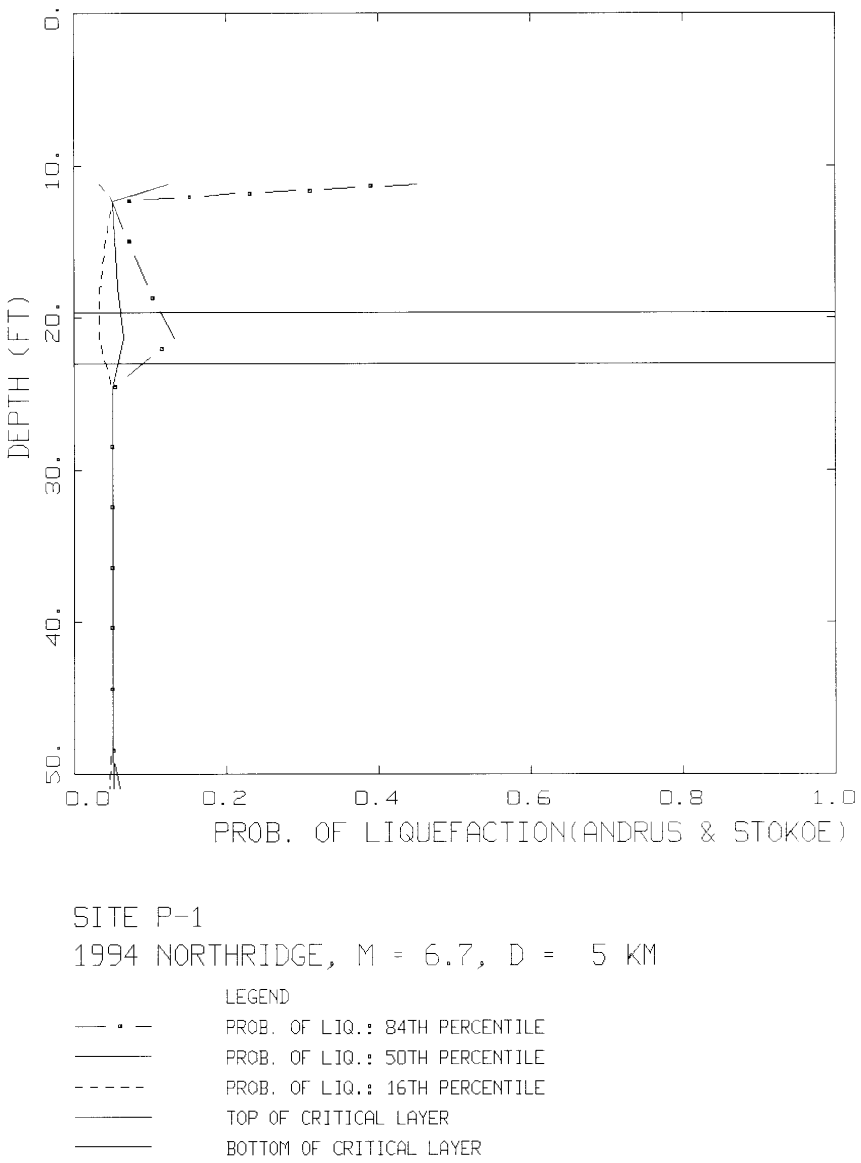


Figure 13n. Variation of the probability of liquefaction using the Andrus and Stokoe (2004) shear-wave velocity based approach verses depth computed for a suite of random profiles at the West Pico Canyon, P-1 site. Average horizontal spectrum (Figure 13a) based on recorded motions used as control motions. Critical layer indicated with horizontal lines.

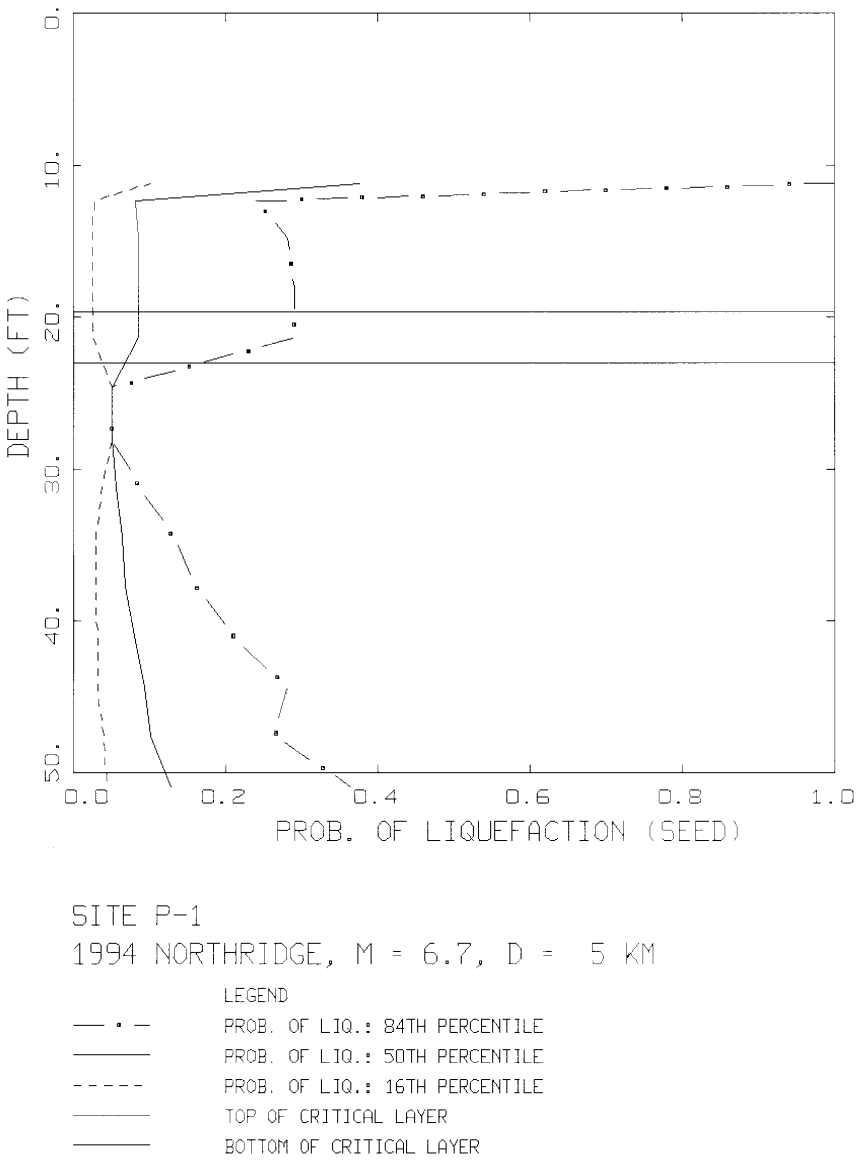


Figure 13o. Variation probability of liquefaction using the Seed et al. (2002) SPT based approach verses depth computed for a suite of random profiles at the West Pico Canyon, P-1 site. Average horizontal spectrum (Figure 13a) based on recorded motions used as control motions. Critical layer indicated with horizontal lines.

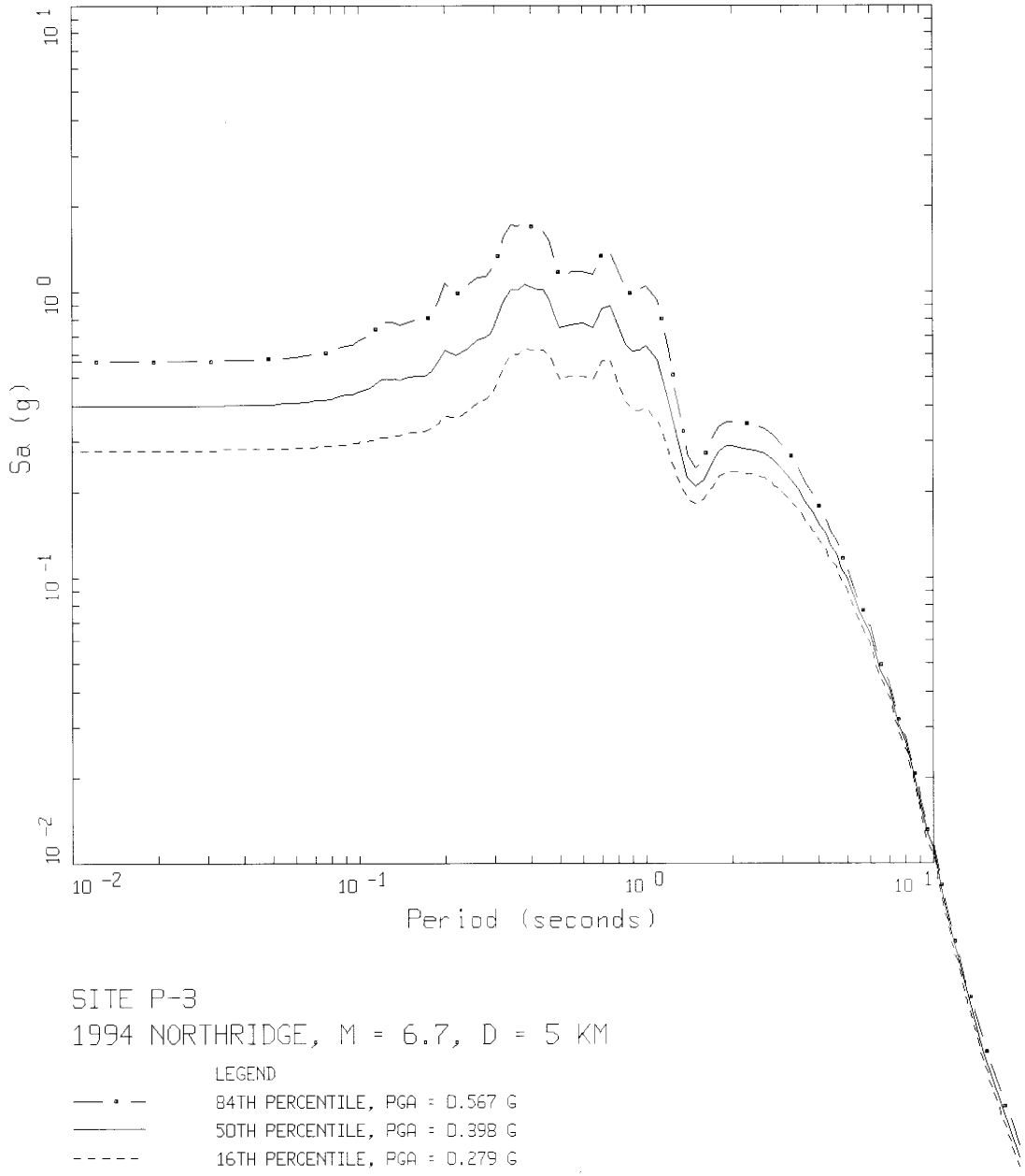


Figure 14a. Average horizontal component response spectra computed from simulated motions: West Pico Canyon, P-3 site, 1994 Northridge earthquake.

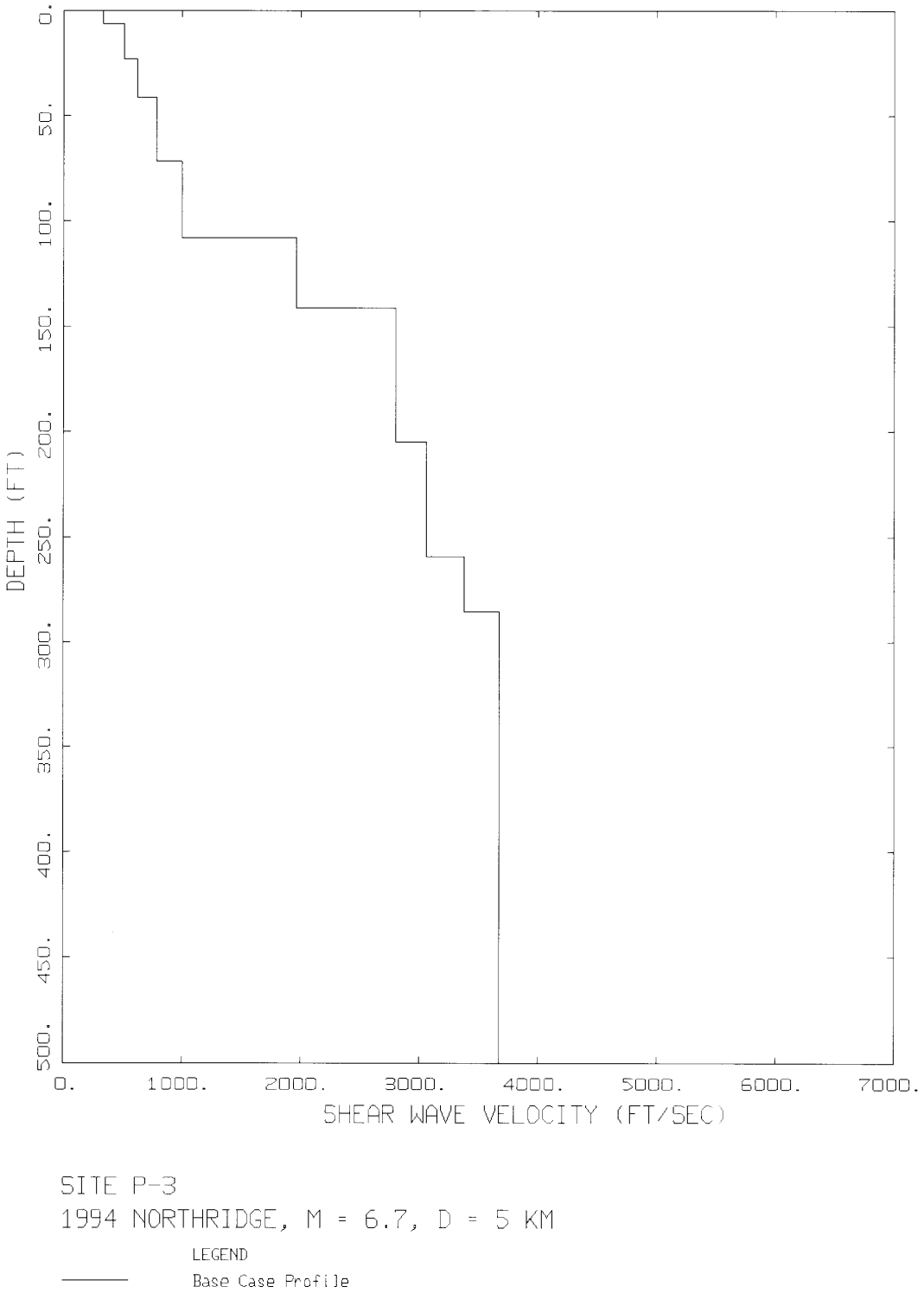


Figure 14b. Shear-wave velocity profile (measured) at the West Pico Canyon, P-3 site to a depth of 500 ft.

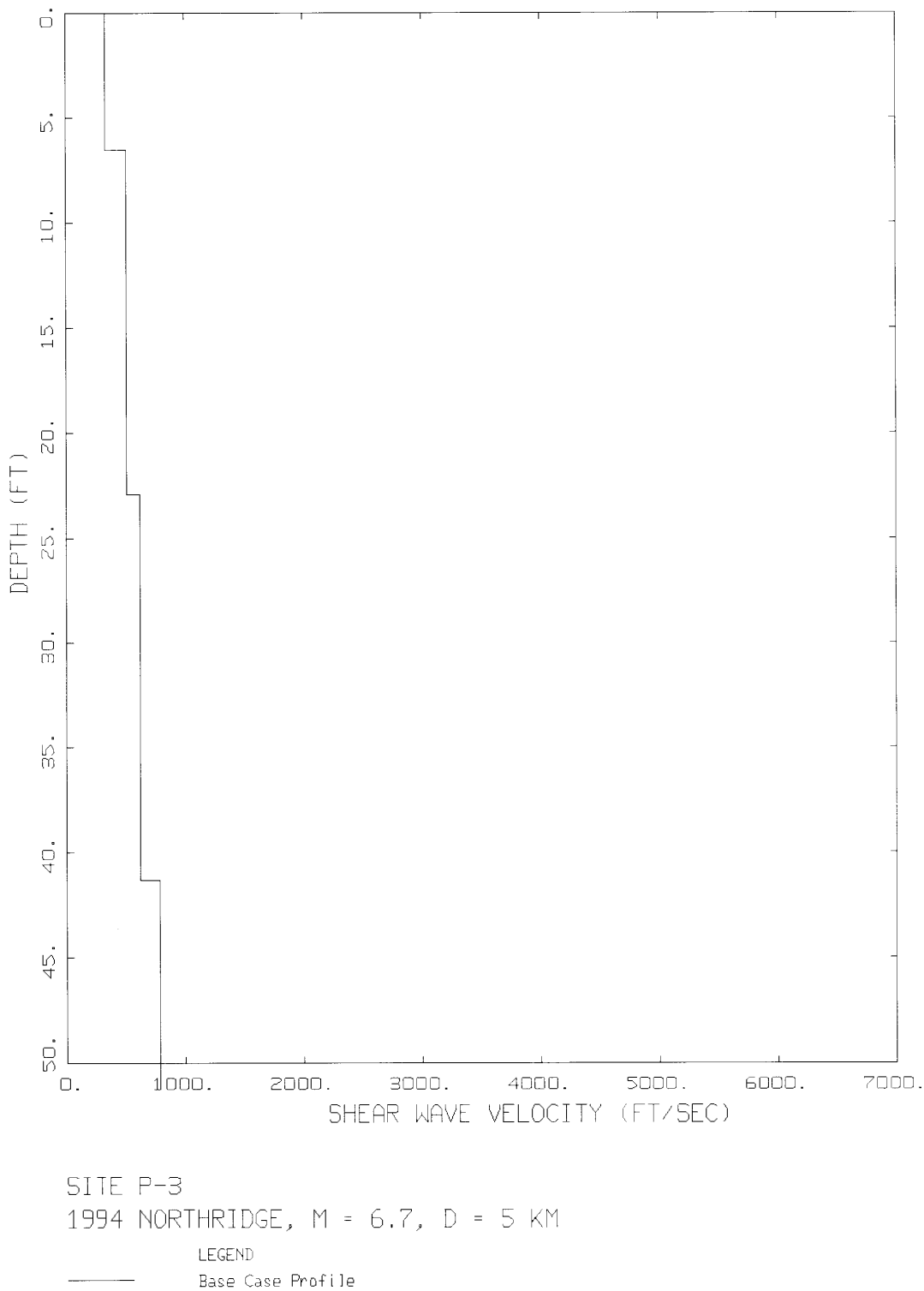


Figure 14c. Shear-wave velocity profile (measured) at the West Pico Canyon, P-3 site to a depth of 50 ft.

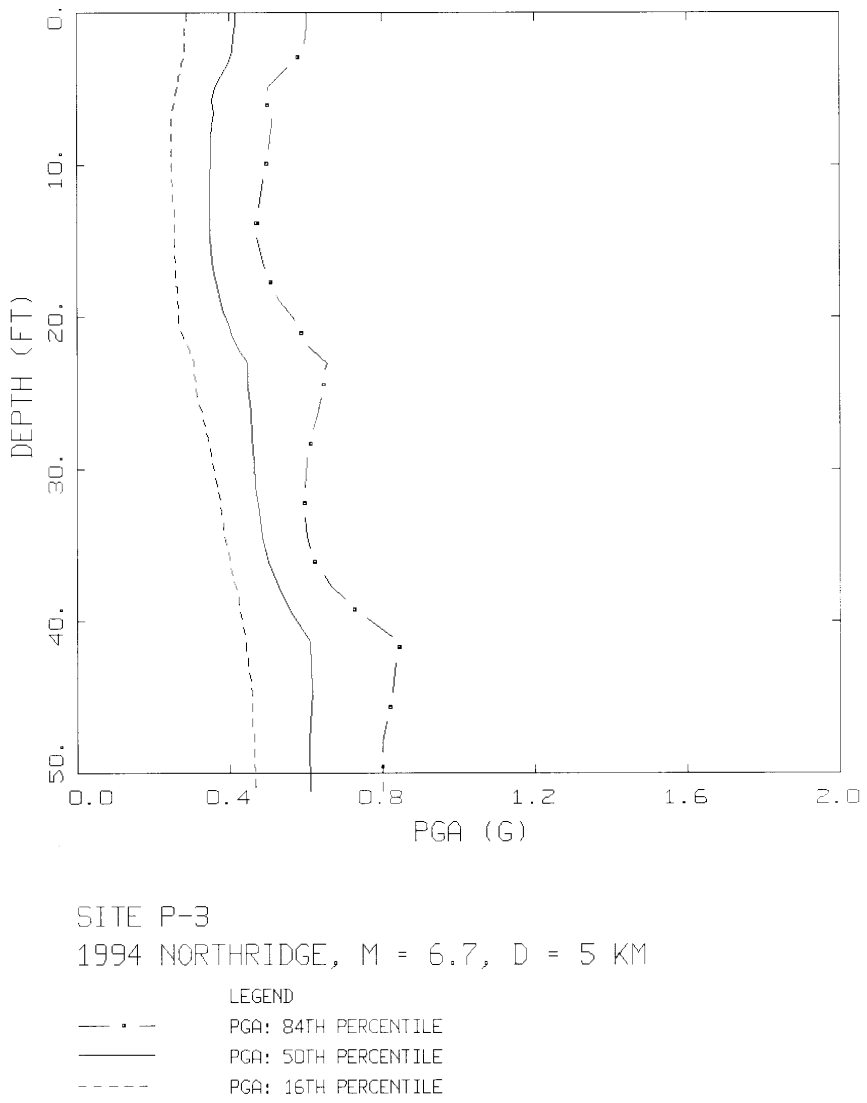


Figure 14d. Variation of peak acceleration(g) (Average horizontal component) verses depth computed for a suite of random profiles at the West Pico Canyon, P-3 site. Average horizontal spectrum (Figure 14a) based on simulated motions used as control motions.

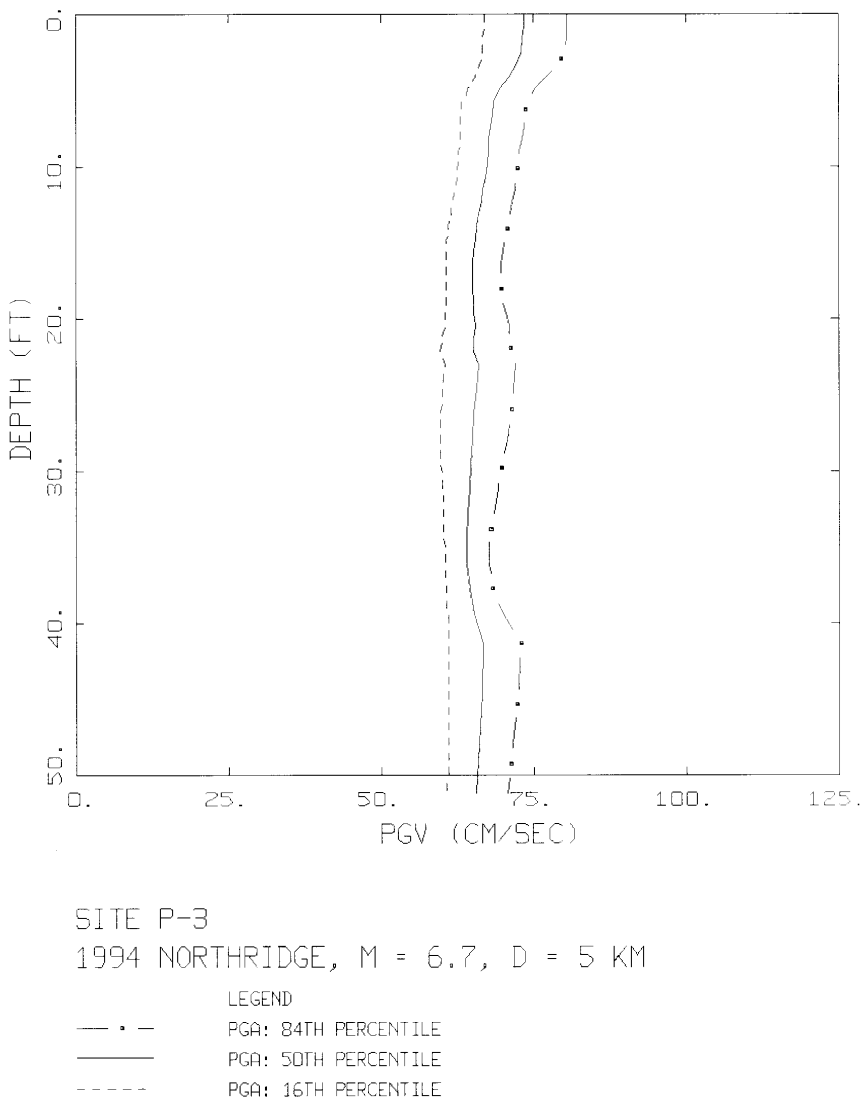


Figure 14e. Variation of peak particle velocity (cm/sec) verses depth computed for a suite of random profiles at the West Pico Canyon, P-3 site. Average horizontal spectrum (Figure 14a) based on simulated motions used as control motions.

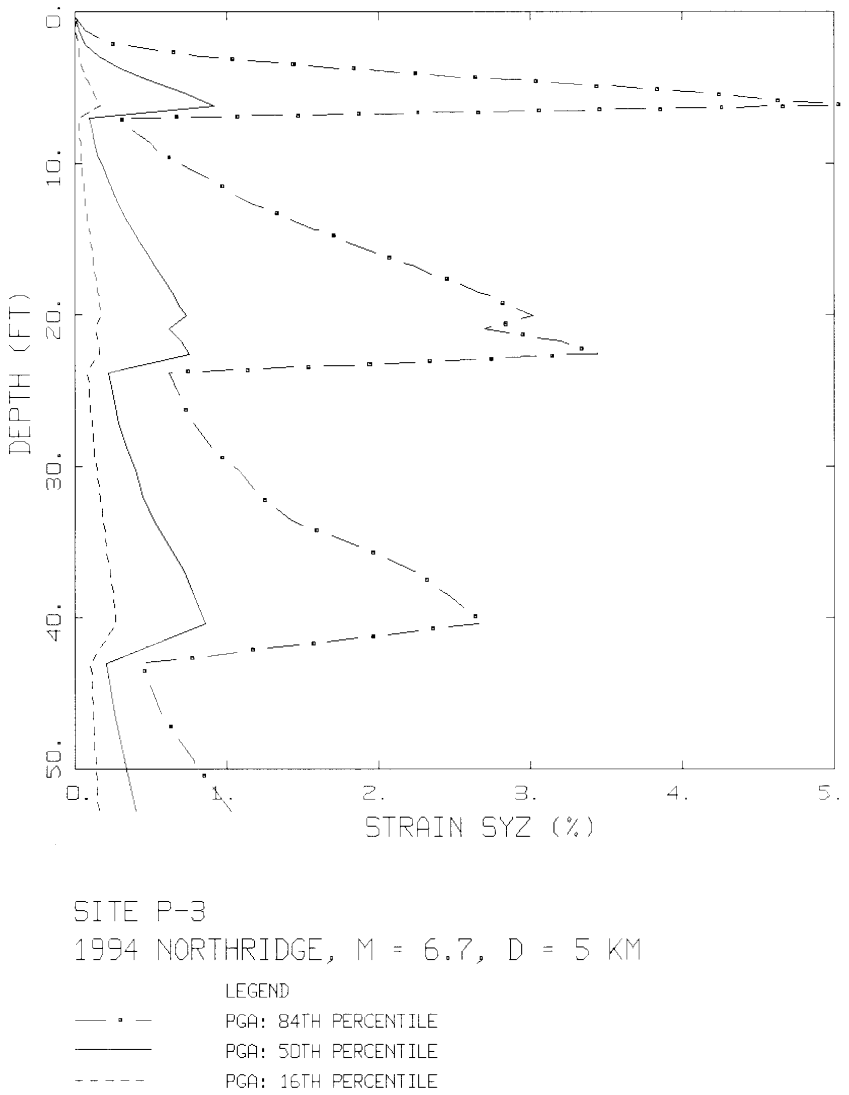


Figure 14f. Variation of peak shear strain(%) verses depth computed for a suite of random profiles at the West Pico Canyon, P-3 site. Average horizontal spectrum (Figure 14a) based on simulated motions used as control motions.

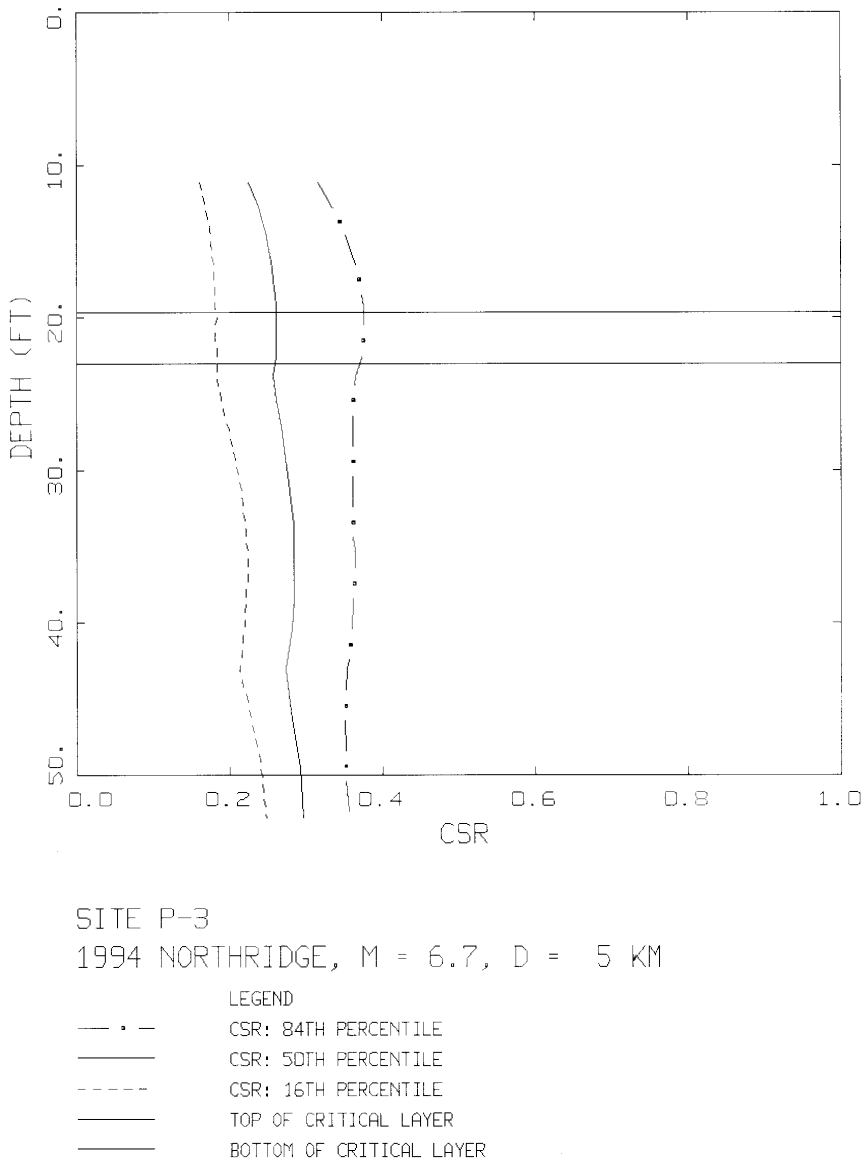


Figure 14g. Variation of CSR verses depth computed for a suite of random profiles for at West Pico Canyon, P-3 site. Average horizontal spectrum (Figure 14a) based on simulated motions used as control motions. Critical layer indicated with horizontal lines.

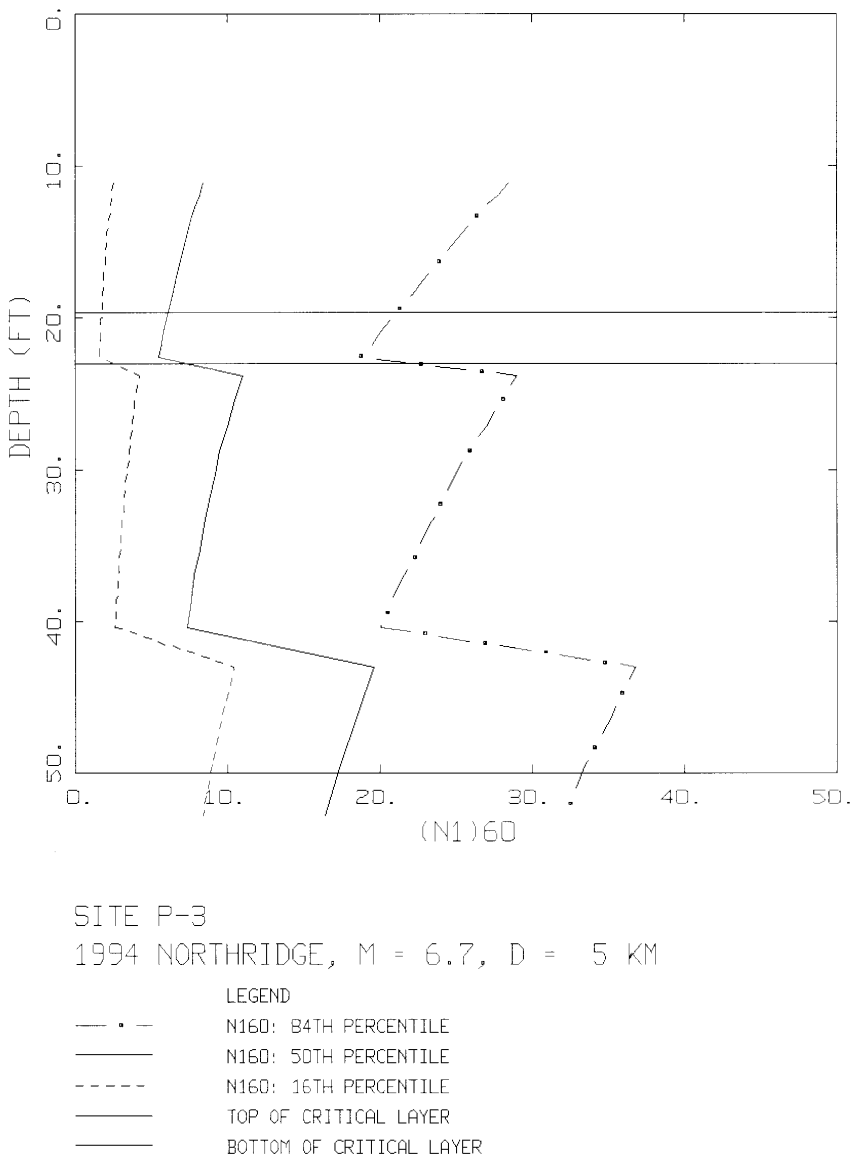


Figure 14h. Variation of peak $(N_1)_{60}$ verses depth computed for a suite of random profiles at the West Pico Canyon, P-3 site using the shear-wave velocity correlation model of Iwasaki et al., (1987). Average horizontal spectrum (Figure 14a) based on simulated motions used as control motions. Critical layer indicated with horizontal lines.

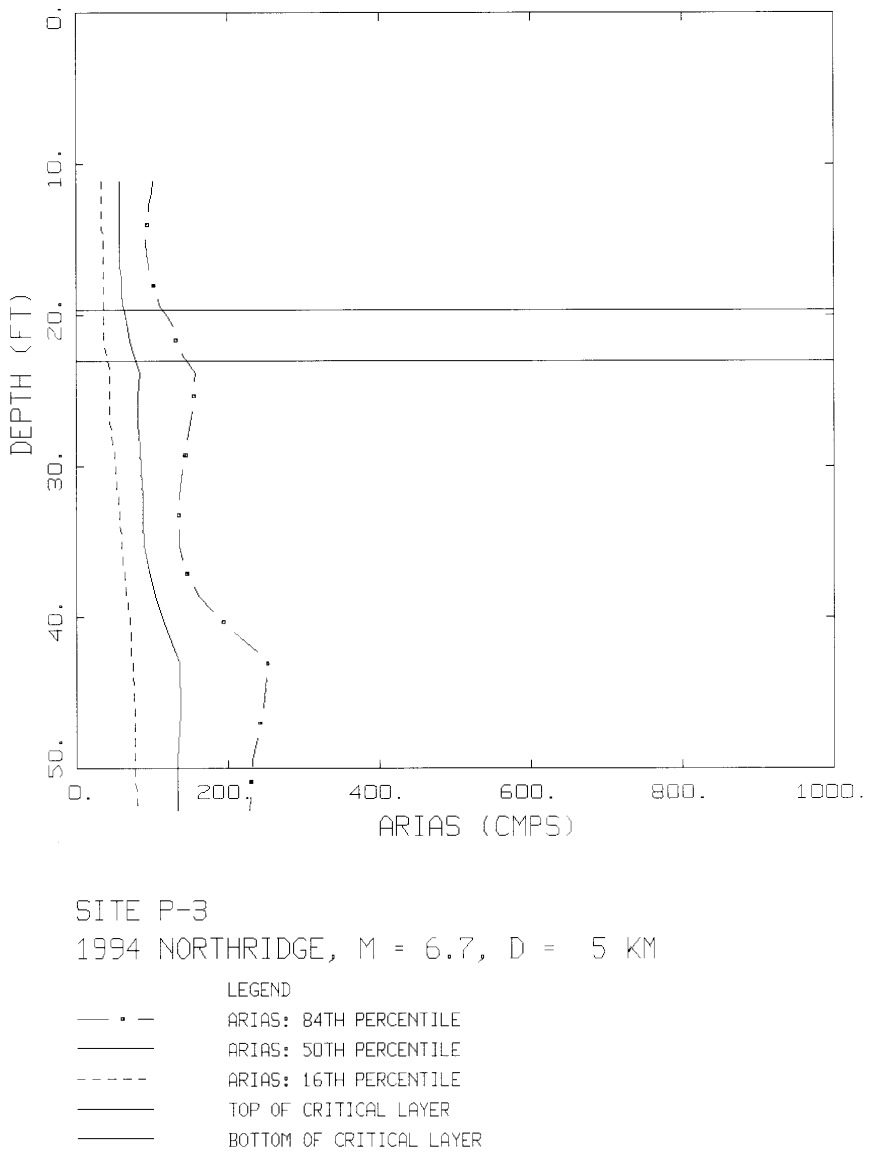


Figure 14i. Variation of Arias Intensity (cm/sec) verses depth computed for a suite of random profiles at the West Pico Canyon, P-3 site. Average horizontal spectrum (Figure 14a) based on simulated motions used as control motions. Critical layer indicated with horizontal lines.

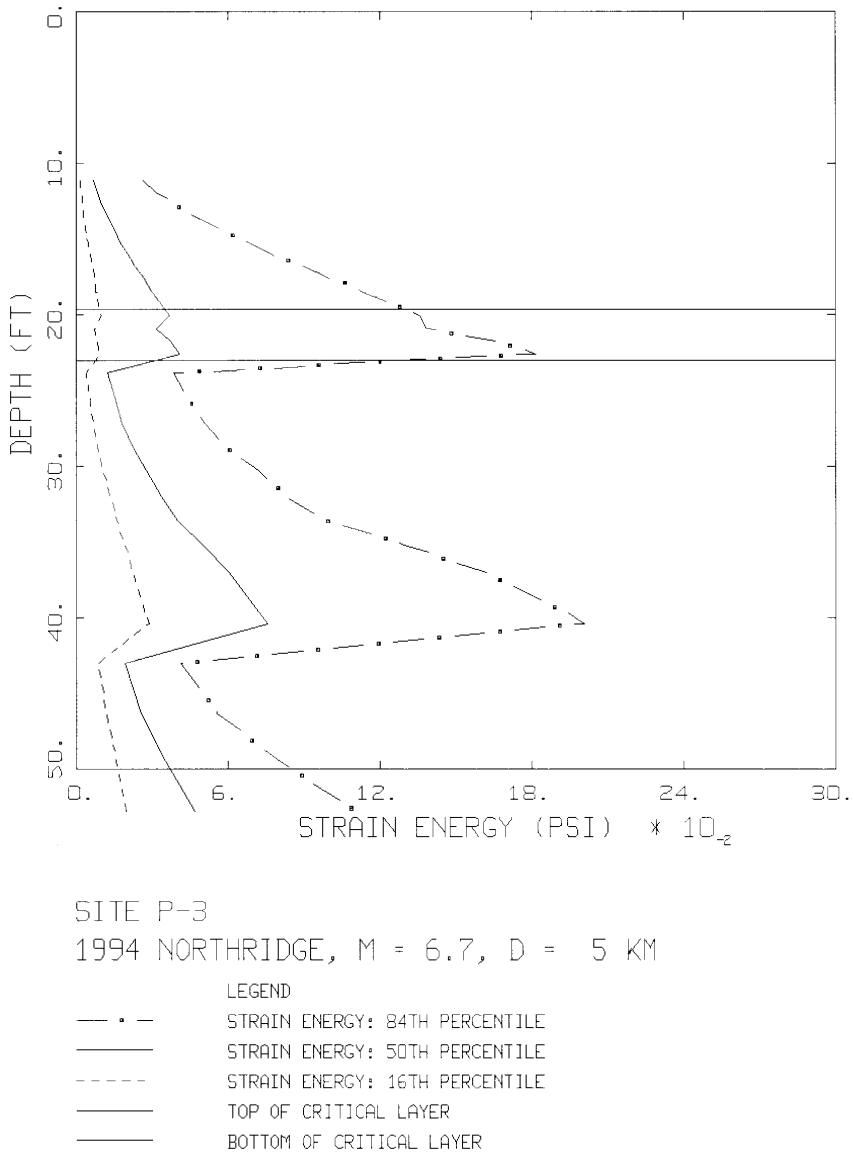


Figure 14j Variation of strain energy (PSI) verses depth computed for a suite of random profiles at the West Pico Canyon, P-3 site. Average horizontal spectrum (Figure 14a) based on simulated motions used as control motions. Critical layer indicated with horizontal lines.

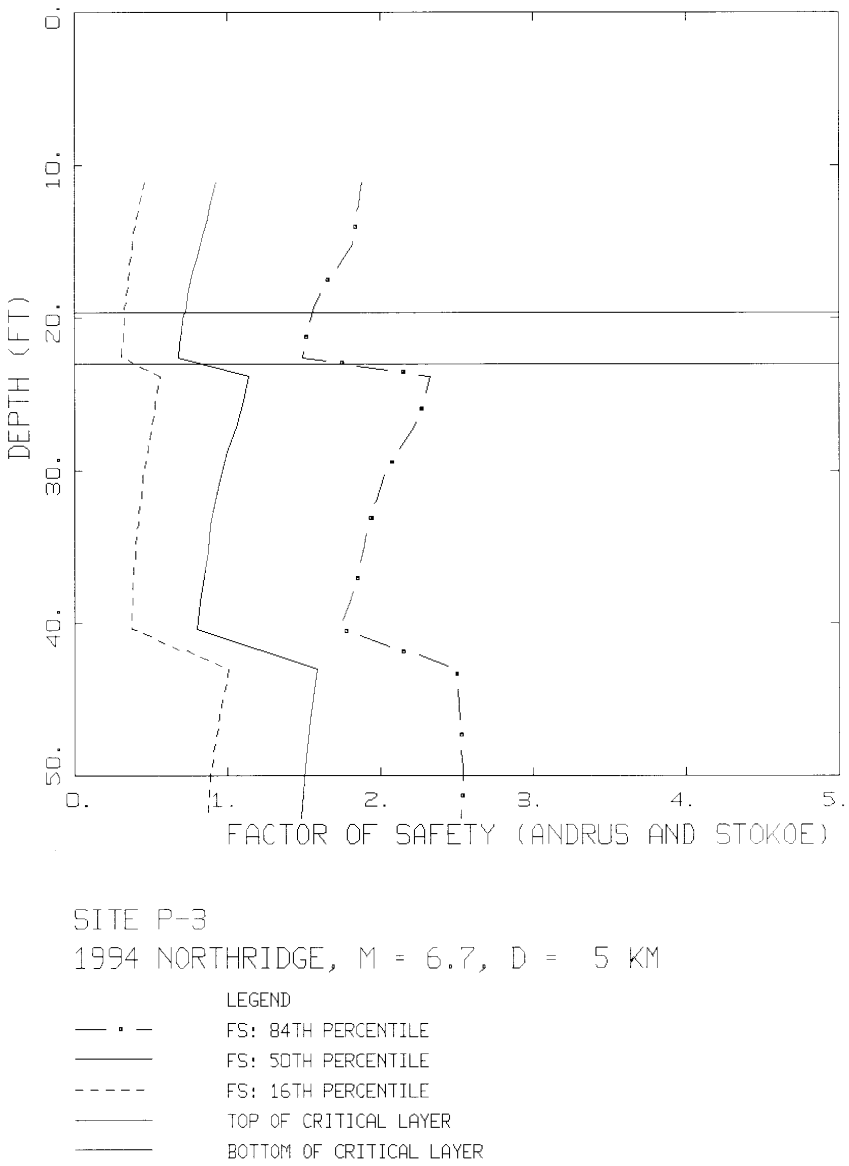


Figure 14k. Variation of the factor of safety (FS) using the Andrus and Stokoe (2004) shear-wave velocity based approach verses depth computed for a suite of random profiles at the West Pico Canyon, P-3 site. Average horizontal spectrum (Figure 14a) based on simulated motions used as control motions. Critical layer indicated with horizontal lines.

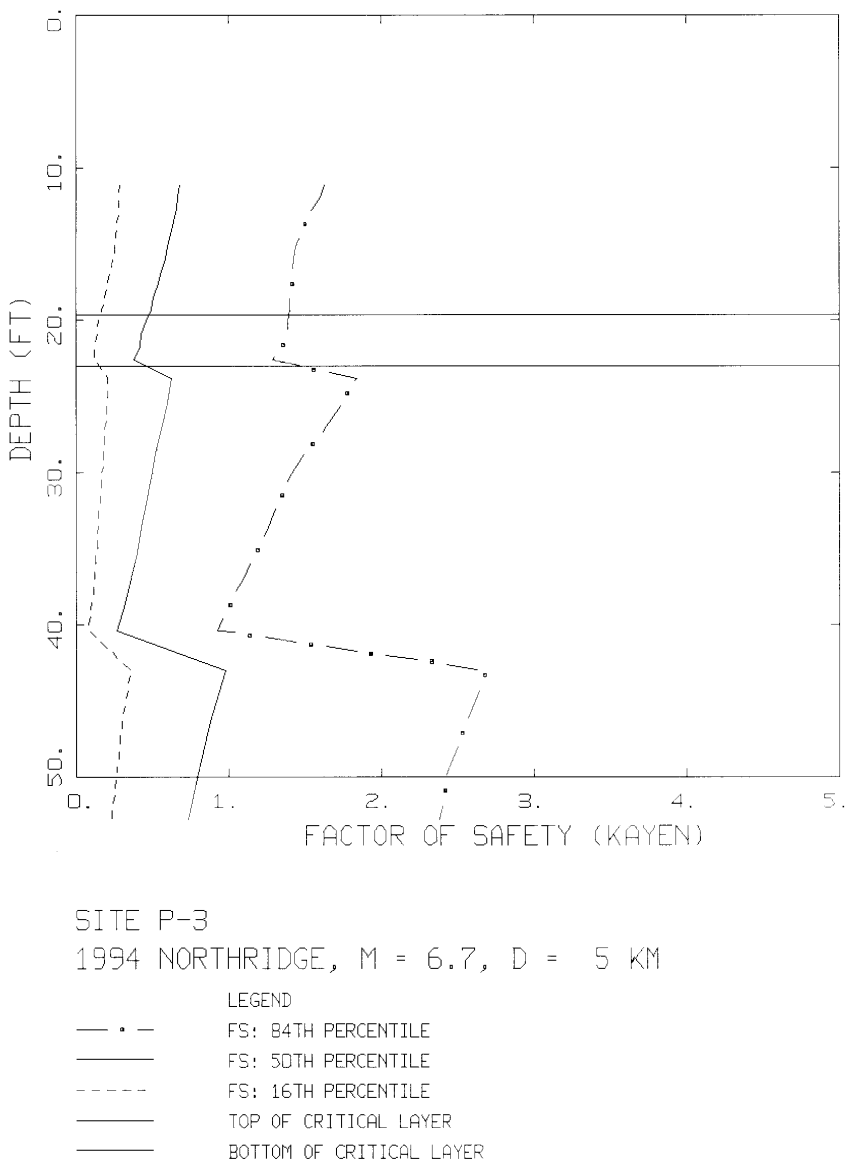


Figure 14l. Variation of the factor of safety using the Kayen and Mitchell (1979) Arias Intensity based approach verses depth computed for a suite of random profiles at the West Pico Canyon, P-3 site. Average horizontal spectrum (Figure 14a) based on simulated motions used as control motions. Critical layer indicated with horizontal lines.

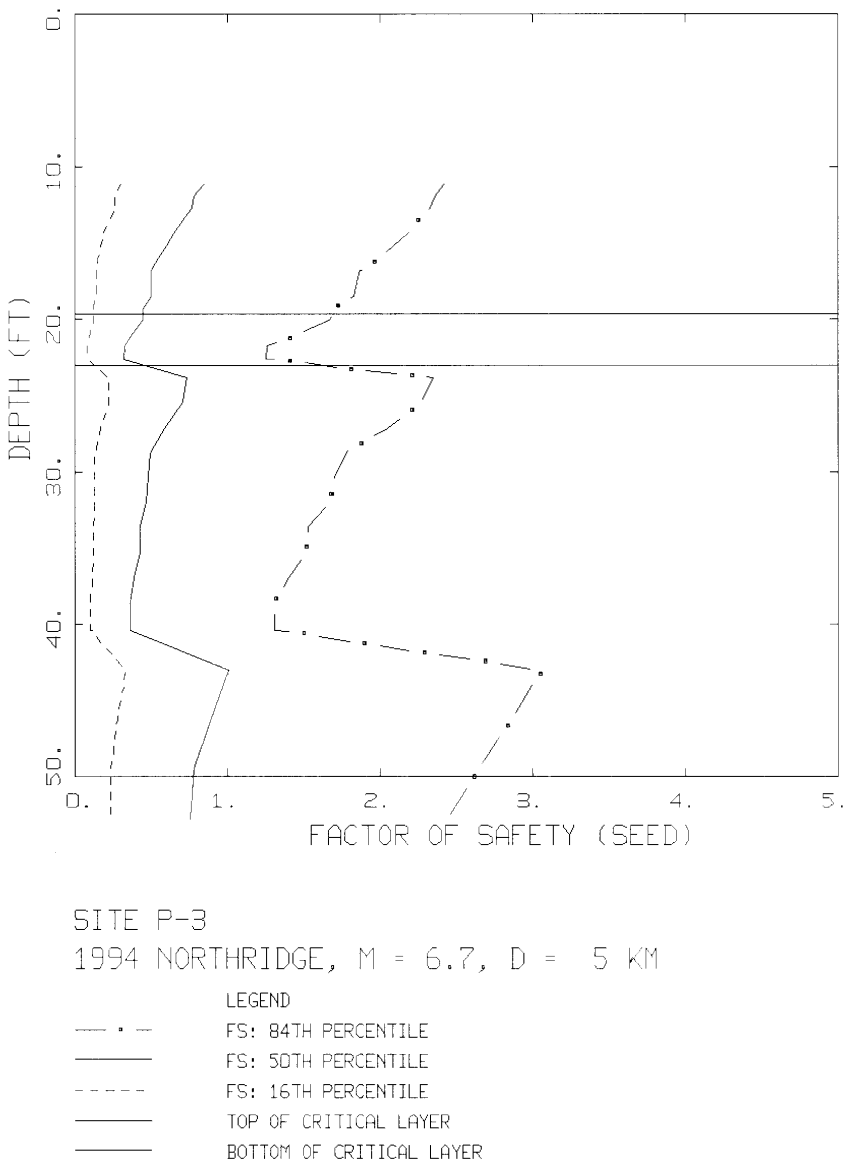


Figure 14m. Variation of the factor of the factor of safety using the Seed et al., (2002) SPT based approach verses depth computed for a suite of random profiles at the West Pico Canyon, P-3 site. Average horizontal spectrum (Figure 14a) based on simulated motions used as control motions. Critical layer indicated with horizontal lines.

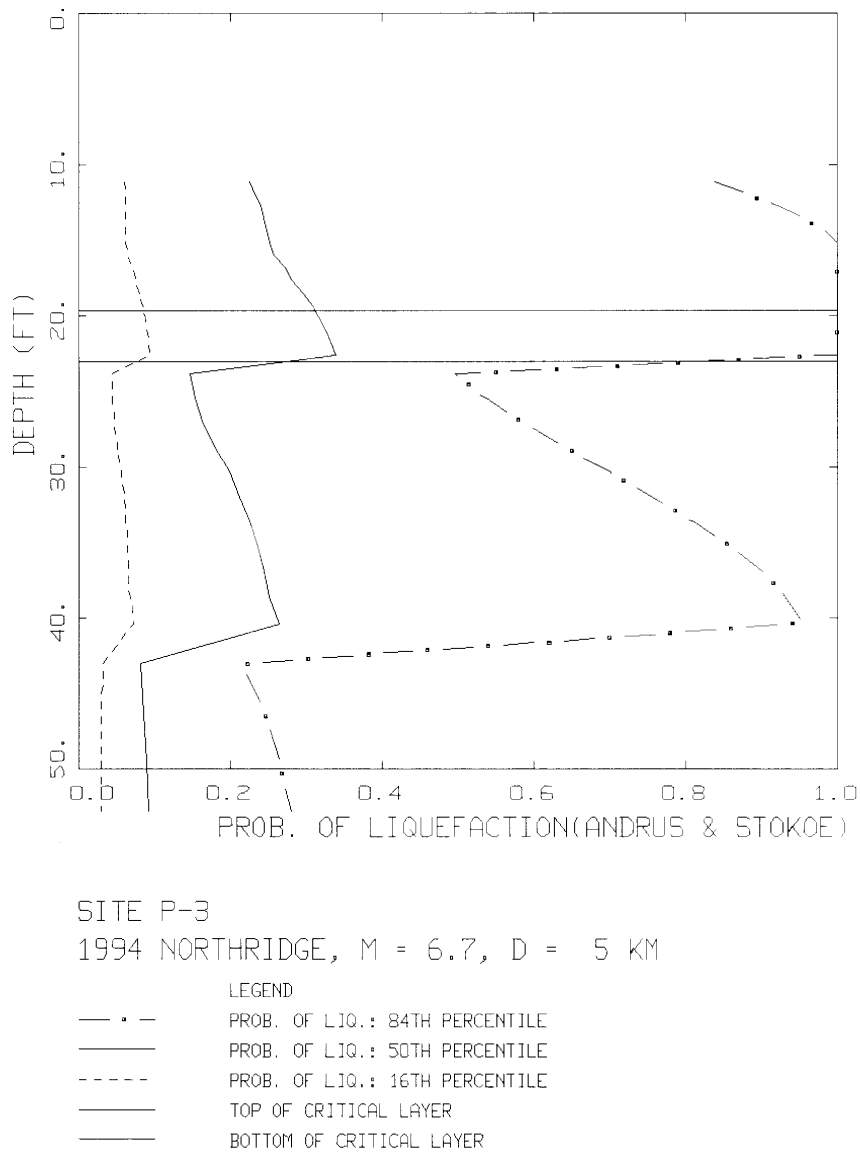


Figure 14n. Variation of the probability of liquefaction using the Andrus and Stokoe (2004) shear-wave velocity based approach verses depth computed for a suite of random profiles at the West Pico Canyon, P-3 site. Average horizontal spectrum (Figure 14a) based on simulated motions used as control motions. Critical layer indicated with horizontal lines.

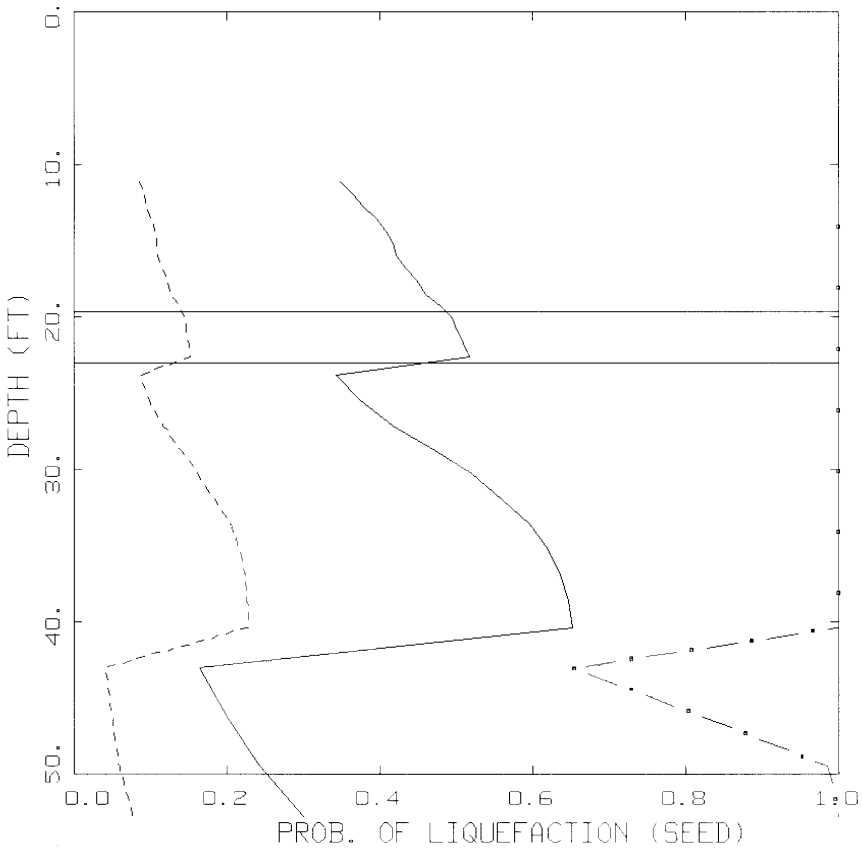


SITE P-3
1994 NORTHRIDGE, M = 6.7, D = 5 KM

LEGEND
PROB. OF LIQ.: 84TH PERCENTILE
PROB. OF LIQ.: 50TH PERCENTILE
PROB. OF LIQ.: 16TH PERCENTILE
TOP OF CRITICAL LAYER
BOTTOM OF CRITICAL LAYER

Figure 14o. Variation probability of liquefaction using the Seed et al. (2002) SPT based approach verses depth computed for a suite of random profiles at the West Pico Canyon, P-3 site. Average horizontal spectrum (Figure 14a) based on simulated motions used as control motions. Critical layer indicated with horizontal lines.

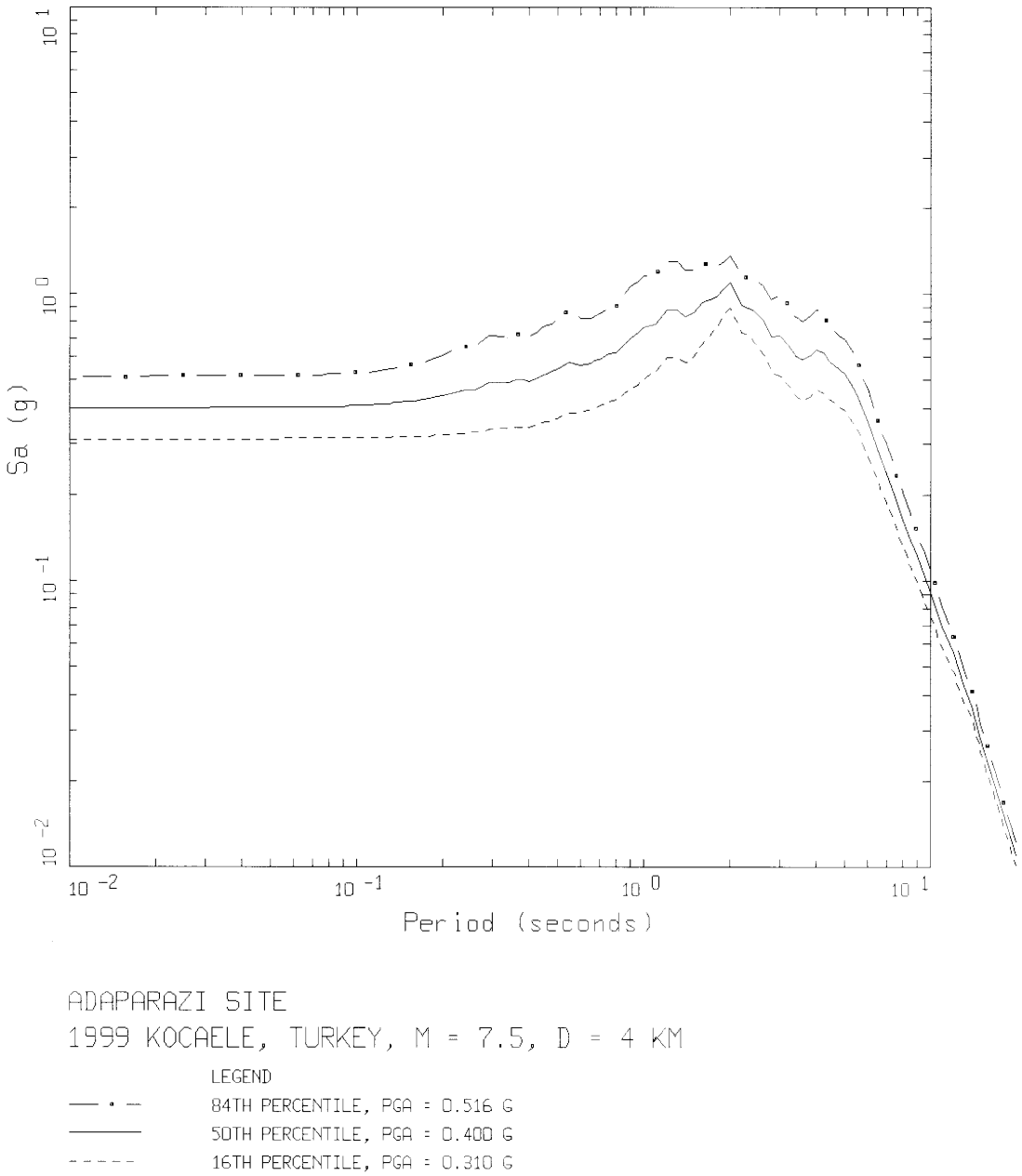


Figure 15a. Average horizontal component response spectra computed from simulated motions: Adaparazi site, 1999 Kocaele, Turkey earthquake.

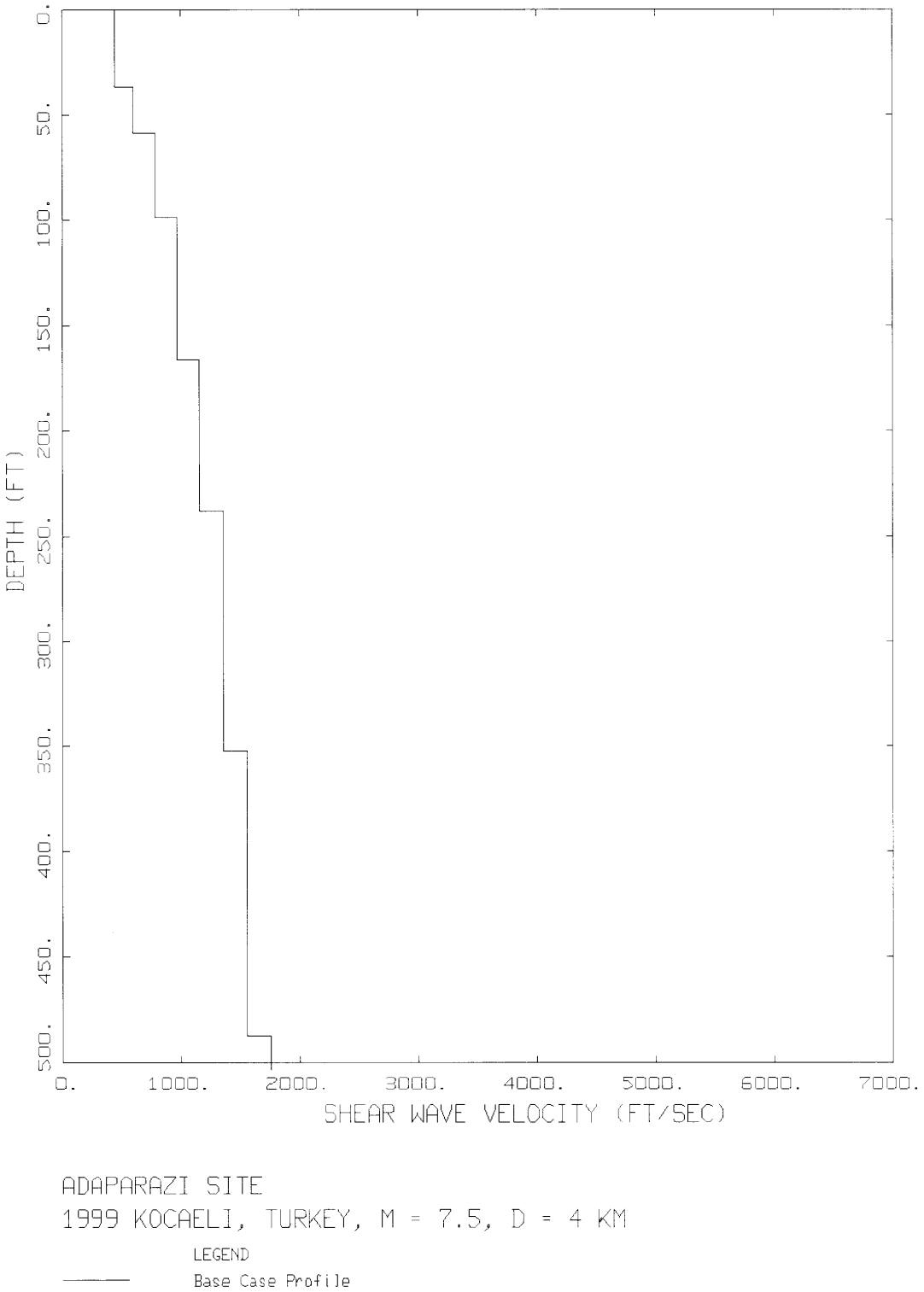


Figure 15b. Shear-wave velocity profile (assumed) at the Adaparazi site to a depth of 500 ft.

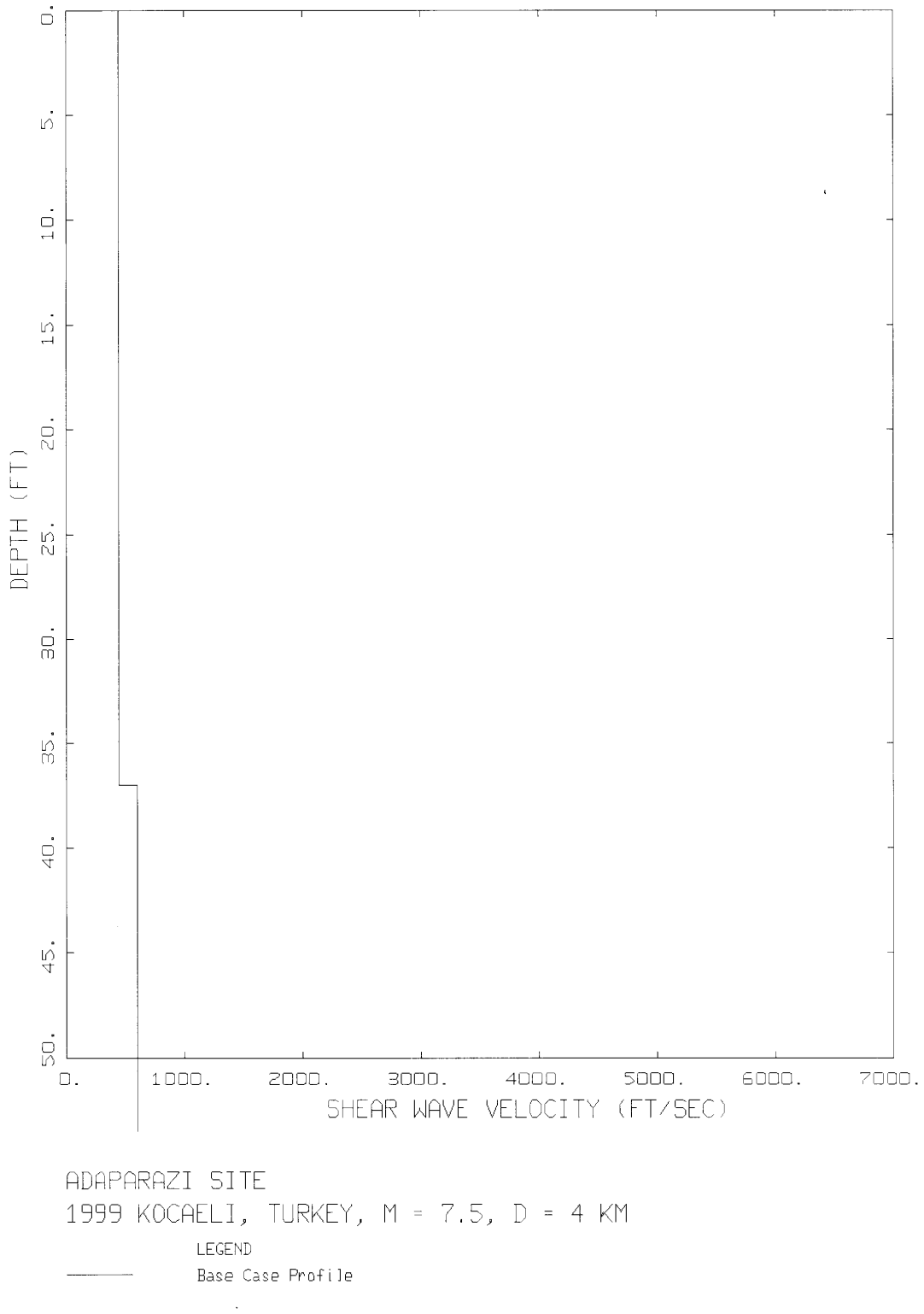


Figure 15c. Shear-wave velocity profile (assumed) at the Adaparazi site to a depth of 50 ft.

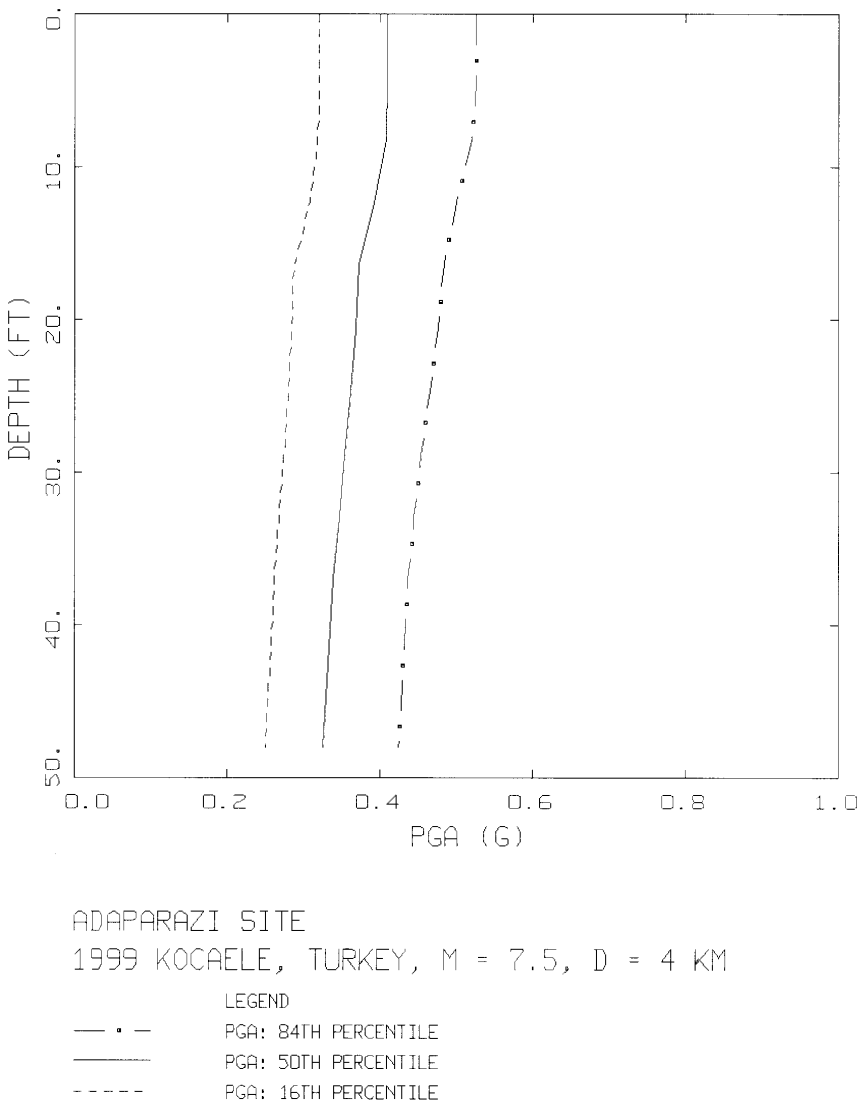


Figure 15d. Variation of peak acceleration(g) (Average horizontal component) verses depth computed for a suite of random profiles at the Adaparazi site. Average horizontal spectrum (Figure 15a) based on simulated motions used as control motions.

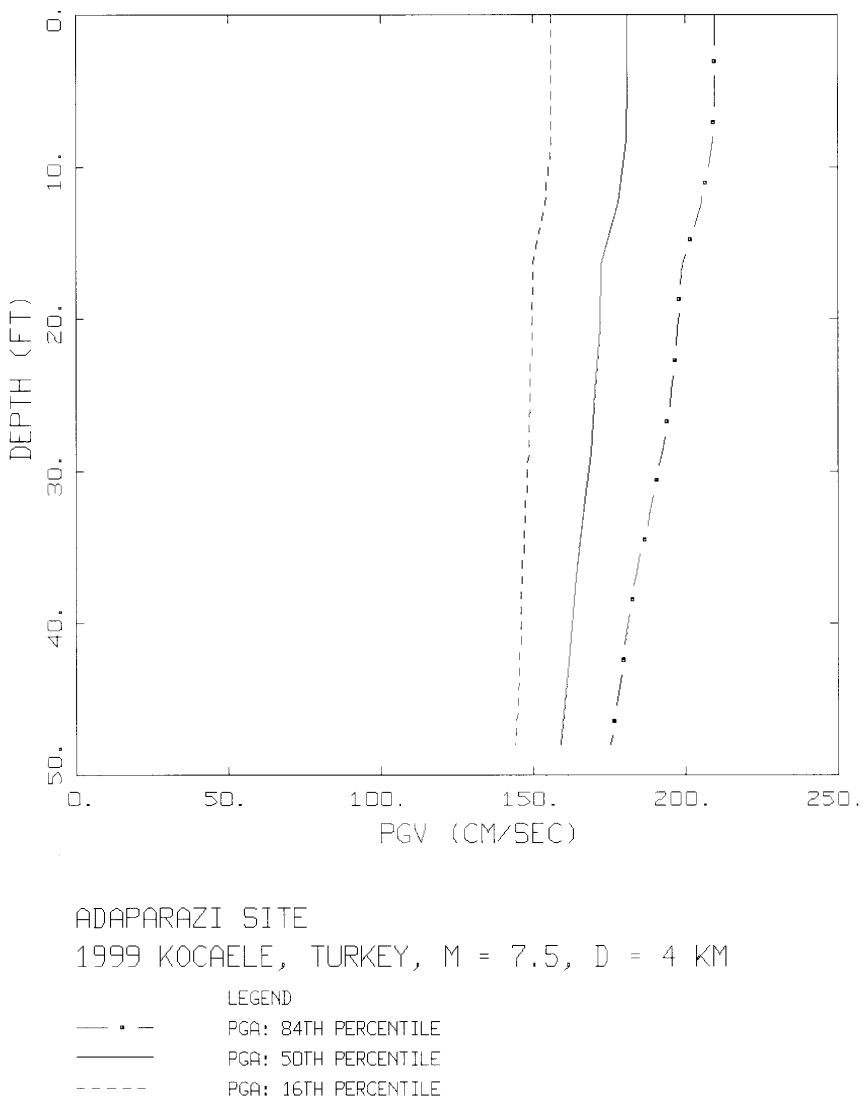


Figure 15e. Variation of peak particle velocity (cm/sec) verses depth computed for a suite of random profiles at the Adaparazi site. Average horizontal spectrum (Figure 15a) based on simulated motions used as control motions.

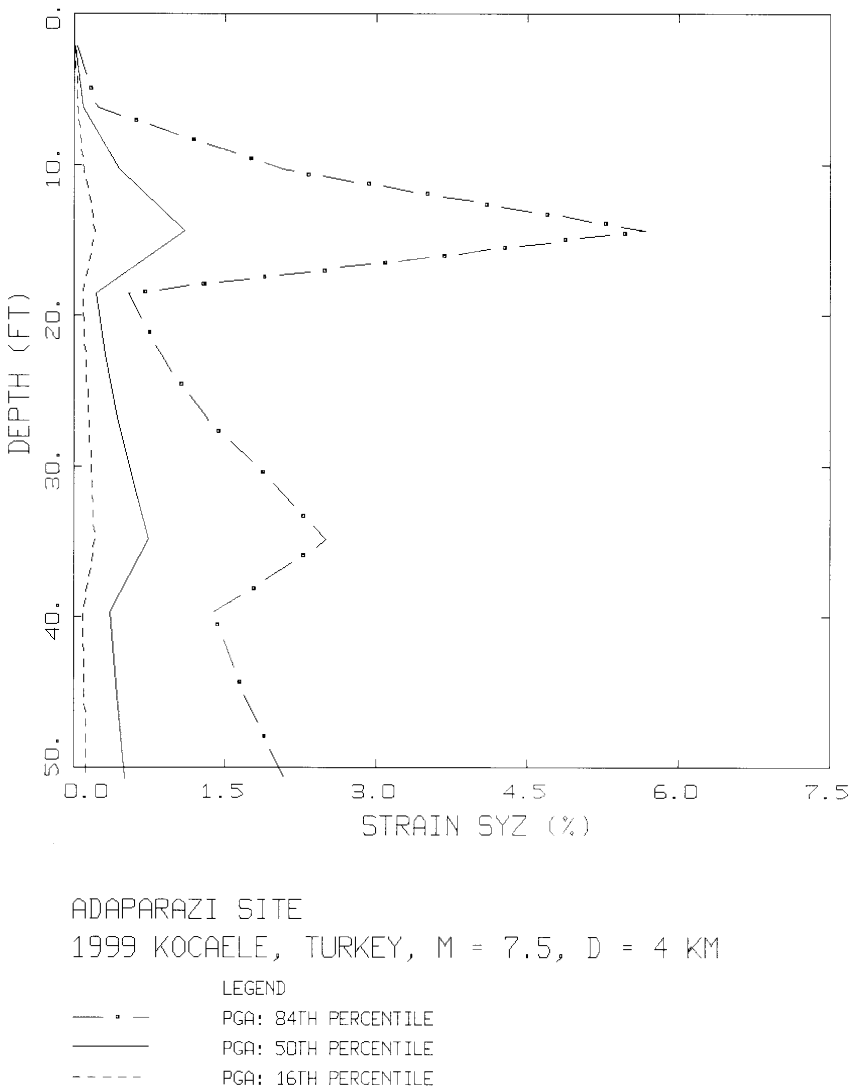


Figure 15f. Variation of peak shear strain(%) verses depth computed for a suite of random profiles at the Adaparazi site. Average horizontal spectrum (Figure 15a) based on simulated motions used as control motions.

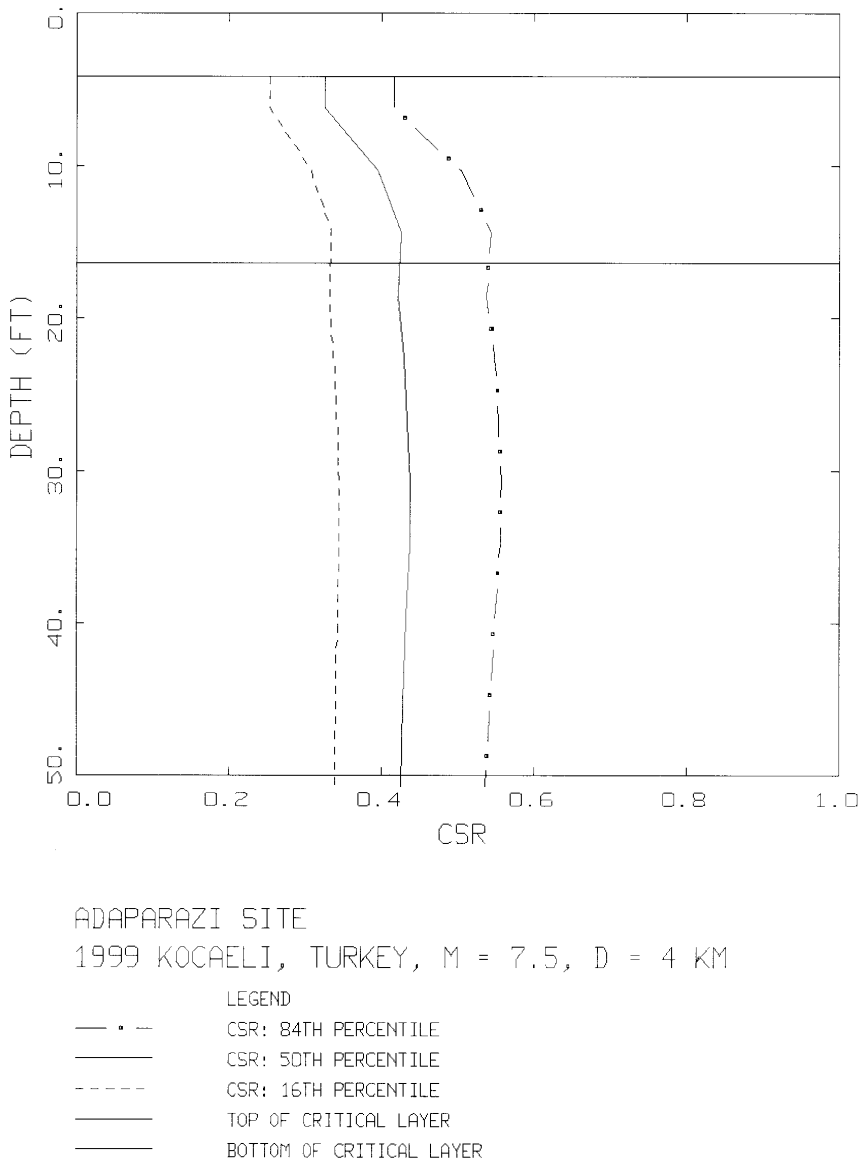


Figure 15g. Variation of CSR verses depth computed for a suite of random profiles for at Adaparazi site. Average horizontal spectrum (Figure 15a) based on simulated motions used as control motions. Critical layer indicated with horizontal lines.

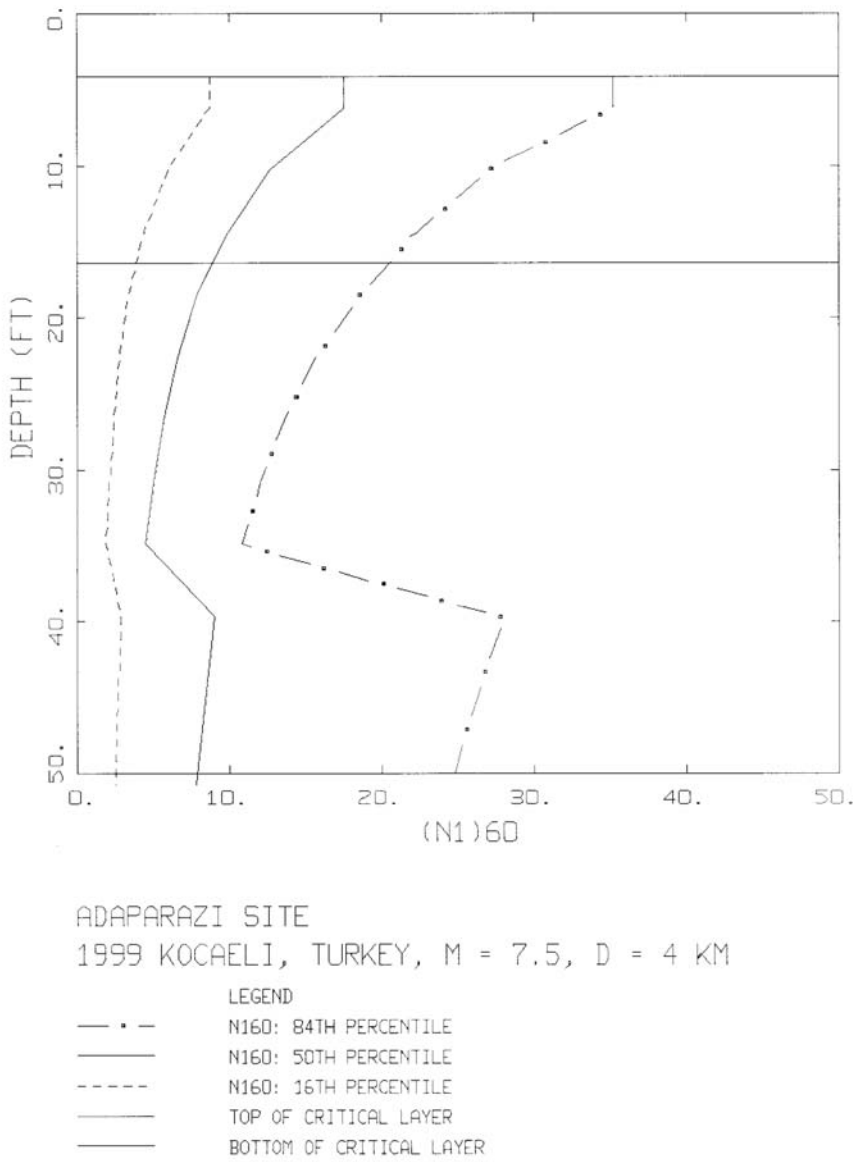


Figure 15h. Variation of peak $(N_1)_{60}$ verses depth computed for a suite of random profiles at the Adaparazi site using the shear-wave velocity correlation model of Iwasaki et al., (1987). Average horizontal spectrum (Figure 15a) based on simulated motions used as control motions. Critical layer indicated with horizontal lines.

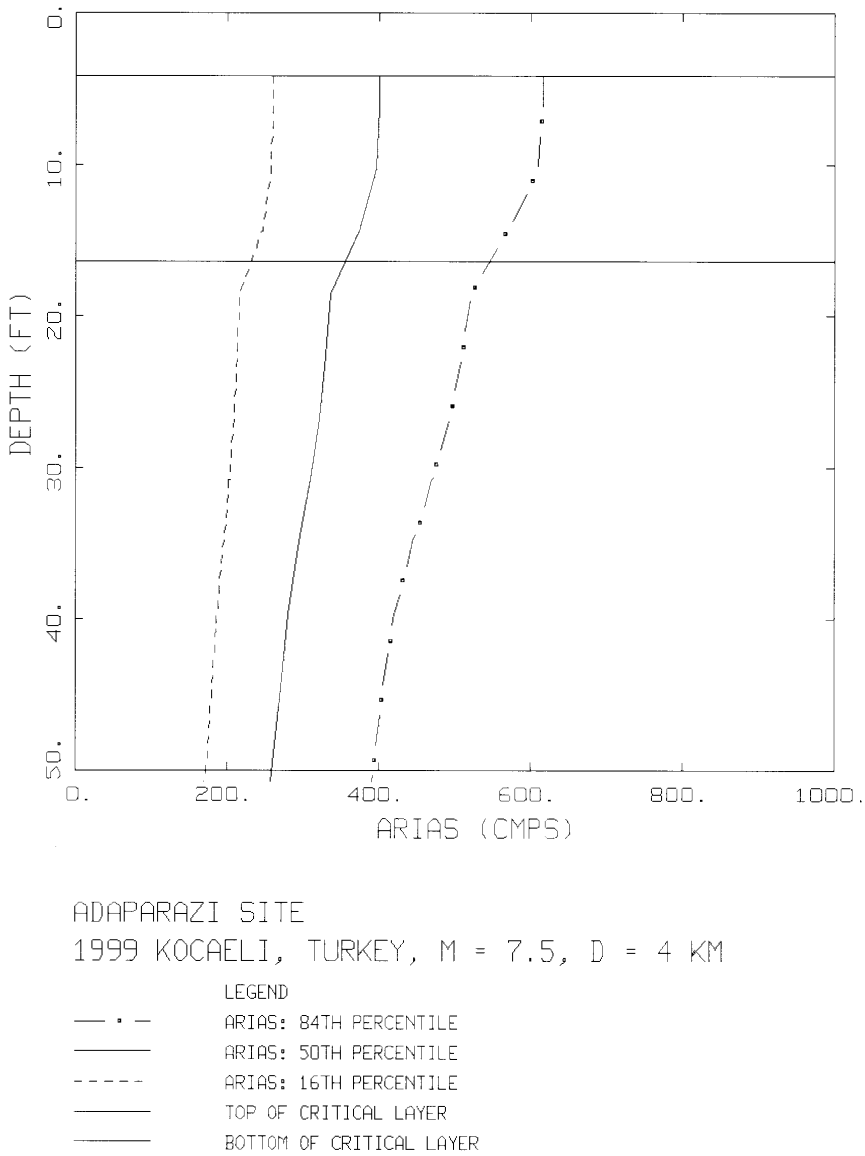


Figure 15i. Variation of Arias Intensity (cm/sec) verses depth computed for a suite of random profiles at the Adaparazi site. Average horizontal spectrum (Figure 15a) based on simulated motions used as control motions. Critical layer indicated with horizontal lines.

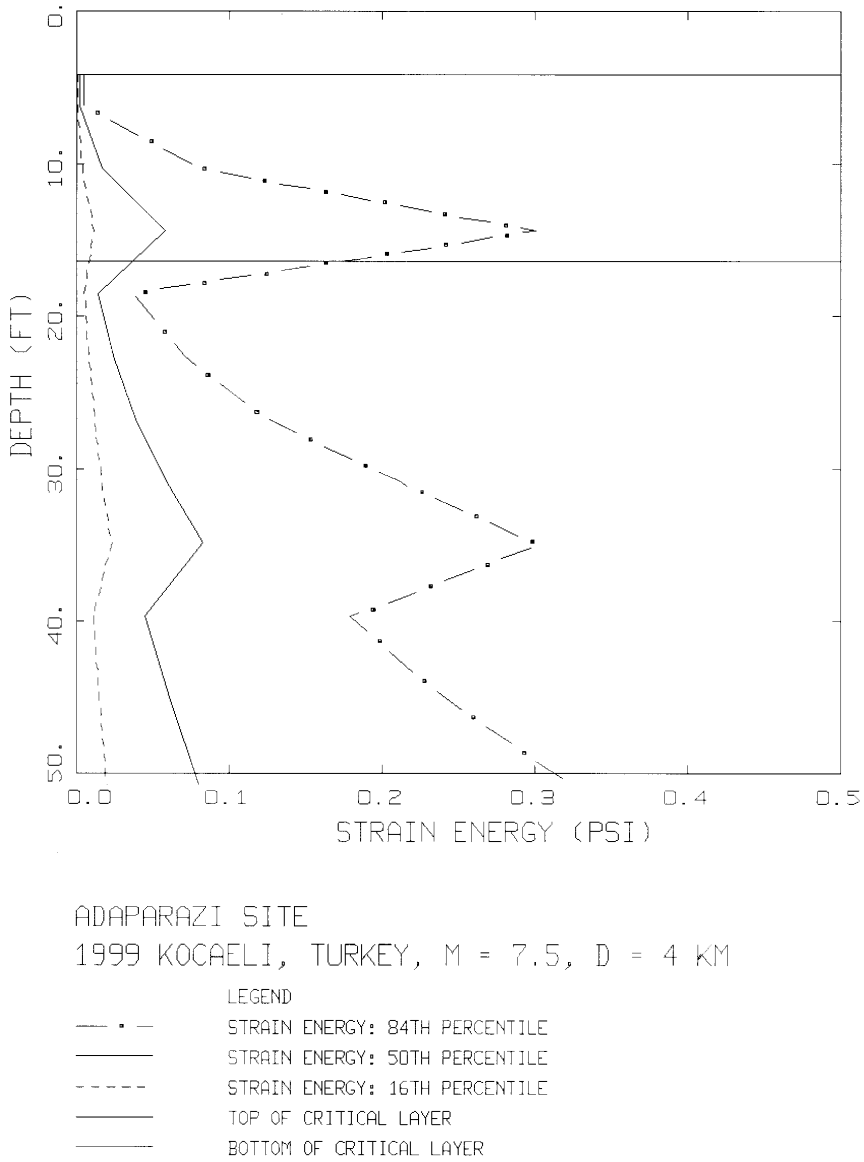


Figure 15j Variation of strain energy (PSI) verses depth computed for a suite of random profiles at the Adaparazi site. Average horizontal spectrum (Figure 15a) based on simulated motions used as control motions. Critical layer indicated with horizontal lines.

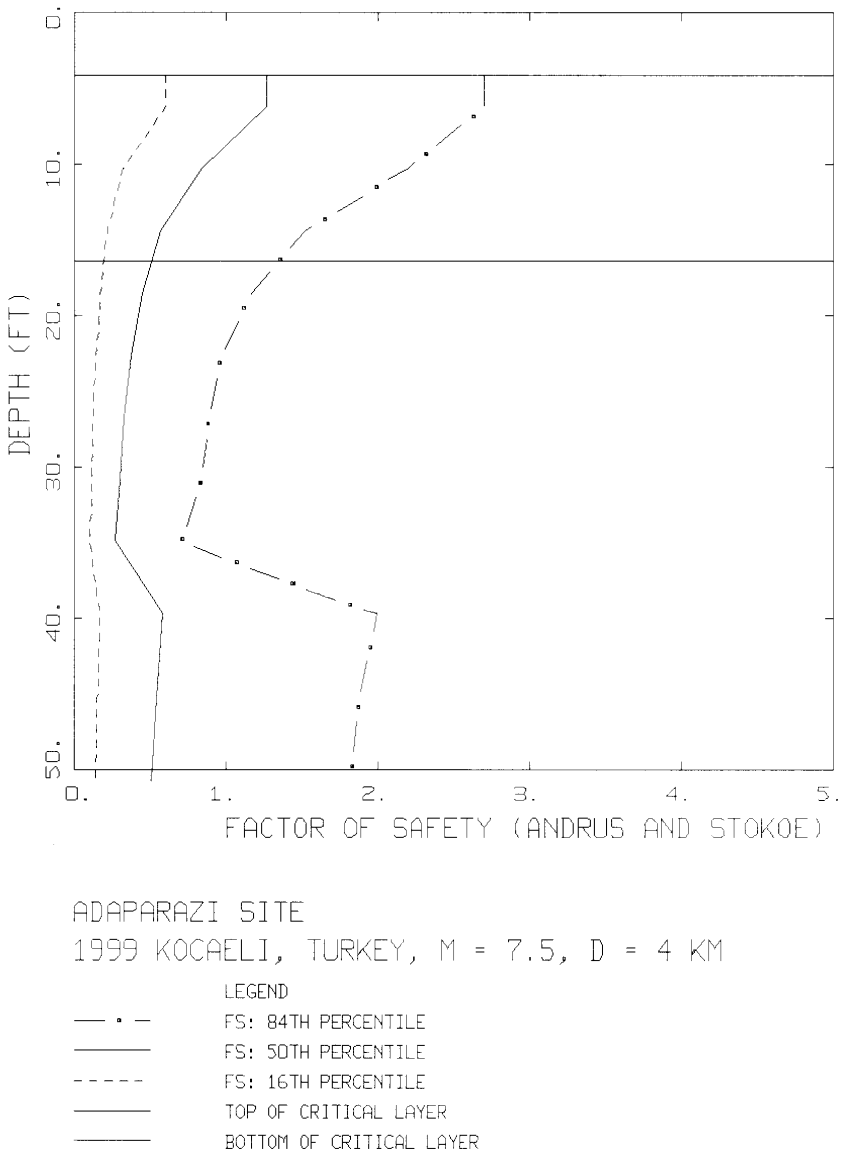


Figure 15k. Variation of the factor of safety (FS) using the Andrus and Stokoe (2004) shear-wave velocity based approach verses depth computed for a suite of random profiles at the Adaparazi site. Average horizontal spectrum (Figure 15a) based on simulated motions used as control motions. Critical layer indicated with horizontal lines.

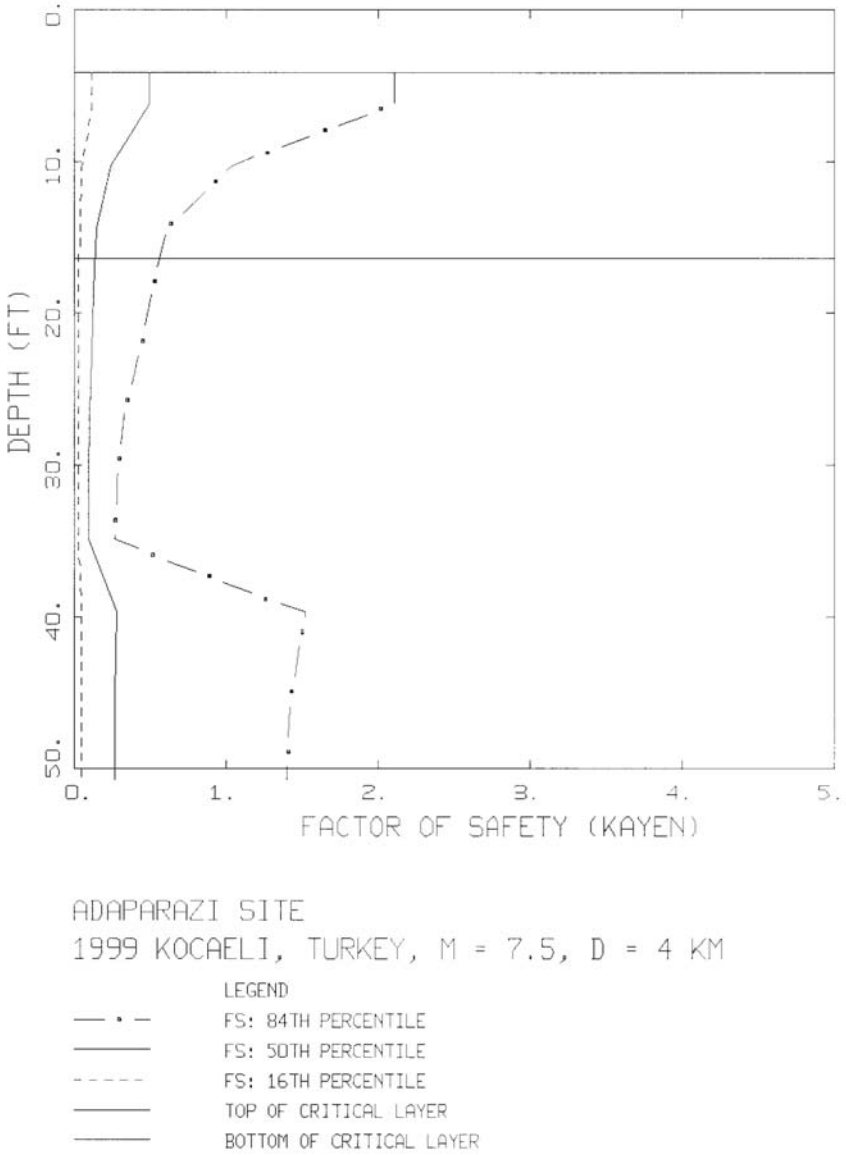


Figure 15l. Variation of the factor of safety using the Kayen and Mitchell (1979) Arias Intensity based approach verses depth computed for a suite of random profiles at the Adaparazi site. Average horizontal spectrum (Figure 15a) based on simulated motions used as control motions. Critical layer indicated with horizontal lines.

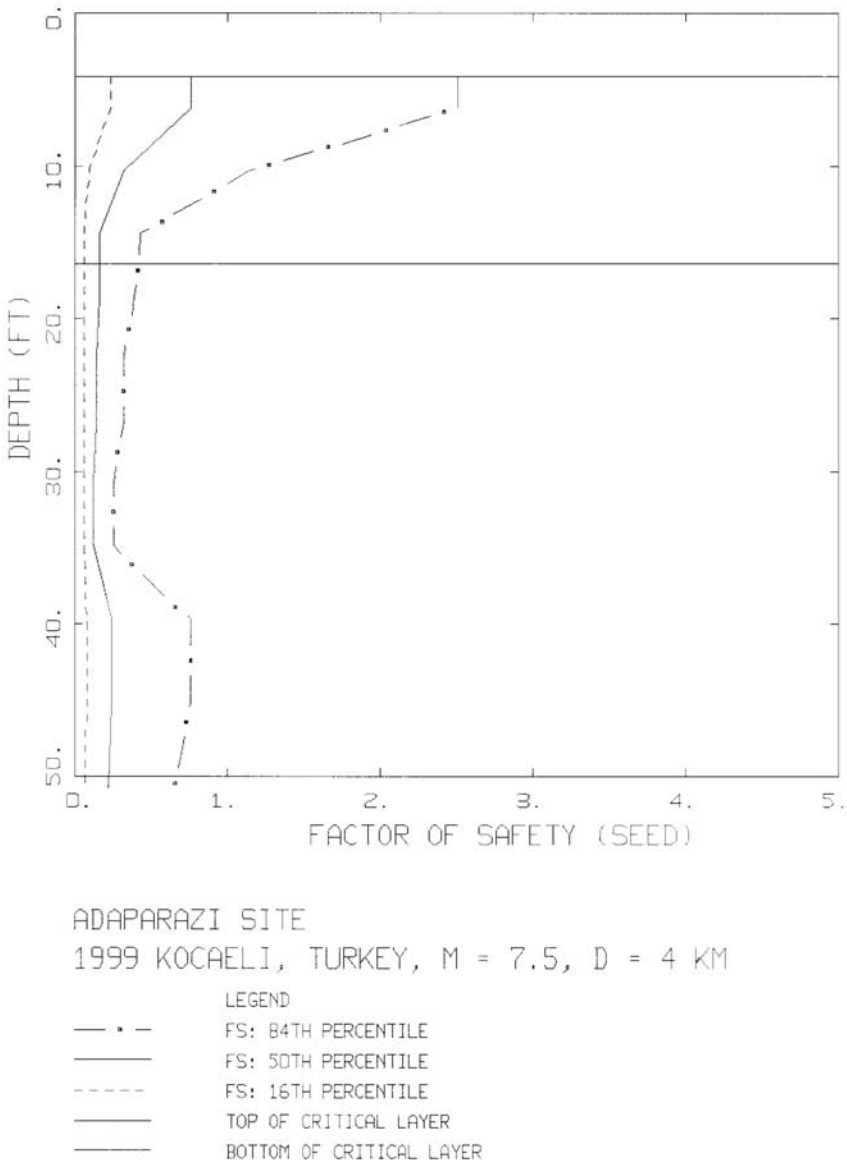


Figure 15m. Variation of the factor of the factor of safety using the Seed et al., (2002) SPT based approach verses depth computed for a suite of random profiles at the Adaparazi site. Average horizontal spectrum (Figure 15a) based on simulated motions used as control motions. Critical layer indicated with horizontal lines.

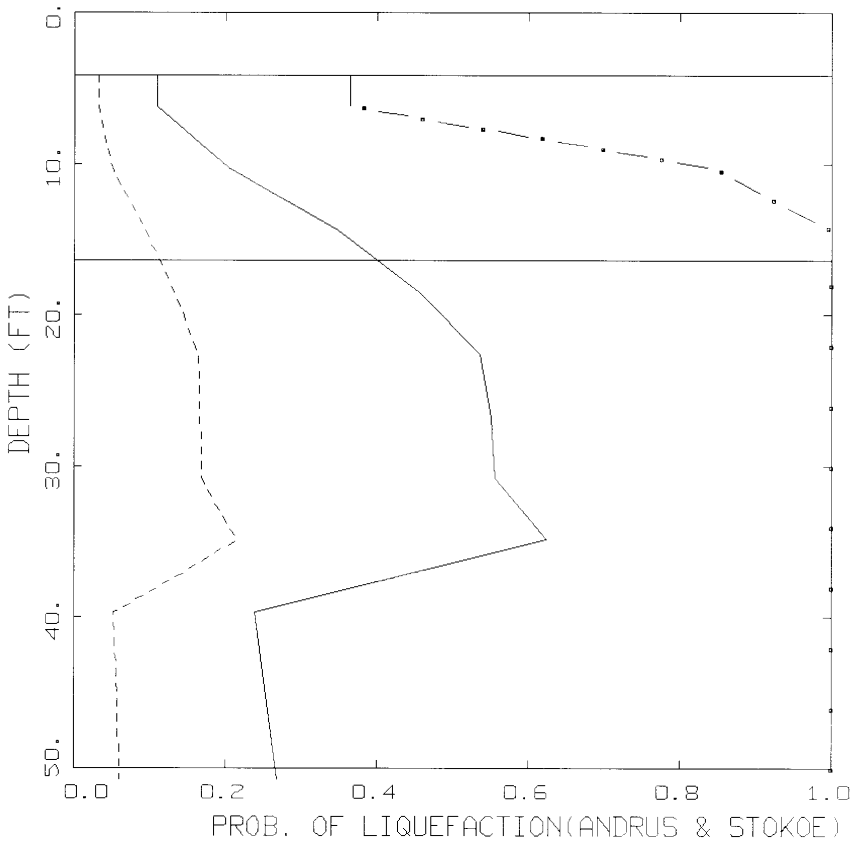


ADAPARAZI SITE
1999 KOCAELI, TURKEY, M = 7.5, D = 4 KM

LEGEND

| | |
|---|---|
| — · — | PROB. OF LIQ.: 84TH PERCENTILE |
| ——— | PROB. OF LIQ.: 50TH PERCENTILE |
| - - - - - | PROB. OF LIQ.: 16TH PERCENTILE |
| ——— | TOP OF CRITICAL LAYER |
| ——— | BOTTOM OF CRITICAL LAYER |

Figure 15n. Variation of the probability of liquefaction using the Andrus and Stokoe (2004) shear-wave velocity based approach verses depth computed for a suite of random profiles at the Adaparazi site. Average horizontal spectrum (Figure 15a) based on simulated motions used as control motions. Critical layer indicated with horizontal lines.

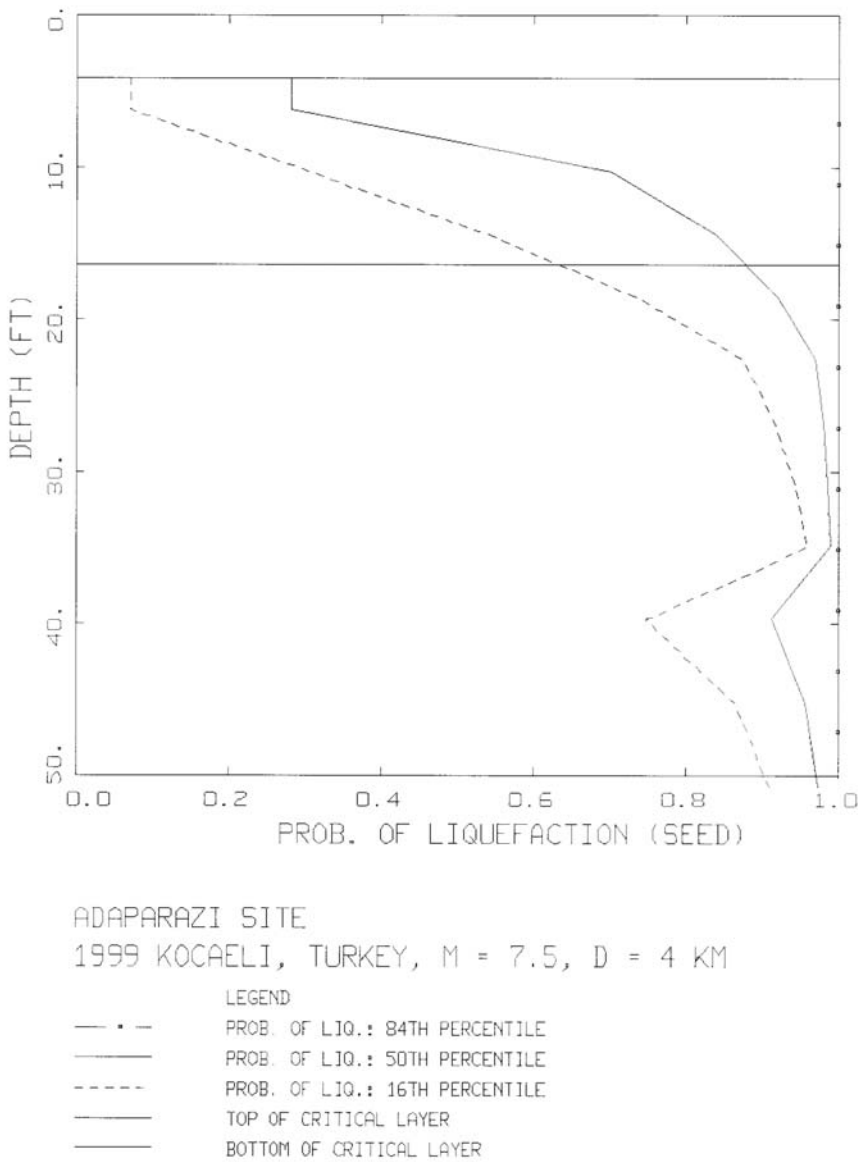


Figure 15o. Variation probability of liquefaction using the Seed et al. (2002) SPT based approach verses depth computed for a suite of random profiles at the Adaparazi site. Average horizontal spectrum (Figure 15a) based on simulated motions used as control motions. Critical layer indicated with horizontal lines.

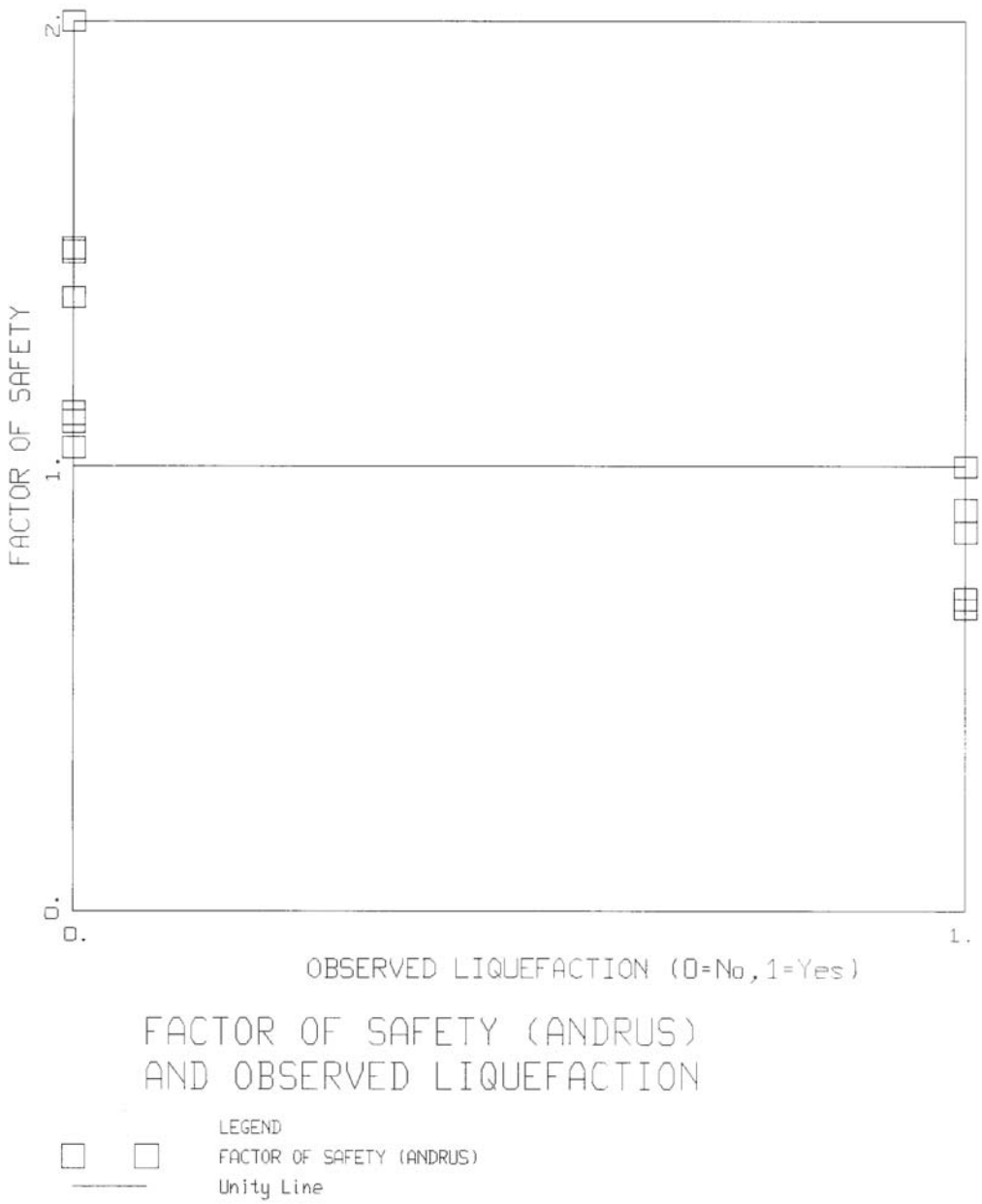


Figure 16a. Comparison of estimated factor of safety with observed presence (1) or absence (0) of liquefaction at the twelve site-specific study sites: Andrus and Stokoe (2000) shear-wave velocity approach.

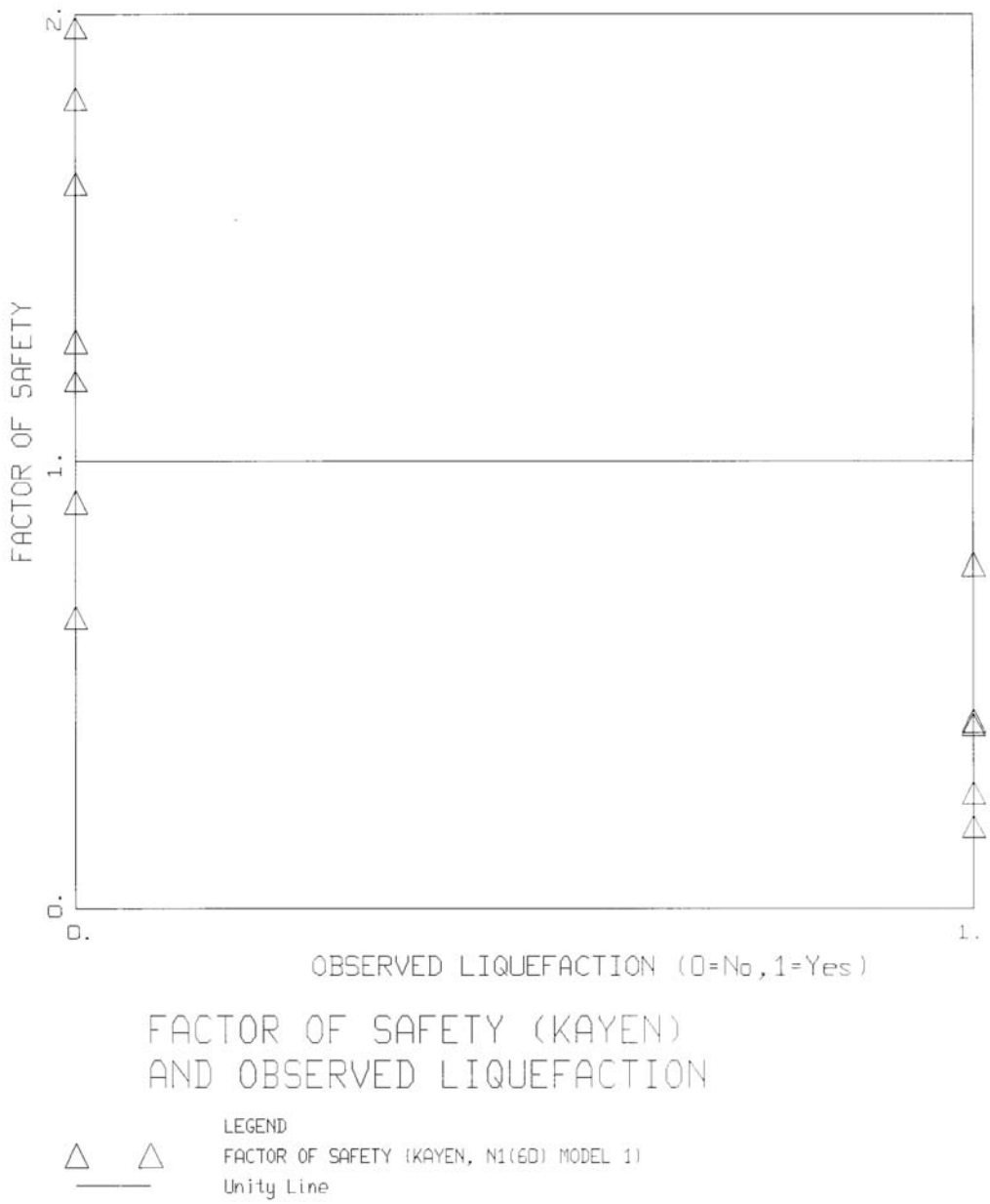


Figure 16b. Comparison of estimated factor of safety with observed presence (1) or absence (0) of liquefaction at the twelve site-specific study sites: Kayen and Mitchell (1997) cumulative Arias Intensity approach.

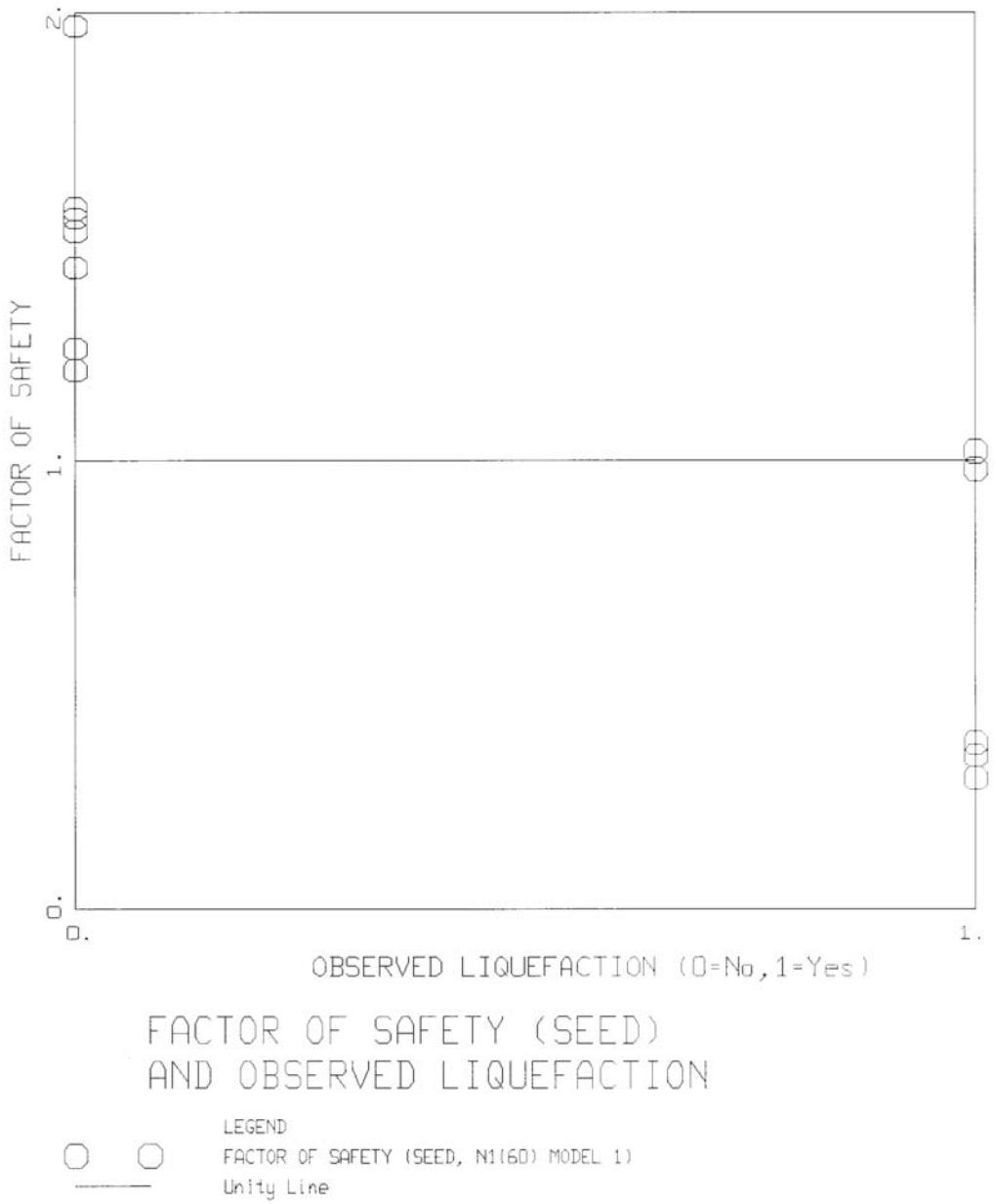


Figure 16c. Comparison of estimated factor of safety with observed presence (1) or absence (0) of liquefaction at the twelve site-specific study sites: Seed et al. (2001) SPT approach.

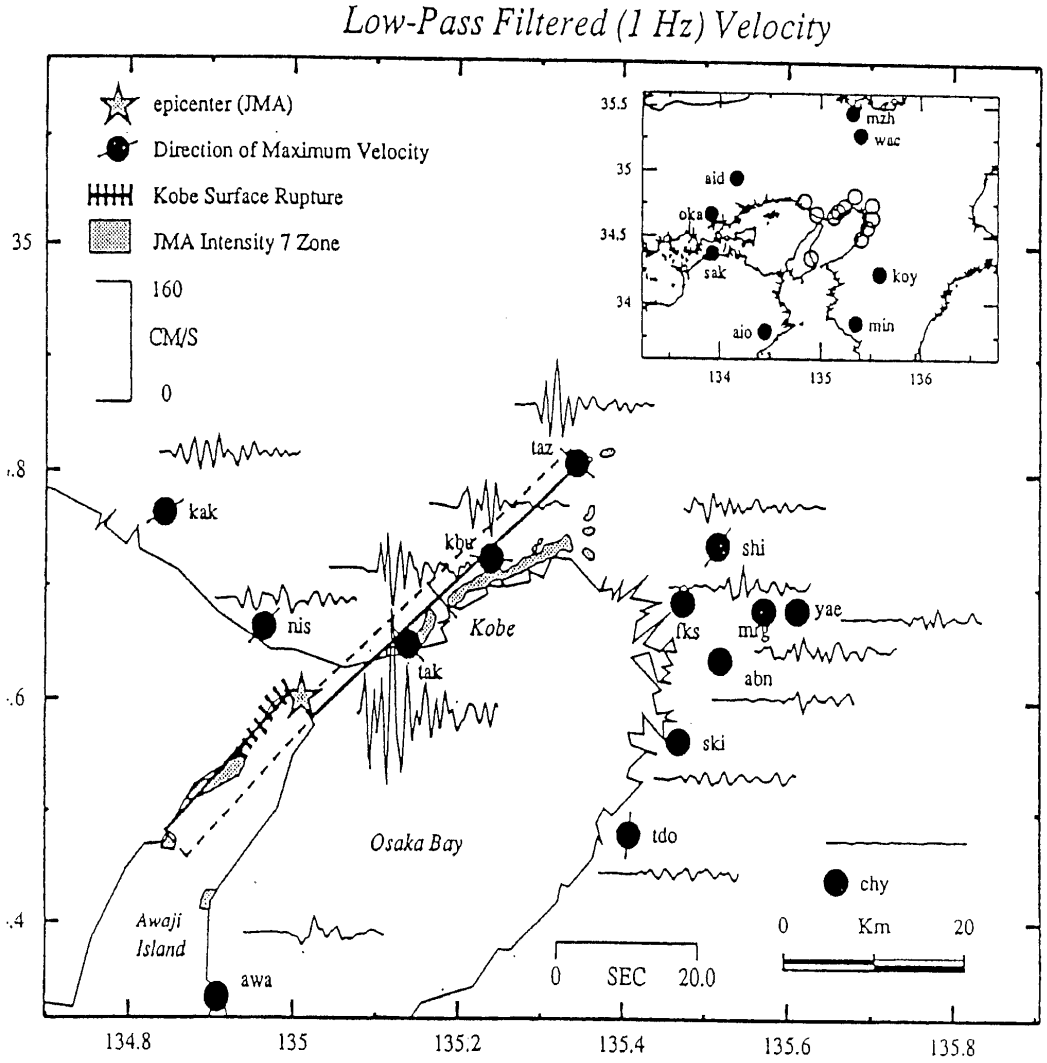


Figure 17. Recording station map of the Kobe, Osaka, and surrounding regions (from Wald, 1996)

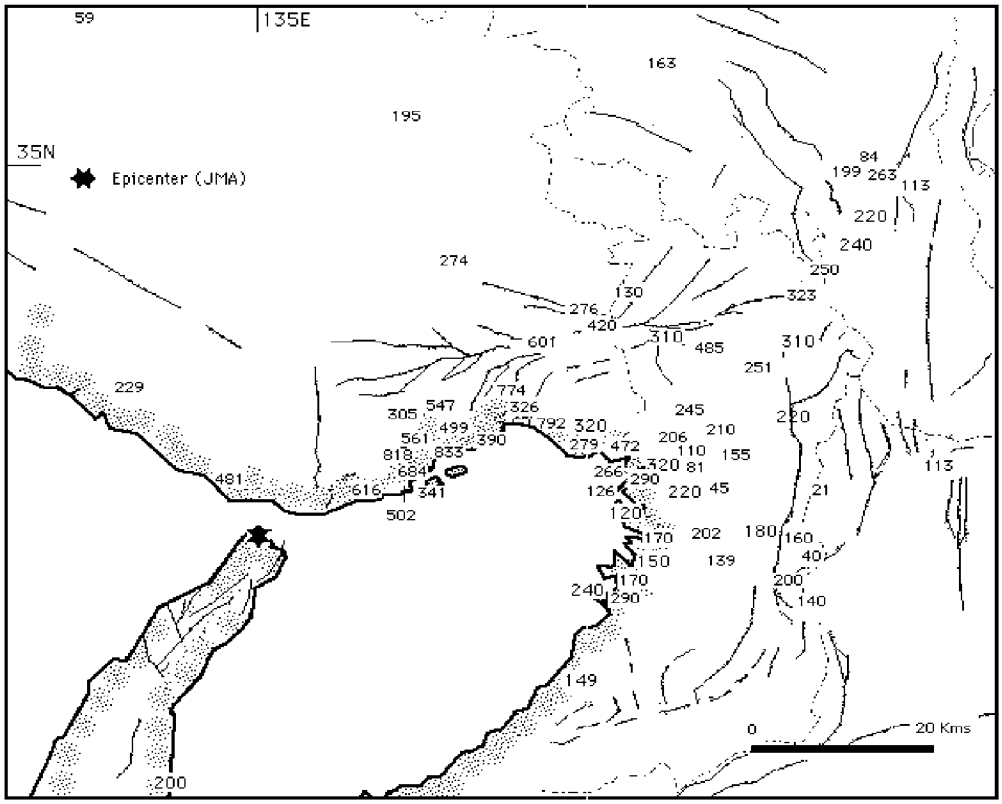


Figure 18. Recorded horizontal PGA's (in gals).

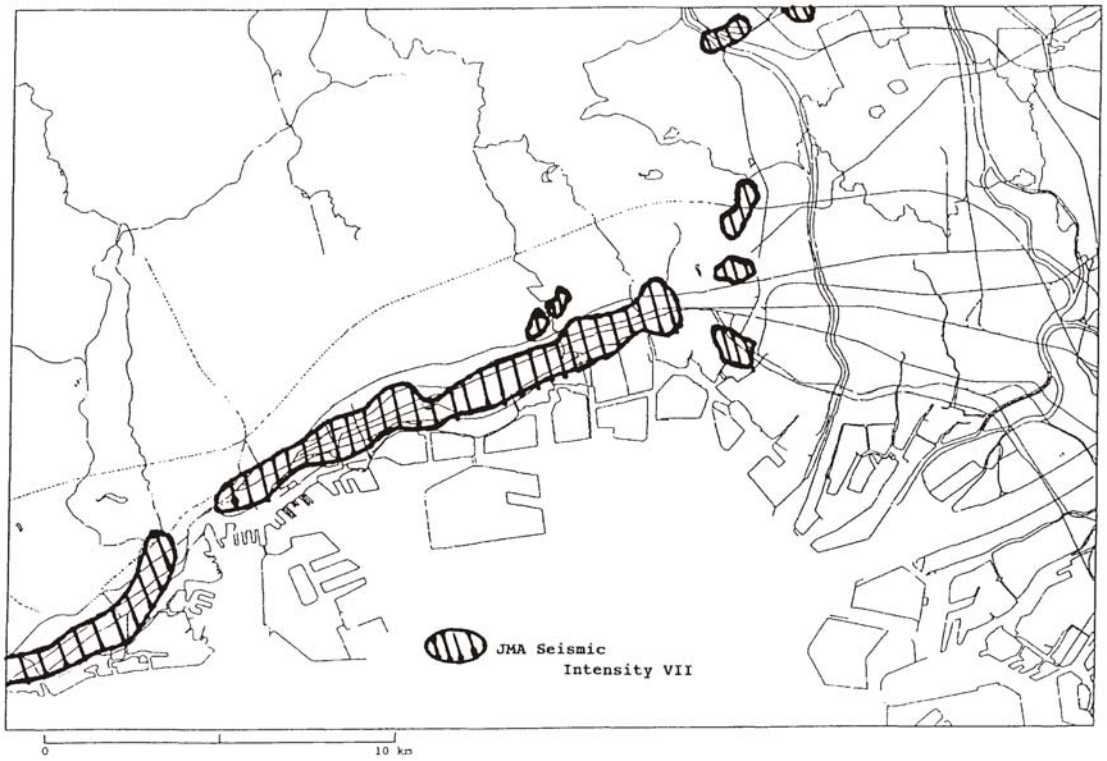


Figure 19. Approximate zones of JMA intensity VII (from Kimura, 1996)

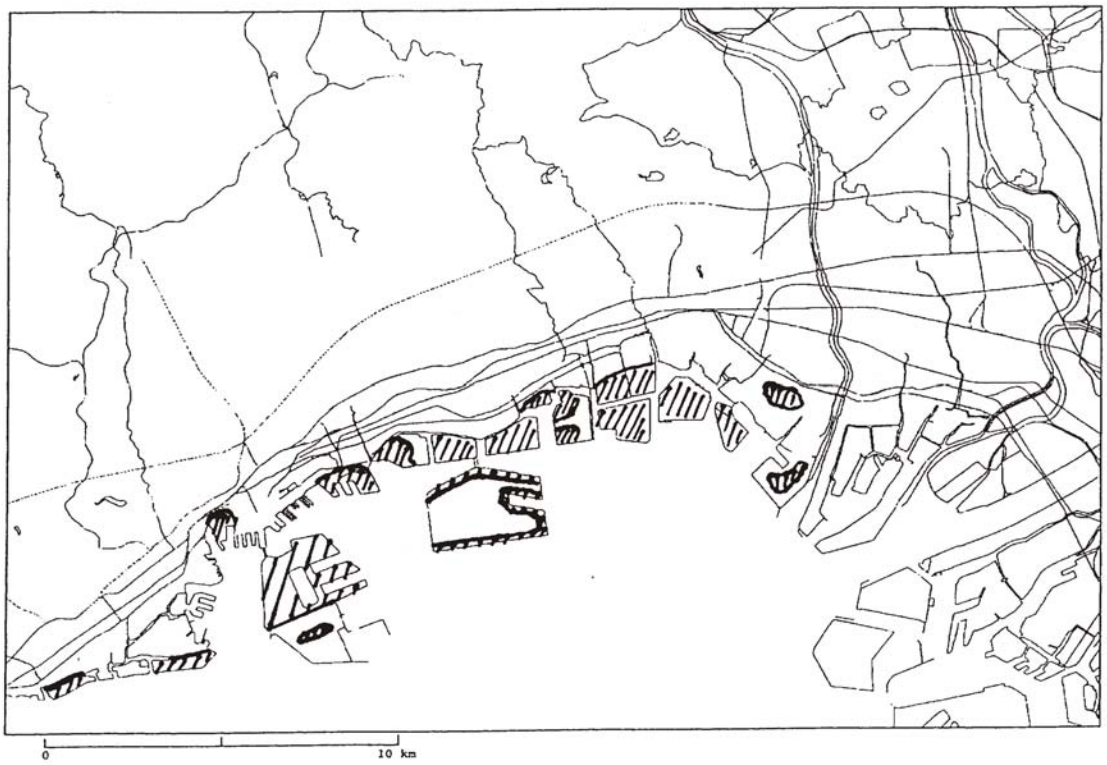


Figure 20. Zones of surface expression of ground failure (from Iwasaki, 1997).

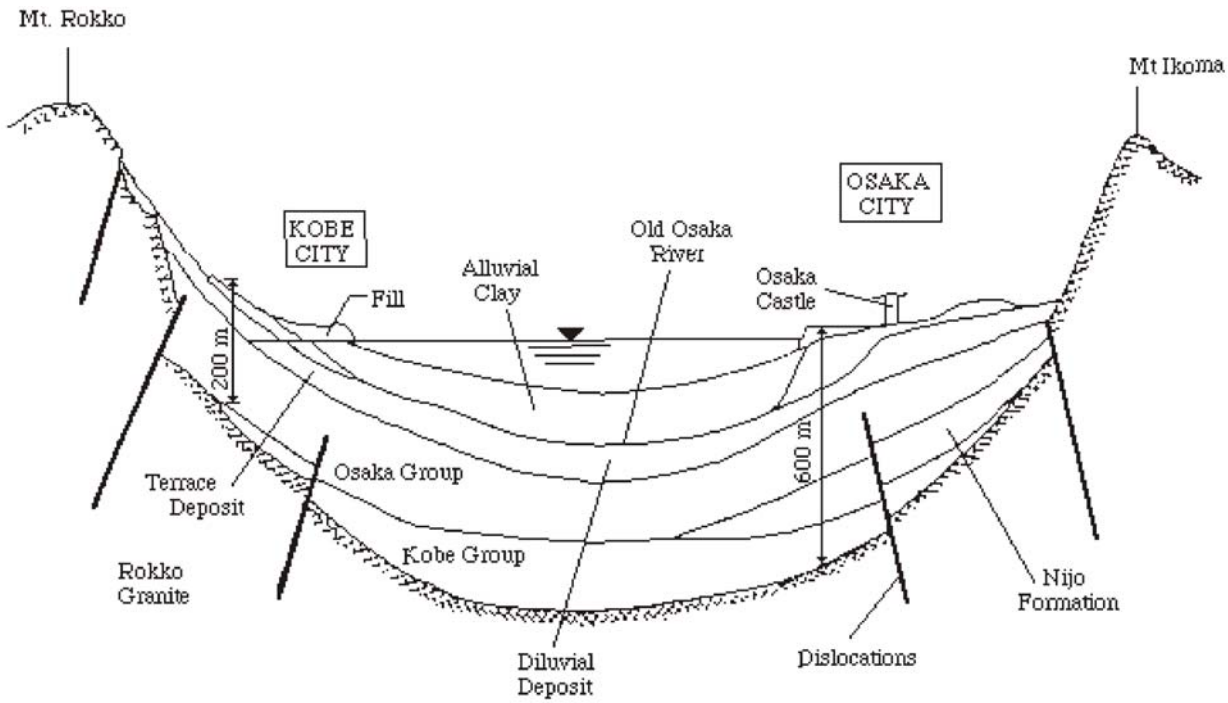


Figure 21. Schematic description of rock/soil profile beneath Kobe and Osaka cities.

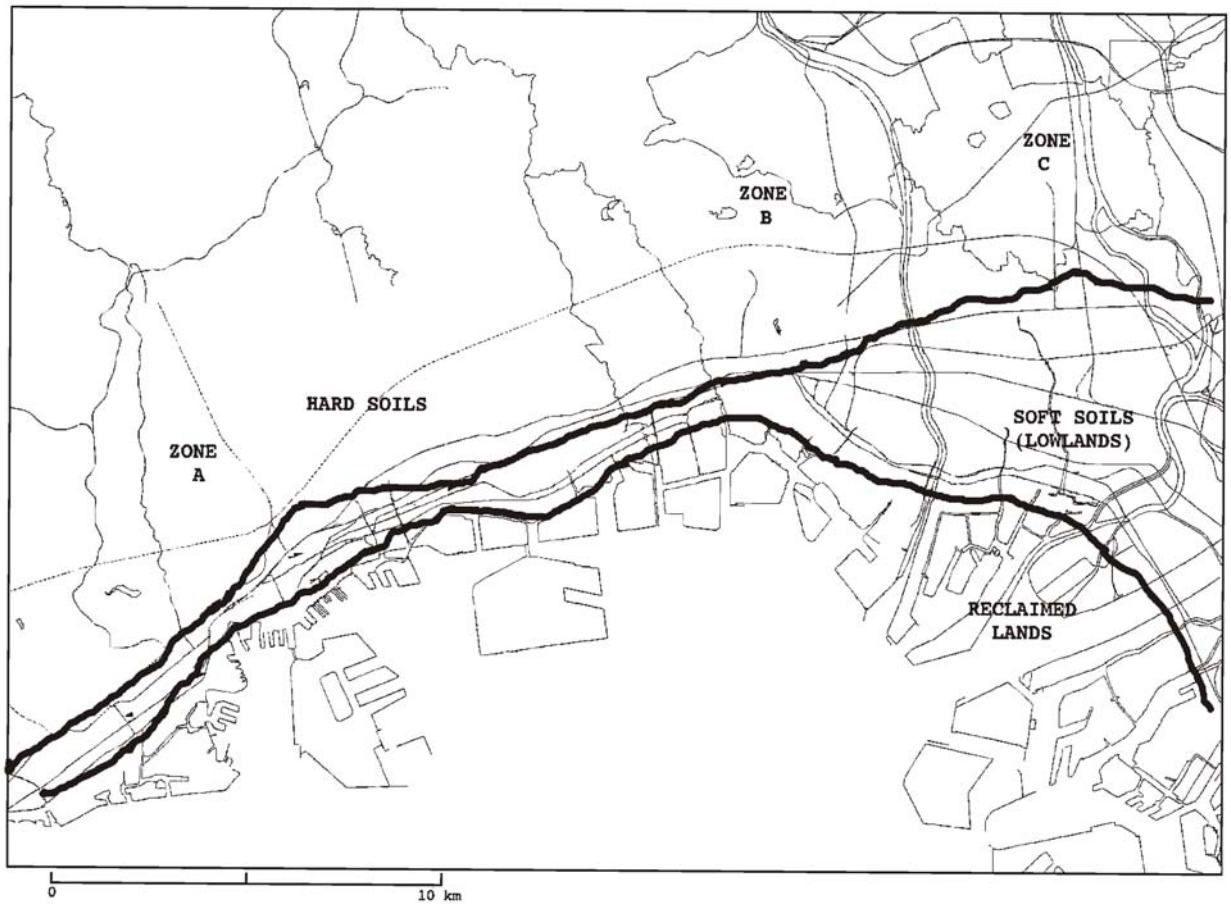


Figure 22. General site categories (rock, hard, soft, and fill soils).

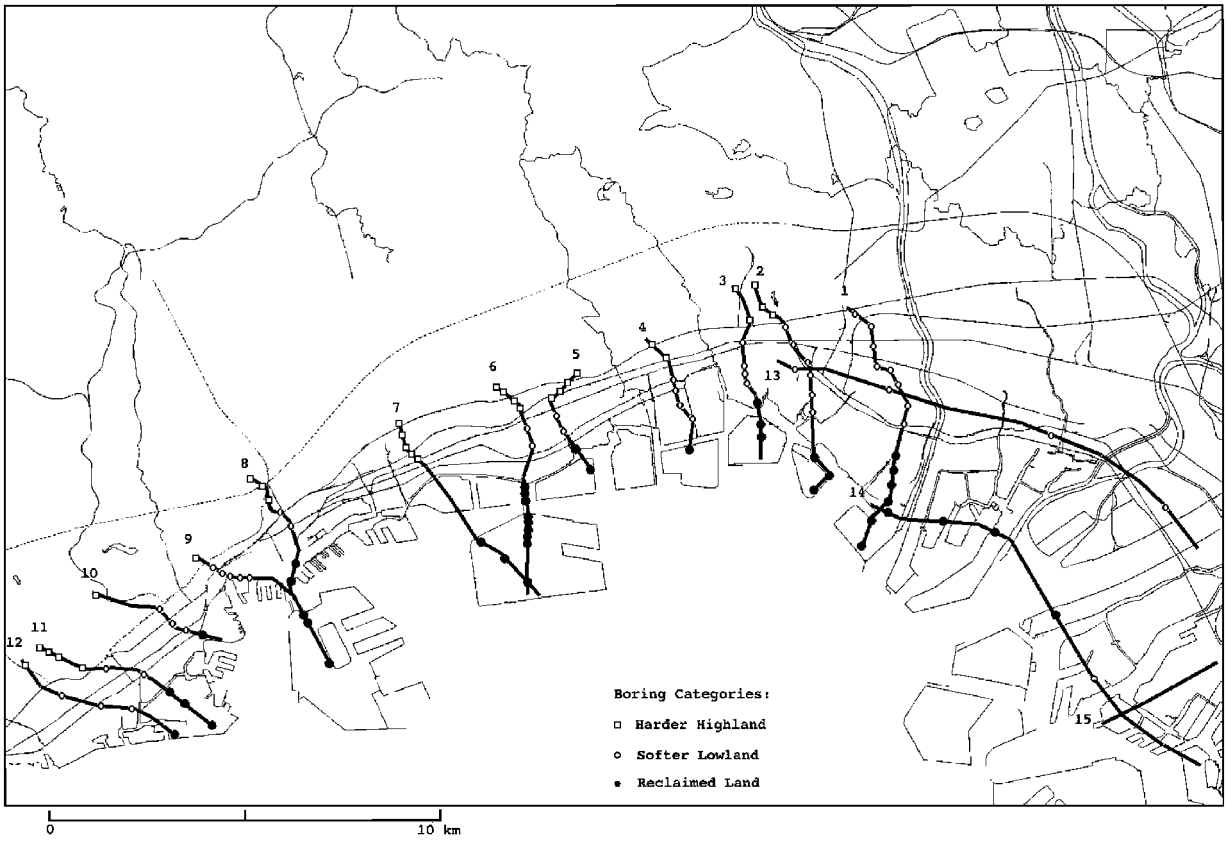


Figure 23. Soil profiles evaluated (from WES, 1999).

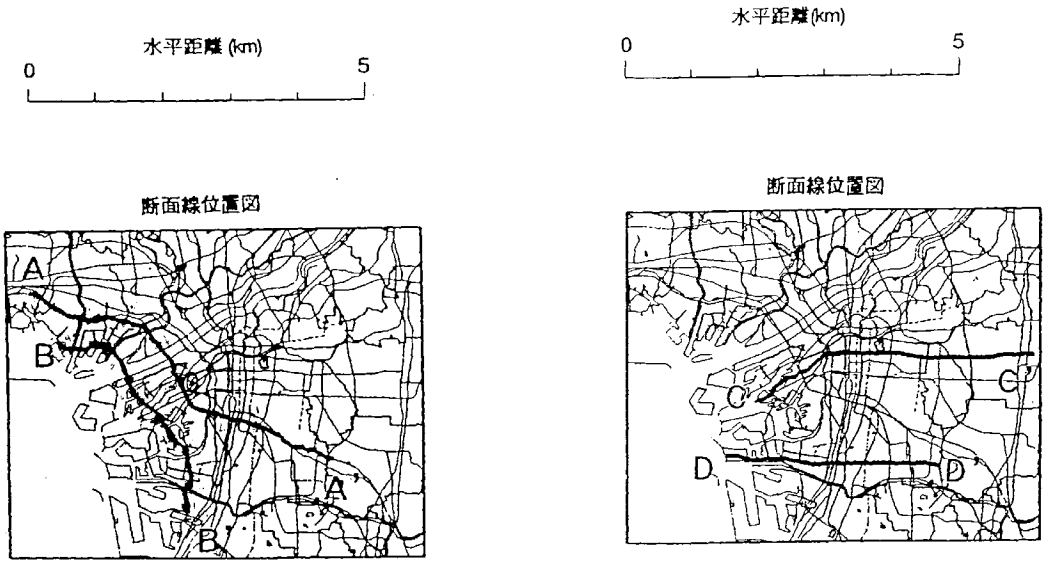


Figure 24. Additional soil profiles evaluated (from WES, 1999).

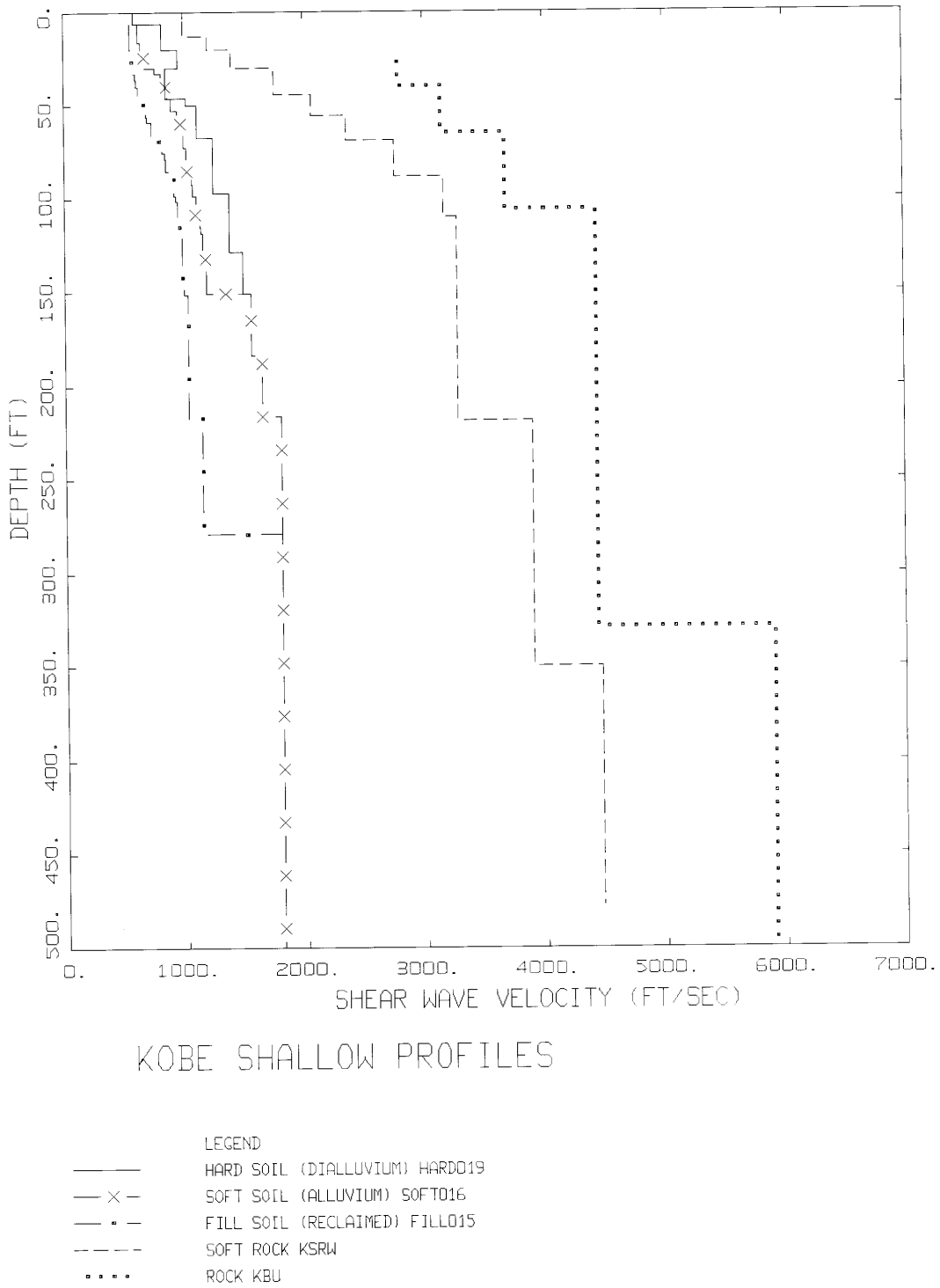


Figure 25. Shallow hard, soft, and fill (reclaimed) soil profiles and generic soft rock as well as site specific Kobe University rock site profile.

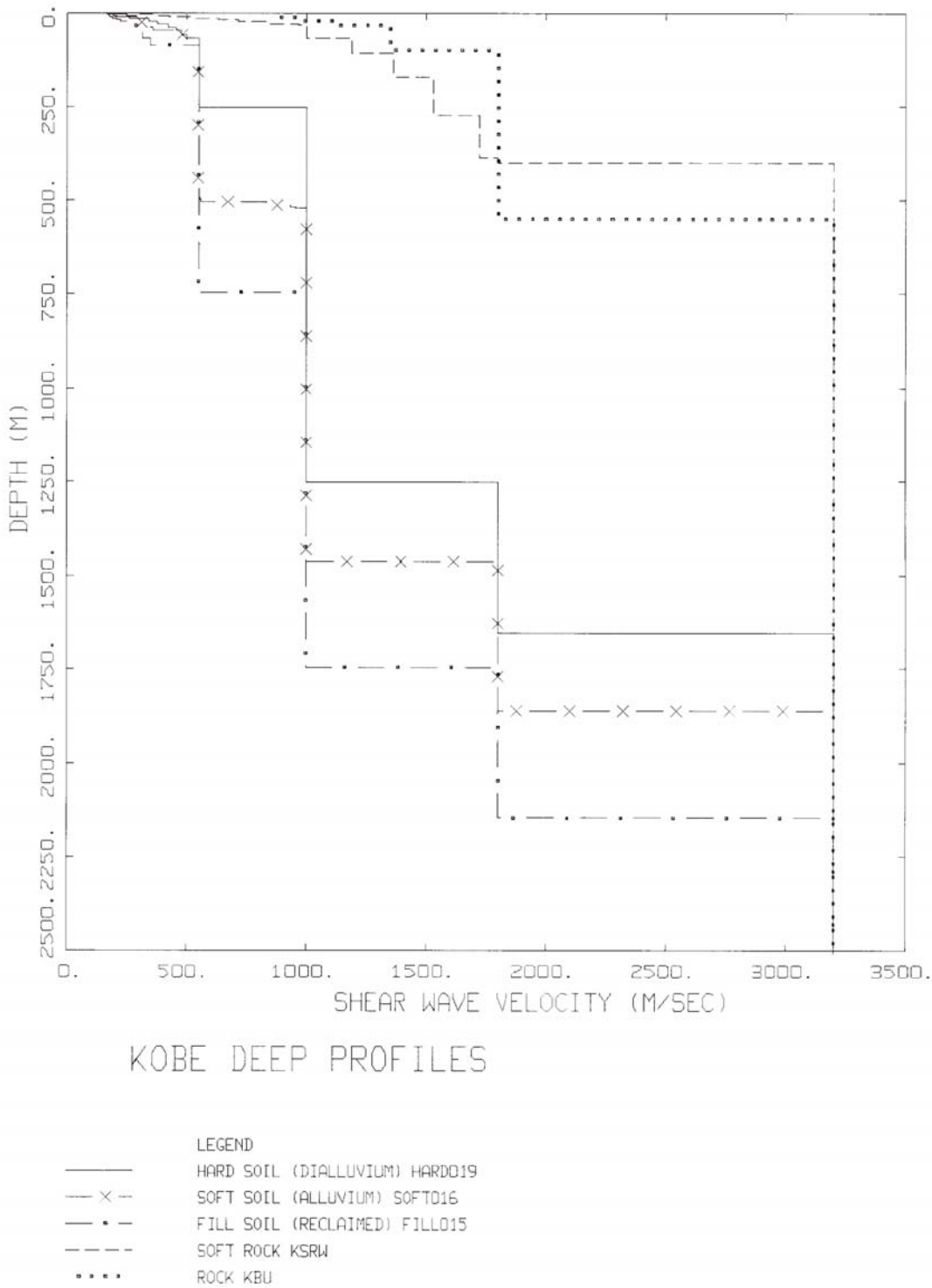


Figure 26. Deep hard, soft, and fill (reclaimed) soil profiles and generic soft rock as well as site specific Kobe University rock site profile.

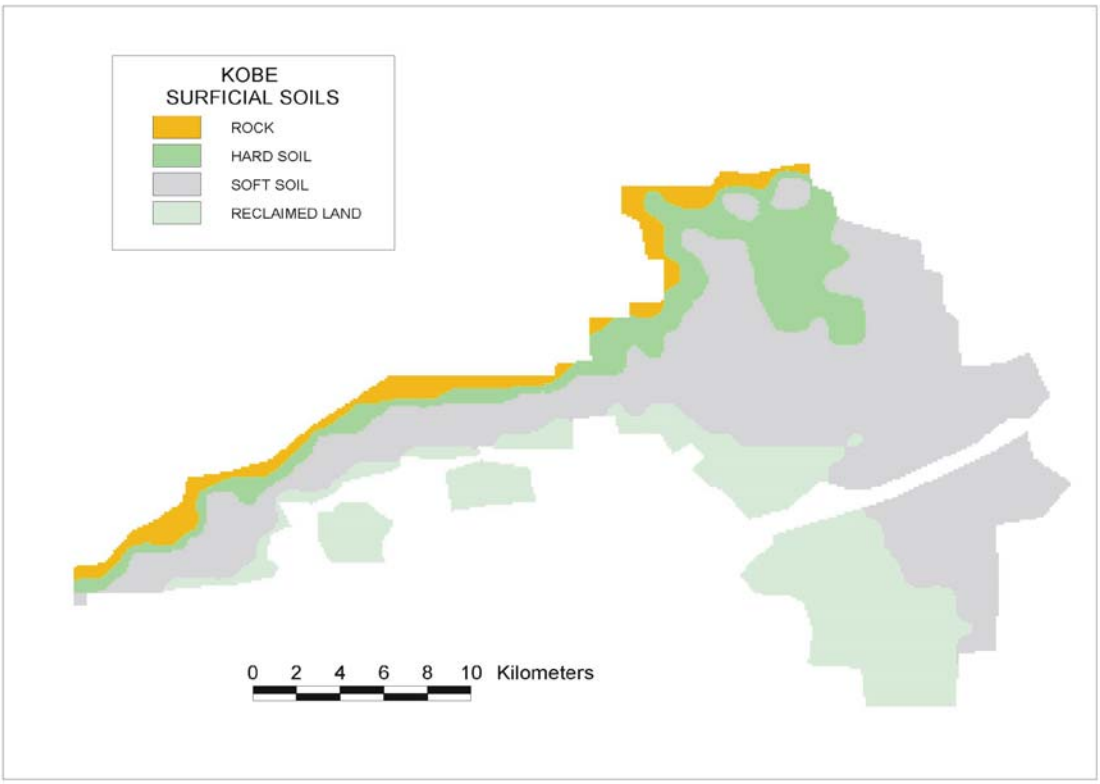


Figure 27. Surficial geology of the Kobe, Nishinomiya, and Osaka areas.

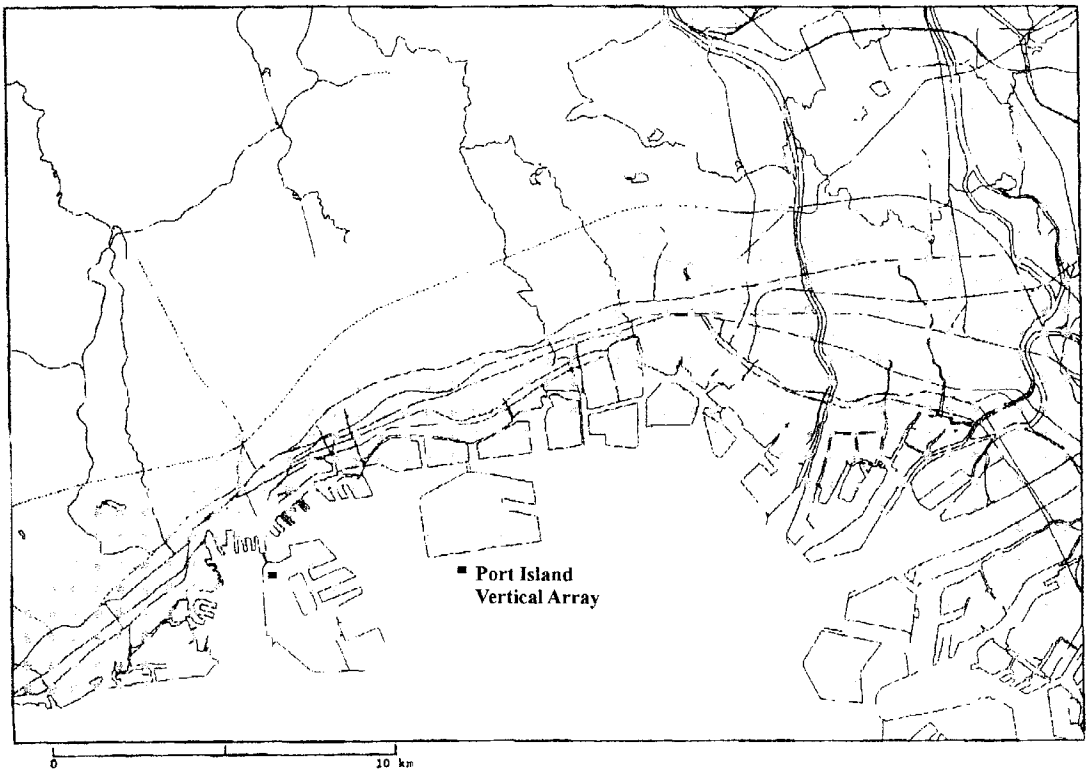


Figure 28. Site locations for liquefaction assessment.

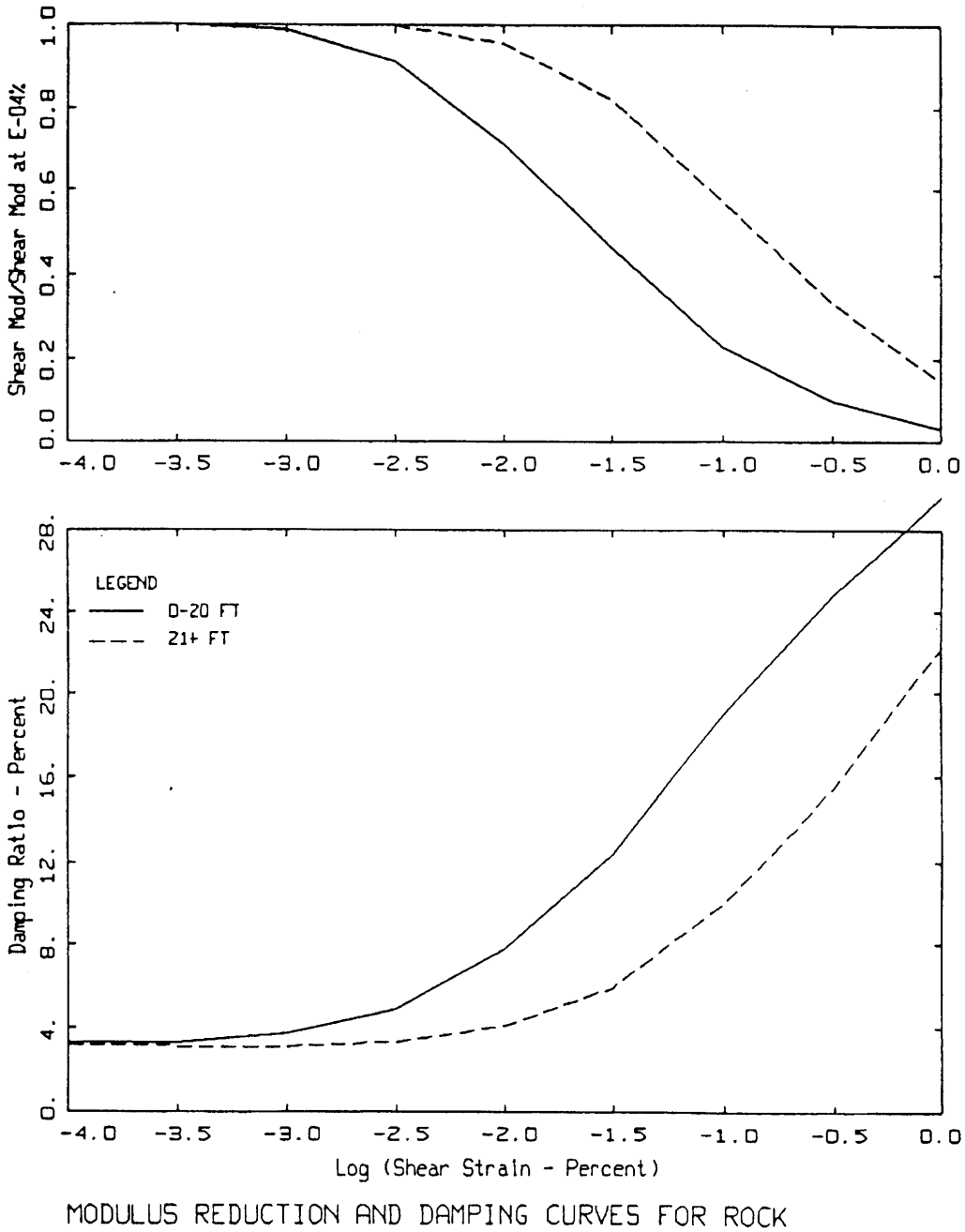


Figure 29. Generic $G/G_{max}$ and hysteretic damping curves for soft rock.

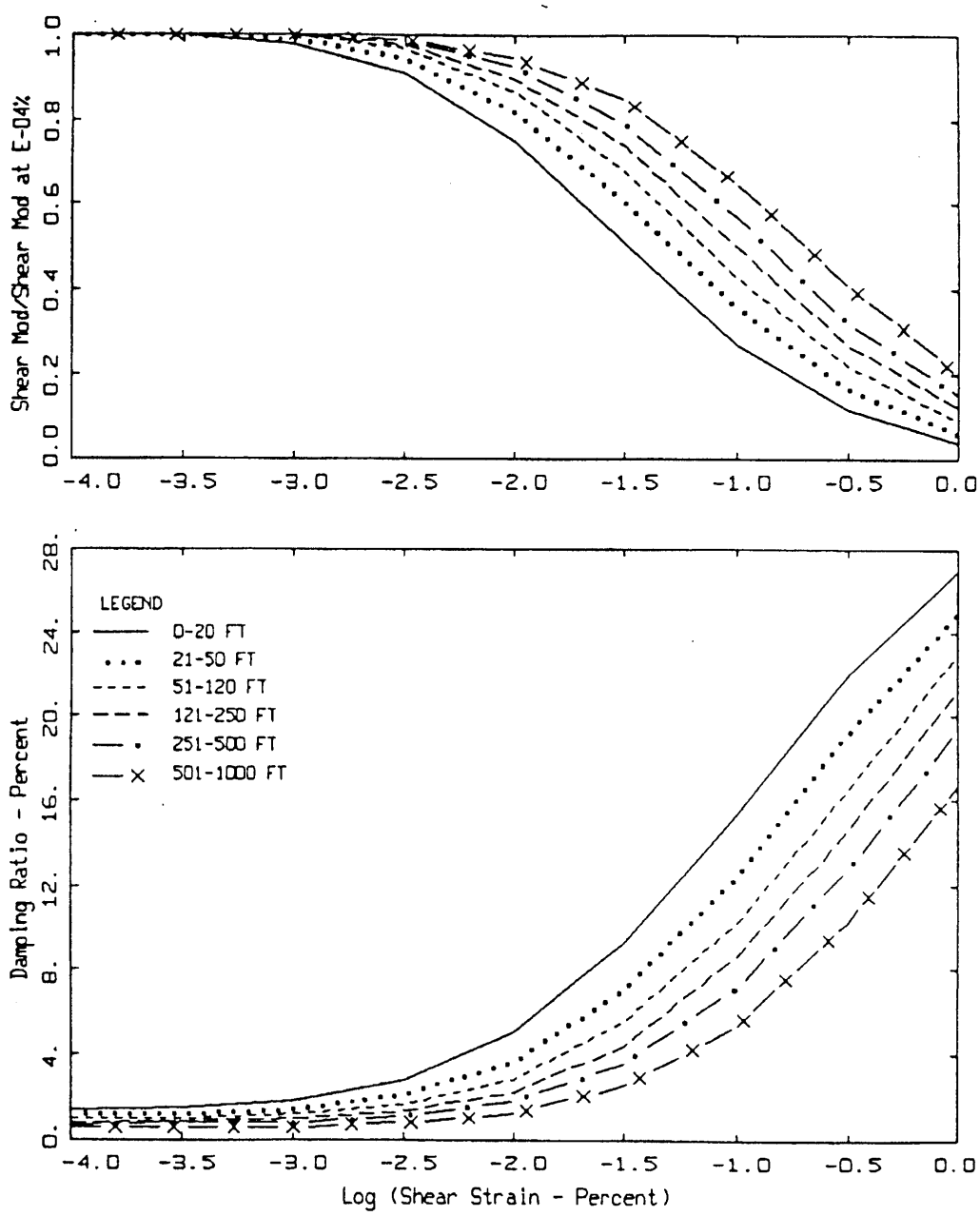


Figure 30. Generic $G/G_{max}$ and hysteretic damping curves for cohesionless soils (EPRI, 1993).

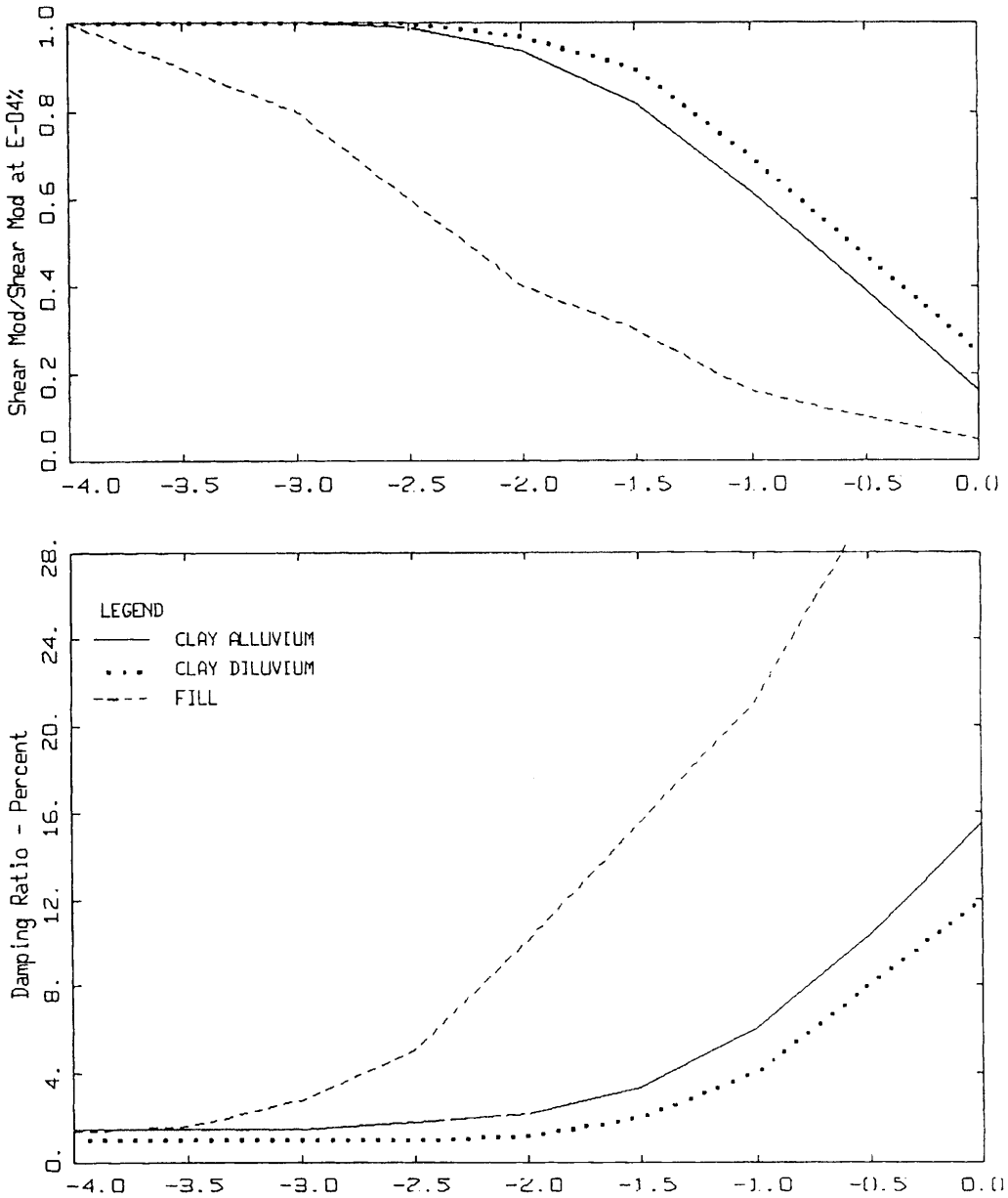


Figure 31. Generic $G/G_{max}$ and hysteric damping curves for Kobe cohesive soils (alluvial and diluvial clays) and fill materials (weathered granite, Masado).

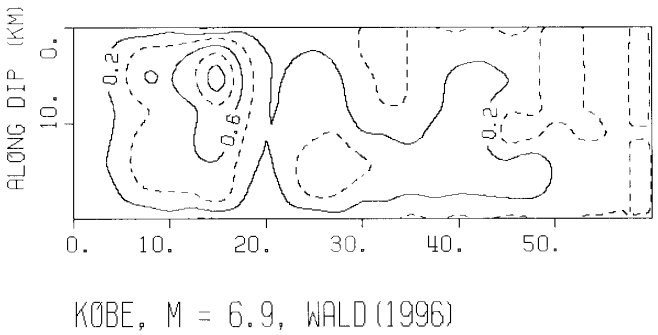


Figure 32. Slip model for the Kobe earthquake.

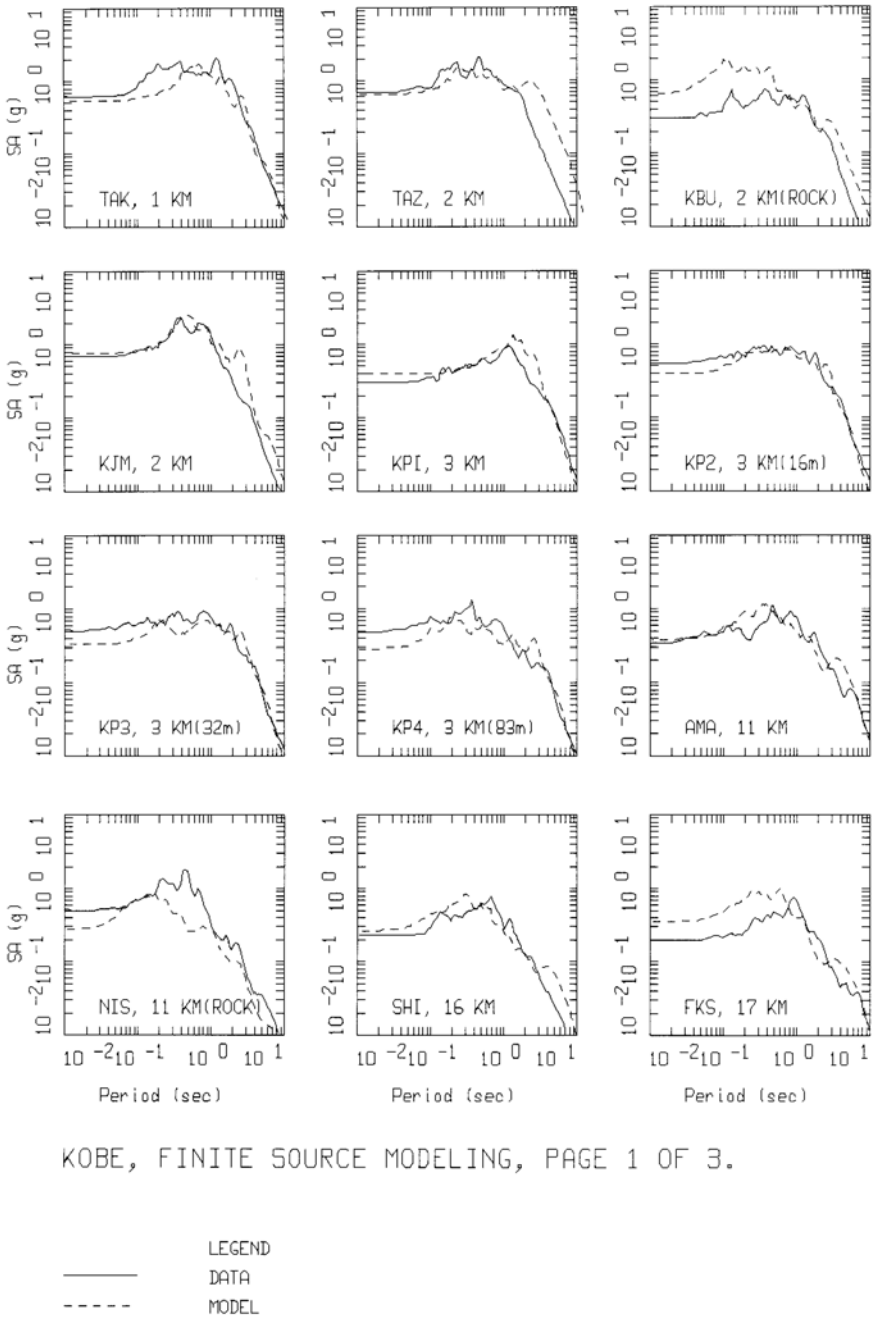


Figure Set 33. Comparison of simulations to recorded motions (5% damped response spectra).

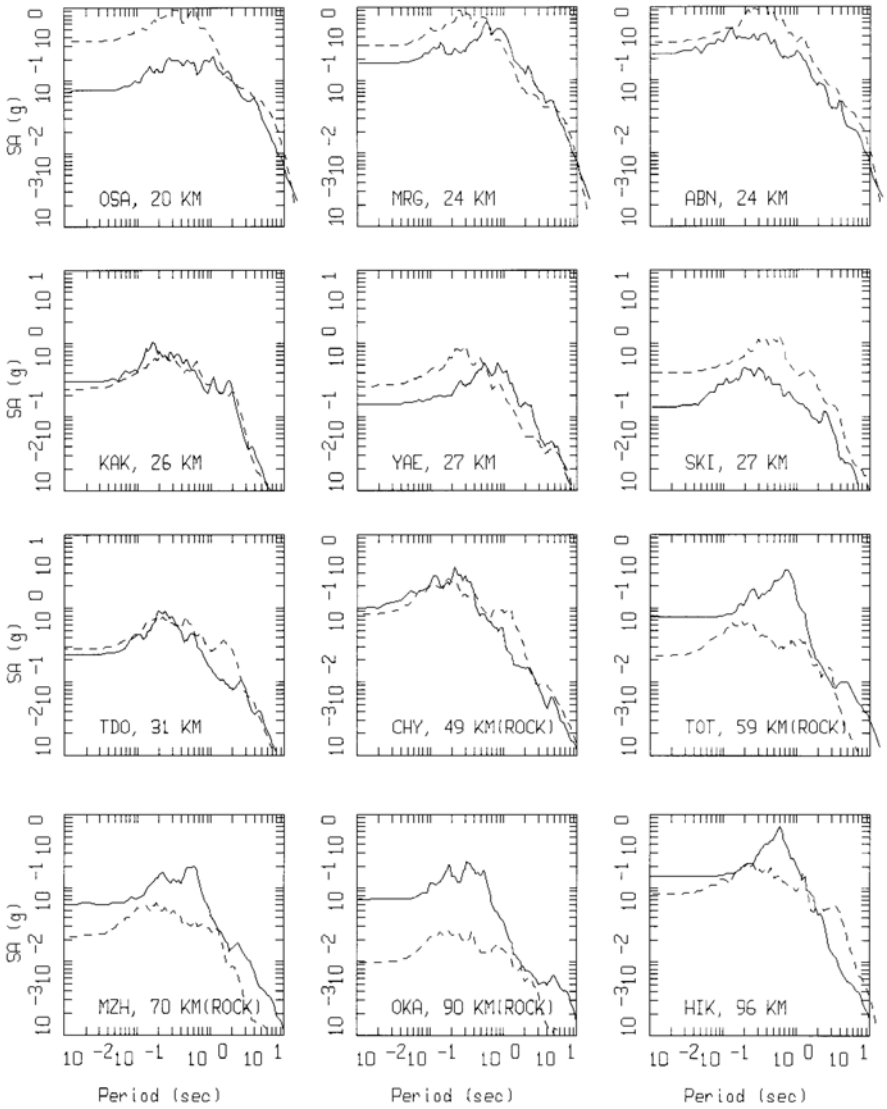


KOBE, FINITE SOURCE MODELING, PAGE 2 OF 3.

LEGEND
——— DATA
- - - - - MODEL

Figure Set 33. (Continued)

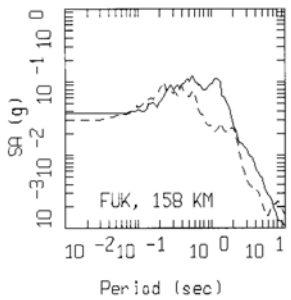


KOBE, FINITE SOURCE MODELING, PAGE 3 OF 3.

LEGEND
——— DATA
- - - - - MODEL

Figure Set 33. (Continued)

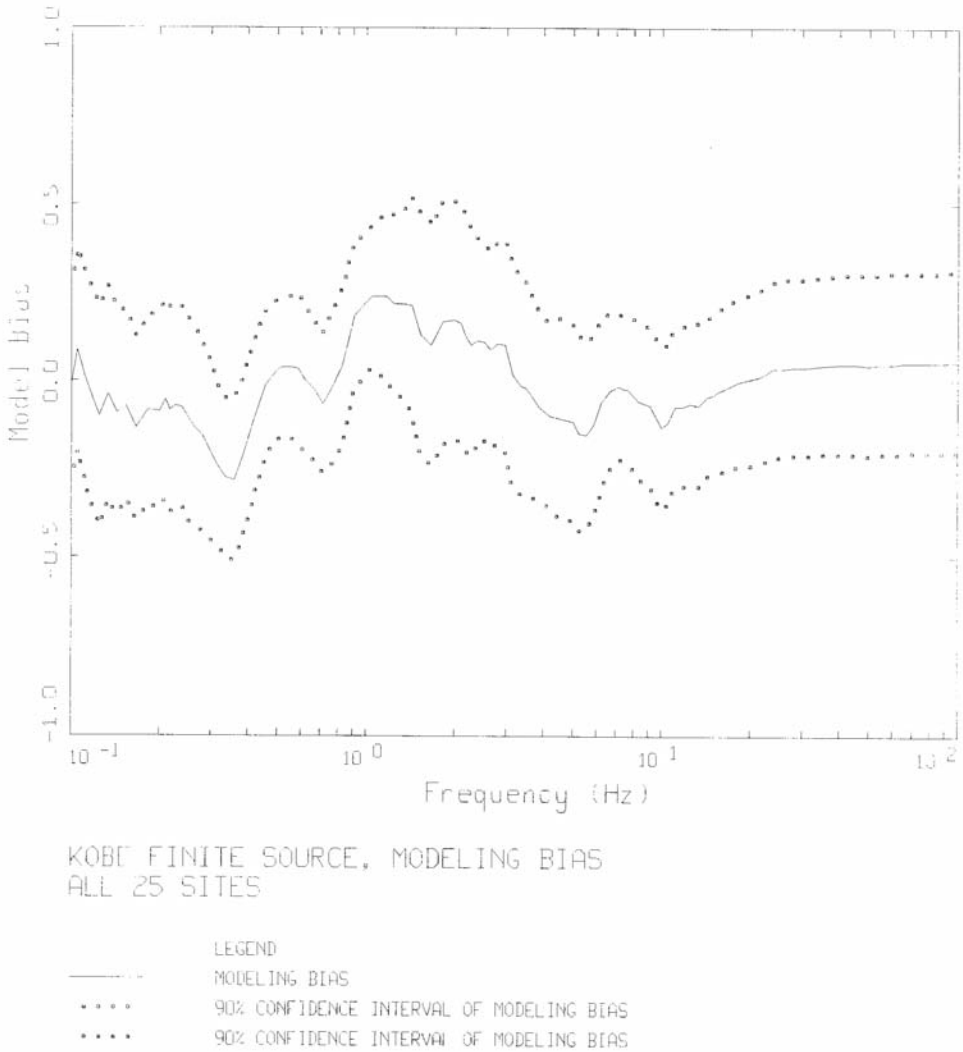


Figure 34. Model Bias estimates computed over the 25 recording sites (fault distance range of 1 – 158 km).

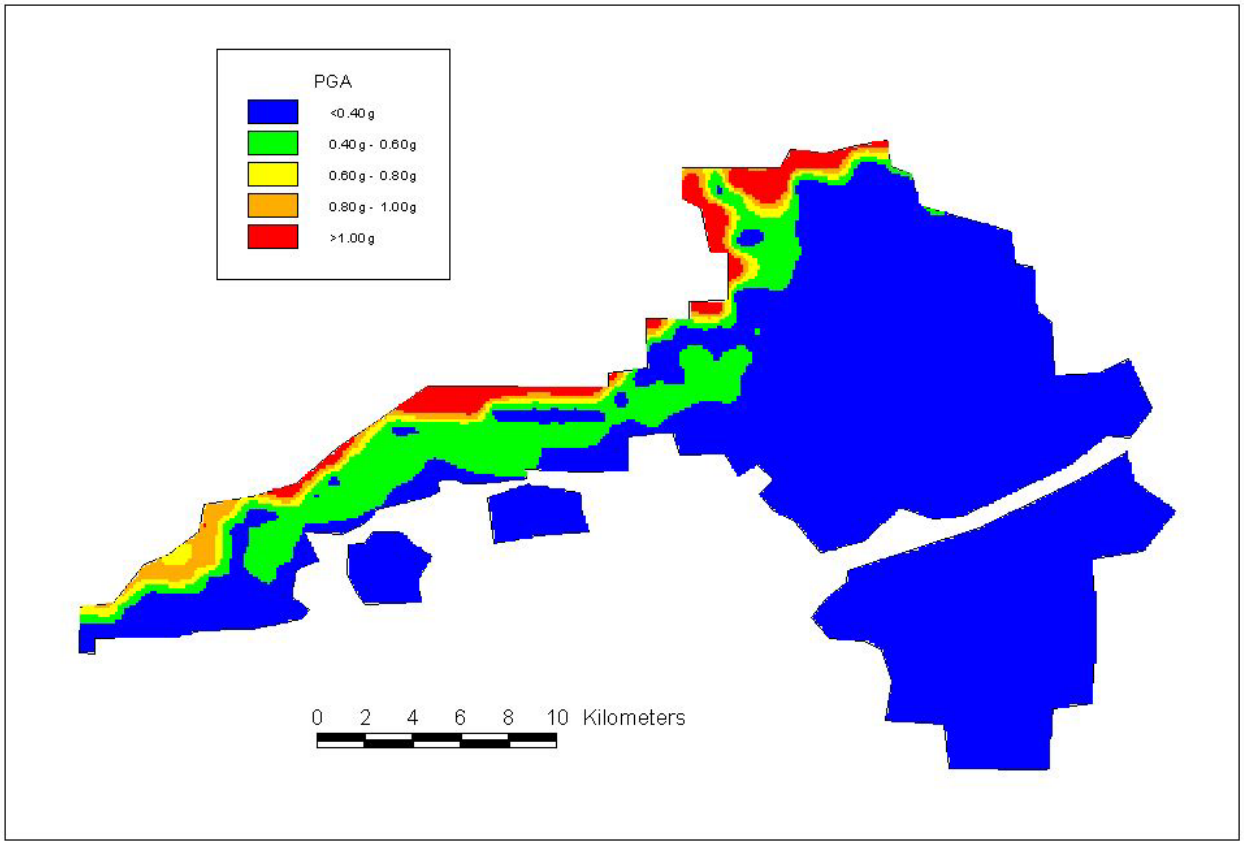


Figure 35. Median estimates of peak acceleration values at the rock, hard, soft, and fill areas of Kobe, Nishinomiya, and Osaka.

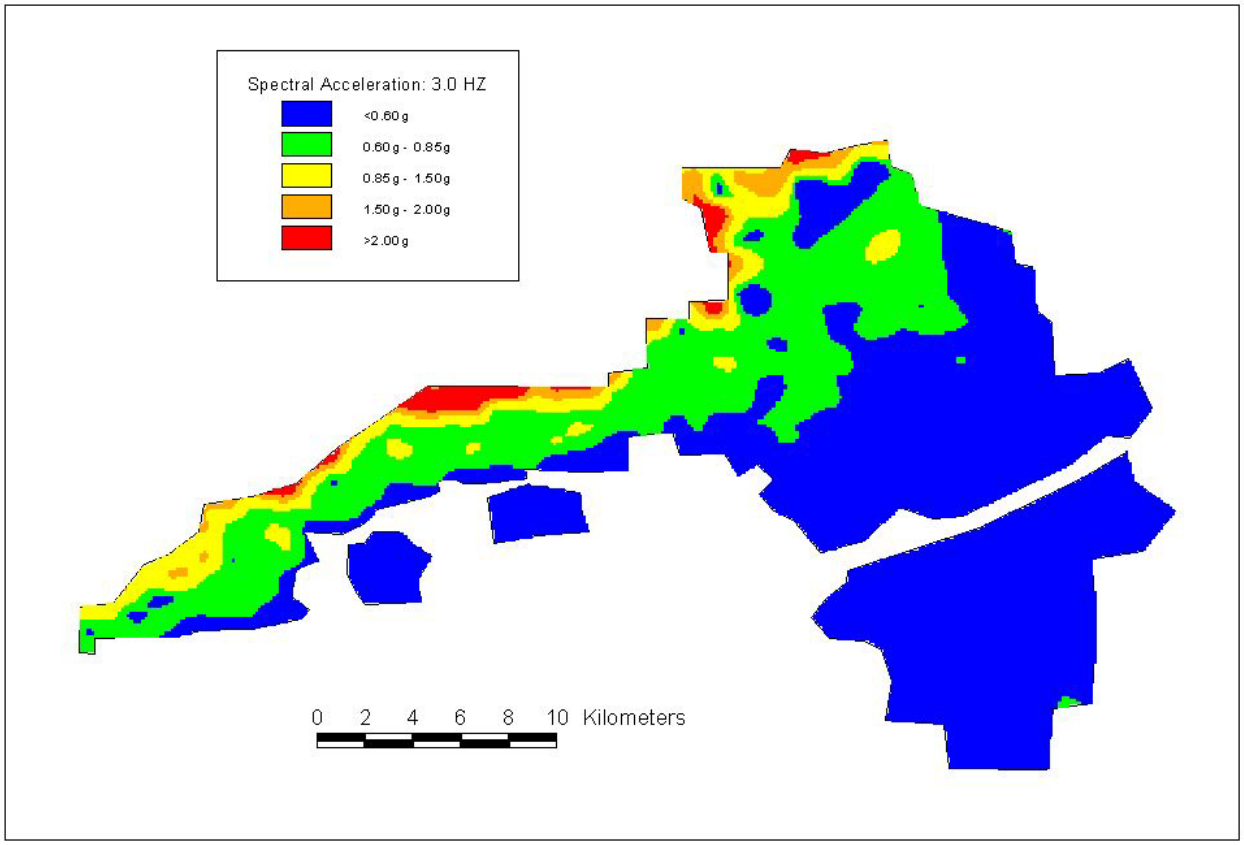


Figure 36. Median estimates of 3.0 Hz response spectra (5% damped) at the rock, hard, soft, and fill areas of Kobe, Nishinomiya, and Osaka.

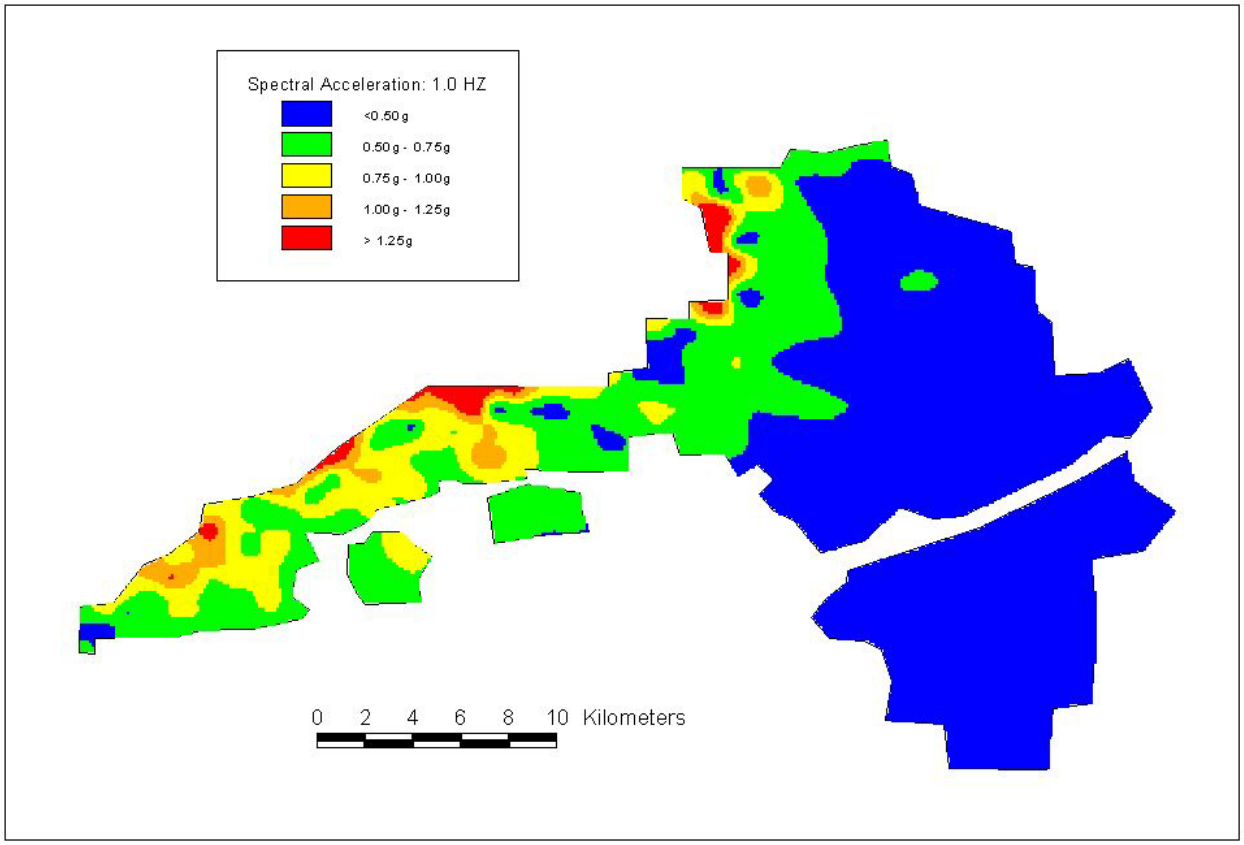


Figure 37. Median estimates of 1.0 Hz response spectra (5% damped) at the rock, hard, soft, and fill areas of Kobe, Nishinomiya, and Osaka.

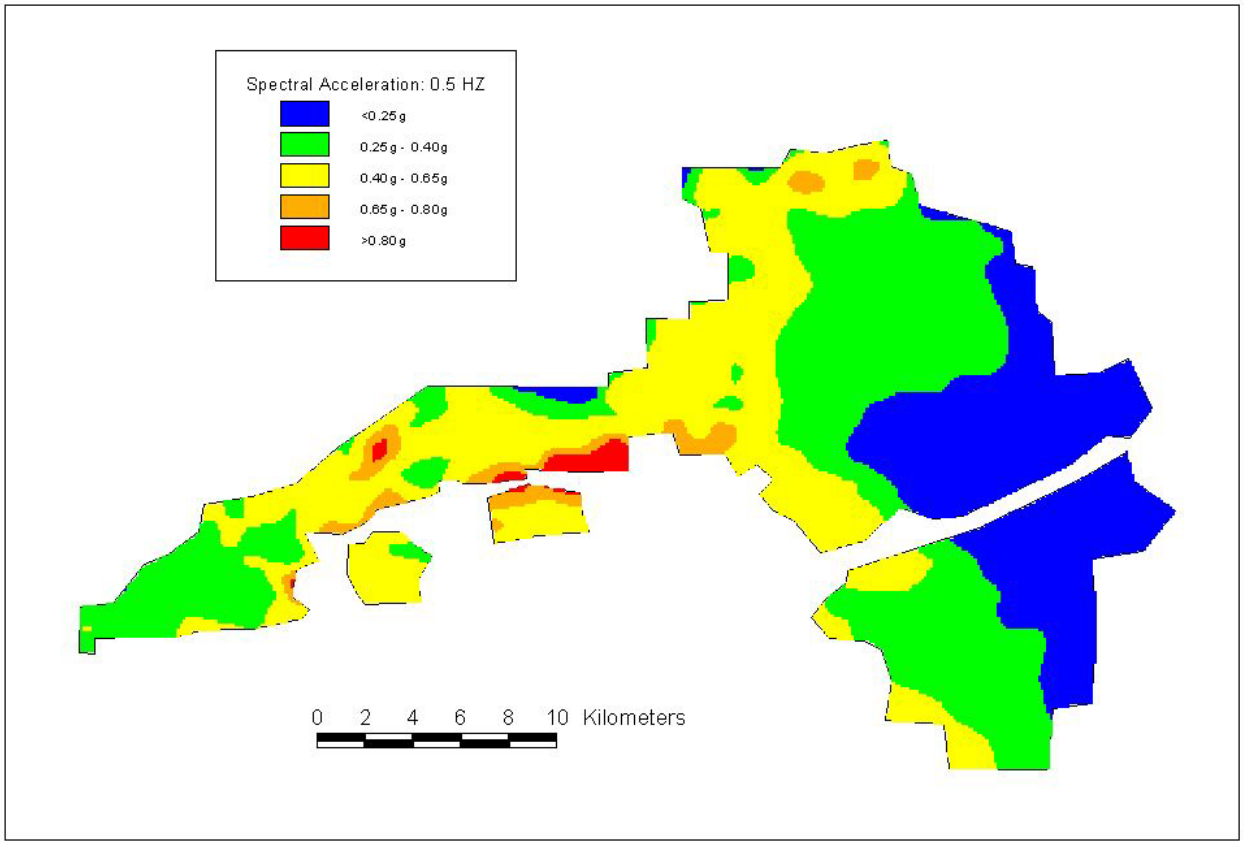


Figure 38. Median estimates of 0.5 Hz response spectra (5% damped) at the rock, hard, soft, and fill areas of Kobe, Nishinomiya, and Osaka.

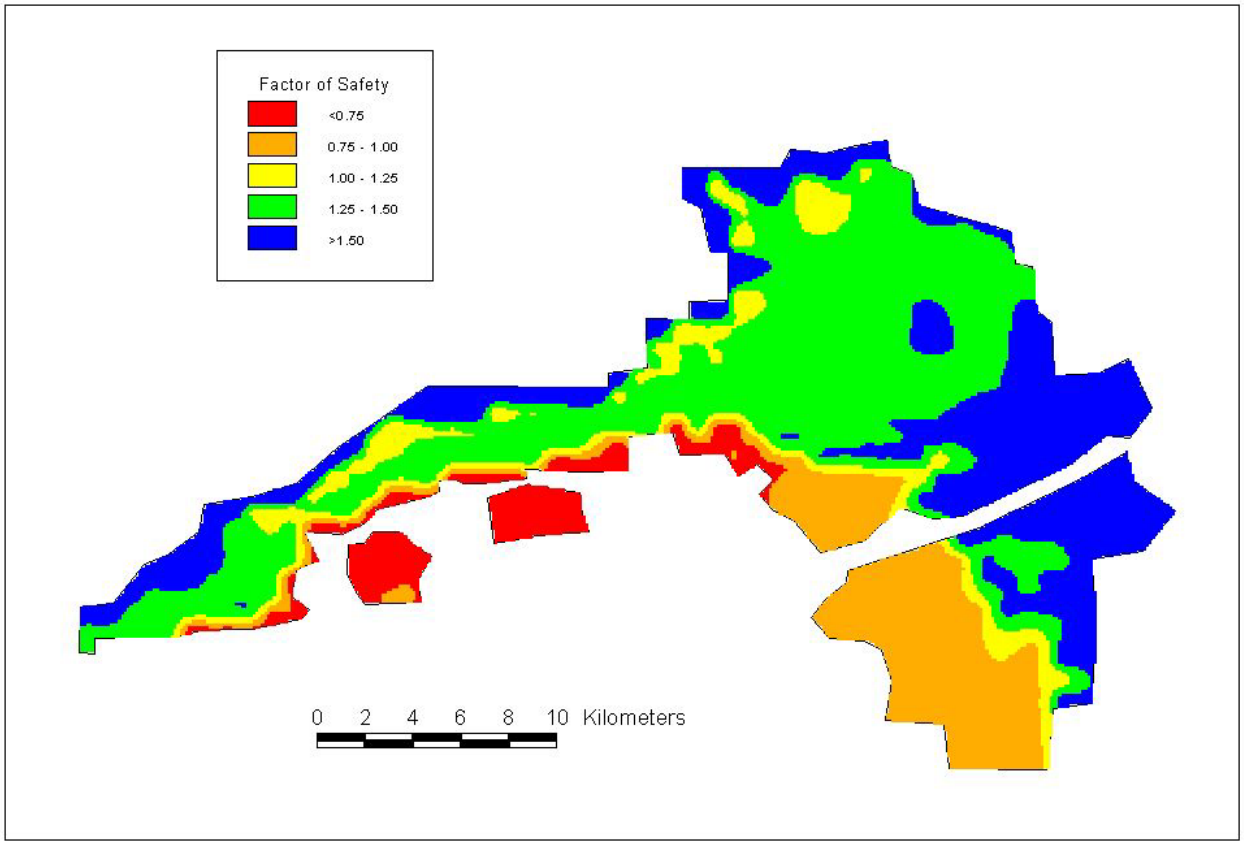


Figure 39. Median estimates of the factor of safety using the Andrus and Stokoe (2000) approach at the rock, hard, soft, and fill areas of Kobe, Nishinomiya, and Osaka.

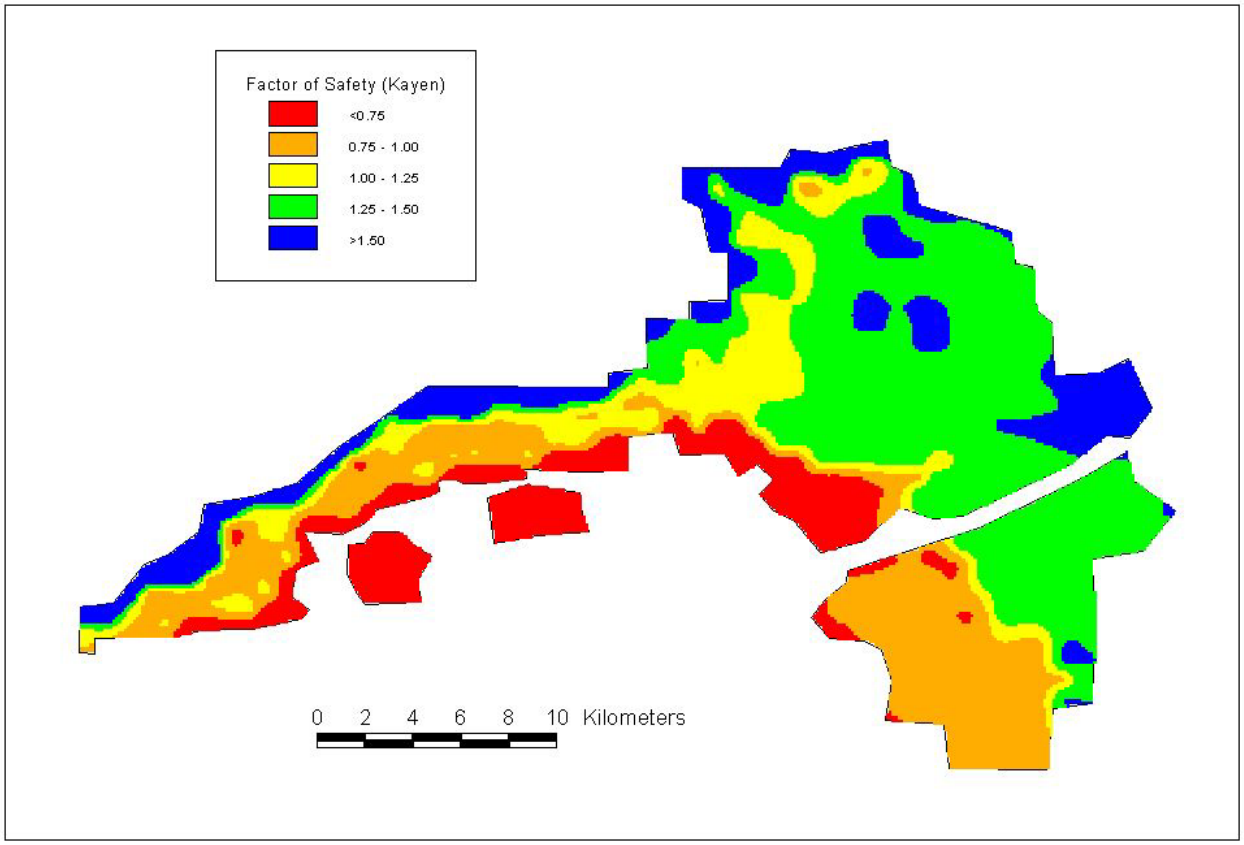


Figure 40. Median estimates of the factor of safety using the Kayen and Mitchell (1997) approach at the rock, hard, soft, and fill areas of Kobe, Nishinomiya, and Osaka.

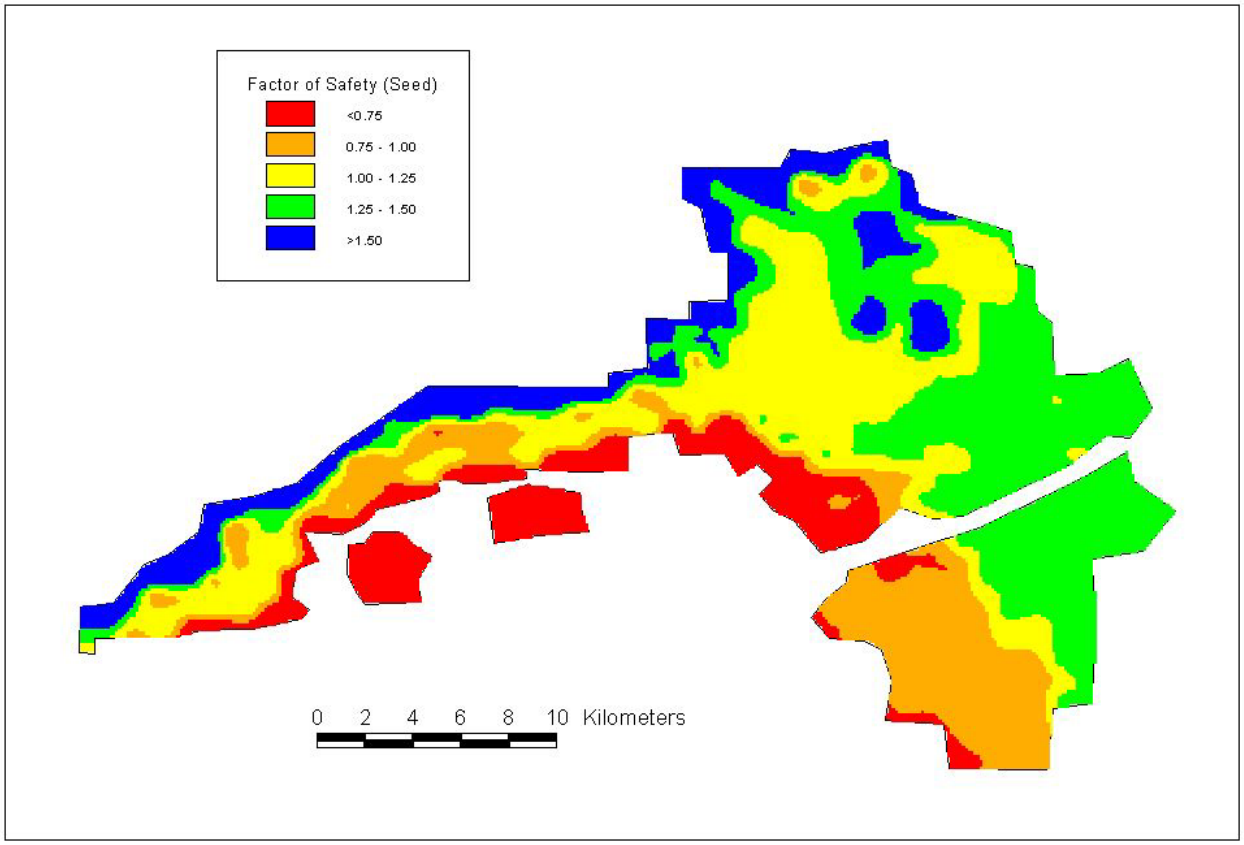


Figure 41. Median estimates of the factor of safety using the Seed et al. (2001) approach at the rock, hard, soft, and fill areas of Kobe, Nishinomiya, and Osaka.

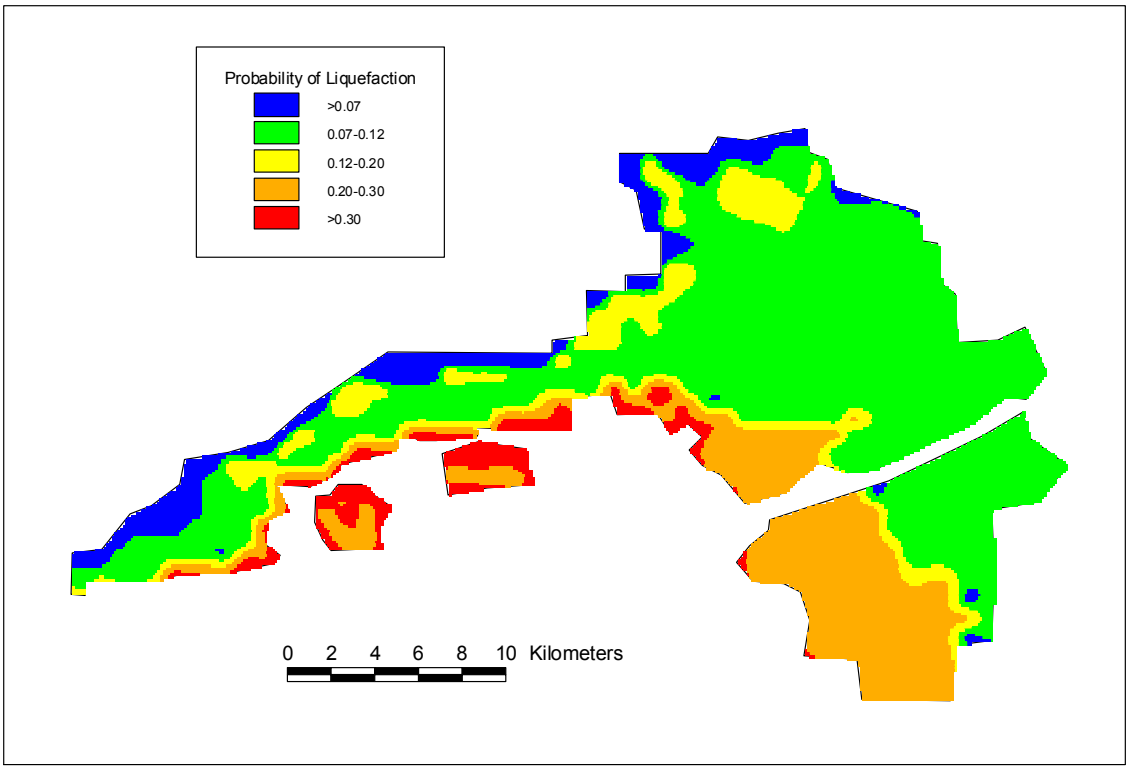


Figure 42. Median estimates of probability of liquefaction using the Andrus and Stokoe (2000) approach at the rock, hard, soft, and fill areas of Kobe, Nishinomiya, and Osaka.

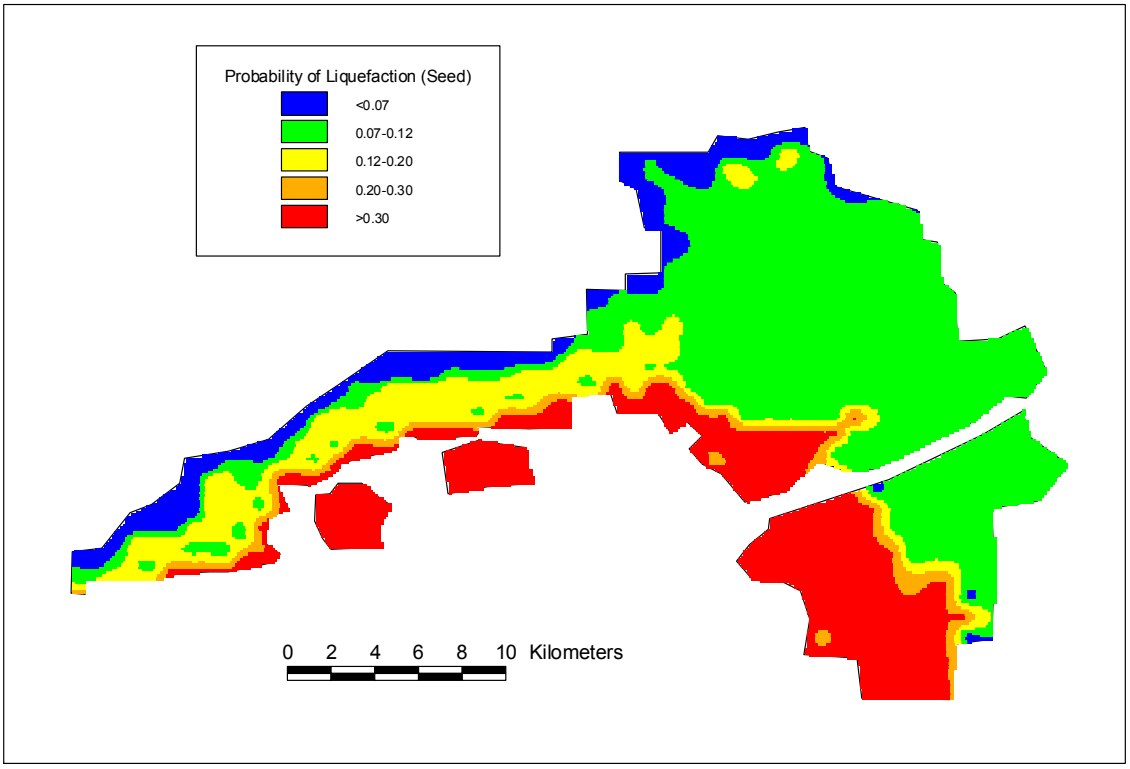


Figure 43. Median estimates of probability of liquefaction using the Seed et al. (2001) approach at the rock, hard, soft, and fill areas of Kobe, Nishinomiya, and Osaka.

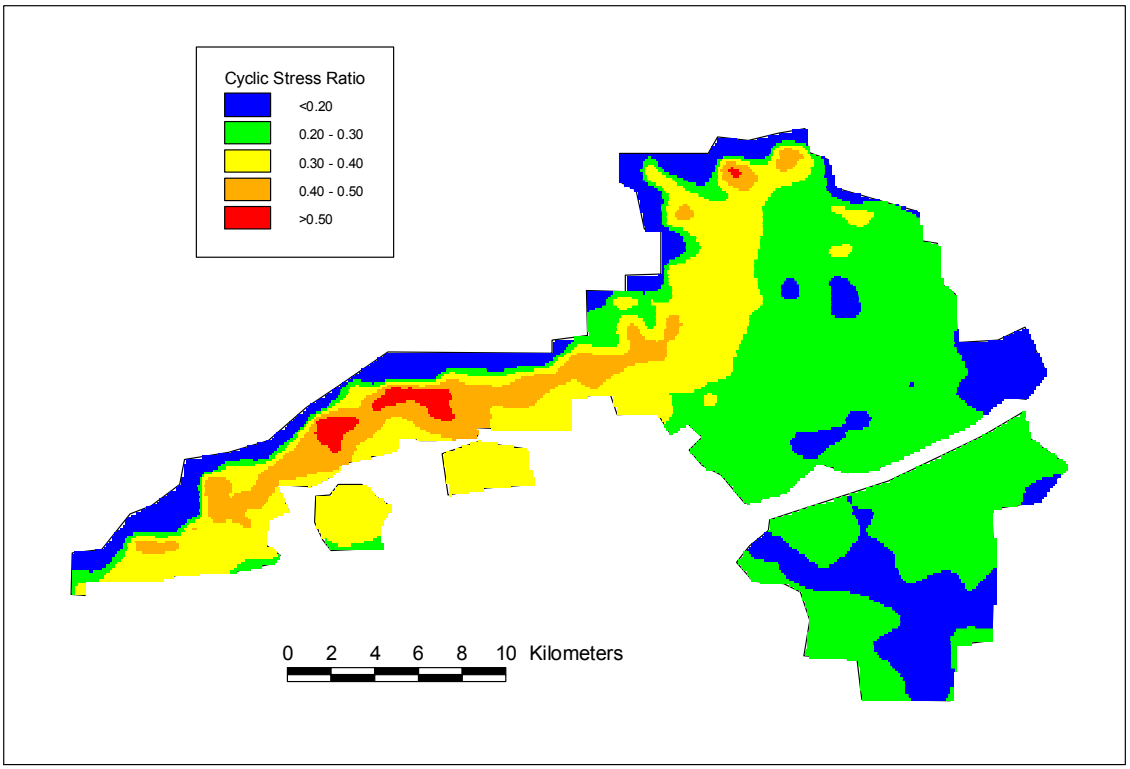


Figure 44. Median estimates of CSR for the rock, hard, soft, and fill areas of Kobe, Nishinomiya, and Osaka.

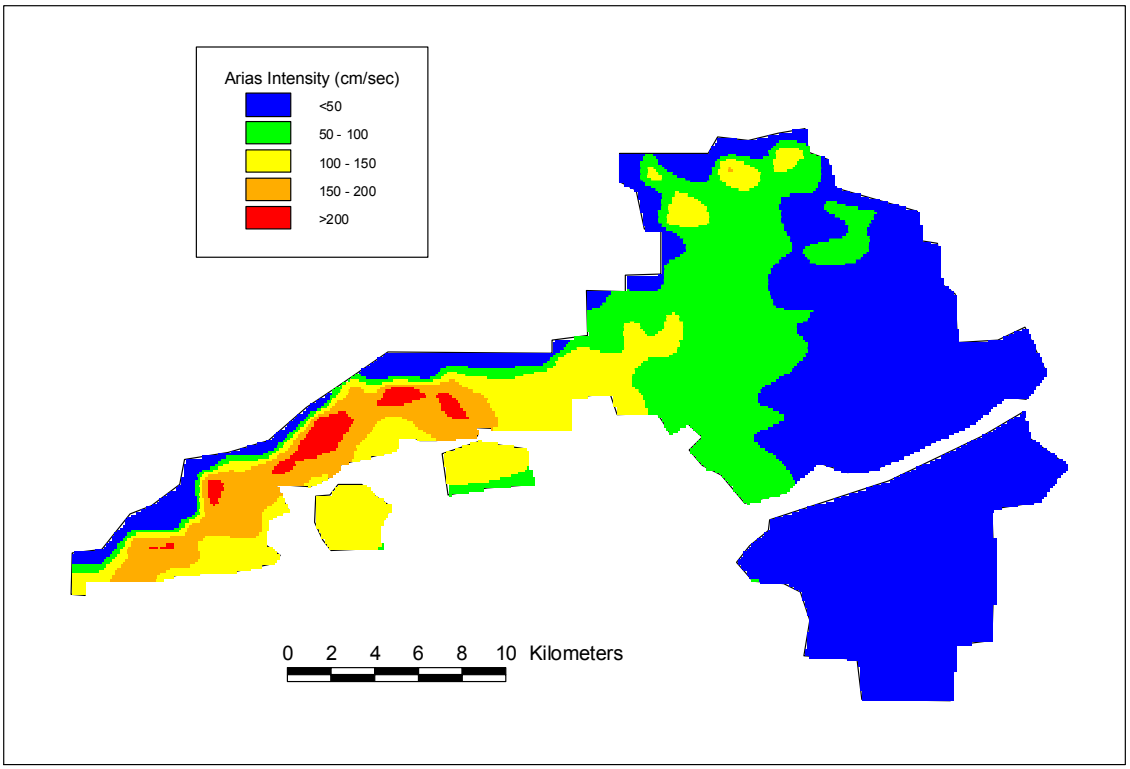


Figure 45. Median estimates of Arias Intensity for the rock, hard, soft, and fill areas of Kobe, Nishinomiya, and Osaka.

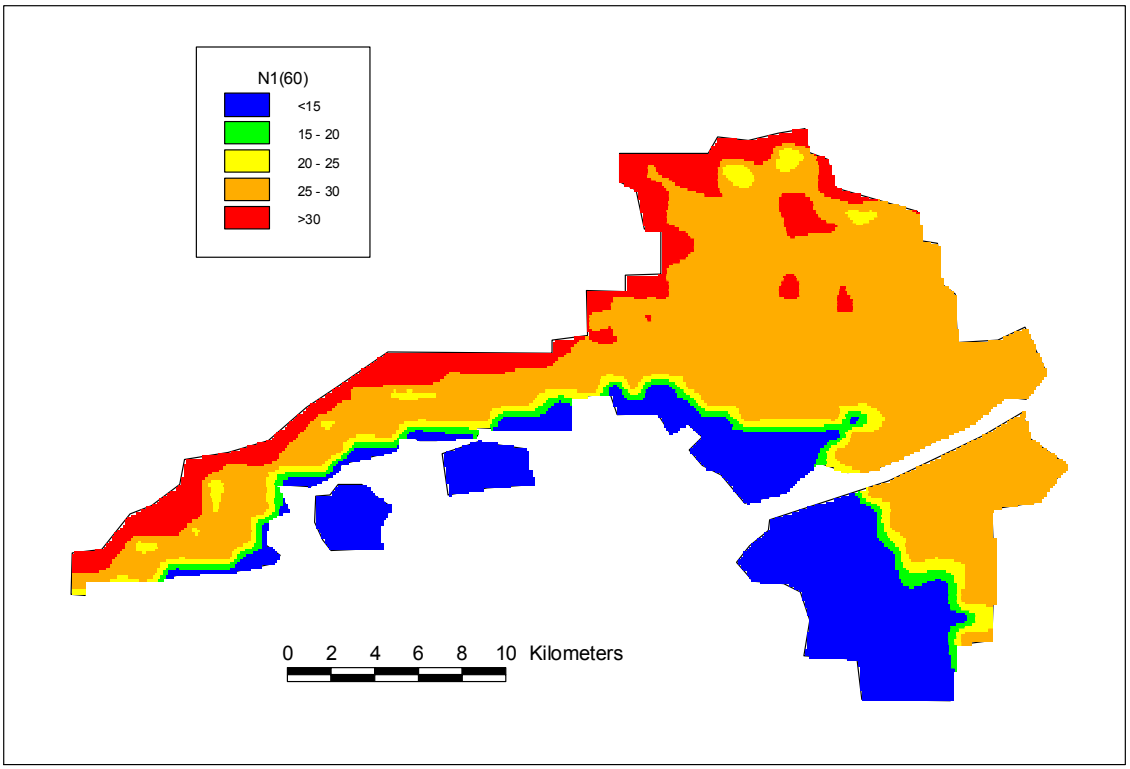


Figure 46. Median estimates of $(N_1)_{60}$ for the rock, hard, soft, and fill areas of Kobe, Nishinomiya, and Osaka.

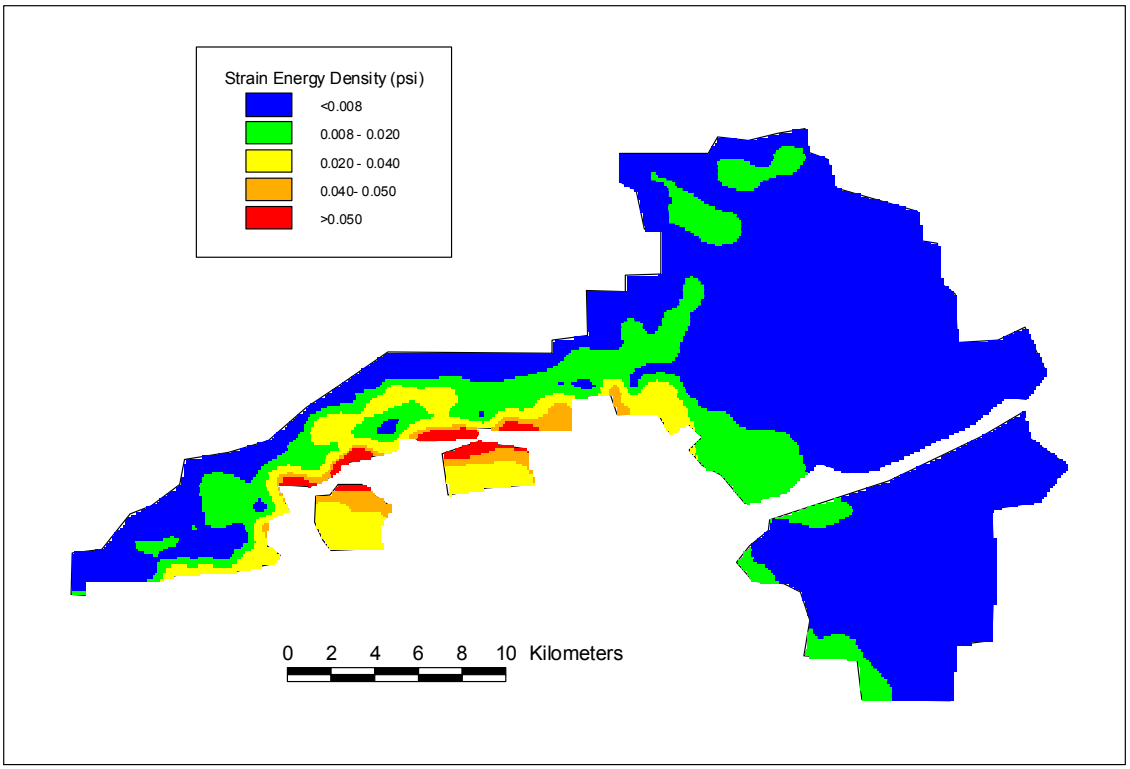


Figure 47. Median estimates of strain energy density for the rock, hard, soft, and fill areas of Kobe, Nishinomiya, and Osaka.